N d'ordre : 2012ISAL0032 Année 2012

THÈSE

Bubble dynamics and boiling heat transfer: a study in the absence and in the presence of electric fields

présentée devant

L'INSTITUT NATIONAL DES SCIENCES APPLIQUÉES DE LYON

pour obtenir le grade de

Docteur

École Doctorale MEGA

(Mécanique, Énergétique, Génie Civil, Acoustique)

Spécialité : THERMIQUE ET ÉNERGÉTIQUE

par

Samuel SIEDEL

Soutenue le 13 avril 2012 devant la commission d'examen :

BONJOUR Jocelyn	Professeur (INSA de Lyon)	-	*Directeur de Thèse*
CIOULACHTJIAN Serge	Maître de Conférences (INSA de Lyon)	-	*Co-encadrant*
COLIN Catherine	Professeur (Université de Toulouse)	-	*Rapporteur*
DI MARCO Paolo	Professeur (Università di Pisa)	-	*Rapporteur*
ROBINSON Tony	Professeur (University of Dublin)	-	*Examinateur*
TADRIST Lounès	Professeur (Université de Provence)	-	*Examinateur*

Thèse préparée au Centre de Thermique de Lyon - CETHIL UMR5008
Université de Lyon

Acknowledgements

This study has been carried out at the Centre de Thermique de Lyon (CETHIL UMR5008), National Institute of Applied Sciences (INSA de Lyon), under the direction of Prof. Jocelyn Bonjour and Dr. Serge Cioulachtjian. This PhD Thesis has been supported financially by the French ministry of National Education, Research and Technology (MENRT), which is gratefully acknowledged.

I gratefully thank Jocelyn for his advice, direction and scientific discussion, Serge for the everyday work together and his precious advices in experimental work, and Tony for his welcome in the Thermofluid Lab. in Trinity College, and for his implication in my work. Beyond our work together, I am grateful for the friendship we built along these years.

I would like to thank Prof. Paolo Di Marco from Università Di Pisa and Prof. Catherine Colin from Université de Toulouse for being reviewers of this thesis. I also thank Prof. Lounès Tadrist from Université de Provence for being examiner of this work.

I thank Florence and all the administrative staff in CETHIL. Thank you for your kindness and your help. I also thank the technicians of the lab. All our work would be impossible without you.

I thank my colleagues, and particularly all the office-mates I had during the PhD. Thanks for the time, coffee and fun spent together.

I thank Pops my lovely wife, and my daughters Luna and Ketsia. Life is good with you. Thanks for your support and for taking my mind off things when being back home.

I finally thank God my creator. Life is from Him, and my new life and relation with Him is thanks to my Lord and Saviour Jesus-Christ.

Bubble dynamics and boiling heat transfer: a study in the absence and in the presence of electric fields

Abstract:

Since boiling heat transfer affords a very effective means to transfer heat, it is implemented in numerous technologies and industries ranging from large power generation plants to micro-electronic thermal management. No matter what the scale of the technology, industries are continually demanding smarter and smaller heat exchangers. In order to achieve the design of heat exchangers with ever increasing heat flux densities, a good prediction of boiling heat transfer is required, and heat transfer enhancement techniques are to be developed.

Although having been a subject of research for several decades, an accurate prediction of boiling heat transfer is still challenging due to the complexity of the coupled mechanisms involved. It appears that the boiling heat transfer coefficient is intimately related to bubble dynamics (i.e. bubble nucleation, growth and detachment) as well as factors such as nucleation site density and interaction between neighbouring and successive bubbles. In order to contribute to the understanding of the boiling phenomenon, an experimental investigation of saturated pool boiling from a single or two neighbouring artificial nucleation sites on a polished copper surface has been performed.

The bubble growth dynamics has been characterized for different wall superheats and a experimental growth law has been established. The interaction between successive bubbles from the same nucleation site has been studied, showing the bubble shape oscillations that can be caused by these interactions. The forces acting on a growing bubble has been reviewed, and a complete momentum balance has been made for all stages of bubble growth. The curvature along the interface has been measured, and indications concerning the mechanism of bubble detachment have been suggested. The rise of bubble after detachment has been investigated, and the maximum velocity reached before a change of direction has been estimated and compared to existing models from the literature. The interaction between bubbles growing side by side has been studied: the generation and propagation of a wave front during the coalescence of two bubbles has been highlighted.

As boiling heat transfer enhancement techniques are being imagined and developed, this study also focuses on the electrohydrodynamic enhancement technique. Boiling experiments have been performed in the presence of electric fields, and their effects on heat transfer and bubble dynamics have been characterized.

The heat transfer and convective structures have been investigated in the specific experimental conditions, first in the absence of electric fields. The thermal field and convective instabilities have been described both from experimental visualizations and by numerical simulations. The modification of the convective structures by the presence of electric field has been described, showing smaller convective cells and more intense convective activity. The consequent enhancement of heat transfer has been quantified.

The electrohydrodynamic effects on bubble dynamics has then been investigated. Although the volume of the bubbles at detachment and the relationship between the bubble frequency and the wall superheat were not affected, the bubble growth curve was modified. The bubbles were elongated in the direction of the electric field, and this elongation was estimated and compared to other studies from the literature. The rising velocity of the bubble was reduced in the presence of electric field, and the behaviour of bubbles growing side by side was modified, the electric field causing the bubbles to repeal each other.

These results, obtained in a fully controlled environment, provide compelling evidence that electric fields can be implemented to alter the bubble dynamics and subsequently heat transfer rates during boiling of dielectric fluids.

Keywords: *Pool boiling, bubble dynamics, experimentation, visualization, electrohydrodynamics, EHD*

Dynamique de bulles et transferts thermiques par ébullition: étude en absence et en présence de champs électriques

Résumé:

L'ébullition est un mode de transfert de chaleur très efficace utilisé dans de nombreux systèmes technologiques comme les centrales nucléaires ou refroidissement de micro-électronique. Peu importe la taille du système, les industries ont continuellement besoin d'échangeurs de chaleurs plus petits et plus efficaces. Pour concevoir des échangeurs avec de toujours plus fortes densités de flux échangés, une bonne prédiction des transferts thermiques est nécessaire, et des techniques d'intensification des échanges doivent être développées.

La prédiction des échanges thermiques par ébullition reste actuellement très délicate, en raison de la complexité du phénomène, malgré des décennies de recherche sur le sujet. Le coefficient de transfert thermique est intimement lié à la dynamique de bulles (nucléation des bulles, croissance et détachement) ainsi qu'à des facteurs tels la densité de sites de nucléation ou les interactions entre bulles voisines et successives. La présente étude expérimentale concerne l'ébullition saturée sur un site de nucléation artificiel unique (ou deux sites voisins) sur une paroi en cuivre poli.

La dynamique de croissance des bulles a été caractérisée pour différentes surchauffes de paroi et une loi expérimentale de croissance a été établie. Les interactions entre bulles successives issues du même site ont été étudiées, montrant qu'elles peuvent provoquer des oscillations de la bulle en croissance. Les forces agissant sur une bulle en croissance ont été clairement définies, et un bilan de quantité de mouvement a été réalisé à tous les stades de la croissance d'une bulle. La courbure le long de l'interface a été mesurée, ce qui a permis de mieux saisir le mécanisme de détachement de la bulle. L'ascension d'une bulle après son détachement a été analysée, et la vitesse maximale atteinte avant un changement de direction a été estimée et comparée aux modèles existants dans la littérature. L'interaction entre bulles croissant côte à côte a été étudiée. La génération et la propagation d'une onde lors de la coalescence a été mise en évidence.

Dans le contexte de travaux de recherche sur des techniques d'intensification des échanges thermiques, cette étude se penche particulièrement sur l'intensification par électrohydrodynamique. Des expériences d'ébullition ont été réalisées en présence de champs électriques, et leurs effets sur les transferts thermiques et sur la dynamique des bulles ont été analysés.

Les transferts thermiques et les structures convectives ont été étudiées dans les conditions particulières de l'expérience, en absence et en présence d'un champ électrique. Le champ de température et les instabilités convectives ont été décrite par des visualisations expérimentales et par des simulations numériques. La modification des structures convectives par la présence de champs électriques a été décrite, montrant une activité convective intense formée de cellules convectives plus petites. L'augmentation des transferts thermiques qui en résulte a été quantifiée.

Les effets électrohydrodynamiques sur la dynamique de bulle ont été explorés. Bien que le volume au détachement des bulles et la relation entre la fréquence et la surchauffe reste inchangées, la courbe de croissance des bulles est modifiée. Les bulles sont allongées dans la direction du champ électrique, et cette élongation a été estimée et comparée à d'autres résultats de la littérature. La vitesse d'ascension des bulles est réduite en présence de champs électriques, et les interactions de bulles voisines sont modifiées: il s'avère qu'en présence de champs électriques les bulles ont tendance à se repousser.

Ces résultats, obtenus dans un environnement parfaitement contrôlé apportent la preuve que la présence de champs électriques modifie la dynamique des bulles et par conséquents les transferts thermiques associés.

Mots-Clefs: *Ébullition en vase, dynamique de bulles, expérimentation, visualisation, electrohydrodynamique, EHD*

Contents

List of Figures

Chapter 1

Introduction

1.1 Background

From time immemorial, the boiling phenomenon is known by humans. First as a natural phenomenon, as boiling can easily be observed in nature, especially in volcanic situations such as geysers and boiling lava flows. Boiling has soon become familiar by the use of boiling water for domestic needs such as cooking.

Along with the development of technology and the invention of new mechanical systems, innovative uses of boiling processes have been found, especially for the production of steam. One can refer to Hero of Alexandria and his *aeolipyle*, known as the first steam engine, or to industrial processes such as boiling brine into pure salt.

From the 18^{th} century, the industrial revolution brought the boiling phenomenon to the fore by using this process in several of the major inventions. The steam engine, and later the steam turbines (Rankine and Hirn cycles) used a boiler for steam production as a source of thermodynamic energy to produce a mechanical work. At the same period, several refrigeration systems were developed, including those using a vapour-compression refrigeration cycle (inverse Rankine cycle). In such a cycle, a fluid flows in a closed loop, being condensed at high pressure after a compression and boiling at low pressure after an expansion.

In the 20^{th} century, two major reasons led to the expansion of the use of boiling in systems. The first reason is the widespread of the use of electricity which caused the wide development of power plants. Many types of electric power plants use a thermodynamic cycle that requires boiling in order to produce water steam that is expanded in turbines. For example, nuclear power plants use such a cycle.

The second reason is the development and spreading of electronics in all domains of technology. Electronic components produce and dissipate heat. This heat needs to be removed in order to maintain a reasonable temperature within the components. Several sys-

tems ranging from natural convection to complex heat pipes have been developed in order to achieve effective heat removal. Boiling being recognized as a very effective mean to transmit heat, systems using boiling have been developed in order to cool down components dissipated high heat fluxes.

Systems using boiling are now spread everywhere in the modern society. Whether when boiling water to prepare a tea or when taking a fresh beer in the fridge, when using a laptop whose processor is cooled by a heat pipe and which requires electricity produced by a steam turbine power plant, when living in a warm house heated by a heat pump, boiling systems are omnipresent.

In all theses technologies, an optimal control and design is required in order to ensure safety, reliability and effectiveness of the systems. The electronic, the refrigeration and the electricity production industries are continually increasing the power and reducing the size of the components, demanding smarter and smaller heat exchangers. Two major objectives arise in order to meet such requirements: the boiling heat transfer needs to be well understood and predictable, and new methods allowing enhancement of boiling heat transfer need to be developed.

1.2 Motivation of the study

Better designs of heat exchangers are needed in order to achieve heat dissipation of ever increasing heat flux densities. Pool boiling heat transfer, as boiling within a bulk liquid at rest, is characterized by very high dissipated heat fluxes whilst requiring low driving temperature differences. For this reason, pool boiling is a good candidate to meet the needs of high flux densities cooling systems.

In the so-called *nucleate pool boiling regime*, the high heat transfer rates are primarily due to enhanced convection, transient conduction, microlayer evaporation, and contact line heat transfer brought about by the motion of bubbles [93]. The relative contribution of each individual heat transfer mechanism to the overall heat transfer rate is sensitive to the boiling condition and difficult to predict. What is obvious is that the boiling heat transfer coefficient is intimately linked to the bubble dynamics: that roughly being bubble nucleation, growth, and detachment, as well as factors such as nucleation site density and interactions between neighbouring and successive bubbles [53]. Therefore, in order to gain insight into the heat transfer mechanisms during boiling a fundamental understanding of the bubble dynamics is required.

Consequently, bubble dynamics has been a constant subject of research for several decades. The prediction of all parameters governing the fundamental mechanisms of boiling at the scale of a single bubble have been attempted through the means of theoretic modelling, experimental correlation or numerical simulation, with mixed results. The complexity of the phenomenon, due to the diversity of scales involved, to the coupled temperature and

velocity fields and to the characterization of the surface have led to a number of simplification hypotheses in theoretical models that their applicability is often uncertain. The experimental investigations have their own difficulties of measuring accurately and with a high time resolution physical parameters in a *3*-dimensional and multi-scale environment. Numerical simulation, although being a promising prediction method, requires a good understanding and modelling of the mechanisms involved together with reference experimental data to validate the results obtained.

Along with the research of *natural* boiling, new heat transfer enhancement techniques have been conceived and developed. Some methods are called passive as they consume no energy. These methods imply a modification of the surface (such as structuring of the surface [37] or modification of the wettability) or of the fluid used (such as using binary mixtures or solvents). Other methods are called active because they need external forces to interact with the boiling fluid (such as ultrasounds or surface vibration). One of the active techniques is to generate an electric field within the boiling fluid to modify the boiling behaviour by the contribution of electric body forces [104]. This method is commonly called electrohydrodynamics or EHD.

The prediction of heat transfer in the presence of electric fields meets the same difficulties than *natural* boiling due to a partial understanding of the fundamental mechanisms involved. The present work aims at pushing further the actual limits of the understanding of boiling at the scale of a single bubble.

1.3 Objectives

An original experimental facility has been designed and built in order to perform boiling experiments in a fully controlled environment. Experimental test samples have been fabricated in order to obtain boiling on a single or on two neighbouring artificial nucleation sites of known geometry. Advanced measurement techniques and procedures were employed, such as the use of high-speed digital videography coupled with a short field telescope. Specific post-processing of the experimental data has been developed. Such an experimental strategy has been set up in order to achieve the following objectives:

- to gain a better insight and understanding of the fundamental bubble dynamics in the case of boiling.

- to describe and determine the electrohydrodynamic effects on bubble dynamics and heat transfer at the scale of a single or of two bubbles.

1.4 Layout of the thesis

This thesis is divided into seven chapter with several appendices. It is organized as follows:

Chapter 1 is the present chapter. It presents a background to the study as well as its motivation and objectives.

Chapter 2 is an introduction to the fundamental concepts that are necessary to have in mind in order to clearly understand the methods and results presented. It develops only subjects that are not investigated further. The main focus centres of this work are introduced by a proper literature review in the chapters where they are developed.

Chapter 3 presents the experimental facility used in this study. The experimental procedures and the post-processing of the data are explained. The uncertainties on the measurements are discussed.

Chapter 4 focuses on heat transfer and on electrohydrodynamic enhancement of heat transfer. The thermal field is investigated by studying experimentally and numerically the convective structures above the heated surface.

Chapter 5 focuses on bubble dynamics in the absence of electric fields. Bubble growth is investigated along with the bubble frequency and instantaneous vapour production for different wall superheat conditions. The oscillating nature of the time evolution of the bubbles shapes during their growth is analysed. The momentum balance of the bubble is discussed and computed during the whole bubble growth event, as well as the curvature along the interface. The interaction between neighbouring bubbles are investigated. Eventually, the rise of the bubble after detachment is analysed and compared to other studies.

Chapter 6 presents an investigation of the electrohydrodynamic effects on bubble dynamics. The changes to bubble growth dynamics are analysed, as well as the shape deformation induced by electric forces. The influence of electric fields on lateral coalescence of bubbles and on bubble rising velocity are also investigated.

Chapter 7 presents the general conclusions of this study and its perspectives.

Chapter 2

Introduction to fundamental concepts

Boiling heat transfer is characterized by very high dissipated heat fluxes whilst requiring low driving temperature differences. Since it affords a very effective means to transfer heat, it is implemented in numerous technologies and industries ranging from large power generation plants to micro-electronics thermal management. No matter what the scale of the technology, industries are continually demanding smaller and smarter heat exchangers.

For such reasons, boiling heat transfer has been a major field of research for several decades. According to the scientific search engine sciverse.com*, over 1.6 million scientific publications concern boiling. Due to the complexity of the mechanisms involved in boiling, the fundamental processes governing boiling heat transfer are not fully understood and are still a subject of investigation. This work aims at bringing a new contribution towards a better description, understanding and prediction of boiling.*

A complete literature review on the subject of boiling is not possible, and dozens of books have already been written concerning some aspects of boiling. This section aims at providing the necessary information to understand the background and the relevance of the results presented in this work. A deeper literature study and a state-of-the-art of the specific topics investigated will be presented along the document each time a new subject will be tackled (e.g. bubble volumetric growth, momentum balance, thermo-capillary convection, bubble rise velocity, elongation of a bubble due to EHD, etc.). The present section is an introduction to the fundamental concepts, and focuses on topics that will not be developed further.

2.1 Nucleation

In the development of classical thermodynamics, phase transitions are treated as if they occurred as quasi-equilibrium processes at the equilibrium saturation conditions. However,

real phase transformations usually occur under non-equilibrium conditions ([23], page 127). In real vaporization processes, some liquid in the system is almost always superheated above the equilibrium saturation temperature.

In this section will first be described the basic thermodynamics of phase change, and the equilibrium condition of a bubble in a liquid. The case of bubble nucleation will then be presented, first within a homogeneously superheated liquid and then on a heated surface.

2.1.1 Liquid-vapour phase change thermodynamics

In a *Clapeyron* diagram of a fluid (Fig. 2.1), there are several areas where the fluid can be either in a liquid or vapour state, or where both phases coexist. A curve called *binodal* marks the borders of the two-phase region.

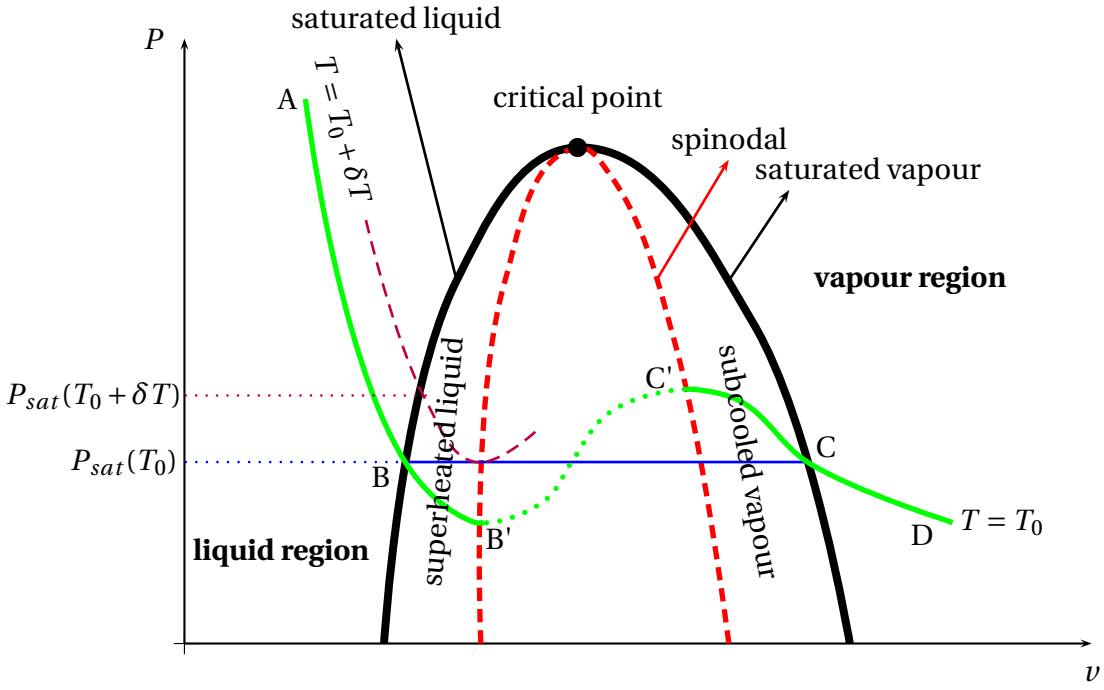

Figure 2.1: Clapeyron diagram of the *liquid-vapour* region of a fluid

Let us consider the isotherm curve $T = T_0$. The fluid is at a stable liquid state between **A** and **B** (subcooled liquid) and at a stable vapour state between **C** and **D** (superheated vapour). On the straight line between **B** and **C**, in equilibrium thermodynamics, liquid and vapour phases coexist in stable equilibrium, with a uniform pressure and with a flat interface.

From the view point of non-equilibrium thermodynamics, other states of the liquid or vapour phase can exist. For example, the volume of the saturated liquid phase at $T = T_0$ (point **B**) can be increased up to point **B'** (this will lead to a reduction of the pressure) while maintaining the same temperature. The liquid would be at a metastable state without the

occurrence of any phase change. This is true as well for the vapour phase between **C** and **C'**. These metastable states are limited by a curve called *spinodal* (drawn as a dashed red line in Fig. 2.1) that corresponds to the minimum and maximum values of the different isotherm curves. The spinodal curve is the ultimate border of a single phase state (with the liquid phase at the left side and the vapour phase at the right side of the spinodal).

Let us now consider a heating transformation at a constant bulk pressure of $P = P_{sat}(T_0)$. Liquid will be heated up to the saturation temperature, and above in the superheated liquid region. When the nucleation conditions of a bubble are fulfilled[1], vapour and liquid phases will coexist. They will be at the same temperature $T = T_0 + \delta T$, but at different pressure. The liquid will be at bulk pressure $P_{sat}(T_0)$ and the vapour will be at a higher pressure $P_{sat}(T_0+\delta T)$ corresponding to the saturation pressure of its temperature. In order to balance the mechanical forces acting on the interface, this latter will be curved towards the vapour phase. The mechanical equilibrium at an interface is detailed in the following section by introducing the Laplace-Young equation.

2.1.2 Pressure difference through an interface

The surface tension σ acting tangentially to an interface results in an over-pressure in bubbles or drops, or in a pressure gap between both sides of any curved interface. Let us introduce a case of study to explain this phenomenon.

A spherical drop of radius R of a fluid A is surrounded by a stagnant fluid B, in the absence of any gravity or acceleration field (see Fig. 2.2).

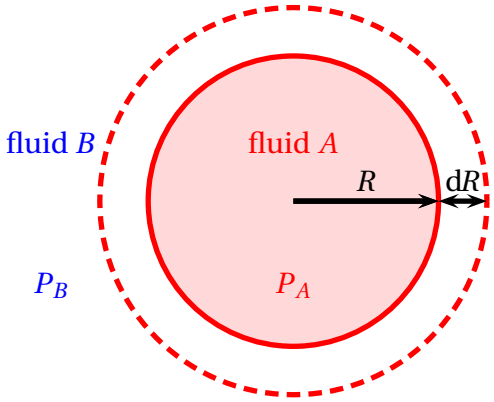

Figure 2.2: Over-pressure inside a drop of fluid A immersed in fluid B.

If the interface is displaced by a distance dR, the work of the pressure and capillary forces can be expressed as follows:

$$\delta W = -P_A \mathrm{d}V_A - P_B \mathrm{d}V_B + \sigma_{AB} \mathrm{d}\aleph \tag{2.1}$$

[1] somewhere between the binodal and the spinodal curves

with P_A and P_B the respective pressures in fluid A and B, $\mathrm{d}V_A$ and $\mathrm{d}V_B$ the respective changes in volume of each fluid, σ_{AB} the surface tension of the interface between A and B and $\mathrm{d}\aleph$ the change in interface area. The following relations can be considered:

$$\begin{aligned} \mathrm{d}V_A &= -\mathrm{d}V_B & (2.2)\\ &= 4\pi R^2 \mathrm{d}R & (2.3) \end{aligned}$$

and

$$\mathrm{d}\aleph = 8\pi R \mathrm{d}R \tag{2.4}$$

The condition for mechanical equilibrium is $\delta W = 0$, leading to:

$$-P_A \mathrm{d}V_A - P_B \mathrm{d}V_B + \sigma_{AB} \mathrm{d}\aleph = 0 \tag{2.5}$$

$$(P_A - P_B) \times 4\pi R^2 \mathrm{d}R = \sigma_{AB} \times 8\pi R \mathrm{d}R \tag{2.6}$$

$$P_A - P_B = \frac{2\sigma_{AB}}{R} \tag{2.7}$$

The mechanical equilibrium of the drop leads to a pressure difference proportional to the surface tension and inversely proportional to the radius. The same reasoning can be generalized for any non spherical curvature [1]. This leads to the famous Laplace-Young equation[2], which is expressed as follows by de Gennes *et al.* ([50], page 17):

> The increase of hydrostatic pressure that occurs when passing through the separating surface between two fluids is equal to the product of the surface tension σ by the curvature of the interface C:
>
> $$\Delta P = \sigma C \tag{2.8}$$

It should be noted that this equation describes a mechanical equilibrium, and only considers hydrostatic pressures.

2.1.3 Equilibrium condition of a bubble immersed in a liquid

As it is detailed in Section 2.1.1, it is possible to superheat a liquid beyond its saturation and to supercool a vapour below its saturation condition. It is indeed possible in relatively simple experiments to approach the limits of the supersaturation [148]. It can be inferred from this observation that a barrier to the formation of a bubble in a superheated liquid exists[3]. Lets us explain this phenomenon through a case of study.

[2] The detailed history of the determination of this equation can be found in the 11^{th} edition of the Encyclopædia Britannica [22], in the *Capillary action* article.

[3] Or, from the same manner, a barrier to the formation of a drop in a subcooled vapour. The whole development of this section will concern the formation of a bubble as it is the object of this study, but the same reasoning applies for the formation of a drop.

The system considered is composed of a bulk liquid with an imposed pressure P_l and an imposed temperature T_l (see Fig. 2.3). A vapour nucleus is formed within the liquid and has a homogeneous temperature T_v, pressure P_v, volume V_v, number of moles n_v and surface $\aleph_v$. The effect of gravity is neglected[4], and the shape of the vapour nucleus is a sphere, of radius R, due to the surface tension stress. In this case of study, the vapour nucleus is not necessary in an equilibrium state.

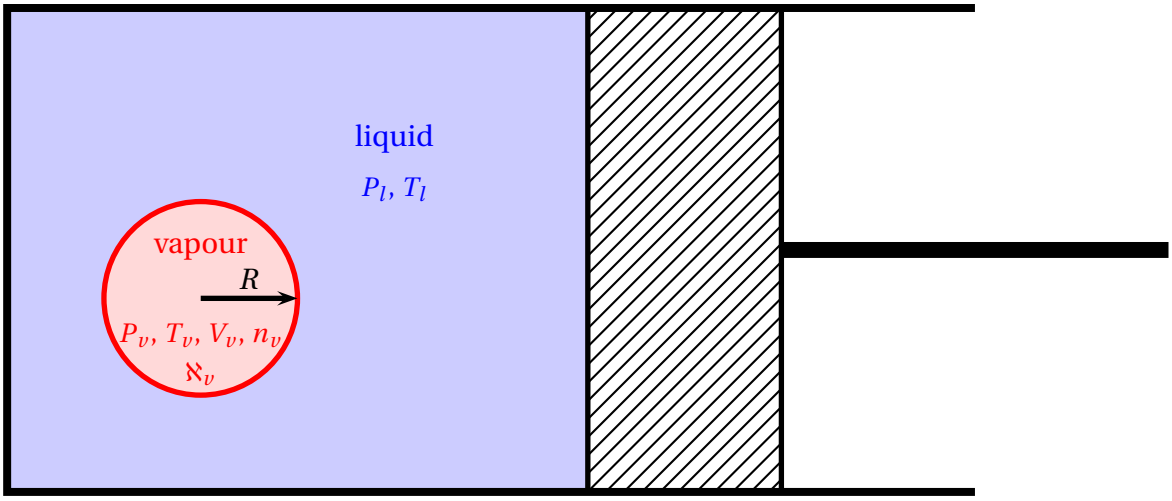

Figure 2.3: Vapour nucleus immersed inside superheated liquid with imposed pressure and temperature.

With basic thermodynamic considerations, the Helmholtz free energy of formation of the nucleus can be expressed as follows [148]:

$$A = n(\mu_{c,v} - \mu_{c,l}) + \mathscr{S}_v(T_v - T_l) - V_v(P_v - P_l) + \sigma\aleph_v \tag{2.9}$$

with μ_c being the chemical potential and σ the surface tension.

In order to obtain an equilibrium (which can be stable or unstable), the condition $\mathrm{d}A = 0$ should be realized. This leads to the three following relations:

$$\begin{cases} \mu_{c,v} &= \mu_{c,l} \\ T_v &= T_l \\ P_v - P_l &= \frac{2\sigma}{R} \end{cases} \tag{2.10}$$

The resolution of this system in order to calculate the equilibrium is detailed by Papon and Leblond [148]. It is shown that this equilibrium corresponds to a maximum of the Helmholtz free energy A. It is thus an unstable equilibrium. As P_v, T_v and n_v are independent thermodynamic variables, there are several manners to move away from the equilibrium state. Considering a mechanical loss of equilibrium caused by a change of pressure inside the bubble, the Helmholtz free energy of the bubble can be expressed as a function of the bubble radius R. This function is schematically represented in Fig. 2.4.

[4]This assumption is realistic due to the very small size of a nucleus.

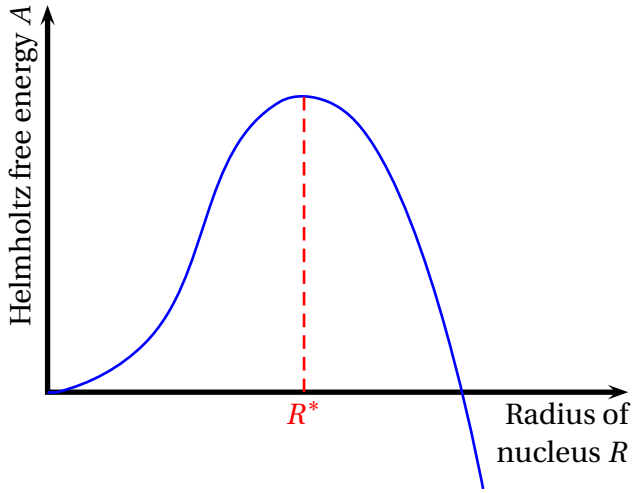

Figure 2.4: Helmholtz free energy of a vapour nucleus within a liquid.

The radius R^* of the nucleus that corresponds to the unstable equilibrium is named *critical radius*. It infers from Fig. 2.4 that a nucleus with a radius smaller that the critical radius will automatically vanish. On the other side, a radius having a radius bigger than the critical radius will grow. This growth will be limited by either:

liquid inertia: this is typically the case when boiling at a low pressure, or in the case of cavitation
thermal diffusion: this is most often the case in boiling
mass diffusion as for gas desorption in a mixture
viscosity when boiling in a very viscous liquid

It should be noted that the critical radius R^* decreases with the liquid superheat and with the bulk liquid pressure. When the liquid superheat approaches the spinodal line, the size of the equilibrium radius gets close to molecular dimensions [41].

2.1.4 Homogeneous nucleation

Thermal fluctuations occur in the metastable liquid [40, 84] and there is a small but finite probability of a cluster of molecules with vapour-like energies coming together to form a vapour embryo of the size of the equilibrium nucleus [41]. This process of vapour formation in a metastable liquid is referred to as *homogeneous nucleation*.

The probability of the formation of a vapour nuclei of the necessary size can be estimated from the Boltzmann equation for the distribution of molecular clusters of size R^*. The number of nuclei of radius R per unit of volume, $N(R)$, is given by [41]:

$$N(R) = Ne^{-A(R)/kT_v} \tag{2.11}$$

with N a constant approximately equal to the number of molecules per unit of volume, $A(R)$ the Helmholtz free energy of formation of a nucleus of radius R, T_v the temperature of the

vapour nucleus and bulk liquid and k the Boltzmann constant. It can be deduced from this equation that the number of nuclei of size R increases with an increasing temperature.

As detailed in Section 2.1.3, bubbles smaller that R^* will collapse and bubbles larger than R^* will grow spontaneously. Homogeneous nucleation will thus occur if one further molecule collides with an equilibrium embryo. The rate of nucleation $\mathrm{d}N/\mathrm{d}t$ in a metastable liquid at a temperature T_v is given by the product of the number of equilibrium nuclei per unit of volume by a collision frequency λ_C:

$$\frac{\mathrm{d}N}{\mathrm{d}t} = \lambda_C N(R^*) \tag{2.12}$$

Several expressions have been given for λ_C linking it either to the temperature [191] or to the surface tension [16]. The rate of nucleation is an extremely sensitive function of the superheated liquid temperature. Simpson and Wall [173] have suggested that significant nucleation occurs for values of $\mathrm{d}N/\mathrm{d}t$ between 10^9 and 10^{13} $\mathrm{m}^3{\cdot}\mathrm{s}^{-1}$. This usually corresponds to narrow ranges of temperature[5] [41].

The upper temperature limit reached when creating homogeneous nucleation in laboratory controlled experiments are very close to the theoretical values for organic fluids [155]. However, for water at atmospheric pressure, boiling always occurs with liquid temperature values far lower than the theoretical homogeneous boiling temperature [97]. It is possible to state that, for water at least, homogeneous nucleation from a metastable liquid state can be discounted as a mechanism for vapour formation [41].

In all cases, nucleating within a liquid requires high liquid superheat. If the liquid pressure is far from the critical pressure of the fluid, the order of magnitude of the required superheat is typically several hundreds of Kelvins[6]. These values are one or several order of magnitude above the superheat usually encountered for the onset of boiling, because nucleation usually occurs on a solid surface, on particles or on entrapped incondensable gases.

2.1.5 Heterogeneous nucleation

Heterogeneous nucleations refers to vapour nucleation in a liquid helped by the presence of a foreign body. Foreign bodies can be either a solid container, which may have surface structures, entrapped gas or even impurities within the liquid.

In many applications, vaporization of a liquid is made to occur by transferring heat through the solid walls of some containing structure. In such cases, the hottest liquid in the system will be in the region immediately adjacent to the wall. If enough heat is added to

[5] For benzene at atmospheric pressure, it corresponds to the range of temperature from 224 °C to 225.2 °C.

[6] For water at atmospheric pressure, the theoretical liquid superheat for homogeneous nucleation is 220.7 K [41]. For propane and n-butane at 1 bar, the respective theoretical liquid superheats are respectively 328.5 K and 378.3 K [155]. For n-pentane at atmospheric pressure, the required superheat has been measured to be equal to 418.8 K [6]

the system, the liquid near the wall may reach and slightly exceed the equilibrium saturation temperature. Since the temperature is highest right at the solid interface, the formation of a vapour embryo is most likely to occur at the *solid-liquid* interface.

2.1.5.1 Nucleation in the presence of dissolved gas

The presence of a dissolved gas, say air, in the liquid phase necessitates the gas partial pressure to be taken into account when considering the mechanical equilibrium of the vapour nucleus. The presence of dissolved gas reduces the superheat required to maintain a bubble of a given diameter in unstable equilibrium. In practice, the evaluation of the gas partial pressure may be complicated by the presence of temperature gradients and by finite rates of diffusion of the gas through the liquid [41].

2.1.5.2 Nucleation at solid surface in a uniform temperature field

Wall superheats encountered in the case of nucleation on a clean, smooth and plane wall in a uniformly superheated liquid are usually below those of homogeneous nucleation. Such a system can be described as for homogeneous nucleation in Section 2.1.4. The Helmholtz free energy of a bubble attached to the wall will be lowered by the presence of the wall. For a bubble of the equilibrium radius attached to the wall, the reduction of the free energy can be expressed by multiplying the free energy of the homogeneous nucleation case by a function $f(\theta)$ [8, 40]:

$$f(\theta) = \frac{2 + 3\cos\theta - \cos^3\theta}{4} \tag{2.13}$$

with θ being the contact angle at the triple line between the solid wall and the *liquid-vapour* interface, on the liquid side (see Fig. 2.5).

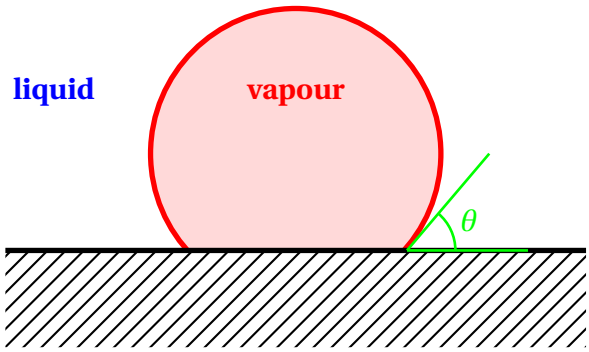

Figure 2.5: Bubble nucleating on a solid wall.

If the liquid is completely wetting the solid surface ($\theta = 0$), $f(\theta) = 1$ and the required liquid superheat to nucleate a bubble is identical to that of homogeneous nucleation. If the

liquid is not wetting at all ($\theta = 180°$), no liquid superheat is theoretically needed to nucleate a bubble. However, in practical situations, the value of θ lies between 0 and 100°.

2.1.5.3 Nucleation on natural surfaces

On real surfaces, the onset of boiling corresponds to even lower superheat values than those described earlier [145]. Natural surfaces[7] usually present many pits or cavities of various shapes. The presence of such cavities facilitates nucleation for two different reasons:

- If the contact line between the vapour, liquid and solid phases is located within a cavity, the apparent contact angle[8] is increased. As illustrated in Fig. 2.6, in a conical cavity, the apparent contact angle increases with a decreasing apex angle. Consequently, as detailed in Section 2.1.5.2, the superheat required to nucleate a bubble is decreased[9].

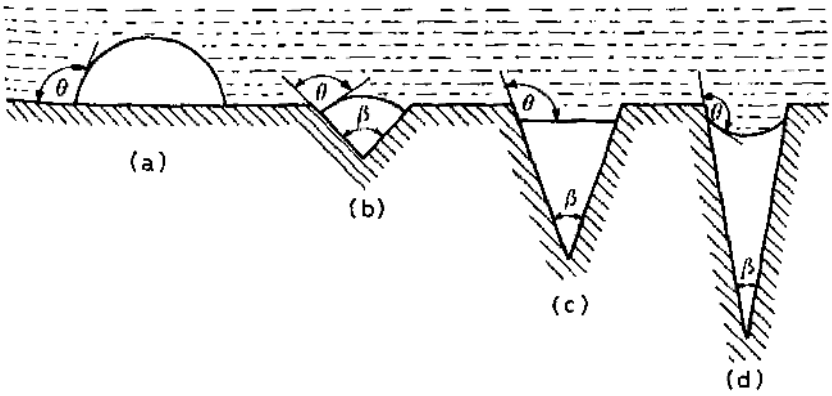

Figure 2.6: Liquid-vapour interfaces in conical cavities. Illustration from Collier and Thome [41].

- The roughness of natural surface usually presents fractal features, and may be analysed at different scales. Cavities or pits often have irregular shape, as illustrated in Fig. 2.7. The geometry of these cavities may result in the presence of entrapped gas or vapour if the liquid does not fill the entire cavity [9, 10]. Nucleation in such cavities will require very low superheats[10].

Several experimental and theoretical studies were made to investigate and predict the size range of the active cavities[11] (e.g. Clark *et al.* [39] and Hsu [83]). It has been shown

[7] *Natural* is employed to define surface that did not receive a special treatment as a surface structuring or polishing.

[8] defined as the angle between the *liquid-vapour* interface and the horizontal plane

[9] The function $f(\theta)$ in Eq. 2.13 uses the apparent contact angle when the bubble nucleates on a wall that is not plane.

[10] Such cavities are sometimes referred to as *pre-activated* cavities

[11] i.e. the cavities in which bubbles nucleate

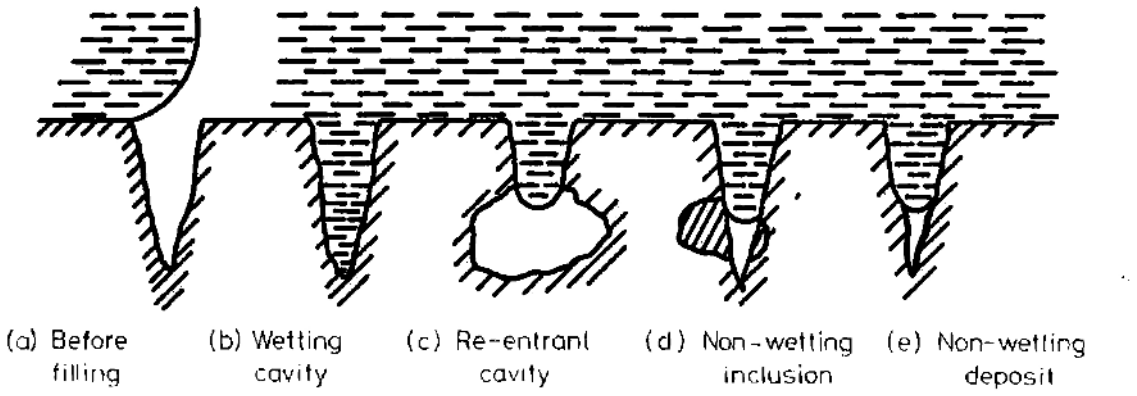

Figure 2.7: Formation of an active nucleation site in a real cavity. Illustration from Collier and Thome [41].

that only cavities of a narrow range of size were the location of bubble nucleation on a rough surface.

2.2 Pool boiling curve

Pool boiling is defined as boiling from a heated surface to a large amount of quiescent bulk liquid. Pool boiling is qualified as *saturated* if the liquid is at thermodynamic saturation temperature and as *subcooled* when the liquid is below that temperature. Saturated pool boiling heat transfer has been first described by Nukiyama [138] in 1934. He considered the relation between the heat flux from the heated surface (q_w) and the temperature difference between the heated surface and the saturated liquid ($T_w - T_{sat}$). His boiling curve differs depending on whether a temperature or a heat flux is imposed on the heated surface (fig. 2.8).

The different sections of the boiling curve refer to a specific boiling regime [176]. The imposed heat flux boiling curve can be read as follows:

Natural convection (A-B): as the heat flux imposed on the surface is increased, its temperature increases as well. The temperature of the liquid surrounding the surface increases as well above the saturation temperature and is qualified as *superheated* liquid. A thermal boundary layer is formed and the heat flux is dissipated by natural convection in the bulk liquid. Phase change occurs at the free surface.

Onset of boiling (B-B'): as the imposed heat flux increases, the surface temperature will be sufficient for bubbles to nucleate. Heat transfer will be enhanced by the presence of these bubbles resulting in a temperature drop.

Isolated bubble regime (B'-C): after the onset of boiling (ONB), a very effective boiling regime is reached, where the surface temperature raises very slowly with the heat flux. More and more nucleation sites become active on the surface. Part of the heat flux is dissipated in the phase change process, and part of it is convected into the bulk liquid.

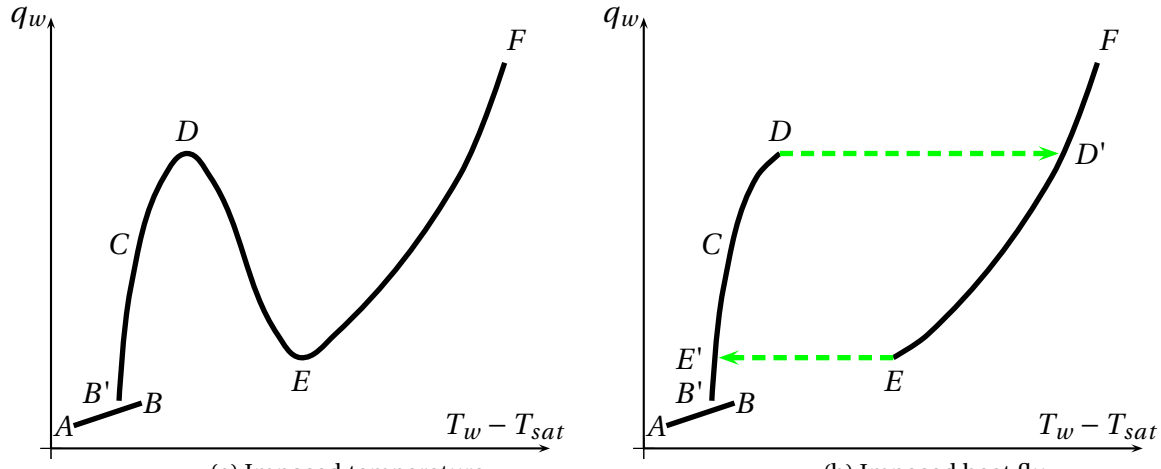

(a) Imposed temperature (b) Imposed heat flux

Figure 2.8: Pool boiling curves: imposed temperature (left) and imposed heat flux (right).

The bubble motion as they growth and depart from the surface enhances the convection of the liquid.

Fully developped nucleate boiling regime (C-D) : once many nucleation sites are active on the surface, they get close enough to each other that bubbles coming from neighbouring sites merge. With the rise of the heat flux, bubble grow faster so that that successive bubbles from the same nucleation site get close enough to merge as well. These two phenomena are known as *lateral coalescence* and *vertical coalescence*. Large masses of vapour restrict the liquid motion close to the heated surface decreasing the heat transfer coefficient.

Critical heat flux (D-D'): the heat flux reaches a critical value (CHF) when the vapour mass above the surface prevents the liquid from re-wetting the surface. A vapour film forms on the surface. Its thermal resistance leads to a sudden rise of the surface temperature. The system can be damaged during this temperature rise (phenomenon known as *burn out*).

Film boiling regime (E-F): the vapour layer formed on the surface become stable. The heat flux from the surface is dissipated by conduction and convection to the vapour layer. Phase change occurs at the interface between the vapour layer and the liquid and bubbles periodically detach, forming evenly spaced bubble columns. When the heat flux raises, the temperature increases and radiative heat transfer through the vapour layer become a major heat transfer mode. The heat flux is limited by the burn out when the temperature is too high to be supported by the system.

Minimum film boiling point (E-E'): if the heat flux is decreased after a stable film boiling regime has been established, the temperature decreases as well, still keeping the same regime far below the CHF temperature. A critical value, called Leidenfrost point, is reached when the heat flux is low enough that the vapour film breaks. Liquid rewets the surface, leading to much better heat transfer and a sudden temperature drop. The isolated bubble regime appear again.

The heat transfer effectiveness of the isolated bubble and fully developed boiling regimes

make them particularly interesting to the engineering designer. Therefore, many different experimental correlations have been developed to predict quantitatively the relation between the heat flux and the surface temperature in a given system. Yet, many parameters are involved such as the nature of the fluid, the working pressure, the system geometry and the surface roughness, so that the experimental correlations are valid only close to the conditions they have been designed for. This lack of compatibility strongly motivated the investigation for a better understanding of the basic mechanisms governing nucleated boiling. The single bubble system, its nucleation, growth, detachment and rise in the liquid is hence the main subject of this work. Focus will also be given to the basic interaction between neighbouring bubbles.

2.3 Electrohydrodynamics

Although pool and convective boiling heat transfer are characterized by very high dissipated heat fluxes whilst requiring low temperature differences, industries are continually demanding smarter and smaller heat exchangers allowing the dissipation of always increasing heat density. Besides the improvement of the performance of heat exchangers by improving design and manufacturing, heat transfer enhancement techniques enable a considerable decrease in the size of heat exchangers at the same performance [104].

In general, enhancement techniques can be divided into two groups: namely active and passive techniques. The active techniques require energy sources[12], whereas the passive techniques require special surface geometry[13] or fluid additives.

A promising active technique for improving and controlling the heat transfer during boiling is the introduction of an electric field. This technique is generally termed electrohydrodynamics (EHD). Whether for pool boiling or convective boiling scenarios, several studies have shown that EHD can considerably augment two-phase heat transfer. Some papers have presented the review of these researches as Allen and Karayiannis [4], Eames and Sabir [59] or more recently Laohalertdecha *et al.* [104].

The application of an electric field above a boiling surface results in the addition of electric body forces. A good understanding of the effects of these forces of the boiling behaviour is necessary for the following reasons:

- As mentioned previously, EHD is a promising technique of heat transfer enhancement. A good understanding of electrohydrodynamic effects will provide the means to design better heat exchangers.
- Several electronic systems impose an electric field at their vicinity due to their functions. They might as well be the source of heat production and require two-phase heat transfer techniques to provide heat removal. A good understanding of the modifica-

[12] e.g. electric field, acoustic or surface vibration
[13] such as rough surface, extended surface for liquids, etc. [104]

tion of boiling due to the presence of the electric field is necessary for a good design of such systems.

- EHD is also seen as a promising technique to compensate for the lack of gravity in micro-gravity heat management applications. For this reason, a number studies focusing on electrohydrodynamic enhancement of boiling concern microgravity [78, 79, 124, 125, 126].
- As the basic mechanisms of boiling still need investigation for an improved understanding, the application of external forces as EHD may be a tool for a modification of boiling in order to achieve such a better understanding [24].

2.3.1 Forces induced by the presence of an electric field

The presence of an electric field within a dielectric fluid results in an added electric body force applied to the fluid particles. This force is due to the free charges contained in the fluid and to the inhomogeneity of the electric properties of the fluid. For the case of a two-phase fluid, the discontinuity of the electric properties at the interface also cause an electric stress on the surface.

The most generally accepted expression from the electric body force $\vec{f_e}$ (expressed in [N·m^{-3}]) that acts on a fluid, to be included in the momentum equation, is [27, 102, 147]:

$$\vec{f_e} = \rho_e \vec{E} - \frac{1}{2}\vec{E}^2 \vec{\nabla}\varepsilon_r + \frac{1}{2}\vec{\nabla}\left[\rho \vec{E}^2 \left(\frac{\partial \varepsilon_r}{\partial \rho}\right)_T\right] \tag{2.14}$$

with ρ_e being the free charge density within the fluid, ε_r being the relative dielectric permittivity[14], $\vec{E}$ being the electric field intensity and ρ being the fluid density.

The three terms on the right-hand side of eq. 2.14 are respectively:

the *electrophoretic* force or the Coulomb force. This force results from the net free charge within the fluid or injected from the electrodes. This is the only force which depends on the direction of the electric field.

the *dielectrophoretic* force. This force is a consequence of inhomogeneous or spatial change in the permittivity of the dielectric fluid due to non-uniform electric fields, temperature gradients, and phase discontinuities.

the *electrostrictive* force. This force[15] is caused by inhomogeneous electric field strength and the variation in dielectric constant with temperature and density[16].

[14] that is: $\varepsilon_r = \varepsilon/\varepsilon_0$

[15] Cattide *et al.* [24] suggest a negative sign before this term, unlike most authors. This might simply be a typographic error as other publications from the same research group indicate a positive sign [123, 125].

[16] It should be noted that some authors do not precise a constant temperature for the calculation of the permittivity derivative with the density [19, 136, 188, 192, 196]. This follows the reasonning of Durand ([57], page 267) who states that for an isotropic dielectric fluid, ε depends only on the fluid density. The derivative should in this case be written as a total derivative and not a partial derivative. Landau and Lifšitz ([103], page 94) consider instead the fluid permittivity to be a function of both the temperature and the fluid density, leading to the partial derivative of the permittivity to density at constant temperature in Eq. 2.14.

The electrostrictive term can be expanded into two components:

$$\frac{1}{2}\overrightarrow{\nabla}\left[\rho\overrightarrow{E}^2\left(\frac{\partial\varepsilon_r}{\partial\rho}\right)_T\right]=\frac{1}{2}\rho\left(\frac{\partial\varepsilon_r}{\partial\rho}\right)_T\overrightarrow{\nabla}\overrightarrow{E}^2+\frac{1}{2}\overrightarrow{E}^2\overrightarrow{\nabla}\left[\rho\left(\frac{\partial\varepsilon_r}{\partial\rho}\right)_T\right] \tag{2.15}$$

For non-polar fluid, the Clausius-Mossotti's relationship can be used [177, 195]:

$$\rho\left(\frac{\partial\varepsilon}{\partial\rho}\right)_T\approx\frac{\varepsilon_0(\varepsilon_r-1)(\varepsilon_r+2)}{3} \tag{2.16}$$

This simplifies Eq. 2.15 to:

$$\frac{1}{2}\overrightarrow{\nabla}\left[\rho\overrightarrow{E}^2\left(\frac{\partial\varepsilon_r}{\partial\rho}\right)_T\right]\approx\frac{\varepsilon_0(\varepsilon_r-1)(\varepsilon_r+2)}{6}\overrightarrow{\nabla}\overrightarrow{E}^2+\frac{\varepsilon_0\overrightarrow{E}^2}{6}\overrightarrow{\nabla}\left[(\varepsilon_r-1)(\varepsilon_r+2)\right] \tag{2.17}$$

The electric charge density of the electrostrictive force can also be expressed as a function of the electric field intensity and of the fluid properties if only the net free charge within the fluid is considered[17] [4]:

$$\rho_e=\overrightarrow{E}\cdot\overrightarrow{\nabla}\varepsilon-\frac{\varepsilon}{\sigma_e}\overrightarrow{E}\cdot\overrightarrow{\nabla}\sigma_e \tag{2.18}$$

with σ_e being the fluid conductivity.

Equation 2.14 can be rewritten as a sum of 4 different terms [20, 104, 195]:

$$\overrightarrow{f_e}=\overrightarrow{f_{e,1}}+\overrightarrow{f_{e,2}}+\overrightarrow{f_{e,3}}+\overrightarrow{f_{e,4}} \tag{2.19}$$

$$\overrightarrow{f_{e,1}}=\left(\overrightarrow{E}\cdot\overrightarrow{\nabla}\varepsilon-\frac{\varepsilon}{\sigma_e}\overrightarrow{E}\cdot\overrightarrow{\nabla}\sigma_e\right)\overrightarrow{E} \tag{2.20}$$

$$\overrightarrow{f_{e,2}}=-\frac{1}{2}\overrightarrow{E}^2\overrightarrow{\nabla}\varepsilon \tag{2.21}$$

$$\overrightarrow{f_{e,3}}=\frac{\varepsilon_0(\varepsilon_r-1)(\varepsilon_r+2)}{6}\overrightarrow{\nabla}\overrightarrow{E}^2 \tag{2.22}$$

$$\overrightarrow{f_{e,4}}=\frac{\varepsilon_0\overrightarrow{E}^2}{6}\overrightarrow{\nabla}\left[(\varepsilon_r-1)(\varepsilon_r+2)\right] \tag{2.23}$$

Such an expression of the electric body force as a function of the electric field and of the fluid properties allows a finer description of the forces components [195]:

$\overrightarrow{f_{e,1}}$ is the Coulomb force. It depends on the fluid permittivity and conductivity and their variations and on the electric field intensity. Both the permittivity and the conductivity depend on the fluid temperature and density. Density variations are significant at the interface of different phases, leading to the local production of electric charges on the interface [195]. The direction of the Coulomb force is the same as the direction of the electric field.

[17] Is it really a realistic assumption? Considering a perfectly pure dielectric fluid, the presence of ions can be neglected and the injection of charges from the electrodes as well. However, as it is stated by Felici [62], most fluids naturally contain impurities that are dissolved into ions in the presence of electric fields. A particular care should be taken concerning the purity of fluids when experimenting with EHD.

$\overrightarrow{f_{e,2}}$ depends on the variations of fluid permittivity. As for the Coulomb force, this force is significant at the interface between two phases. The direction of this force is the direction of the permittivity gradient, from higher to lower permittivity. On an interface, this force acts normally to the interface on the fluid particles, in the direction from the liquid phase towards the vapour phase.

$\overrightarrow{f_{e,3}}$ is due to the non-uniformity of the electric field. This force acts as a translation force on the liquid particles[18]. The liquid tends to be moved to the area with higher electric field intensity. It should be noted that this force is independent of the electric field direction, but only depends on the square of absolute intensity.

$\overrightarrow{f_{e,4}}$ depends on the variation of fluid permittivity, as for $\overrightarrow{f_{e,2}}$. This force acts on the fluid particles normally to the interface, but in the opposite direction to $\overrightarrow{f_{e,2}}$: from the vapour phase towards the liquid phase.

Since $\overrightarrow{f_{e,2}}$ and $\overrightarrow{f_{e,4}}$ possess similar characteristics, they can be combined together as:

$$\overrightarrow{f_{e,5}} = \overrightarrow{f_{e,2}} + \overrightarrow{f_{e,4}} \tag{2.24}$$

$$= \frac{1}{6}\varepsilon_0 \overrightarrow{E}^2 \overrightarrow{\nabla}\left(\varepsilon_r^2 - 2\varepsilon_r - 2\right) \tag{2.25}$$

On an interface, $\overrightarrow{f_{e,5}}$ will always be directed from the vapour phase towards the liquid phase[19], as mentioned by Yu *et al.* [195].

Several expressions have been proposed to express the net electric stress acting across a liquid-vapour interface. Using the continuity relations on electric induction at the interface:

$$\varepsilon_l E_{l,n} = \varepsilon_v E_{v,n} \tag{2.26}$$

$$E_{l,t} = E_{v,t} \tag{2.27}$$

with n and t referring respectively to the normal direction $\vec{n}$ and the tangential direction $\vec{t}$, Taylor [182] and later Zaghdoudi [196, 197, 198] expressed the normal electric stress (expressed in [N·m^{-2}]) on the fluid particles at the interface for a non-polar fluid whose interface is not electrically charged as follows:

$$\overrightarrow{f_{s,n}} = -\varepsilon_0 \frac{\left(\varepsilon_{r,l} - 1\right)^2}{6}\left[2E_{l,n}^2 - E_{l,t}^2\right]\vec{n} \tag{2.28}$$

with $\vec{n}$ referring to the normal direction of the liquid at the interface. For the case of perfect dielectrics or of perfect conductors, the tangential component is equal to 0 [182]. Another expression is also demonstrated for the case of an interface electrically charged [196].

As a conclusion about the forces induced by the presence of an electric field within a dielectric fluid, it can be stated that:

[18] This force is negligible on the vapour particles as the vapour relative permittivity ε_r is close to unity.

[19] In the vapour phase, $\varepsilon_{r,v} \approx 1$ as $\varepsilon_v \approx \varepsilon_0$, leading to $\varepsilon_{r,v}^2 - 2\varepsilon_{r,v} - 2 \approx -3$. In the liquid phase, $\varepsilon_{r,l} > 1$ leading to $\varepsilon_{r,l}^2 - 2\varepsilon_{r,l} - 2 > -3$. Consequently, on the interface, $\overrightarrow{\nabla}\left(\varepsilon_r^2 - 2\varepsilon_r - 2\right)$ will be normal to the interface and directed towards the liquid phase.

1. The expression of the forces is rather complex. The determination of the forces is coupled with the phase field, the temperature field and the exact geometry of the problem, and necessitates a good knowledge of the variation of the fluid properties.
2. In the case of heat transfer with a liquid, the electrohydrodynamic effects produce a force field that is coupled with the temperature field. Natural or forced convection is likely to be strongly modified by EHD.
3. In the case of boiling, the liquid vapour interfaces on the bubbles are affected by the electrohydrodynamic effects. As bubble shape, growth, rise and interactions are governed or coupled with the superficial forces, bubble dynamics may also be strongly modified by EHD.
4. The presence of free charges within the liquid or at the liquid-vapour interface may be a source of electrohydrodynamic effects. The presence of charges may be due to the dissolution of components into ions within the fluid or to the injection of free charges from the electrodes.

2.3.2 Changes to heat transfer and bubble dynamics caused by EHD

The application of an electric field to a boiling surface usually results to an enhancement of the heat transfer coefficient. Several studies focus on the enhancement of heat transfer for different geometries (plane horizontal and vertical surfaces, smooth and finned tubes, etc.) and different fluids[20]. Laohalertdecha *et al.* [104] have proposed a literature review on electrohydrodynamic enhancement of heat transfer. They note that most studies have shown a heat transfer enhancement of a factor of 2 to 7 when applying an electric field (e.g. [34, 48, 63, 90, 17, 115, 137]). Some studies have shown an even higher enhancement [46, 89] up to an enhancement factor of 60 [3].

The mechanisms by which EHD techniques enhance boiling heat transfer are summarized by Eames and Sabir [59] as follows:

- movement of vapour bubbles on the heated surface due to Maxwell stress
- spreading of the vapour bubble base over the heat transfer surface
- increasing the number of bubbles by breaking up large bubbles, there by decreasing the bubble detachment diameter and creating more turbulence
- elimination of boiling hysteresis, thereby decreasing the degree of the superheat required to start nucleate boiling
- improving the transitional and minimum film boiling conditions by destabilizing the blanketing vapour film
- improving the wetting of the heating surface due to the decrease of surface tension
- introducing the waves and perturbations at the surface of a boiling liquid, due to the instability of the *liquid/vapour* interface

Even though the mechanisms suggested by Eames and Sabir are plausible and reflect the complexity of the effects induced by the action of electric forces, the effects of EHD on

[20]The dielectric fluids used are organic fluids, and are usually common refrigerants as a main application of EHD can be the enhancement of heat exchangers in heat pumps and thermodynamic systems.

boiling are in fact not so clear and understood yet. For example, Cattide *et al.* [24] found two different modifications of the bubble departure diameter in the presence of electric fields: in the case of HFE-7100, the departure diameter is increasing whereas for FC-72, the departure diameter is increasing. As another example, the effect of polarity and the role of injected charges is not completely understood, as it is explain by Liu *et al.* [114].

From the same manner, some effects caused by electrohydrodynamics and observed experimentally as an elongation of the bubble in the direction of the electric field [29, 35, 151] are assessed but the prediction of their magnitude and influence on the mechanisms of boiling still needs further investigation. Other effects were observed as the break-up of large bubble into smaller bubble, but the basic mechanisms that lead to the break-up of the bubble are not fully understood.

As a conclusion, natural boiling requires more research and investigation for a better understanding, and the modification of boiling by means of electrohydrodynamics , being recognized as a promising heat transfer enhancement technique, requires even more investigation for a good understanding and prediction.

The present section is an introduction to the fundamental concepts that need to be understood prior to the presentation of the main work of this thesis. The concept of phase change and liquid superheat has been introduced, and the mechanism of bubble nucleation has been developed. The complexity of the nucleation process has been highlighted, especially in the case of heterogeneous nucleation on a surface which presents a roughness at different scales. A good understanding of the nucleation process is required to perform experiments with controlled nucleation on artificial nucleation sites.

The boiling curve has then been explained, showing the relation between the superheat of a boiling surface and the heat flux density. The different boiling regimes have been described. The present study which focuses at the scale of a single bubble and of the interaction between two bubbles is representative of the isolated bubble regime encountered at low heat flux.

The electrohydrodynamic effect has finally been introduced as a promising heat transfer enhancement technique. The electric forces acting on the fluid particles have been detailed, and a brief state-of-the-art *of the mechanisms of heat transfer enhancement has been presented.*

In the next chapters, the experimental facility and procedures will be detailed, the heat transfer mechanisms and electrohydrodynamic enhancement will be investigated, and the bubble dynamics will be studied first without electric field and then with the application of an electric field above the boiling surface. For each subject investigated (such as convection enhancement, bubble growth, detachment, rise and shape, momentum balance of the bubble, thermo-capillary convection, bubble curvature, bubble elongation with EHD, etc.), a brief literature review or state-of-the-art will be proposed.

Chapter 3

Experimental facility and procedures

The purpose of our experimental facility is to be able to analyse accurately the basic mechanisms of single bubble boiling or the interactions between two bubbles, in the presence of a D.C. electric field on a metal surface. A test sample and a boiling vessel have been designed and built (section 3.1). The setup was operated following an accurate procedure (section 3.2). Temperatures, heat fluxes and voltages were measured and images were recorded (section 3.3) to obtain original and workable results in these operating conditions (section 3.4).

3.1 Experimental setup

3.1.1 Short description of the overall view

The experimental apparatus, shown schematically in Fig. 3.1, consists of a sealed parallelipedic vessel. To facilitate observation and photography within the vessel the vertical faces of the vessel are equipped with rectangular windows which are sealed to the main housing of the tank. Initially, the tank is evacuated and subsequently filled with 99 % purity n-pentane. The free surface between the liquid and the vapour phases is at a height of about 220 mm from the base of the container. A cartridge heater is immersed in the liquid pentane in order to maintain the desired saturation and pressure conditions of the working fluid during the experiments. A test sample is inserted in the vessel from the base face (Fig. 3.1). The surface of the test sample is upward facing in the bulk liquid and in the centre of the vessel.

During the experiments, boiling was taking place on this surface from either a single nucleation site or from two adjacent nucleation sites. Each configuration was studied with a specific test sample. Boiling was recorded through a lateral window by a high speed camera while the boiling area was illuminated through the opposite window.

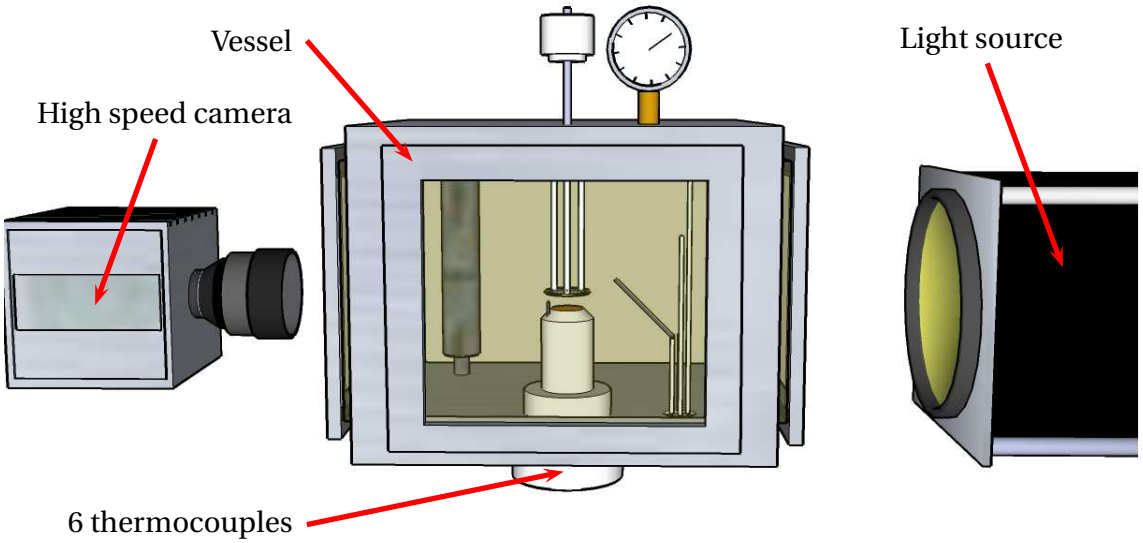

Figure 3.1: Experimental apparatus

3.1.2 Vessel

The experimental vessel (Fig. 3.2) is a sealed $250 \times 250 \times 180$ mm aluminium tank. Three vertical sides are equipped with glass windows to allow illumination of the boiling surface and area of interest, visualization and recording of the images. The bottom part of the tank includes a hole to insert and fix the test sample, as well as a drain used to empty the vessel. The upper part of the tank includes a pipe with a valve used to fill the vessel with pentane, a pressure gauge and a rod with a micro-metric vertical displacement system. The high voltage electrode, described later, is attached to this rod.

The test sample described in 3.1.3 is inserted from the base face of the vessel, and properly sealed to avoid any leakage. The boiling surface is thus placed horizontally at the center of the vessel as shown in Fig. 3.2. The copper boiling surface is connected to the electric ground, as well as the outer parts of the vessel.

A brass mesh electrode is attached to the micrometer and placed horizontally facing the boiling surface. The electrode is connected by a cable to the high voltage source. The mesh stand and the rod are made of PTFE and nylon so that they do not conduct electricity. The brass mesh electrode has been chosen with the dimensions described in Fig. 3.3. This design has been tested among with other electrode designs by Zaghdoudi [196] and aims at having the finest mesh while still allowing pentane bubbles to pass easily through it. With a finer mesh, the bubbles agglomerate below the grid forming a large flat bubble that distort the electric field. With a rougher mesh, the electric field would more likely be non-homogeneous in the vicinity of the electrode.

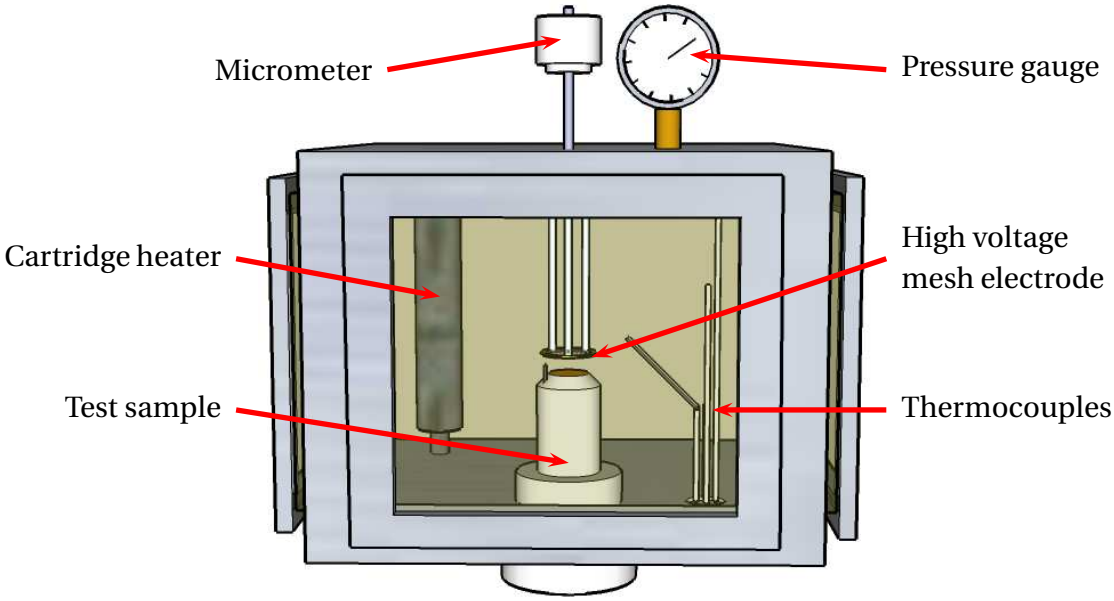

Figure 3.2: Vessel

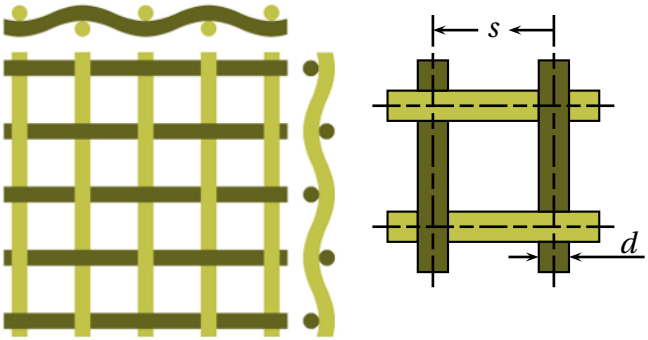

wire diameter [mm]	0.25
step [mm]	1.85
void fraction [%]	75

Figure 3.3: Geometrical properties of the brass mesh

3.1.3 Test sample

3.1.3.1 Geometry of the test sample

Several test samples have been used for this work, which were slightly different from each other. The main test sample used is described here, and information is provided regarding the differences between samples. The test sample is shown with its dimensions in Fig. 3.4. An 8 mm diameter cartridge heater is inserted in a 12 mm outer diameter copper tube. The copper tube section narrows over the heater to form a 5 mm diameter and 60 mm long copper rod. This rod is equipped with six K-type thermocouples used to measure the thermal heat flux passing through the rod and the surface temperature. An 18 mm diameter and 40 µm copper plate is soldered atop the rod using melted tin. The assembly is insulated in a

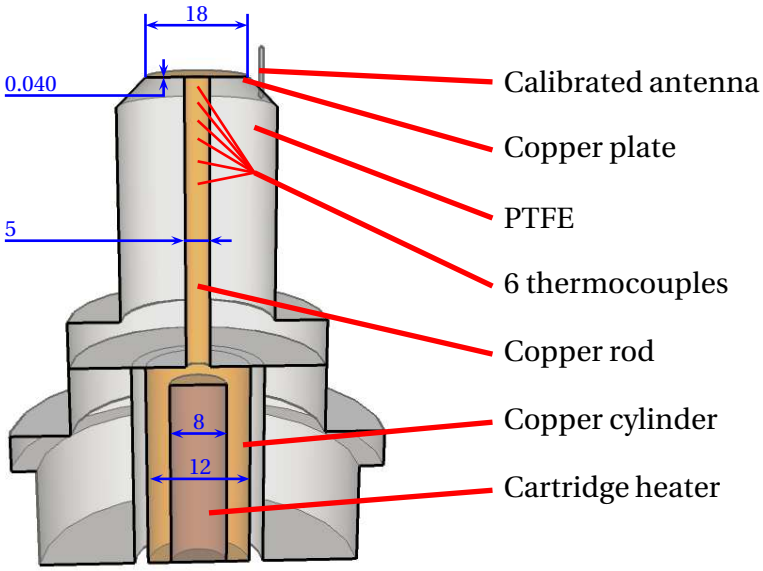

Figure 3.4: Main test sample design (length given in [mm])

PTFE structure. The rod is fixed inside the upper PTFE part using an araldite epoxy resin. The upper and lower PTFE sections are screwed together and sealed by a toric seal. The whole test sample is inserted through the hole at the base of the vessel and fastened in place. The watertightness in ensured by a toric seal as well. The copper structure is connected to the electric ground and the cartridge heater is connected to a power generator whose output can be set either in current or voltage modes.

3.1.3.2 Heated surface preparation

The copper plate surface is carefully prepared to avoid any parasite boiling. The surface is polished with a diamond paste until reaching a roughness lower than 0.5 µm. The outer edge of the plate is sealed with a cyanoacrylate adhesive to prevent the liquid from soaking under it. An artificial nucleation site was created by mechanical indentation at the centre of the plate. A tungsten carbide needle was constructed in-house and was positioned to be in intimate contact with the surface. It was then forced into the surface with its displacements accurately measured during the entire indentation process. The surface geometry of the site was measured with a confocal white light microscope (Fig. 3.5a, 3.5b and 3.6a). The nucleation site had a paraboloidal shape, a diameter of 180 µm and a depth of about 500 µm. The curvature radius at its edge was about 20 µm. For lateral coalescence experiments, a second nucleation site was created using the same process, with a distance of 660 µm between the centres of the sites (Fig. 3.5c, 3.5d and 3.6b). The diameter and depth are the same, but the curvature radius at its edge was about 50 µm (Fig. 3.6b).

A surface of 2 50 × 600 µm close to the nucleation site has been analysed to determine the surface roughness. A map of the area has been measured with a confocal white light micro-

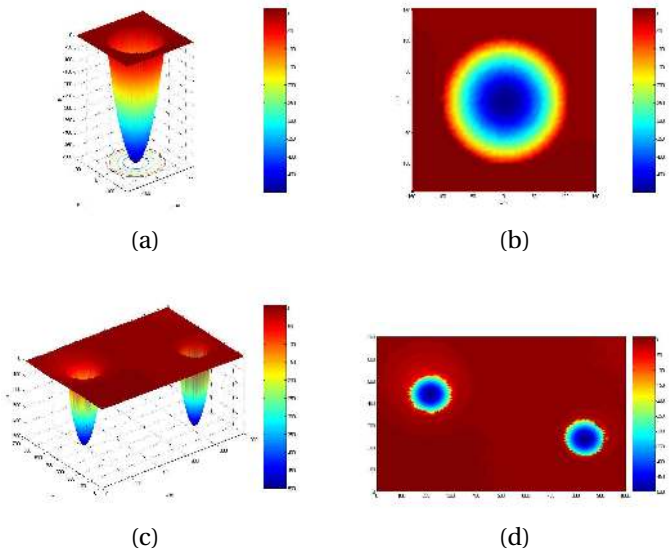

Figure 3.5: Nucleation sites geometries for single site test sample ((a) and (b)) and double site test sample ((c) and (d))

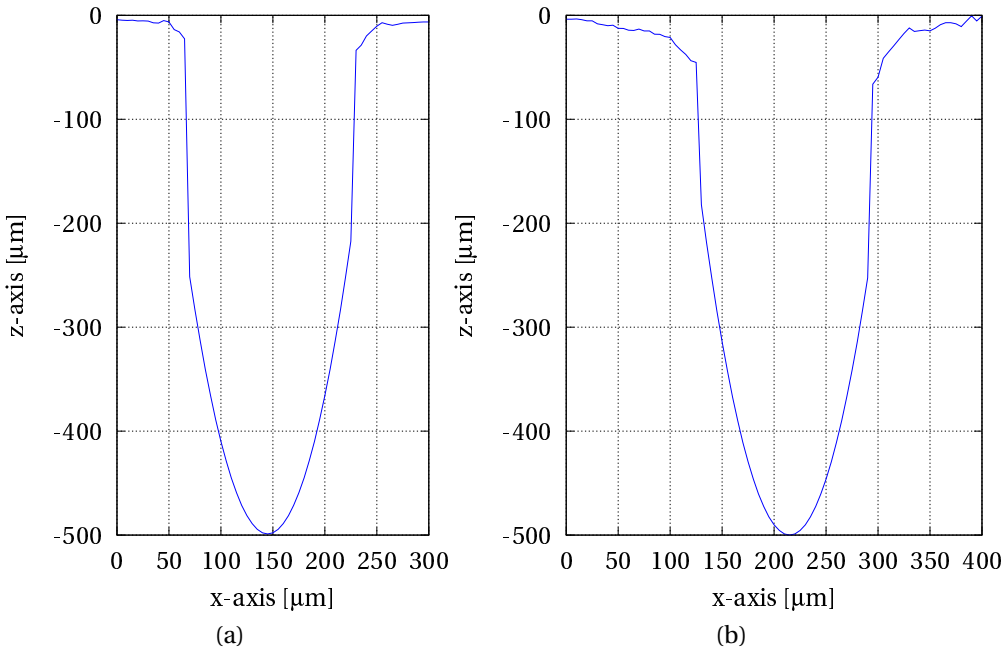

Figure 3.6: Cross-section of the main nucleation site (a) and of the secondary nucleation site used for lateral bubble coalescence (b)

scope, each data point being at a distance of 5 µm from the previous one (see Fig. 3.7). The arithmetic average of absolute height values R_a was equal to 0.42 µm. Although being a common parameter for surface roughness, R_a seems unsuitable for boiling surface description as a local peak would have the same value as a local trough even though having a completely different effect on nucleation. Moreover, R_a, being a single average value, does not described the typical size of local roughness.

A distribution of the signed difference of the data points to the average value of the 8 data points around has been performed (Fig. 3.7 and Fig. 3.8). The interval of 5 µm between each measurement is a balanced size for local roughness description as it is one order of magnitude smaller than the nucleation sites. The graph in Fig. 3.8 shows that at this scale, the distribution of local maxima and minima (respectively positive and negative values) is identical and that almost no local peak or trough of more than 2 µm is found.

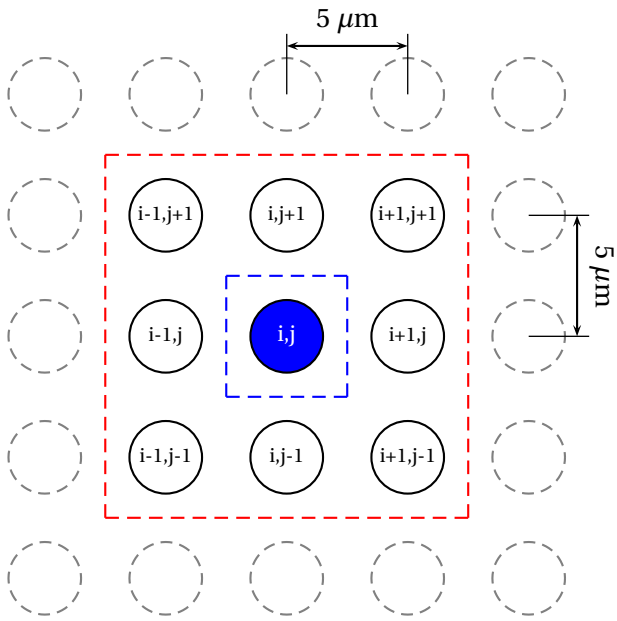

Figure 3.7: Schematic of a data point with 8 data points around

3.1.4 Visualization, measurement and control equipment

As for the test sample, the measurement equipment changed somewhat between the first and last experiments. The equipment detailed here describes what was used during most of the experiments.

Temperature: several temperature measurements are performed at different locations, all using K-type thermocouples. Four thermocouples are placed strategically in the bulk liquid and vapour to check temperature homogeneity. One thermocouple is placed in the vapour phase above the free surface, one is placed in the upper part of the liquid

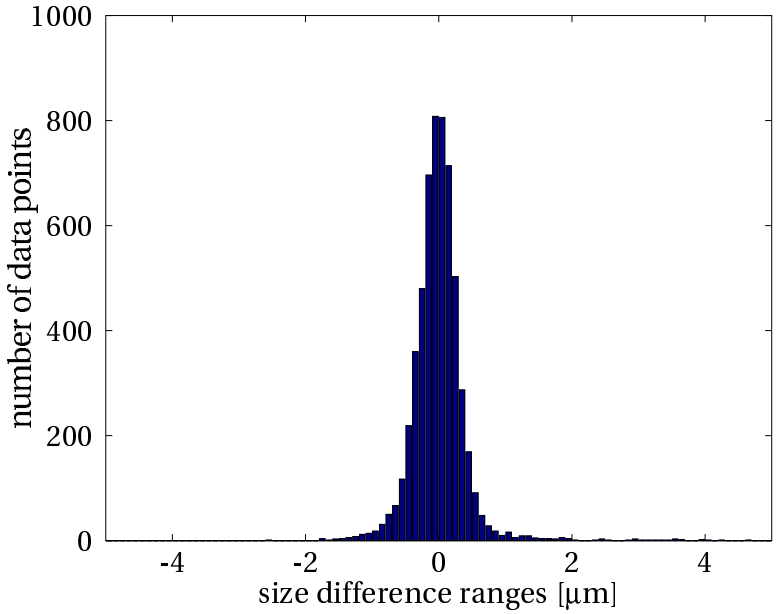

Figure 3.8: Signed size difference of the data points to the average value of the 8 data points around distribution

phase just below the free surface, and two are at the same level as the boiling surface of which one is at a distance of 1 cm and the other one at a distance of 4 cm. Six 80 µm thermocouples are soldered along the test sample copper rod in order to measure the heat flux dissipated to the liquid and the boiling surface temperature. The thermocouples are enclosed into notches along the rod, and soldered with tin solder to allow a low thermal contact resistance. The distance of the thermocouples to the boiling surface were slightly different in each of the test samples built. A representative layout for the respective distances of the thermocouples is : 2, 4, 8, 16, 24 and 32 mm. All ten thermocouple cold junctions were enclosed in an insulated box in which the temperature was measured using a platinium resistance thermometer *Pt-100*. All measurements were then performed by a Keithley 2700 acquisition unit which was controlled by a Microsoft Excel macro called Excelinx.

Pressure: the pressure gauge is mainly used to ensure that no non-condensible gases are present in the system. The pressure should be equal to the saturation pressure corresponding to the bulk temperature. If the pressure is higher, non-condensibles are most probably mixed with the vapour phase or dissolved in the liquid phase.

Electric fields: the brass mesh electrode is placed horizontally above the boiling surface. Its horizontal alignment and distance from the boiling surface are checked and measured using a scope with micro-metric displacement measurement. The high voltage between this electrode and the ground is produced by a Heinziger PNC 30 000 high voltage power supply capable of producing between 0 and 30 kV D.C.

Bulk temperature control: all experiments were performed with a bulk temperature of about 35.9 °C. Depending on the season, the temperature difference to the ambient

air was 5 to 15 K. A 350 W cartridge heater was immersed in the liquid phase and controlled by a on/off control system to maintain the chosen bulk temperature. Enhanced convection due to boiling on the cartridge heater was sufficient to quickly homogenize the temperature throughout the system. Measurements were taken while the heater was off and several minutes after the last on/off control cycle. Heat was dissipated by natural convection on the outer walls of the vessel. The cartridge heater of the test sample was connected to a DC power generator equipped with voltage and current measurement systems.

Vizualisation: In order to capture bubble growth, departure and rise with high enough temporal and spatial resolution, a Photron Fastcam 1024 PCI high speed camera was utilized. The bubble was illuminated with a strong diffuse back-light at a frequency of 200 kHz. The recording frequency was either 1000 fps with a resolution of 1024 × 1024 pixels or 3000 fps with a resolution of 512 × 512 pixels, depending on the resolution needed. In a few coalescence sequences when very quick phenomena were involved, an acquisition frequency of 27,000 fps was used. Two optical systems have been used together with the camera. In most experiments, a 100 mm focal Olympus lens plus a 6 dioptre lens was used. With this system, each pixel on the pictures represented a 17× 17 µm area. Later on, a Questar QM1 short field telescope was utilized. This optical system was capable of magnifying to an area of about 2 × 2 µm per pixel.

3.2 Experimental procedures

3.2.1 Mounting and starting the experimental setup

Before assembling the rig, all thermocouples were calibrated together with their acquisition chain. All thermocouples were immersed in a stirred bath with controlled temperature, and their voltages were measured at 12 different temperatures to obtain their calibration curves. The absolute uncertainties on the temperature measurement were estimated to be ±0.1 K. An improved uncertainty of ±0.05 K for the temperature differences between the thermocouples within the test sample was made possible by ensuring that the exact same thermocouple wire was used for each sensor.

All pieces of the vessel were then assembled. The tank was evacuated and maintained at a pressure of about 1.3 mbar for several hours. This was done in order to allow a full desorption of vapour and gases from the tank and to ensure the airtightness of the vessel. The vessel was subsequently filled with 99% pure n-pentane. It was ensured that the heater cartridge was fully immersed in the liquid phase to avoid any superheating the vapour phase.

The bulk liquid was brought to a temperature corresponding to a pressure of about 1.2 bar and maintained at this temperature for several hours. Regular degassing was performed by evacuating most of the vapour phase to the atmosphere in order to ensure that no non-condensible gases were present in the vessel. The bulk liquid was then cooled down and

maintained at a temperature of about 36.9 °C which corresponds to a saturation pressure of 1 bar.

At this stage, the cartridge heater of the test sample was turned on to superheat the boiling surface. Approximately 20-30 K of superheat was required to initiate boiling at the artificial nucleation site. As a result of the care taken in the surface preparation and cleaning, boiling only occurred at the artificial nucleation site. At such high wall superheats, the nucleation site produces bubbles at such a rate as to generate a nearly continuous vapour column. As this boiling regime was not the focus of this investigation, the heat flux was then reduced to an extent that the wall superheat was maintain between 1.5 and 8 K. This superheat range was low enough to generate discrete bubble events, albeit with very small waiting times, whilst being high enough to keep the nucleation site active.

3.2.2 Avoiding mirage effect

Mirage effects occur when light rays are refracted by passing through a medium of non-constant optical index of refraction. They cause a distortion of the object image, and alter the perception of reality. As the optical index usually varies with temperature, mirage effects can be a source of error when studying and observing boiling. Avoiding mirage effects was one of the concerns in this study and particular care has been given to this issue. Experiments have been performed by placing a 1 mm diameter spherical plastic ball on the surface. A picture was first taken without heating the surface (thus without any mirage effect, see Fig. 3.9a). The surface was then heated as if in the real experimental conditions. If no particular care was taken, the ball looked like that in Fig. 3.9b with a 10 K superheat.

The lower part shows a strong mirage effect leading to the impression of a very large foot. The procedure to avoid this effect is to use only very pure (more than 99% purity) and fresh pentane that has small optical index variation with temperature. In addition, the recording angle was slightly modified to allow a 3° angle with the horizontal plane. This allows the optical path to cross a much thinner superheated layer of liquid, without distorting much the image. Eventually, the thermal control of the bulk liquid was stopped a few minutes before the recordings. Fig. 3.9c shows the image of the plastic ball with the same 10 K of superheat. It is now clear that the image is not significantly distorted by the optical index gradients.

3.2.3 Detecting hysteresis

Boiling often presents hysteresis phenomena that are generally due to nucleation site activation and de-activation and to boiling regime transitions. Particular care has been taken in the experiments to detect any hysteresis effects that may occur. For this purpose, all measurement data sets have been performed by increasing the heat flux as well as by decreasing

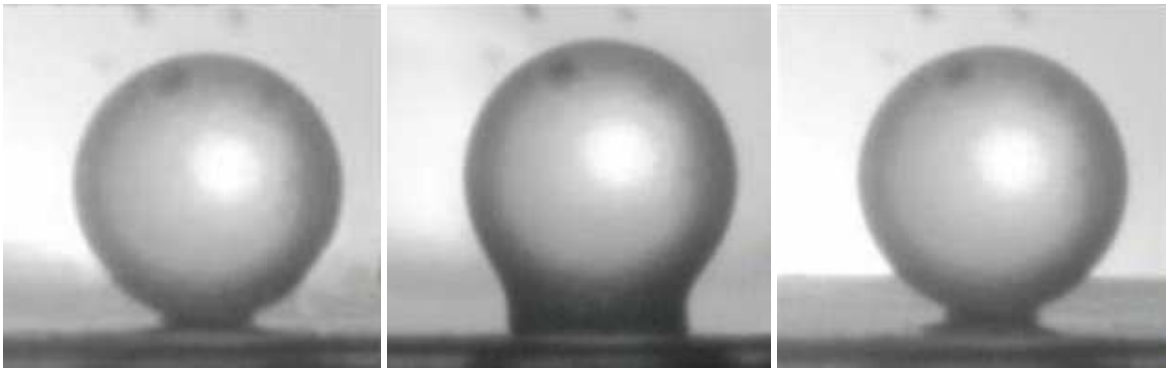

(a) (b) (c)

Figure 3.9: Plastic ball without any superheat(a), with 10 K of superheat and mirage effect (b) and with 10 K of superheat without mirage effect (c)

the heat flux. Like in Fig. 3.10, it has been verified that the same behaviour is observed when increasing or decreasing the heat flux.

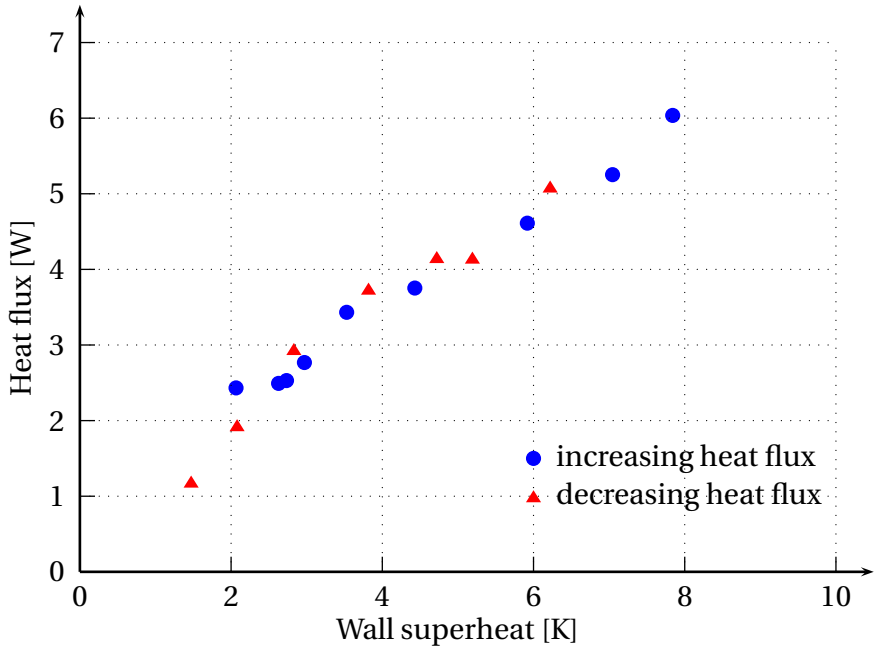

Figure 3.10: Heat flux vs wall superheat without electric field - increasing and decreasing heat flux

3.3 Measurement techniques

3.3.1 Heat flux and boiling surface temperature measurement

The heat flux dissipated to the fluid by the boiling surface as well as the boiling surface temperature were calculated using the six thermocouples along the copper rod of the test sample. The heat flux across a section of the copper rod was assumed to be uniform, the system was assumed to be axisymmetric and the radial heat losses through the PTFE were assumed to be uniform along the rod. The thermal conductivity of copper was assumed to be constant within the temperature range investigated. Figure 3.11 schematically shows the positions of the thermocouples along the rod, and an example of temperature data obtain from the six thermocouples.

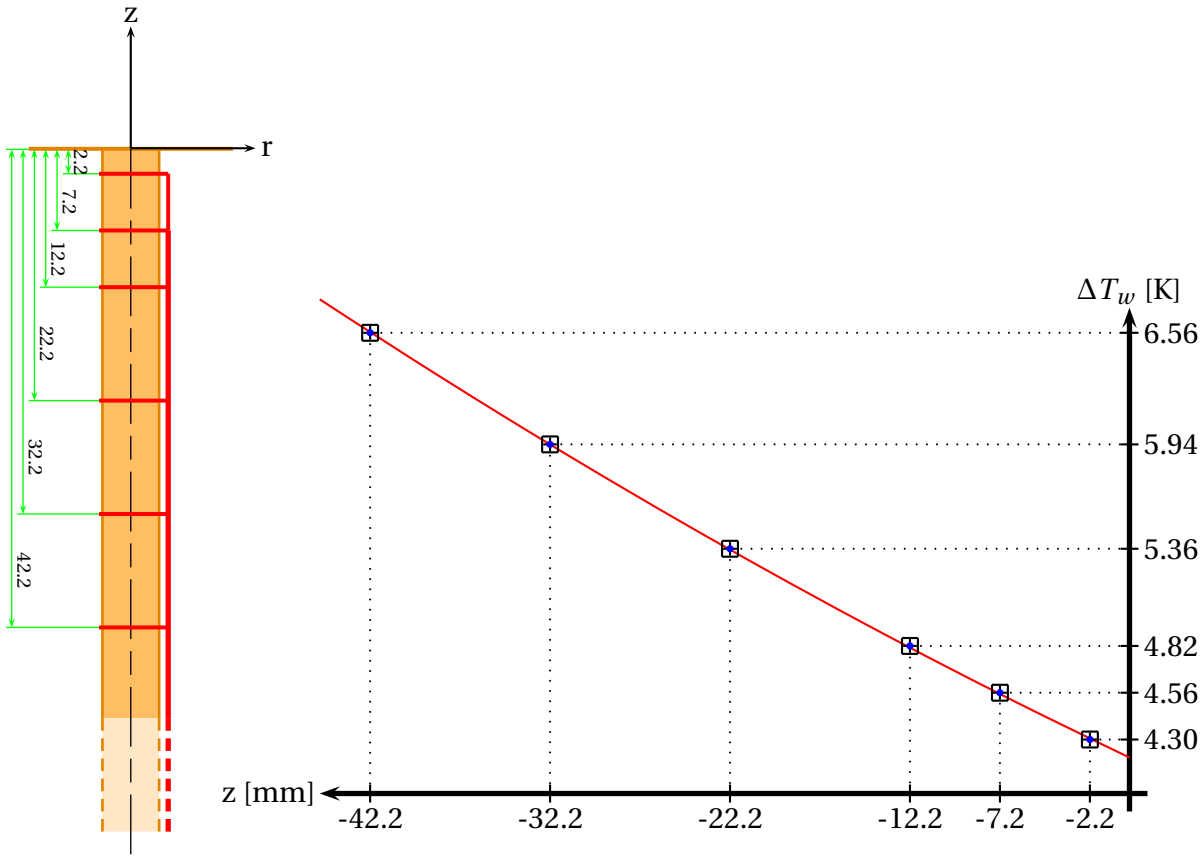

Figure 3.11: Test sample thermocouples positions and temperature example

With these previous assumptions, the temperature along the z-axis of the rod can be written as follow :

$$T(z) = a \times z^2 - b \times z + c \tag{3.1}$$

In this equation:

$$b = -\left.\frac{\partial T}{\partial z}\right|_{z_0} \tag{3.2}$$

$$a = \frac{1}{2}\frac{\partial^2 T}{\partial z^2} \tag{3.3}$$

In this case, c is the boiling surface temperature. With λ_{Cu} the copper thermal conductivity,

$$q_w = b \times \lambda_{Cu} \tag{3.4}$$

with q_w the heat flux at the boiling surface, and

$$\frac{\partial q}{\partial z} = 2 \times a \times \lambda_{Cu} \tag{3.5}$$

where $\frac{\partial q}{\partial z}$ is the rate of heat flux dissipation along the rod.

From the six temperature measurements, a second order polynomial data fit allows the determination of the coefficients a, b and c. From these coefficients, the heat flux at the boiling surface and the boiling surface temperature are determined.

The respective uncertainties on the temperature and thermocouple position measurements are estimated to be ±0.05 K and ±0.5 mm, as plotted in Fig. 3.11. As suggested by Kempers et al. [91], the temperature values were considered as being distributed normally within their uncertainty band, while the thermocouple locations were considered as being distributed uniformly within their uncertainty interval. A 2-D Monte-Carlo method described by Kempers et al. [91] was used to estimate the heat flux and surface temperature uncertainty with a 95% confidence interval: taking a temperature measurement data set in given conditions, several thousand temperature and thermocouple position estimation sets are created, respecting the previously detailed distribution. For each estimation set, a second order polynomial data fit is performed, and the heat flux at the surface and the surface temperature are computed. The best estimations of the heat flux and the surface temperature are the mean values, and the true value is believed to be within twice the mean absolute deviation with 95% confidence.

With this method and the measurement data sets, the surface temperature uncertainty was estimated to be within ±0.15 K, leading to a ±0.18 K uncertainty for the wall superheat.

The heat flux uncertainty was ±47 % for low heat flux and reduced to ±15 % for high heat flux levels. Included in this uncertainty is the additional error associated with the thermal conductivity of copper. This error had no influence on the temperature computations and is an offset error, hence it is the same for each heat flux computation and does not influence the differences in the observed trends, i.e. it is not a random error. No detailed quantitative analysis is performed on the heat flux, in the sense that only the relative trends are considered. In that context, this error can be viewed as acceptable.

3.3.2 Image processing

All phenomena studied (bubble growth, departure, rise and coalescence) are recorded by a high speed camera. An image processing program and methodology has been developed to

compute the bubble volume, the height of its center of gravity, its shape or simply to follow its trajectory while rising in the bulk liquid. In order to facilitate straight forward measurement of these parameters for thousands of pictures, an automated bubble contour detection is performed. The different steps can be seen in Fig. 3.12 and are described as follows:

1. On an image of the calibrated antenna recorded with the same magnification (Fig. 3.13), the size of a pixel is measured.
2. The batch of images are cropped to keep only the area of interest. Particular care is taken to cut the bottom of the image exactly on the nucleation site.
3. The batch of images are pre-processed by increasing the contrast and setting an appropriate brightness. The brightness level is chosen visually on a key picture and applied to the entire batch. In some cases, the natural brightness of parts of the background vary too much to apply one setting of brightness for the whole picture. Different brightness settings are then applied on each part of the pictures. A script for Gimp software has been written to automate these batch transformations.
4. Highest grey gradients are then detected using a Sobel method. This is done by a script written for the commercial Matlab software platform, using its Image Processing Toolbox.
5. All items of the black and white picture are analysed to detect the bubbles from other contours like reflection on the bubbles. Sometimes there is only one bubble attached to the nucleation site, sometime it has detached and is rising in the bulk liquid, and sometimes there is a new bubble growing on the surface bellow a rising bubble. Each bubble is tracked between successive images.

(a)

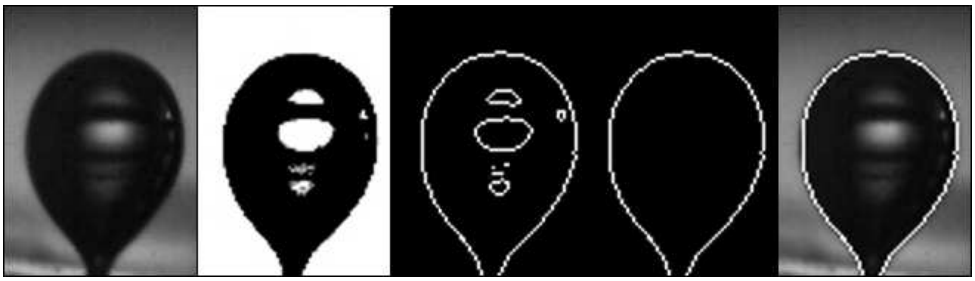

(b)

Figure 3.12: Image processing sample without EHD (a) and with EHD (b)

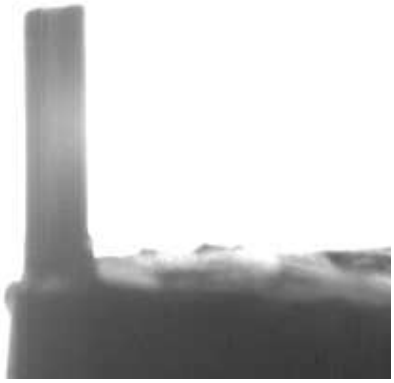

Figure 3.13: Calibrated antenna picture

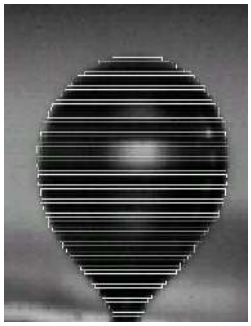

Figure 3.14: Volume discretization of a bubble

Once the contour of a bubble is detected, it is used to compute the geometric parameters of the bubble. For volume and center of gravity calculations, the bubble is divided into slices of 1 pixel height, as shown in Fig. 3.14. Each slice is considered as a cylinder (thus axisymmetric), and the volume is the sum of each cylinder. This method has the advantage of taking into account the whole contour rather than simplifying the bubble as a sphere or a truncated prolate spheroid as it is sometimes the case ([151], [54], [106] and [29]). A prolate spheroid approximation could lead to as much as 20% error on the volume determination when there is a neck at the base of the bubble. Another advantage of this method is that the bubble is not considered as fully axisymmetric. In a case where the bubble is slightly tilting (like when the electric field around the bubble is not fully axisymmetric), the error on the volume determination remains low.

The height of the center of gravity of the bubble is computed assuming that the density is homogeneous inside the bubble. Using the same discretization of the bubble as a stack of cylinders, the height of the center of gravity is obtained by dividing the sum of the volume each cylinder weighted by its average height by the total volume of the bubble. Another method to compute the height of the center of gravity, presented by Siedel *et al.* [169], is compared to the present method in Appendix B.

The uncertainty on the volume and height of center of gravity determination is difficult to assess. The distortion of the image due the mirage effect or due to the whole optical system can not be estimated. From the experience detailed in 3.2.2, it can only be stated that utmost care is taken to ensure that the images represent reality. The uncertainty due to the contour determination can be estimated to 1 pixel normal to the surface. This uncertainty on the volume would be about 3% before bubble detachment and more than 20% when the bubble is still small.

3.4 Operating conditions

Although the influence of many parameters on boiling could be studied, only a chosen set has been selected for this work. The fluid that was used during all experiment was n-pentane, and the working pressure was always set to 1 bar. The thermodynamic properties of saturated pentane at this pressure are detailed in Table 3.1. It should be noted that compared to water, the density difference between liquid and vapour phases is much lower. Also, the surface tension is about 5 times smaller, leading to a lower capillary length defined as:

$$L_c = \sqrt{\frac{\sigma}{(\rho_l - \rho_v)g}} \tag{3.6}$$

$$L_c(\text{pentane}) \approx 1.56\,\text{mm}$$

P	bar	1
T_{sat}	°C	35.7
ρ_l	$\text{kg}\cdot\text{m}^{-3}$	610.5
ρ_v	$\text{kg}\cdot\text{m}^{-3}$	2.96
h_{fg}	$\text{kJ}\cdot\text{kg}^{-1}$	358.4
$c_{p,l}$	$\text{J}\cdot\text{kg}^{-1}\cdot\text{K}^{-1}$	2338
$c_{p,v}$	$\text{J}\cdot\text{kg}^{-1}\cdot\text{K}^{-1}$	1788
$\mu_l \times 10^6$	$\text{kg}\cdot\text{m}^{-1}\cdot\text{s}^{-1}$	196
$\mu_v \times 10^6$	$\text{kg}\cdot\text{m}^{-1}\cdot\text{s}^{-1}$	6.89
λ_l	$\text{W}\cdot\text{m}^{-1}\cdot\text{K}^{-1}$	0.107102
λ_v	$\text{W}\cdot\text{m}^{-1}\cdot\text{K}^{-1}$	0.0167
σ	$\text{N}\cdot\text{m}^{-1}$	0.014506
$\varepsilon_{r,l}$	-	1.8

Table 3.1: Properties of saturated n-pentane at 1 bar

Concerning the electrical properties of pentane, it is a non-polar fluid with a relatively low permittivity (Table 3.1). Its conductivity is so low that it was never accurately measured, though it is below $1\,\text{pS}\cdot\text{m}^{-1}$. The electric fields involved during experiments was within the range of 0 to $30\,\text{kV}\cdot\text{cm}^{-1}$, which is one order of magnitude below the breakdown voltage.

Figure 3.15: Vertical coalescence of succesive bubbles

Concerning safety and the environment, it is a non-toxic fluid but a good solvent that can dissolve many materials. It is highly flammable and very volatile at ambient temperature, and it is explosive when mixed with air at 1.4 to 7.8%. Particular attention has been given to this issue to avoid any risk of fire or explosion.

The range of heated surface superheat during the experiments was set between about 1.5 to 8 K. Below 1.5 K, the nucleation site was not active, and above 8 K, vertical coalescence between successive bubbles from the same nucleation site would occur (Fig. 3.15). This regime of coalescence was not the focus of this study.

The original design of this experimental facility, combined with appropriate measurement systems, procedures and data analysis facilitates:

- *the production of discrete bubbles from a single nucleation site of known geometry*
- *control of the growth rate via controlled system and surface temperatures*
- *measurement of bubble dimensions with unprecedented accuracy and repeatability*

Such a facility enabled us to produce original results that were not available in the open literature and are fundamental with regard to gaining a clear and unambiguous understanding of boiling.

Chapter 4

Heat transfer

The novel design of this experimental setup results in a controlled thermal environment in which bubbles nucleate, grow and move. In order to understand the behaviour and dynamics of bubbles, the thermal environment should first be accurately described.

Section 4.1 details the assumptions and analysis that was performed prior to performing experiments while designing the experimental facility. The temperature distribution within the test sample and on its upper surface is analysed in order to define the reference surface temperature used to compute the wall superheat. The convective structures and plume above the heated surface are then described from recorded pictures, and analysed in order to investigate the thermal environment in which a bubble will nucleate and rise in the liquid. Indeed, phase change occurs owing to the available heat from the superheated liquid in the vicinity of the interface. The temperature of the liquid surrounding the bubbles plays a major role in bubble growth dynamics.

The assumptions and analyses have been verified afterwards by performing CFD numerical simulations of coupled conduction inside the test sample and convection above the heated surface (section 4.2). Good agreement is found between the experiments and the numerical simulations as well qualitatively, concerning the convective instabilities developing on the surface as quantitatively, concerning the average convective heat transfer coefficient on the surface.

The third section (4.3) analyses the heat transfer from the test sample to the fluid. Convective coefficients and heat transfer enhancement due to the application of electric fields are investigated.

4.1 Temperature field and fluid motion

4.1.1 Temperature field in the experimental sample

Our experimental test samples have been designed to allow single isolated bubble nucleation without the occurrence of unwanted bubbles which may nucleate at other places. The heat flux is imposed at the lower part of the test sample by the heater (see Fig. 3.4 in section 3.1.3). In most experiments, the electrical power provided is less than 2 W. The thermal energy is mainly conducted through the copper rod. However, some of this heat is diffused through the insulation material (PTFE), or convected to the room from the lower end of the test sample. The heat flux through the pin is almost constant except for small radial losses through the PTFE (see subsection 3.3.1). The temperature profile is thus almost linear along the vertical z-axis. The order of magnitude of temperature drop is about $1\,\mathrm{K{\cdot}cm^{-1}}$. Atop the rod is soldered a very thin copper plate of about 40 µm thickness. Tin is used for the heterogeneous welding which was done under pressure. Due to the known compatibility between these two metals and the fact that both are soft, any eventual contact thermal resistance has been minimized. Concerning thermal resistance by conduction through the tin layer, its effect is negligible as the tin thickness is less than 20 µm and its conductivity is more than $65\,\mathrm{W{\cdot}m^{-1}{\cdot}K^{-1}}$.

The temperature distribution in the copper plate is axisymmetric. It can be considered as one-dimensional as the plate is very thin. The heat flux is dissipated by the upper surface to the fluid as the lower side of the plate is insulated. The temperature is highest at the center of the plate and remains high atop the copper rod. The temperature then drops radially in the plate as it is acting like a fin. The superheat at the outer edge of the plate is thus low enough to prevent bubbles from nucleating in this region.

Another concern in the experimental design was avoiding inhomogeneous and non-constant temperature at the center of the plate where bubbles are forming. In many experiments, the wall temperature is known to be non-homogeneous and to vary with time under the bubble base, as no wall temperature boundary condition can be imposed. The heat flux is always controlled and conducted through the wall. Many experimental works or numerical simulations bring to the fore the existence of a non-homogeneous and a non-constant temperature on the wall surface ([174], [85], [93] and [132]) and some experimenters developed complex temperature control systems to avoid temperature fluctuations [95]. Our experimental apparatus has been designed to minimize the variations of temperature under the bubble. Copper has an extremely high thermal diffusivity (about $1.1 \times 10^{-4}\,\mathrm{m^2{\cdot}s^{-1}}$). The bubble size (about 1 mm diameter at departure) is small compared to the copper pin diameter (5 mm). Furthermore, the heat flux transmitted through the bubble is assumed to be small compared to the overall heat transfer to the fluid due the geometry of the test sample. It was estimated that less than 2 % of the heat flux transmitted to the fluid was latent heat transfer (see section 4.1.2).

Once the temperature variation are minimized, there is a need to define a wall temper-

ature used as a reference to describe boiling conditions. However, this temperature can be defined only if the wall temperature is assumed to be homogeneous (at least around the bubble base) and constant with time at the time scale of the described phenomena. Our assumptions to define this reference wall temperature are that:

- the heat flux is homogeneous over the copper pin: this is aided by the high thermal diffusivity of copper. The copper rod below the surface is thus acting like a heat reservoir.
- the side effects (on the sides of the pin) due to the copper plate are negligible at the place of the bubble: this is ensured by the small size of the bubble compared to the size of the pin.
- the local wall temperature fluctuations are negligible: this is reasonable due to the low ratio of latent heat transfer to the overall heat transfer. If this assumption were not verified, the reference temperature is at least a mean temperature.

4.1.2 Ratio of latent and sensible heat transfer

Boiling heat transfer is a complex combination of several heat transfer mechanisms. Energy from the heated surface is first transferred by conduction to the neighbouring liquid which is cooler. The liquid temperature increases, and thus diffuses heat to the cooler bulk liquid above. The liquid density decreases with increasing temperature, so the buoyancy force tends to move the hotter liquid upwards and the cooler liquid downwards. Flow structures appear because of these buoyancy forces. These structures are strongly dependent on the liquid properties, the temperature gradients and the system geometry. Within the flow, heat is diffusing, in the direction of decreasing temperature gradient. The combination of these mechanisms of heat diffusion and fluid motion is natural convection.

In the superheated liquid close to the heated surface, or directly on the heated surface, a bubble may nucleate. In the case of this study, bubbles can only nucleate inside the artificial nucleation site. Heat is then transferred from the superheated liquid phase to the bubble and will change liquid into vapour. The heat dissipated as phase change enthalpy is known as latent energy. As a bubble is attached to the heated wall, some heat is also transferred from the surface directly to the vapour, heating the vapour layer close to the wall.

When liquid is transformed into vapour, its volume is multiplied by more than 200, causing the bubble to grow in volume. The pressure inside the bubble is balanced, giving the bubble its particular shape and moving its interface. This motion of the interface is a new source of liquid motion, thus enhancing convective movement around the bubble. Once the bubble is detached from the wall, its buoyancy makes it rise above the surface, causing liquid motion in its wake, and thus enhancing convection.

All convection effects induced by the presence of bubbles is generally assembled into the term of convective heat transfer. Its influence on the overall heat transfer remain small as long as few bubbles are present, but may become important when many nucleation sites are active.

A rough estimation of the influence of the active nucleation site on heat transfer in our experiments has been performed. The ratio of latent heat flux over the total heat flux transferred to the fluid has been computed, using the phase change enthalpy and the vapour volume produced (see Fig. 4.1). The data points include experiments with different electric fields applied on the boiling surface. It is shown that typically 0.5 to 1 % of the total heat is latent heat. In our case, as only one nucleation site is active, the effect of the bubbles on the overall heat flux can be considered as negligible, and only natural convection will be taken into account in the heat transfer considerations. This is consistent with the results of Barthès (see [13] p. 160).

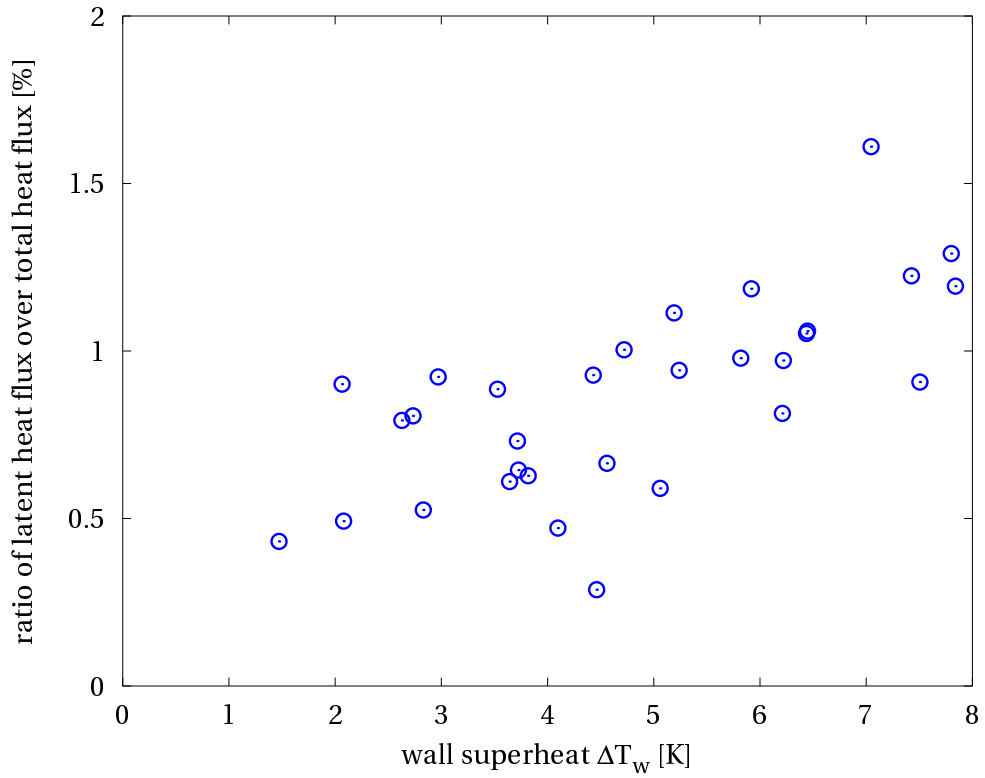

Figure 4.1: Ratio of latent heat flux over total heat flux

4.1.3 Plume

As explained in section 4.1.2, the main means of heat dissipation from the heated surface to the fluid is natural convection. The convective motion is coupled or driven by the temperature distribution on the heated surface. The liquid in the vicinity of the surface is superheated by conduction through the thermal boundary layer. The highest liquid temperatures are reached at the center of the plate due to its geometry. The superheated liquid, because of its lower density, is rising in the bulk liquid, forming a plume at the center of the plate. The superheated liquid rises until reaching the free surface about 10 cm above the heated plate where it is cooled by evaporation.

As a plume is rising from the center of the plate, superheated liquid from the surface is driven to this plume, leading to a superheated zone above the center of the plate where bubbles are nucleating and growing. Bubble dynamics will most probably be impacted by the fact that the bubble will nucleate in a sufficiently superheated liquid.

This particular flow structure is related to the design and geometry of the experiment, but is similar to the flow pattern that develops during boiling at low heat flux or wall superheat. Between the onset of boiling and the fully developed nucleate boiling regime (see section 2.2), the isolated bubble regime is made up of scattered active nucleation sites from which columns of bubbles are departing. Convective structures form as the liquid is drawn up in the wake of the bubbles while saturated liquid is brought to the surface between the active nucleation sites (see Fig. 4.2 taken from V.P. Carey [23]).

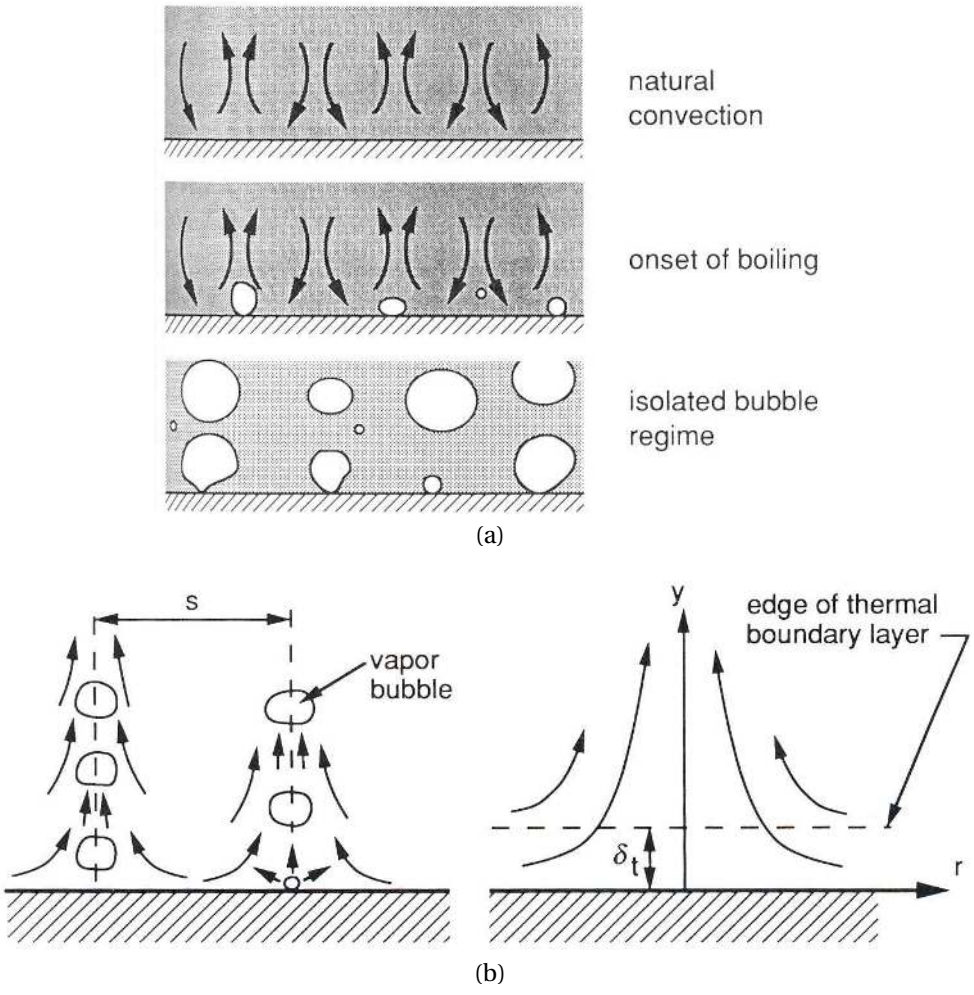

Figure 4.2: Schematic of boiling regimes (a) and fluid flows (b) at low superheat from (V.P. Carey [23])

4.1.4 Visualization of convective structures at high wall superheat

Convective structures can be visualized when the liquid is illuminated from the back with a strong directional light. Light rays are deflected by convective structures owing to high refractive index gradients. Dark or light areas appear on the image depending on the diverging or converging effect of the convective structure. These structures are hardly visible in the superheat range of our experiments (2 to 8 K) because temperature gradients are too low. Better visualization has been achieved by increasing the heat flux until reaching a wall superheat of about 30 K. Contrast has then been increased on the picture to make convective structures appear more clearly. These experiments have been performed on the experimental sample before any artificial nucleation site was created, allowing pure natural convection to be obtained.

Figure 4.3 shows a series of pictures with $\Delta t \approx 83$ ms between two successive pictures. No electric fields is applied between picture 1 to 48. Large convective structures are rising slowly at a velocity of about 5 to 10 $\mathrm{mm \cdot s^{-1}}$ [170]. Some structures are vertical while some other have a mushroom-like shape. Such a mushroom-like structure can be visualized between picture 19 and 26: a hemispherical *cap* appears on the center-right part of the picture. This *cap* rises while slowly moving to the left toward the central plume.

Between pictures 49 and 50, a 43 $\mathrm{kV \cdot cm^{-1}}$ electric field is applied above the heated surface. The flow pattern immediately changes. A transient regime is observed between picture 50 and picture 54, then a new regular pattern is observed in the following pictures. The transient regime is described with a finer time step ($\Delta t = 3$ ms) in Fig. 4.4 and Fig. 4.5. Small convective cells (about 0.5 mm) appear from above the heated plate until filling the whole picture in about 100 ms. The convective cells then fade away or seem to fall down again near the plate; 300 ms later, all visible convective cells are concentrated in a 3 mm layer above the heated wall. From picture 54 to picture 96 of Fig. 4.3, the convection flow pattern with the application of the electric field is installed. The structure of the flow is clearly different from the structure without the electric field. The convective cells are much smaller, and only concentrated in a thin layer above the heated surface. Movement of the cells is more intense and faster. The convective structures are sometimes pushed from right to left or from left to right. As it can be seen from picture 76 to 83, all convective structures are pushed to the right side until almost no more convective cells are visible in the field of view. Then, from picture 84 to 88, the convective cells move back to the left, so that the flow pattern of picture 88 is again similar to this of picture 75.

The temperature measurements and convection visualizations detailed in this section show that the bubbles nucleating on the surface grow in a particular thermal environment that is strongly dependent on the natural convective structures developing on the surface. It seems that in the absence of electric field, the convective structures tend to move superheated liquid toward the artificial nucleation site, and further investigations to describe the convective structures are detailed in section 4.2. The presence of an electric field clearly induces a modification of the flow structure above the heated surface into smaller convective cells. The consequences of this new structure is an enhancement of the convective heat

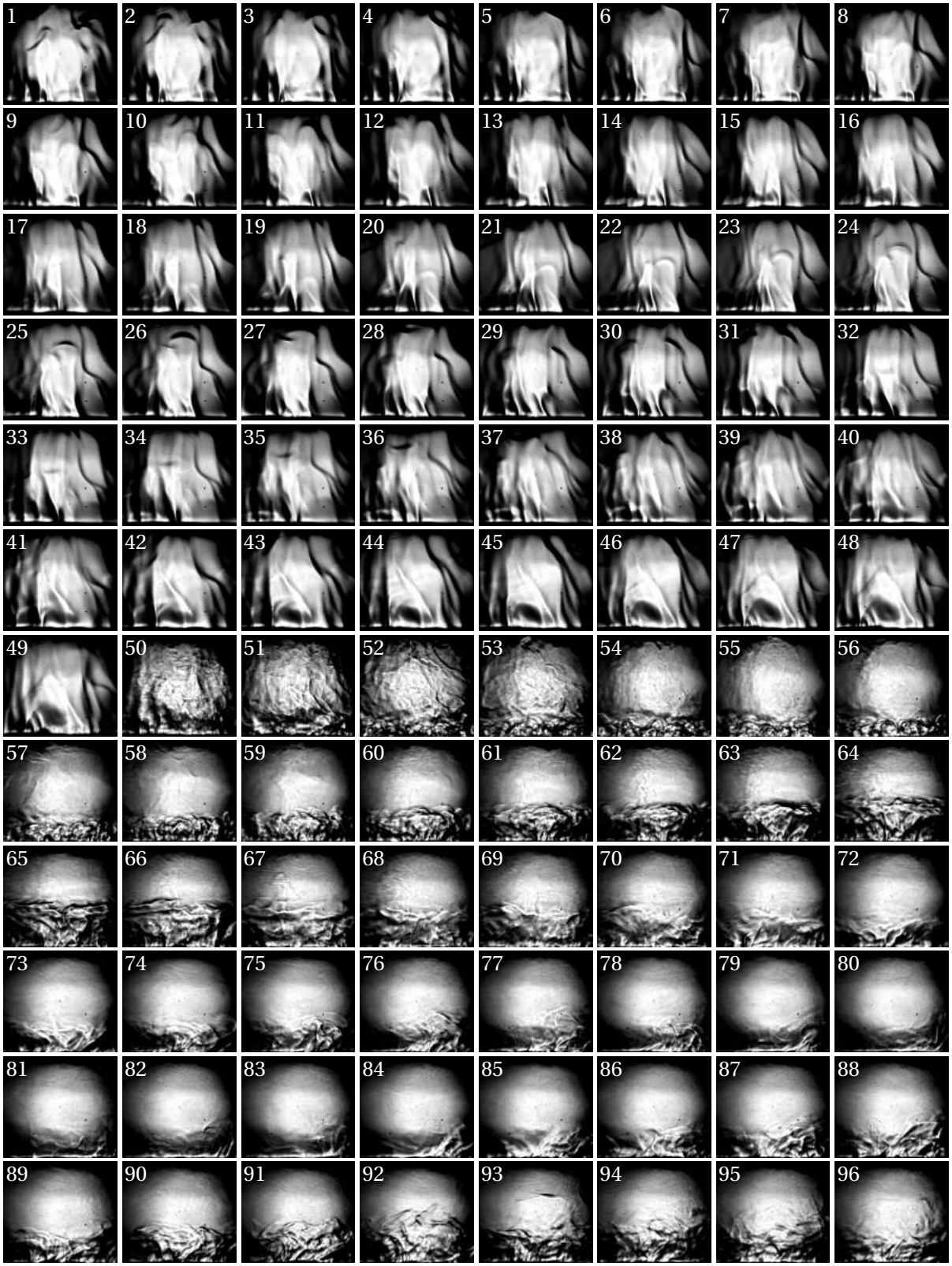

Figure 4.3: Photos of convective structures with $\Delta T_W \approx 30\,\mathrm{K}$ ($\Delta t \approx 83\,\mathrm{ms}$ between two images). A $43\,\mathrm{kV{\cdot}cm^{-1}}$ electric field is suddenly applied at picture 49. Picture width is about 8 mm.

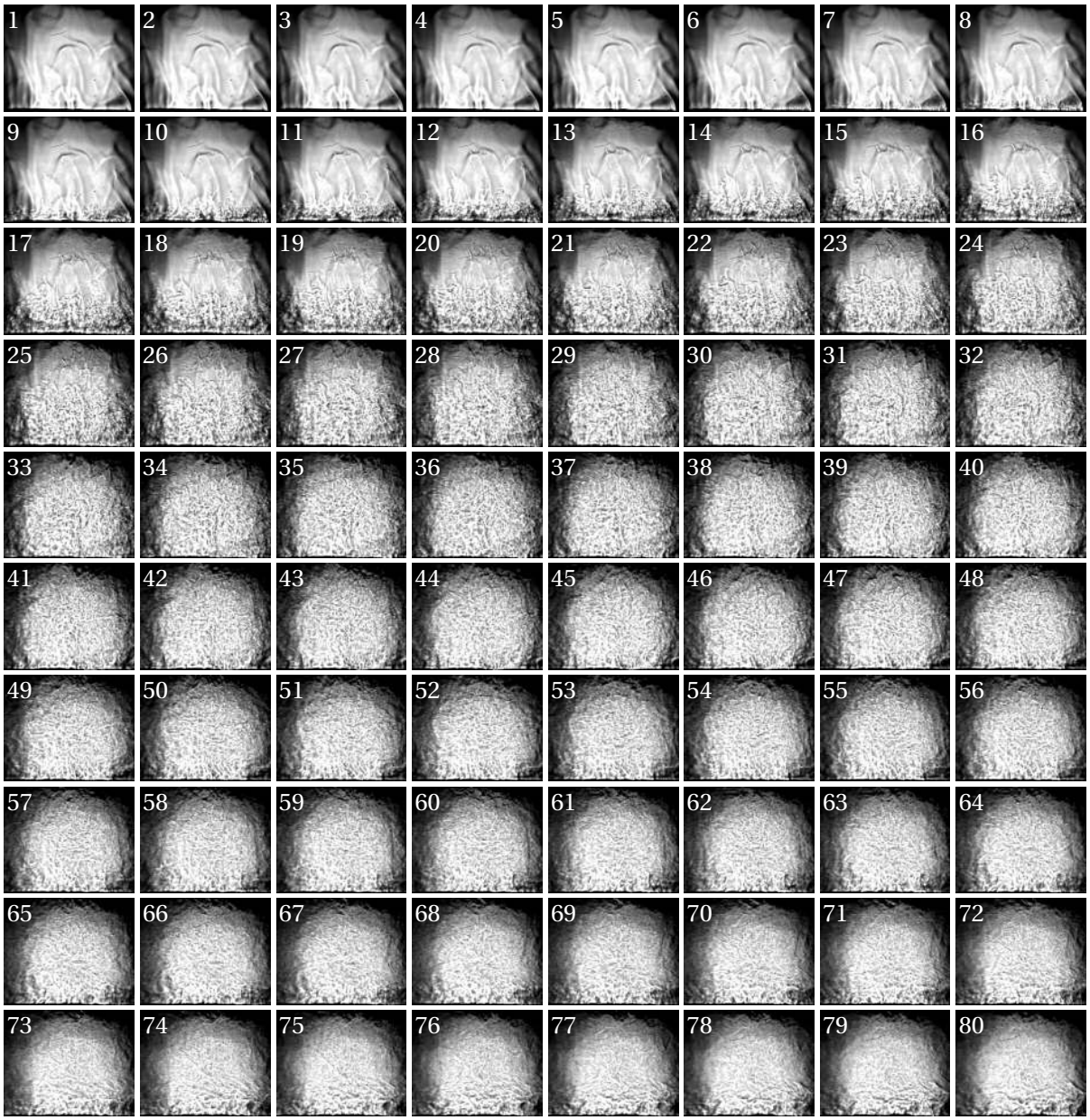

Figure 4.4: Detailed representation of the transient behaviour of convective structures after a 43 kV/cm electric field is applied ($\Delta T_W \approx 30\,\mathrm{K}$, $\Delta t = 3\,\mathrm{ms}$ between two images). Picture width is about 8 mm.

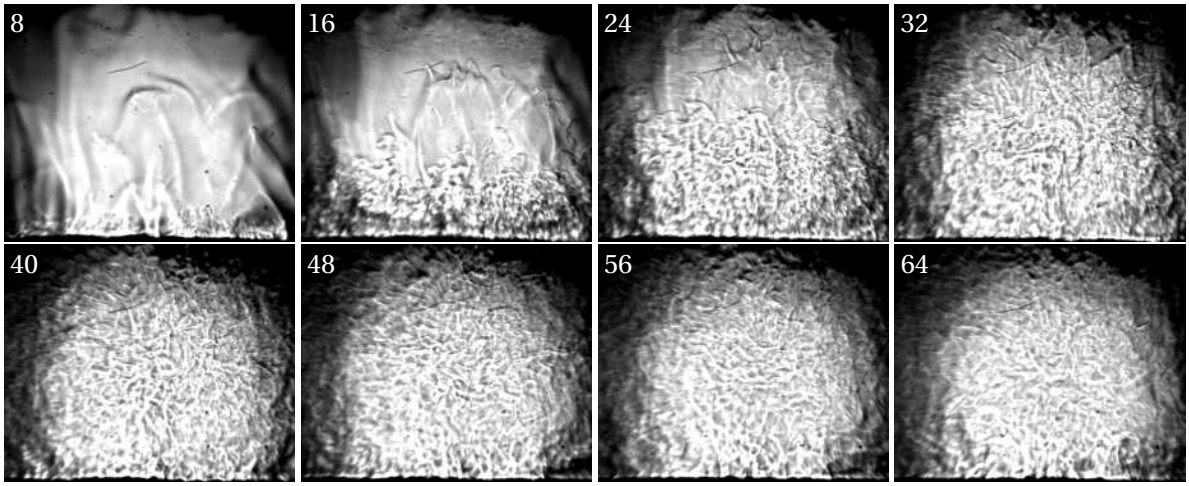

Figure 4.5: Close-ups from selected pictures from Fig. 4.4

transfer, and this is described in section 4.3.

4.2 CFD simulation of convection above the heated surface

As presented in section 4.1, a precise knowledge of the temperature field and of the flow structure at the place where the bubble will nucleate is essential to analyse the different heat transfer mechanisms that govern bubble dynamics. A qualitative analysis has been performed together with the design of the experimental test sample, and some visualizations and measurement have been possible. Nevertheless, the hypotheses made are to be checked, and many parameters cannot be measured nor determined quantitatively. For these reasons, it has been decided to perform numerical simulations of coupled conduction inside the test sample and convection above the heated surface. Steady-state simulations have been performed by A. Albadawi [2] as part of his master thesis under my co-supervision with J. Bonjour. On my side, I performed unsteady simulations at the Department of Mechanical and Manufacturing Engineering in Trinity College Dublin in partnership with Dr. Tony Robinson.

4.2.1 Steady-state convection simulation under TransAT simulation code

A finite volume numerical simulation of natural convection over the heated surface has been performed by Albadawi [2] using the commercial software TransAT. It was a 2D axisymmetric simulation, considering conduction inside the 40 µm copper plate and convection to liquid pentane above the plate. The boundary conditions were constant heat flux on a 5 mm diameter area at the center below the plate, adiabatic condition around the heated area below the plate. The boundary conditions of the fluid domain were an adiabatic wall on the bottom side, and imposed temperature wall on the outer and top sides. The imposed temperature

was the bulk liquid temperature of 35.9 °C.

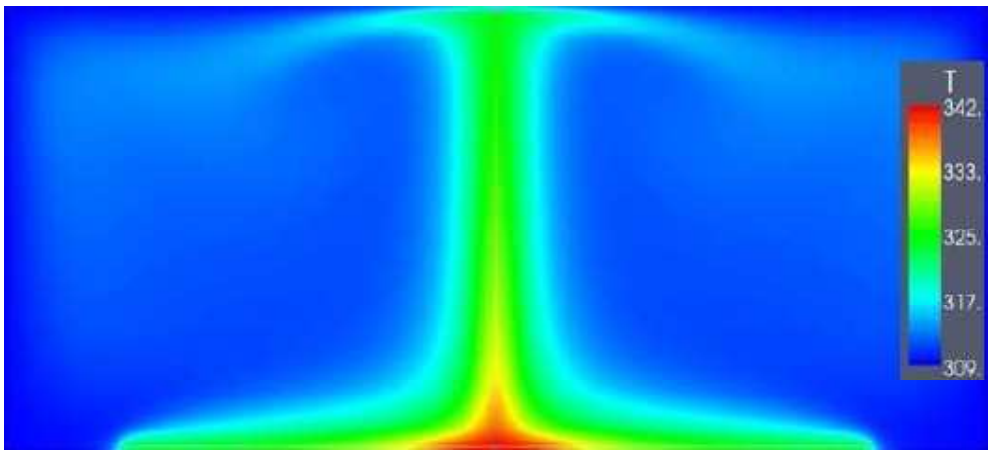

Figure 4.6: Finite-volume simulation of conduction inside the copper plate and convection above the surface. Temperature field in Kelvin.

A result of the temperature field is given in Fig. 4.6 for an imposed heat flux of 1 MW·m^{-2}. A central plume of superheated liquid rises from the center of the copper plate. As the top boundary condition is an imposed temperature, the liquid is cooled down to the saturation temperature, and flows back to the edge of the plate by the side, thus forming a torus. Except for the center of the plate with the plume, the thickness of the thermal boundary layer above the heated plate is between 1 and 2 mm. As it was previously suggested, the surface temperature is highest at its center and decreases with radial distance. The volume above the artificial nucleation site consists of superheated liquid which stores the sensible energy that is to be converted into latent heat as soon as a vapour nucleus appears.

The results brought by these simulations confirm qualitatively the presence of the central plume, but are inadequate to predict quantitatively the temperature and velocity field. Indeed, the geometry of the computational domain does not fully conform to the experimental configuration. Moreover, the top boundary condition of an imposed temperature wall seems inadequate and apparently substantially affects the fluid flow. A part of the experimental sample below the copper plate needs to be included in the computational domain as the PTFE is not a perfect insulator. Finally, convective instabilities may form (as it was observed in Fig. 4.3), so that a steady-state simulation might not be sufficient to accurately represent the convective pattern.

4.2.2 Unsteady convection simulation using Fluent simulation code

Transient numerical simulations have been performed using the Fluent simulation code in order to precisely represent the temperature field and the fluid flow due to natural convection above the heated surface. This work was done in partnership with the Department of Mechanical and Manufacturing Engineering in Trinity College Dublin where I stayed for 6 months.

Coupled conduction and convection simulations have been performed, without taking into account bubble nucleation and phase change in the artificial nucleation site area. The computational domains chosen were *2D*-axisymmetric. Several computational domain were used, including or not including the mesh grid electrode or a part of the test sample below the heated plate (as described in section 4.2.2.2). Results are given in sections 4.2.2.3, 4.2.2.4 and 4.2.2.5.

4.2.2.1 Mathematical modelling

Common Navier-Stokes equations and the energy equation are solved for a *2D* axisymmetric computational domain. The Boussinesq approximation is used to take into account for the temperature dependency of the density. In order to determine whether the flow is laminar or turbulent, the Rayleigh number has been computed:

$$\mathrm{Ra} = \mathrm{GrPrd} \tag{4.1}$$

$$\mathrm{Ra} = \frac{\rho^2 g \beta \Delta T_W r^3}{\mu^2} \frac{\mu c_p}{\lambda} \tag{4.2}$$

with β being the thermal expansion coefficient, ΔT_W being the wall superheat and r being the characteristic length. Using $\Delta T_W = 8\,\mathrm{K}$ for the maximum superheat and $r = 9\,\mathrm{mm}$ for the characteristic length, the Rayleigh number is equal to 3.4×10^6 . The critical Rayleigh number for a homogeneously heated plate at which the flow becomes turbulent is equal to 10^7 . The flow will thus be taken as laminar[1].

Detailed expressions of the equations can be found in the Fluent User's guide [5]. Mass and momentum conservation equations are expressed in cylindrical coordinates as follows.

Mass conservation equation:

$$\frac{\partial \rho}{\partial t} + \frac{\partial}{\partial x}\left(\rho v_x\right) + \frac{\partial}{\partial r}\left(\rho v_r\right) + \frac{\rho v_r}{r} = 0 \tag{4.3}$$

Axial momentum conservation equation:

$$\begin{aligned} \frac{\partial}{\partial t}(\rho v_x) + \frac{1}{r}\frac{\partial}{\partial x}(r\rho v_x^2) + \frac{1}{r}\frac{\partial}{\partial r}(r\rho v_x v_r) &= -\frac{\partial p}{\partial x} + \frac{1}{r}\frac{\partial}{\partial x}\left[r\mu\left(2\frac{\partial v_x}{\partial x} - \frac{2}{3}(\vec{\nabla}\cdot\vec{V})\right)\right] \\ &\quad + \frac{1}{r}\frac{\partial}{\partial r}\left[r\mu\left(\frac{\partial v_x}{\partial r} + \frac{\partial v_r}{\partial x}\right)\right] \end{aligned} \tag{4.4}$$

Radial momentum conservation equation:

$$\begin{aligned} \frac{\partial}{\partial t}(\rho v_r) + \frac{1}{r}\frac{\partial}{\partial x}(r\rho v_x v_r) + \frac{1}{r}\frac{\partial}{\partial r}(r\rho v_r^2) &= -\frac{\partial p}{\partial r} + \frac{1}{r}\frac{\partial}{\partial r}\left[r\mu\left(2\frac{\partial v_r}{\partial r} - \frac{2}{3}(\vec{\nabla}\cdot\vec{V})\right)\right] \\ &\quad + \frac{1}{r}\frac{\partial}{\partial x}\left[r\mu\left(\frac{\partial v_r}{\partial x} + \frac{\partial v_x}{\partial r}\right)\right] \\ &\quad - 2\mu\frac{v_r}{r^2} + \frac{2}{3}\frac{\mu}{r}(\vec{\nabla}\cdot\vec{v}) \end{aligned} \tag{4.5}$$

[1] In the present case, the plate is not homogeneously heated, and the wall superheat is defined at the center of the plate. The average superheat is lower, leading to lower Rayleigh numbers. Moreover, a central plume resulting from the differentially heated plate will cause less turbulence than naturally developping convective cells.

The energy equation is expressed as follows:

$$\frac{\partial}{\partial t}(\rho\mathscr{E}) + \vec{\nabla}\cdot\left(\vec{v}\,(\rho\mathscr{E}+p)\right) = \vec{\nabla}\cdot(\lambda\vec{\nabla}\,T) \tag{4.6}$$

with:

$$\mathscr{E} = h - \frac{p}{\rho} + \frac{v^2}{2} \tag{4.7}$$

As natural convection is a prominent phenomenon in this problem, the variation of density with temperature needs to be modelled. The Boussinesq approximation is used, only for the buoyancy terms in the momentum equations:

$$\rho = \rho_0(1-\beta\Delta T) \tag{4.8}$$

with β defined as follows:

$$\beta = -\frac{1}{\rho}\left(\frac{\partial\rho}{\partial T}\right)_p \tag{4.9}$$

4.2.2.2 Computational domains and boundary conditions

Several computational domains have been used in the simulation. The most complete domain is detailed in Fig. 4.7a and is named C1. The horizontal x-axis is chosen as the axisymmetry axis as imposed by the formalism of the simulation code used. The gravity vector is thus in the $-\vec{x}$ direction. The copper rod is simulated over a length of 7 mm. The diameter of the rod and the dimensions of the copper plate are faithful to the experimental test sample. The PFTE insulator is included in the simulation below the copper plate. A brass mesh electrode is placed 7 mm above the heated surface, like in the experiments. The geometry of the mesh electrode simulated is slightly different from that of the experiments, because it has to be axisymmetric. It is designed as concentric rings of 1 mm square cross-section, with a void fraction of 56 % over the heated surface. The fluid domain is filled with liquid pentane initially at saturation temperature. The outer side and the bottom side (on the left) are adiabatic walls, except for the copper rod where a constant heat flux is applied. The top side (on the right) is an open boundary defined as a pressure outflow. The pressure is kept constant, and the potential back-flow consist of liquid pentane at saturation temperature. In this way, the superheated liquid that will rise by natural convection is free to flow out of the computational domain. The grid chosen was Cartesian, with 100 × 100 µm cells except for the cells in the copper plate which had a 10 µm x-dimension.

A second computational domain C2 with a reduced test sample has been used (see Fig. 4.7b). The purpose of this domain was to reduce simulation time. As a constant heat flux was applied on the copper rod just below the thin plate, the temperature profile in the plate was modified. This domain was still useful to observe qualitatively the formation of convective instabilities on the surface which were similar to the ones observed with the full computational domain.

A third computational domain C3 (Fig. 4.7c) was used to study the influence on the brass mesh electrode on the plume and fluid flow rising from the plate.

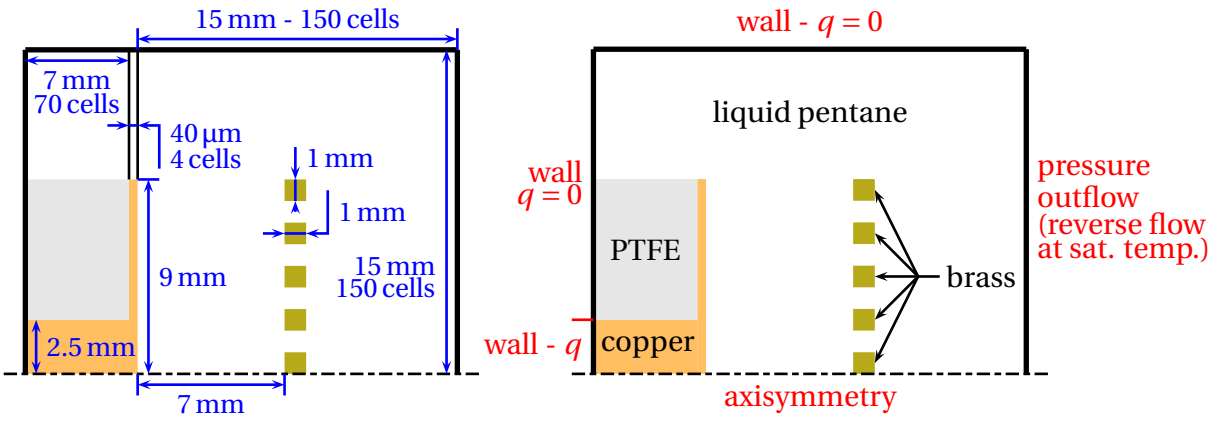

(a) C1: Full computational domain

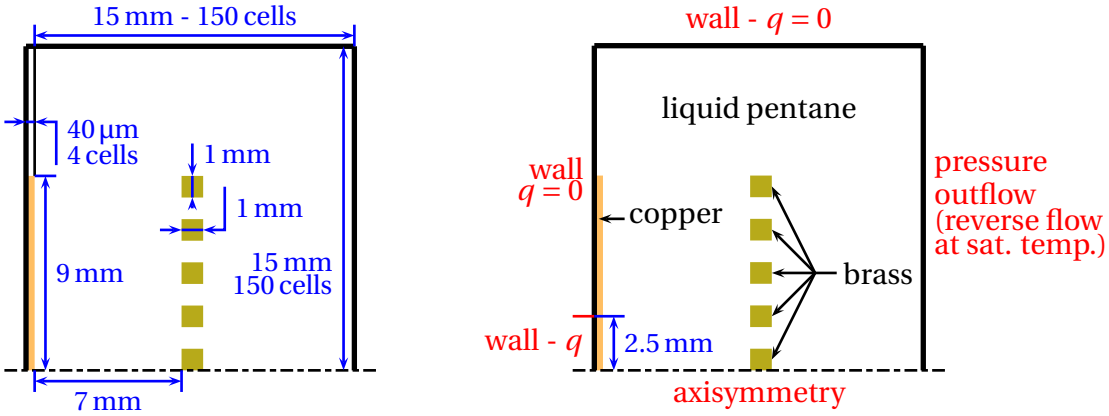

(b) C2: Reduced test sample

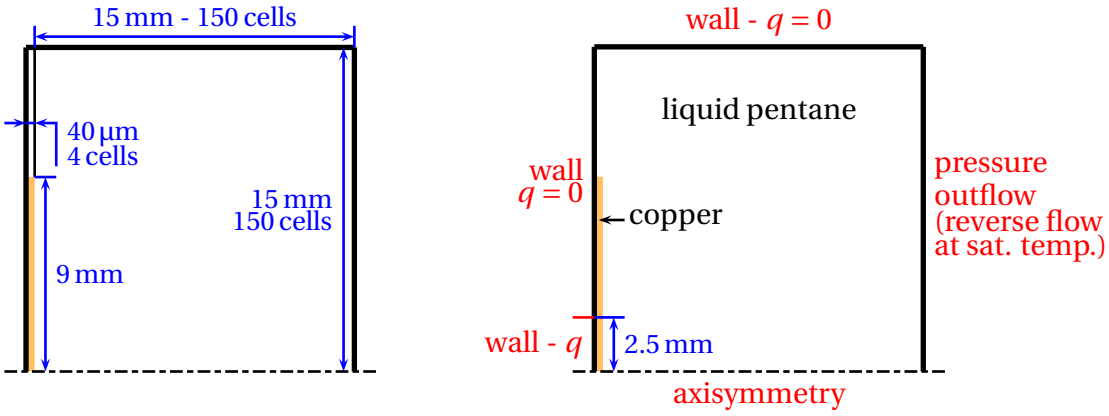

(c) C3: Reduced test sample without grid mesh electrode

Figure 4.7: Computational domains (left) and boundary conditions (right)

4.2.2.3 Temperature fields in the test sample and in the fluid phase

Numerical simulations have been performed and tested for stability and convergence. Mesh was doubled for a key simulation to ensure that the results were not mesh-dependant. The temperature field on the upper face of the copper plate is shown in Fig. 4.8 for a 5 kW·m^{-2} heat flux imposed on the copper rod and with the computational domain C1. As expected, the temperature is almost homogeneous over the copper rod (variations are below 0.05 K). The temperature drops radially in the copper plate over the PTFE. The wall superheat at the outer edge of the plate is decreased by one third.

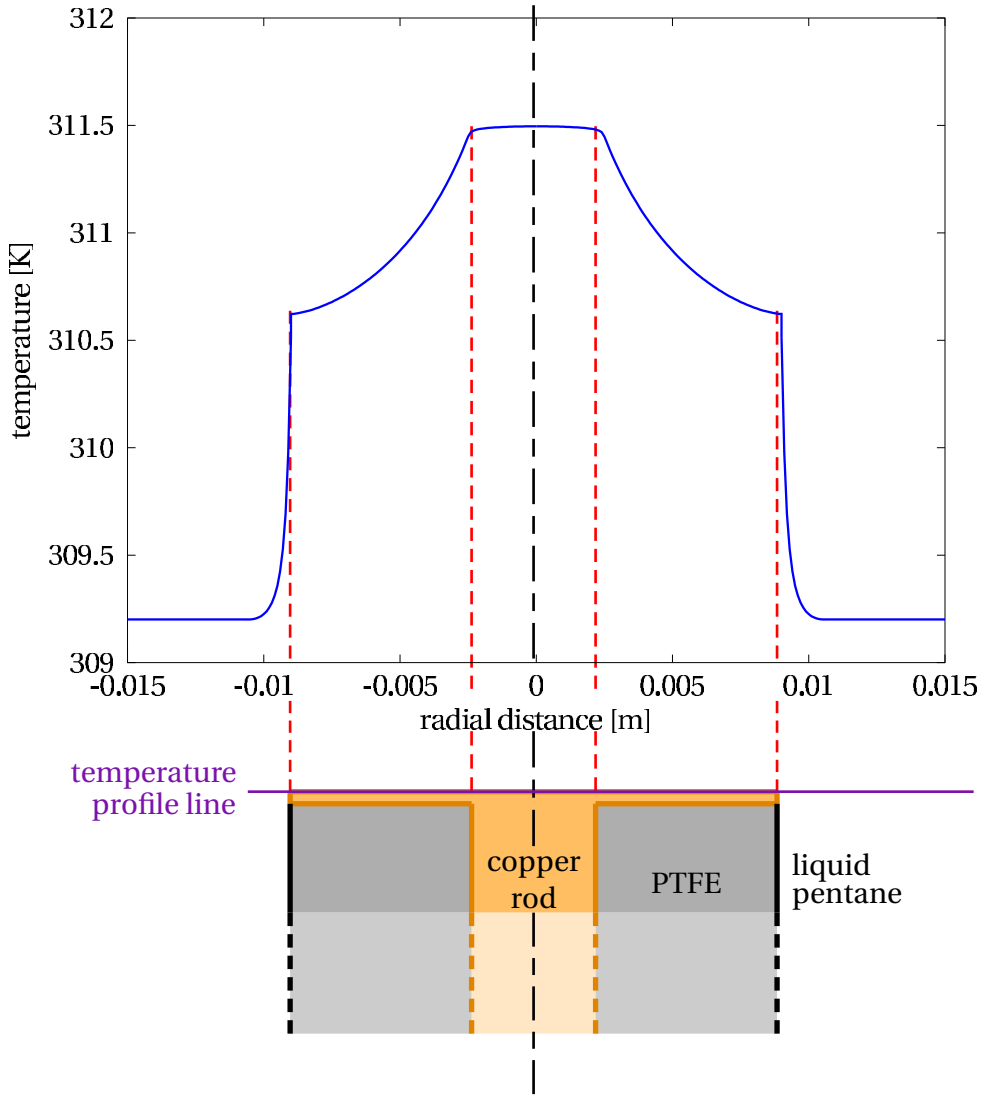

Figure 4.8: Simulation of the temperature profile in a radial section of the upper side of the copper plate for a heat flux of 5 kW·m^{-2} and using computational domain C1.

Comparison of the temperature profile in the copper plate between computational domains C1, C2 and C3 is shown in Fig. 4.9. The overall profile has a similar shape in each case, except for the surface over the copper rod. The temperature values are higher for C2 and C3 than for C1. The temperature over the copper rod is less homogeneous using C2 and

C3 than using C1. The temperature profiles using C2 and C3 coincide for low heat fluxes and are slightly different for high heat fluxes. This will be investigated in subsection 4.2.2.5.

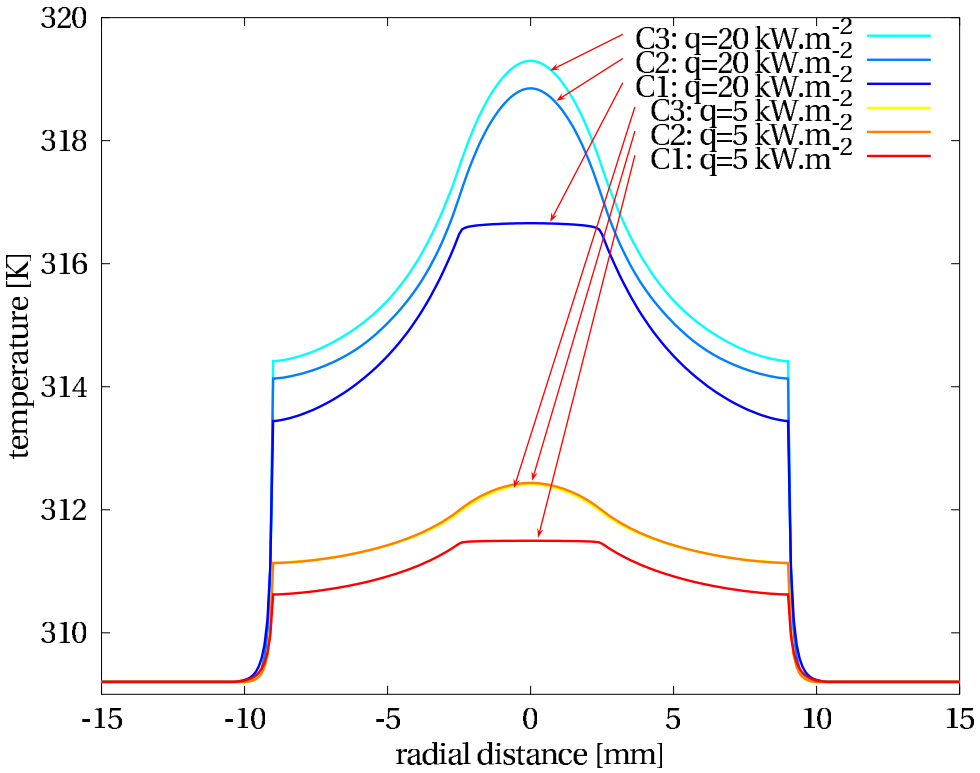

Figure 4.9: Simulation of the temperature profile in a radial section of the upper side of the copper plate. Comparison between computational domains C1, C2 and C3.

It can be inferred from the heated plate temperature profiles that convection above the surface will be different between on one hand C1 and on the second hand C2 and C3. However, the offset of temperature between the computational domains is similar to this caused by a change of heat flux using a single computational domain, except for the area above the copper rod. If the convective instabilities are developing around the copper rod on the surface of the thin plate, the same phenomenon would still be observed as the temperature profile in this area has the same shape.

4.2.2.4 Convective instabilities

The temperature field in the fluid phase has been plotted for all 3 computational domains for a low heat flux of 5 kW·m^{-2} (Fig. 4.10) and for an high heat flux of 20 kW·m^{-2}. According to the results using the most complete computational domain C1 (Fig. 4.10b), no convective instabilities occur while the heat flux remains low. The fluid flow consists in a plume rising from the center of the plate and diffusing through the mesh electrode. On the contrary, simulations using C2 and C3 predict the occurrence of the instabilities, perhaps because of the offset of surface temperature.

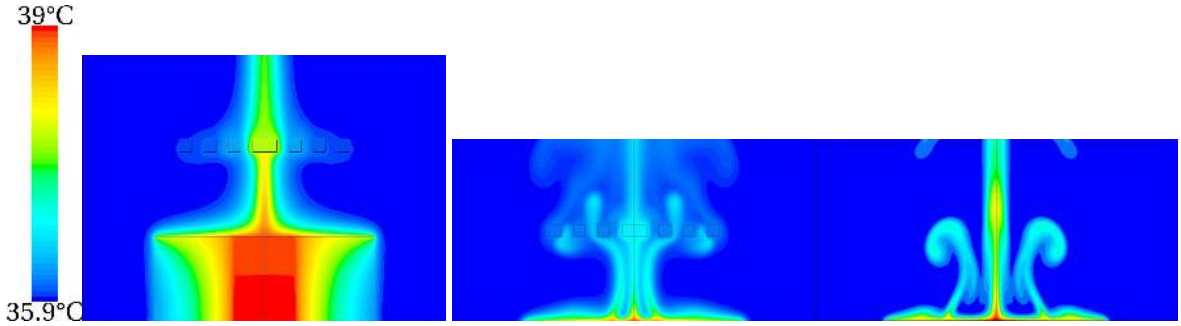

Figure 4.10: Temperature field at q = 5 kW·m^{-2} using C1, C2 and C3

For a nominal heat flux of 20 kW·m^{-2} imposed at the base of the copper rod, instabilities are observed for all of the different computational domains used (see Fig. 4.11). The convective structures are similar in each case, leading to the assumption that the mechanism of formation of the instabilities is the same in each case. In order to decrease the simulation times, the domain C3 will be further used to describe this mechanism.

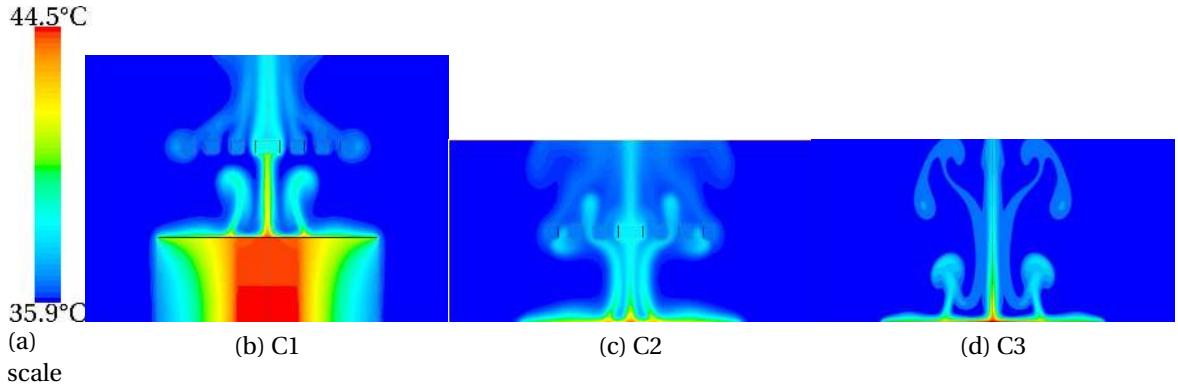

Figure 4.11: Temperature field at q = 20 kW·m^{-2} using C1, C2 and C3

Figure 4.12 shows the successive temperature fields obtained using simulation domain C3, with $\Delta t = 800$ ms between the images. The mechanism of formation of a new instability is easily observed between pictures 5 and 8. The thermal boundary layer above the heated surface is thinner around the base of the central plumes because of higher velocities. The thickness of the boundary layer has thus a maximum between this base and the edge of the surface. The buoyancy of the hotter liquid soon creates a new convective structure from this local maximum.

The shapes of the instabilities observed in the simulations are very similar to those observed in the experiments in section 4.1.4, except that the simulations are by nature axysimmetric. Some structures present a *mushroom-like* shape, and some are like a vertical plume (after the *mushroom-like* shaped ones have raised above the simulation domain).

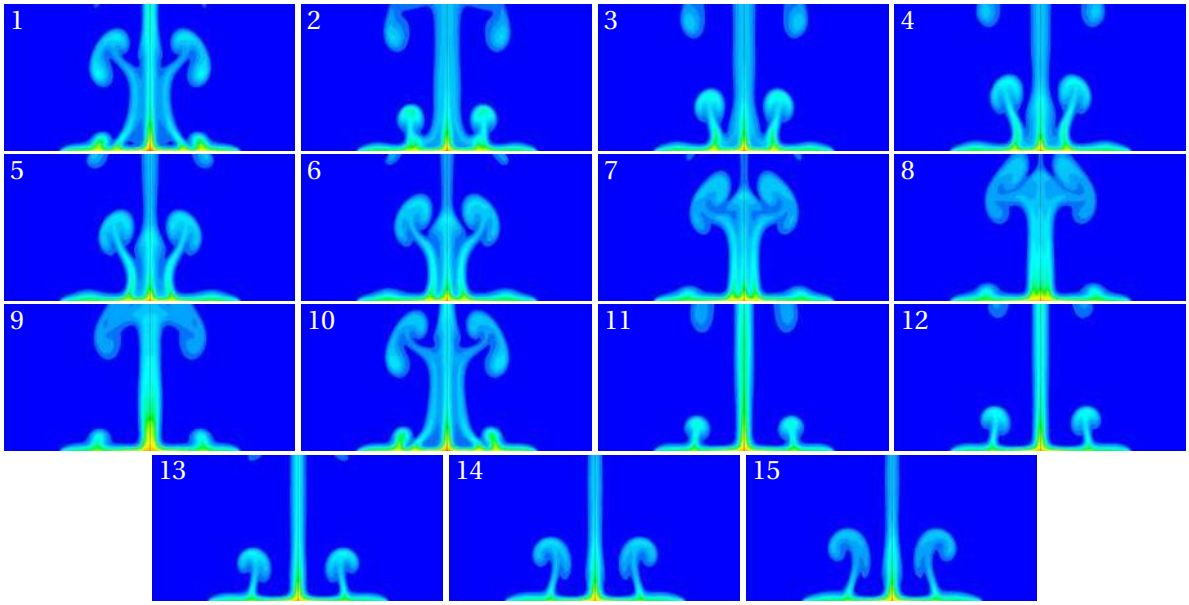

Figure 4.12: Temperature field at $q = 5\,kW{\cdot}m^{-2}$ using C3. $\Delta t = 800\,ms$ between successive images.

4.2.2.5 Influence of the grid mesh electrode

The grid mesh electrode has a clear impact on the fluid flow raising above the heated surface. As it can be observed in Fig. 4.13, the central plume is divided into the free spaces of the grid, resulting in a much larger plume above the grid. Apart from the flow structure, as the flow seems to be modified only 5 mm above the surface, whether the grid has a impact on heat transfer needs to be determined.

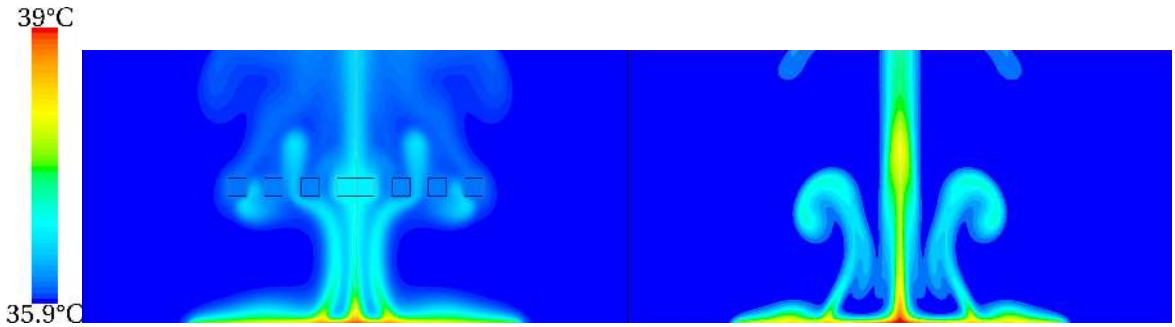

(a) scale (b) C2 (c) C3

Figure 4.13: Temperature field at $q = 5\ kW{\cdot}m^{-2}$ using C2 and C3

The wall superheat and the mean heat transfer coefficient have been computed using C2 and C3 (Fig. 4.14 and 4.15). The mean heat transfer coefficient is defined as :

$$\overline{h} = \frac{q}{S.\Delta T_W} \tag{4.10}$$

with S the copper thin plate area. It can be seen that there is no difference between C2 and C3 at low heat fluxes, and that the wall superheat rises faster with the heat flux when there is no grid above the surface. The effect of this trend is that the heat transfer coefficient slope is higher in the presence of the grid. The grid might cause the central plume to be larger, allowing better heat removal from the thermal boundary layer

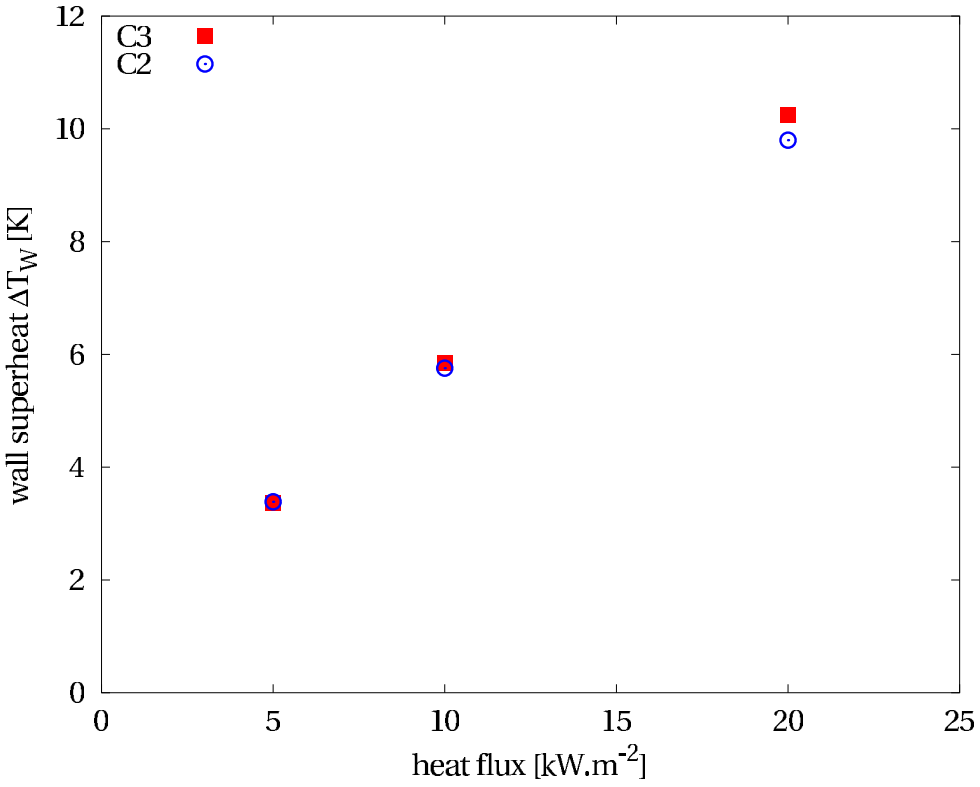

Figure 4.14: Wall superheat versus heat flux using C2 and C3.

The numerical simulations presented in this section allow a better understanding of the thermal field and heat transfer above the heated surface. It has been shown that the natural convective structures bring superheated liquid toward the center of the plate. The formation of convective instabilities over the plate has been explained, and the thermal effect of the presence of the grid mesh electrode has been investigated.

4.3 Heat flux from the surface

4.3.1 Heat flux in the absence of electric field

As described in section 3.3, the total heat flux transmitted to the fluid is computed from the temperatures measured inside the copper rod of the experimental test sample. This heat is mainly transferred to the liquid phase by natural convection as described in Section 4.1. The relation between heat flux and wall superheat has been plotted in Fig. 4.16. It has been

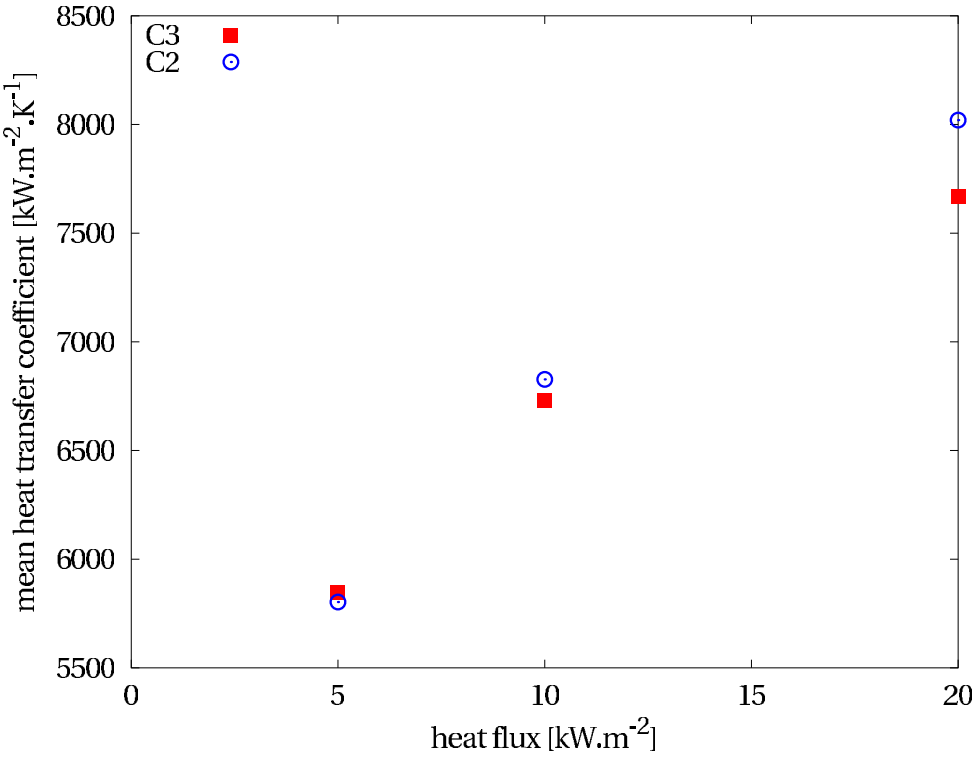

Figure 4.15: Mean heat transfer coefficient versus heat flux using C2 and C3.

measured at increasing or decreasing heat flux to ensure the absence of any hysteresis phenomenon. It is shown that the relation between heat flux and wall superheat is roughly linear[2]. Heat flux values shown are below 1 W, which is a rather small value compared to the size of the whole system (5 L of liquid pentane).

Figure 4.16 also plots the data points obtained with the numerical simulations using the most complete simulation domain C1 (see section 4.2.2). Although there is an offset between the numerical and the experimental values, the trend and the slope is the same. The numerical simulations predict a wall superheat underestimated by 2 K.

4.3.2 EHD enhancement of convective heat flux

Heat flux versus wall superheat has been plotted for different voltages applied to the mesh grid electrode (see Fig. 4.17). Convective heat transfer is enhanced due to the changes in the convective structures observed in section 4.1.4. This enhancement tends to improve with increasing voltage. For an average superheat of 4 K, the heat flux is enhanced by about 50 % for the highest applied voltage of 24 kV. The ratio of heat transfer enhancement tends to decrease with the wall superheat. Indeed, this is as one would expect as the buoyancy forces become stronger and should begin to dominates over electrical forces.

[2]The exact shape might not be linear. However, due to the small range investigated and to the relatively high uncertainty on the heat flux determination, this relation can be modelled as linear.

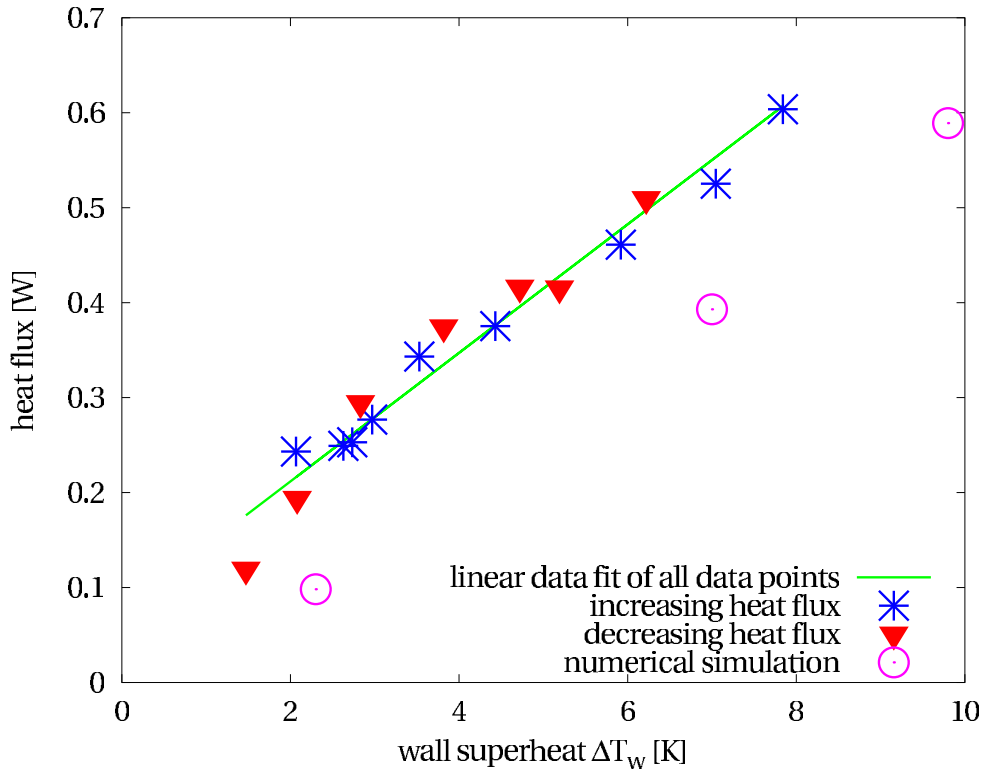

Figure 4.16: Heat flux transmitted to the fluid for different wall superheat values.

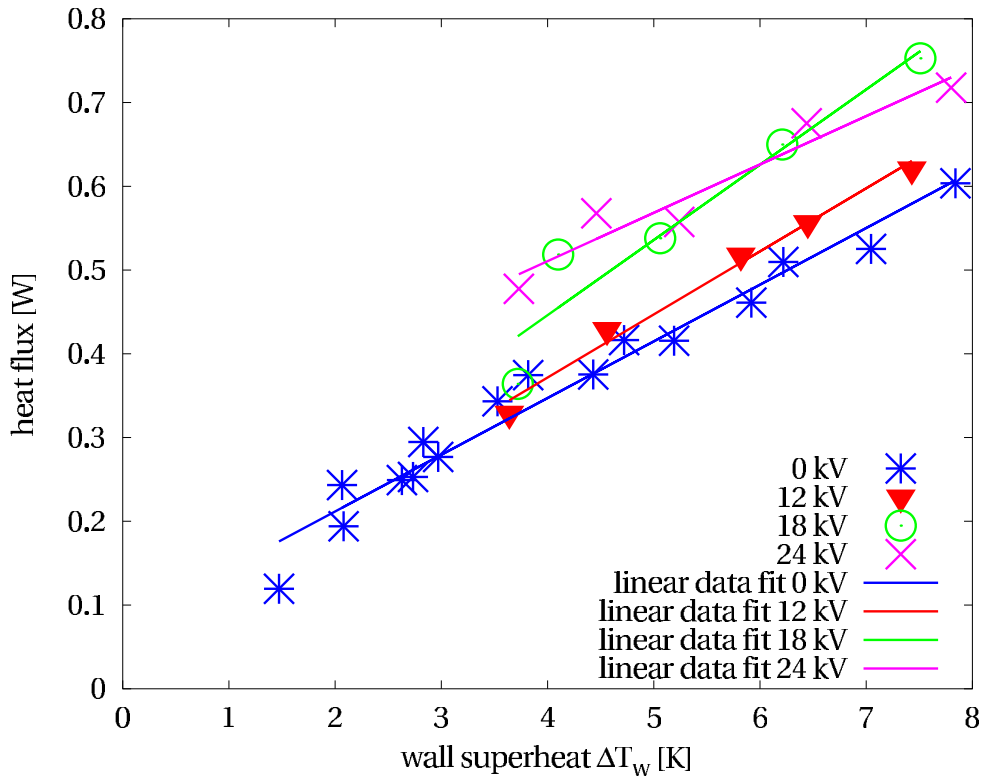

Figure 4.17: Heat flux transmitted to the fluid versus wall superheat for different voltages applied to the grid mesh electrode.

The measured heat fluxes for 18 kV and for 24 kV seem very similar, so that their linear data fit cross within the studied wall superheat range. This is due to the heat flux uncertainty which is quite high at low and moderate heat flux.

4.3.3 Superheat reduction due to EHD at constant heat flux

The superheat reduction due to EHD at constant heat flux has been measured and is plotted in Fig. 4.18. This phenomenon illustrates what happens when an electric field is applied over a device with an imposed heat flux cooled by natural convection. It is also the thermal effect of what was observed in Fig. 4.3 once the electric field was turned on. The electric field instantaneously modifies the convective flow structure, which enhances the heat transfer.

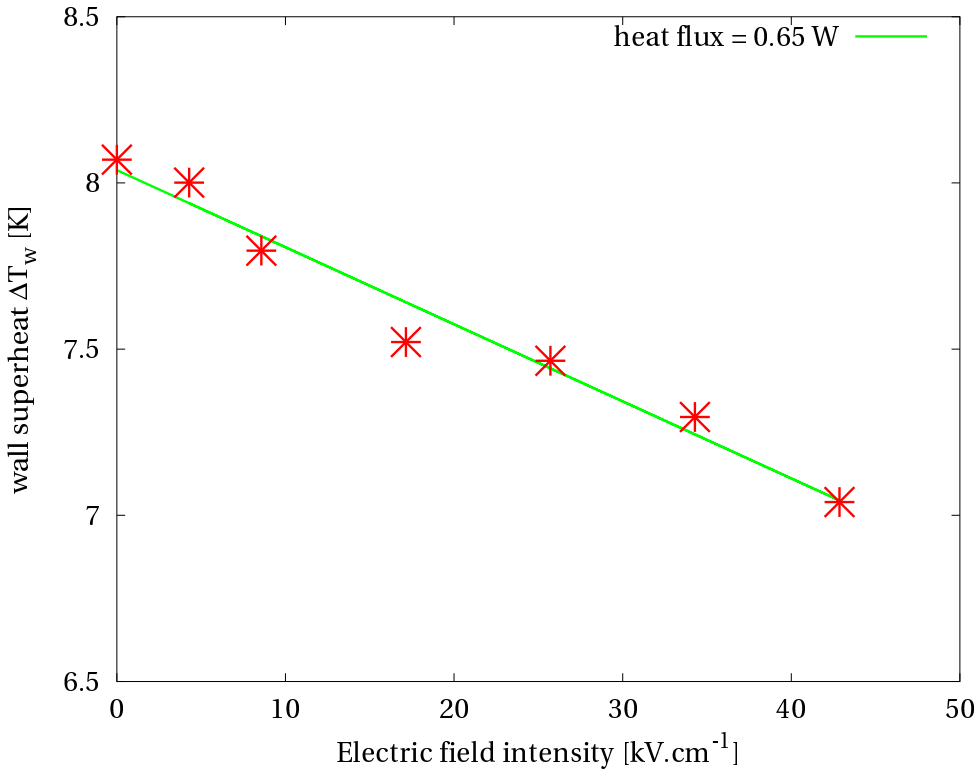

Figure 4.18: Wall superheat Vs. electric field at constant heat flux.

4.3.4 Heat transfer coefficients

As for the heat flux, the mean heat transfer coefficient, defined in eq. 4.10, has been plotted for the absence of an electric field (Fig. 4.19) and with an electric field applied (Fig. 4.20). Surprisingly, the mean heat transfer coefficient decreases with an increasing wall superheat. The reduction cannot be explained and may be due to the uncertainty on the heat flux measurements that can be as high as 47% at low heat flux (see section 3.3.1). The heat transfer

coefficient increases with an increasing voltage applied to the electrode, as one would deduce from the previous heat flux analysis.

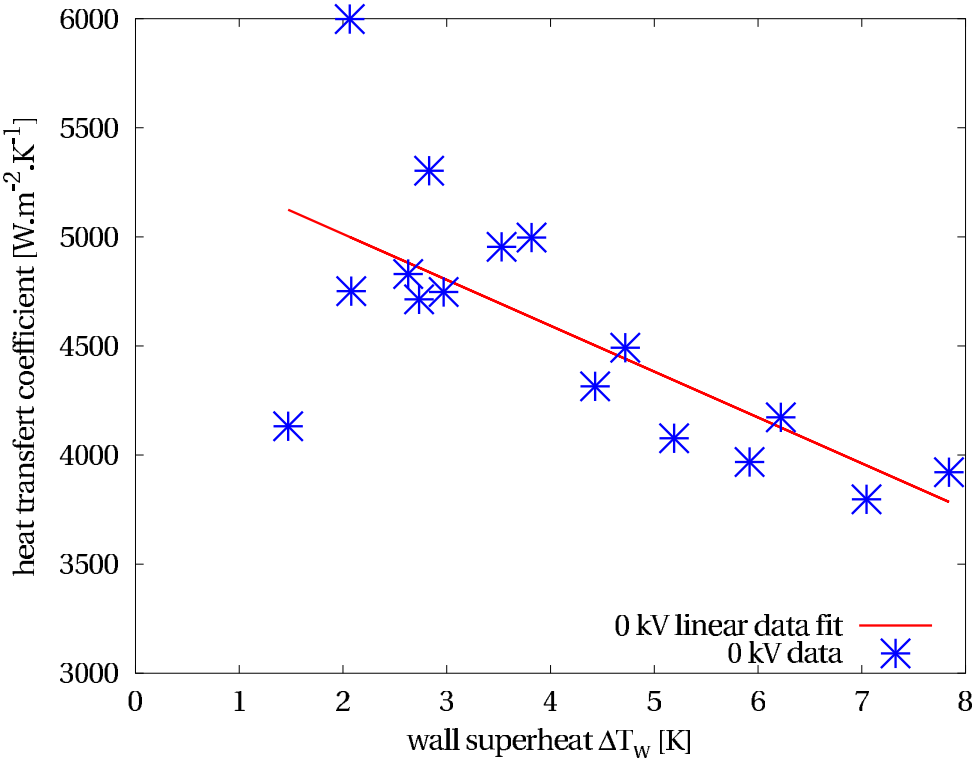

Figure 4.19: Mean heat transfer coefficient over the heated plate.

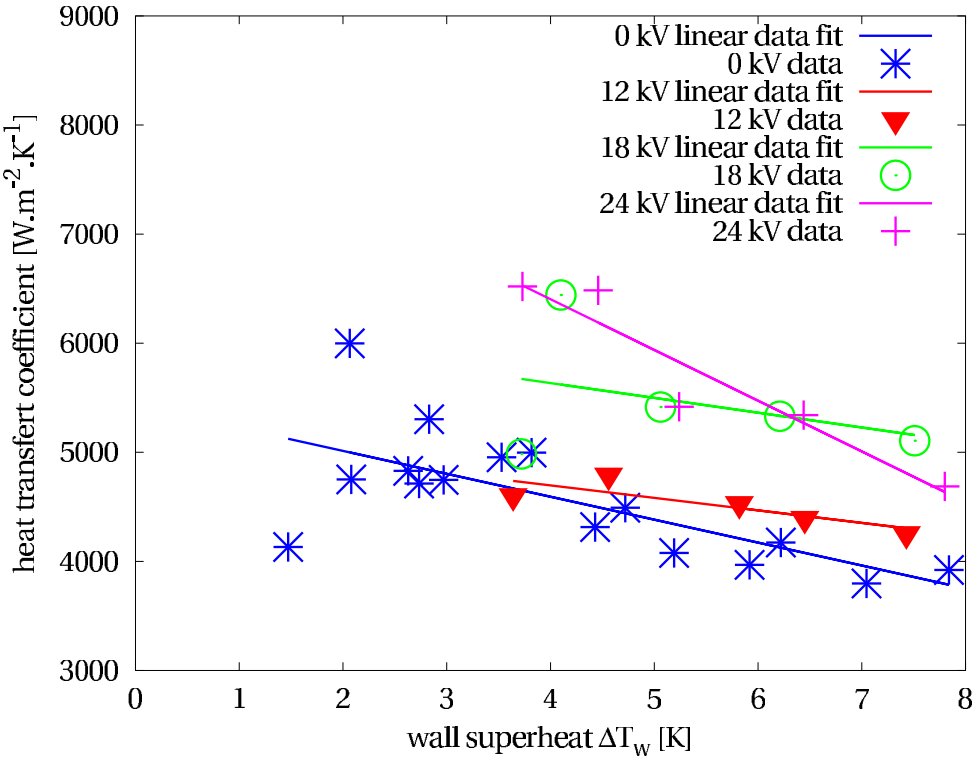

Figure 4.20: Mean heat transfer coefficient for different voltages applied to the grid mesh electrode.

The original design of our experimental setup results in a specific natural convection regime over the heated plate, somehow similar to the flow structure of the isolated bubbles boiling regime. An original experimental procedure completed by transient numerical simulations have been performed, allowing the accurate description of the thermal environment in which bubbles nucleate, grow and move. The augmentation of the flow structure by the application of an electric over the heated surface has been observed, and its enhancement of the heat transfer from the plate has been measured.

Chapter 5

Bubble dynamics

Boiling heat transfer has received much attention for decades because of the high heat transfer coefficients associated to this mode of heat transfer. Many research teams have attempted to predict boiling heat transfer rates since the pioneering description of the pool boiling curve on a wire by Nukiyama ([138], translated in English in [139]). However, boiling being a very complex combination of multi-scale coupled mechanisms, the need for a finer description and understanding of each individual mechanism has been revealed. Dozens of studies of single bubble dynamics have been performed since then, each one bringing new elements to the global understanding. Yet, several key problems still remain concerning bubble nucleation, growth, detachment, rise and interactions with other surrounding bubbles. The present experimental study, benefiting from all previous studies and latest advances in measurement and high-speed recording, aims at bringing new elements to the understanding of boiling at the scale of a single bubble.

In the first section, bubble growth and the associated vapour production rate will be analysed. Bubble shape and oscillations during its growth will be characterized. In a second section, a momentum balance on the bubble will be performed after having accurately defined each force. The bubble curvature along the interface will also be investigated. In a third section, bubble interaction with a neighbouring bubble and the coalescence event will be discussed. In the last section, bubble rise, trajectory and terminal velocity will be analysed.

5.1 Bubble growth

Once a bubble nucleates on a surface, it grows by phase change until the bubble departs from the surface. The growth dynamics is one of the core phenomena in boiling since most of the heat transfer is governed by bubble activity when boiling on a natural surface. However, pre-

dicting or measuring accurately bubble growth is utterly complex, since many parameters and scales are involved. The rate of phase change depends on the bubble exact shape and on the *3D*-temperature field of the liquid (whose temperature is varying with time as it is cooled by the phase change phenomenon). It also depends on the exact layout of the triple-line area, on the properties of the fluid at the temperatures and pressures involved, on the potential interaction with the environment, on the other bubbles, on the heated surface, etc.

Among the different methods considered to understand the bubble growth dynamics, analytical modelling was extensively developed after the work by Lord Rayleigh in 1917 [157] (see chapter 2), who modelled bubble growth (and collapse) for an inertia controlled spherical bubble. Several neglected parameters have been progressively taken into account in the subsequent analytical models, among which a homogeneous superheated bulk liquid [64, 154, 175], the presence of the heated wall [73, 131] and non homogeneous temperature field [73], a more realistic shape of the bubble viewed for instance as a truncated sphere [21, 30, 73, 109, 131], and the presence of a micro-layer beneath the bubble [21, 30, 43, 144]. Some parameters have seldom been considered, e.g. the influence of the previous bubbles from the same nucleation site, the actual non-spherical bubble shapes, the influence of the convective structures above the heated surface, the influence of neighbouring bubbles or the non-homogeneous and time-varying temperature inside the wall.

Another method to determine bubble growth dynamics or to validate/invalidate the analytical models is to perform controlled experiments while measuring all relevant parameters. The first issue is to design a well-controlled experiment with boiling on a single nucleation site. Most boiling experiments involve natural surfaces with multiple nucleation sites interacting with each other, and bubbles coalescing [43, 71, 76, 98, 149, 152, 156, 162, 190]. Among the few experimental works concerning boiling from an individual nucleation site, most are performed over a silicon plate or wafer, or are heated locally by a laser beam or a micro-heater element [24, 28, 51, 52, 85, 94, 106, 107, 108, 132, 146, 163, 166, 187, 194]. The second issue of the experimental approach is measuring meaningful parameters, such as the bubble exact shape, the temperature field in the liquid and in the solid phases, and their variations with time. Capturing the evolution of the bubble shape and size is difficult because bubble growth is typically fast, and because the temperature gradients within the liquid phase cause mirage effects [42]. Measuring the temperature field in the liquid phase was rarely performed. One should nevertheless mention the work by Beer who investigated boiling in a *2D*-temperature field by holography and interferometry [15, 176].

A third method used in order to determine bubble dynamics is complete numerical simulation of the bubble. This method also has its specific issues. *3D*-simulation is costly, choosing a proper mesh is difficult for multi-scale phenomena, bubble inception is usually impossible to achieve numerically, bubble interaction with the surface at the triple line needs to be well understood in order to be correctly modelled, and eventually, key experimental works are needed to validate the simulation results (see V.K. Dhir [53] for a good state-of-the-art of complete numerical simulation of boiling).

The experimental work presented in this chapter aims to be among the reference works on bubble dynamics in a controlled and measured environment. Bubbles nucleate on a cop-

per surface from a single nucleation site, which avoids disturbance from neighbouring bubbles. The metal volume below the surface ensures a good thermal capacity and diffusivity. The wall temperature and bulk fluid temperature are accurately measured (see section 3.3.1), and the fluid flow structure above the surface has been investigated in chapter 4. The nucleation site geometry has been accurately characterized in section 3.1.3. Bubble growth sequences are recorded by a digital high-speed camera and an accurate post-processing technique has been developed to compute bubble characteristics (see section 3.3.2). Particular care has been given to avoid mirage effect (see section 3.2.2) and to minimize distortion of the bubble image. Many of the results shown in this section have been published in 2008 by Siedel *et al.* [169].

5.1.1 Introduction to bubble growth

We will first describe here the entire life cycle of a bubble in the case of our experiments in order to identify the specificities of the bubble growth sequences analysed: bubbles growth is part of a periodic process, and bubbles stay attached to the rim of the nucleation site. We will then explain the choice of methodology that consists of describing the bubble growth using the bubble's volume rather than its equivalent diameter.

Before describing any result obtained, the validity of the measurements needs to be assessed. Bubble growth analysis will generally be performed on a single bubble. In order to generalize the observations made on this particular bubble event, the repeatability between several successive bubbles has been investigated and information on this issue will also be given in the present section.

5.1.1.1 Bubble life cycle

The object of this study is to accurately describe a bubble life cycle: it is a periodic succession of events from nucleation of a bubble at its nucleation site, growth of this bubble until its departure, and rise of the bubble until reaching the free surface. Once the bubble has detached from its nucleation site, the next cycle may start and a new bubble can nucleate. Two successive bubble cycles can overlap each other. A rising bubble or its wake may interact with a new bubble if the latter grows fast enough. As presented in section 3.4, the limit of these interactions has been fixed when a bubble can merge with the following bubble.

The first step of the bubble life cycle is its nucleation. It always happens inside the artificial nucleation site. Little is known about the mechanism of nucleation because it cannot be observed visually. The waiting times are very short (less than 1 ms is observed between the detachment of a bubble and the appearance of the following bubble) and tend to confirm that a vapour seed stays encapsulated inside the site. In this case, the new bubbles are not really nucleating, but instead the departing bubble is breaking into two parts: the main one leaves the surface and a small volume of vapour stays attached inside the site.

The next step of the bubble life cycle is a volumetric growth outside of the cavity while being attached to the heated wall (see Fig. 5.1). In the case of these experiments, the bubble stays attached to the rim of the nucleation site during the entire growth (i.e. the triple line between the solid, the liquid and the vapour does not move outside of the nucleation site on the surface). In the Fig. 5.1, the bubble quickly grows over the surface while the previous bubble is still very close. Its grows by phase change until reaching a critical volume at which the bubble departs from the surface.

Once the bubble has detached from the surface, it accelerates vertically and rises until reaching the free surface. Figure 5.2 shows the first millimetres of the rise of a bubble, which is described in section 5.4.

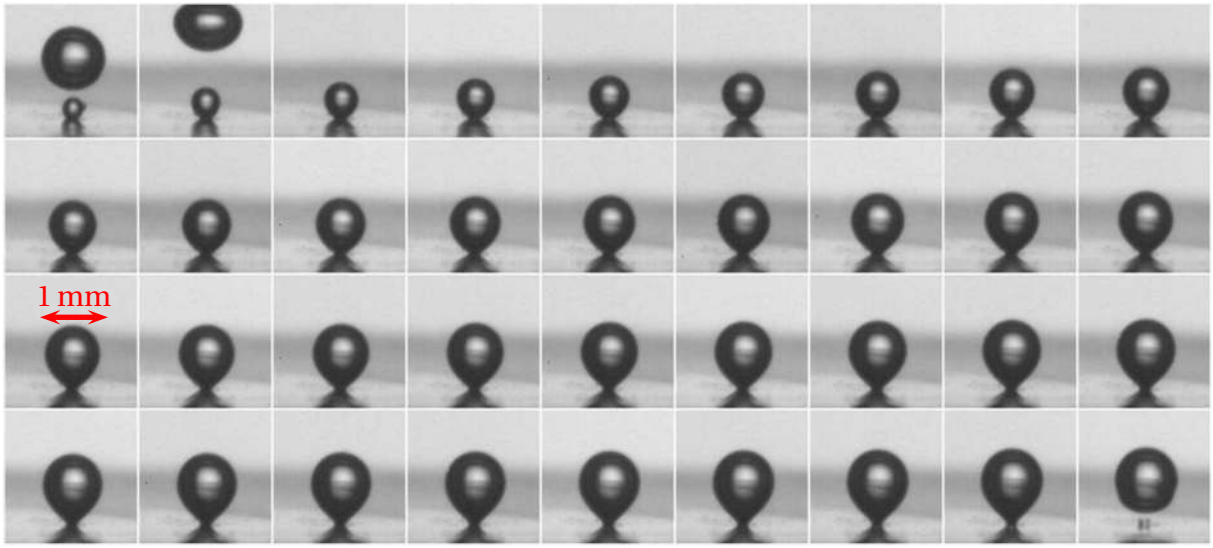

Figure 5.1: Bubble growth at $\Delta T_W = 5.9\,\mathrm{K}$, with $\Delta t = 2.67\,\mathrm{ms}$ between the images.

5.1.1.2 Contact angle

The contact angle is defined for a bubble or a drop attached to a solid surface. It is defined as the macroscopic angle on the liquid side between the bubble interface and the solid wall at the location of the contact line (see P.G. De Gennes [50], page 24-25).

The estimation of the contact angle θ is difficult. Indeed, θ not only depends on the solid and fluid thermodynamic and chemical properties, but also relies on the surface geometry and roughness and on the wall superheat. For a wetting fluid, the contact angle will typically increase with the surface roughness. The contact angle then needs to be determined for the specific *surface-fluid* combination employed in the experiments.

Moreover, the contact angle is a dynamic equilibrium (see P.-G. de Gennes [50], chapter 6). The advancing and receding contact angles are different due to the surface wetting

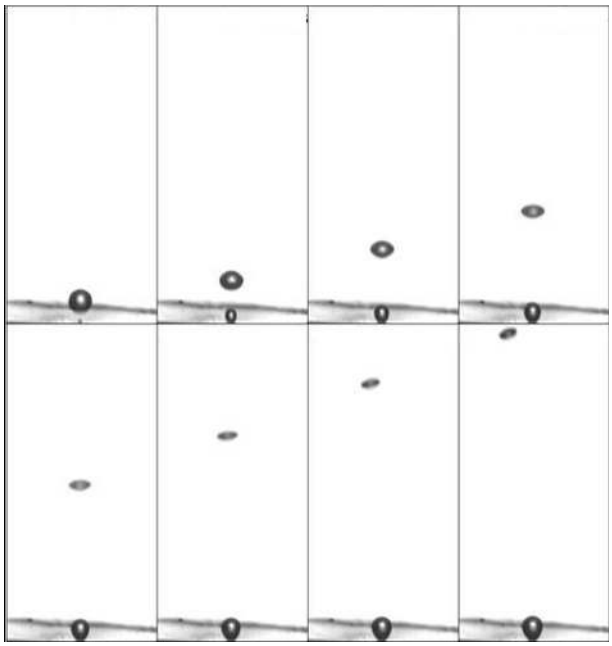

Figure 5.2: Bubble rise at $\Delta T_W = 3.2\,\mathrm{K}$, with $\Delta t = 7\,\mathrm{ms}$ between the images.

and drying processes, leading to even more difficulties to predict the contact angle. The contact angle is thus changing during bubble growth [134, 189].

The experimental method to define the contact angle would be to measure it accurately at each time step through image processing. A new issue comes up in the specific case of these experiments, as the bubble remains attached on the rim of the nucleation site during the entire bubble growth cycle[1]. This leads to a problematic definition of the contact angle[2], which is well defined on a plane surface.

Figure 5.3 illustrates the fact that when the triple line is located on a geometric edge, a microscopic displacement of the contact line can result in a large contact angle difference. The contact angle can therefore not be measured accurately in our experiments.

For the case of a sessile drop of pentane on a metal surface, Stutz *et al.* [178] measured a static contact angle of less than 10°.

5.1.1.3 Volumetric growth

The first analytical models of bubble growth describe bubble size by its diameter. This comes from the first assumption that the bubble is a sphere. The bubble was later assumed to be non-spherical (usually a hemisphere or a truncated sphere). The term of equivalent diameter has been introduced, meaning the diameter of a sphere which would have the same

[1] This is generally the case for well-wetting fluids [24].

[2] The contact angle is defined as a macroscopic angle, which may differ from the microscopic angle that would results from the presence of a liquid microlayer beneath the bubble [122].

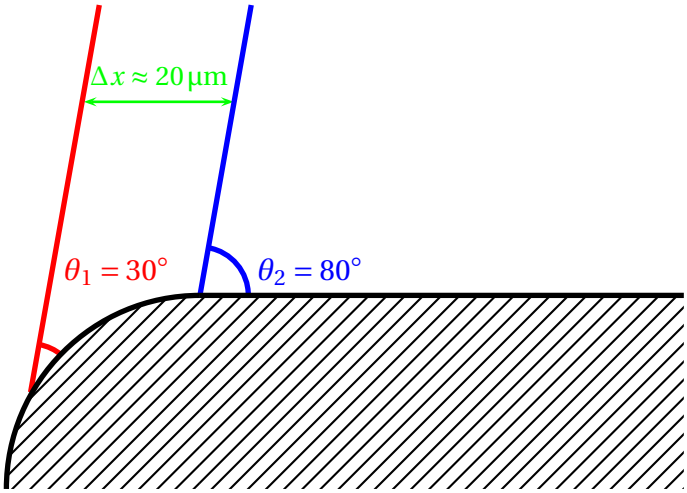

Figure 5.3: Evolution of the contact angle for a small change in the triple line location close to the nucleation site edge.

volume :

$$D_{eq} = \left(\frac{3V}{2\pi}\right)^{\frac{1}{3}} \tag{5.1}$$

This use of the equivalent diameter to describe bubble growth is widely generalized, as well for analytical models as for experimental measurements, even for the most recent publications (for example Nam *et al.* [135]). Yet, this use of a diameter might be a source of inaccuracy and might veil precious information about heat transfer. Indeed, heat transfer to the bubble is roughly proportional to the volumetric flow rate of vapour production. Describing vapour production implies an accurate knowledge of the volume at each moment in time. But as the equivalent diameter is proportional to the cubic root of the volume, any variation or trend of the volumetric growth is ambiguous when reasoning in terms of diameter.

Furthermore, the use of the equivalent diameter is nonsensical for an experimental work when the bubble appears to be not spherical. In the present experiments, bubbles tend to form a neck before detachment, and appear slightly elongated at their lower half. Figure 5.4 shows a bubble just before detachment. The shape is rather like that of a hot-air balloon.

It has thus been chosen to represent the bubble size using its volume. The equivalent diameter might be used subsequently to compare the results with models.

5.1.1.4 Reproducibility of successive bubbles

The bubbles which nucleate, grow and leave the surface are immediately followed by the next bubble nucleating at the same nucleation site. Waiting times observed are less than 1 ms. It is important to investigate if following cycles are identical or if differences exist. Figure 5.5 plots the growth curves of 11 successive bubbles with a low wall superheat of 2.1 K. The

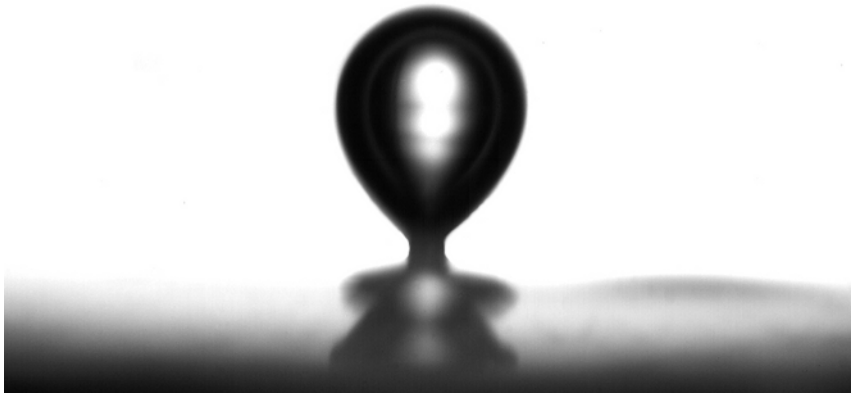

Figure 5.4: Bubble at detachment

overall shape of each curve is the same, and the volume at departure of each bubble remains within a ±2 % dispersion interval. The total growth time to departure decrease by about 15 % between the first and the last bubble of the set. This variation is also observed in subsection 5.1.2.2, where instantaneous bubble frequency is scattered for the same wall superheat. This may be due to fluctuations of temperature of the surrounding liquid with a lower frequency, which may be caused by convective instabilities similar to those observed in section 4.1.4.

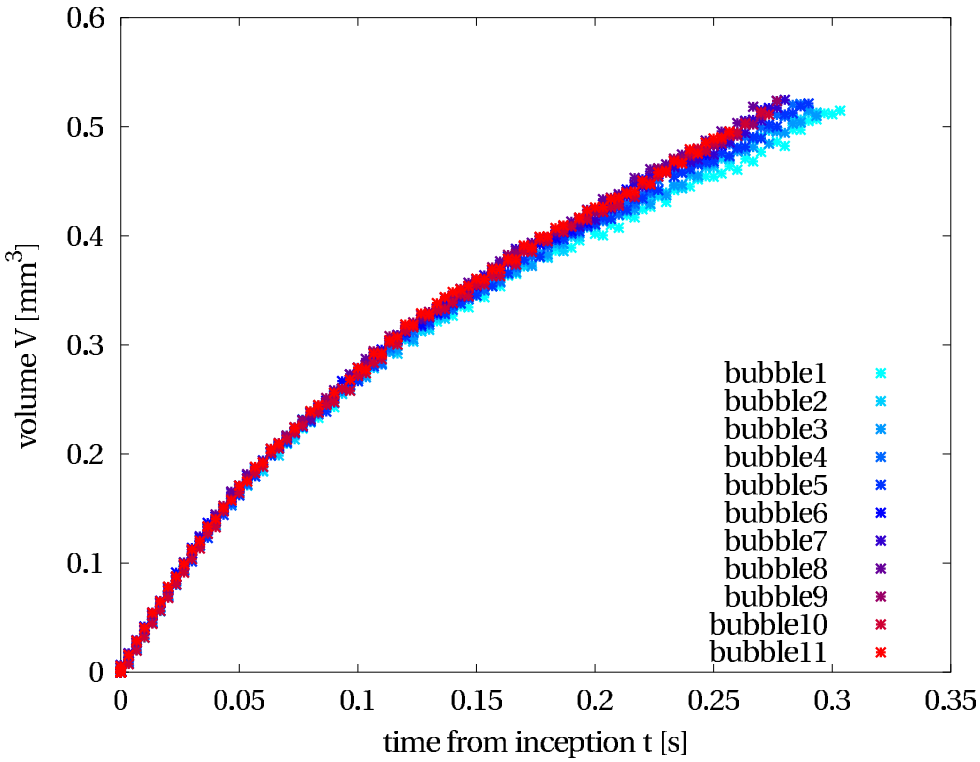

Figure 5.5: Growth curves of 11 following bubbles at $\Delta T_W = 2.1\,\mathrm{K}$

Analyses performed on a single bubble cycle can be generalized to all bubbles with the

same experimental conditions only if the time is non-dimensionnalised by the total growth time. For quantitative analyses about the latent heat flux, the bubble growth time or frequency, several bubbles are needed in order to take into account the dispersion of the values at a single experimental condition.

5.1.1.5 Inertia or diffusion controlled bubble growth ?

In order to provide a consistent analysis of bubble growth, it is useful to determine whether the bubble growth is controlled by diffusion or inertia. As outlined in Siedel *et al.* [171], Robinson and Judd [160] proposed an order of magnitude criterion which should indicate whether bubble growth would be expected to be diffusion controlled or whether inertia influenced, associated with the kinetic energy of the surrounding liquid, would be the dominant influence. Based on a simple scaling argument the criterion was posed as:

$$I_R = \left(\frac{4}{27}\right)\left(\frac{\sigma}{\rho_l {\alpha_l}^2}\right)\frac{R_b}{\mathrm{Ja}^2} \qquad \begin{cases} \ll 1 & \Rightarrow \text{ Inertia controlled} \\ \gg 1 & \Rightarrow \text{ Diffusion controlled} \end{cases} \tag{5.2}$$

where R_b is the bubble radius at nucleation, taken here as the cavity radius, and Ja is the Jakob number defined as:

$$\mathrm{Ja} = \frac{\rho_l c_p \left(T_W - T_{sat}\right)}{\rho_v h_{fg}} \tag{5.3}$$

The Jakob numbers are low in this study, with $2.7 \leq \mathrm{Ja} \leq 10.5$. For this Jakob number range, I_R lies between 500 and 7700, which indicates that bubble growth is definitely diffusion controlled and inertial influences are clearly negligible.

5.1.2 Influence of the wall superheat

Heat transfer in boiling is commonly described by the relationship between the heat flux density and the wall superheat defined as the temperature difference between the heated wall and the bulk liquid:

$$\Delta T_W = T_W - T_{sat}(\infty) \tag{5.4}$$

The parameter imposed is usually the heat flux density corresponding to the heat dissipated by the device that needs to be cooled, and the wall superheat is a result of the heat transfer coefficient due to the boiling regime (see section 2.2). The notion of wall superheat is similar to that in use for description of single phase convection.

In the case of these experiments, only one *boiling regime* is involved – the isolated bubble regime – as only one nucleation site can be active[3]. As the main means of heat dissipation is convection (see section 4.1.2), the wall temperature is dictated by the convective heat transfer coefficient. As the relationship between the heat flux and the wall superheat is fixed

[3] Several regimes can in fact be identified using the vertical coalescence as a distinctive criterion. If the wall superheat is high enough, the bubbles from the nucleation site can even form a vapour column. As vertical coalescence is not investigated in this study, only one boiling regime is considered

without taking into account the boiling phenomenon, one or the other can be relevant as a base parameter to study bubble growth.

The main possible consequence on the bubble growth when changing the heat flux density or the wall superheat is a modification of the vapour production rate, causing a modification of the bubble growth rate and possibly of the bubble departure volume. The vapour production rate is strongly related to the temperature gradient in the fluid surrounding the bubble, and thus to the wall superheat. Hence, the wall superheat will be chosen as the reference parameter to describe the experimental setting.

5.1.2.1 Bubble growth

Bubble growth curves are plotted in Fig. 5.6 for different wall superheats within the range involved. The bubble growth time is significantly reduced when increasing the wall superheat. As expected, the vapour production rate is significantly affected by the wall superheat.

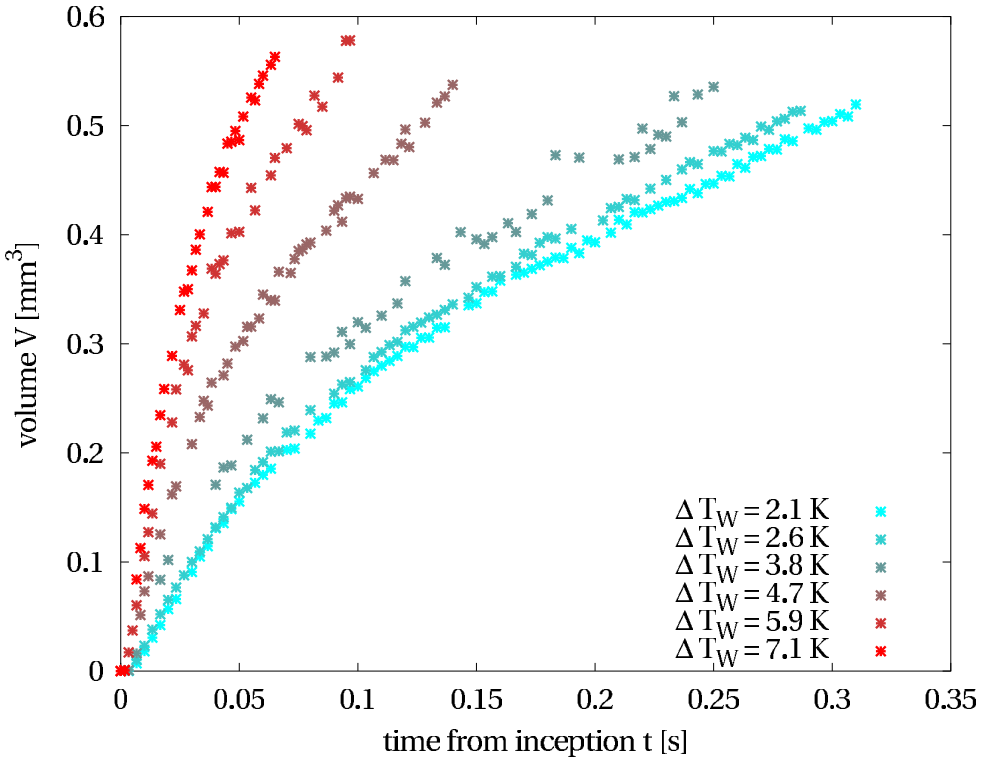

Figure 5.6: Growth curves of 6 bubbles at different wall superheat

The departure volume remains almost unchanged (variations stay within a ±5 % interval) for any wall superheat. This means that the mechanisms that govern bubble departure do not seem to be significantly affected by the wall superheat. The forces acting on the bubble are deeply investigated in section 5.2. For an identical shape at departure, static forces are identical. The dynamic forces involved in the force balance are thus negligible when the bubble departs from the surface.

5.1.2.2 Bubble frequency

As the departure volume of the bubbles can be considered constant for all wall superheats and only the growth time is changed, another parameter to describe the effect of the wall superheat is the bubble frequency. The frequency is based on the count of departing bubbles as long as no coalescence occurs, and on the count of departing coalesced bubbles otherwise[4]. Let the instantaneous frequency be defined as the inverse of the growth time of a single bubble event. As it can be observed in Fig. 5.1, the waiting time between the detachment of a bubble and the nucleation of the next bubble is negligible[5].

As it was foreseen in subsection 5.1.1.4, the bubble growth time of successive bubbles may vary. The instantaneous frequency of 10 successive bubbles is plotted in Fig. 5.7 for different wall superheats. It is observed that at low wall superheat, the bubble frequency is almost constant. On the contrary, at high superheat, higher variations of frequency are observed[6] due to the occurrence of coalescence events. The mean frequency would thus be more likely to vary between separate experiments if the size of the sampling used to calculate the mean frequency is small.

The bubble frequency versus wall superheat is plotted in Fig. 5.8. The bubble frequency is a mean value of the instantaneous bubble frequency of 20 successive bubbles. The overall trend of the frequency increase with the wall superheat and is quite linear. The experimental data are more scattered at high wall superheat because of the occurrence of coalescence events.

In many archival publications, authors have tried to correlate the departure diameter D_d and the bubble departure frequency f_d in the form:

$$f_d \times D_d^n = c \tag{5.5}$$

with c being a constant and n an exponent varying between $^1/_2$ and 3 depending on the experimental conditions [76]. The present results do not follow such a simple expression of the relation between the departing diameter and the frequency as the diameter is constant and the frequency is varying.

5.1.3 Non dimensional bubble growth

Bubble growth curves presented in Fig. 5.6 seem to have a similar shape. The bubble dynamics has thus been compared for different superheats. For a meaningful comparison, the growth curves have been normalized by dividing the time by the total growth time ($t^* = t/t_d$),

[4] Although this study excludes the occurrence of vertical coalescence, the wall superheat threshold for the appearance of the phenomenon is not sharp. Coalescence being a stochastic event, some occurrences are observed at high superheats ($\Delta T_W > 6$ K)

[5] The waiting time can even not be measured as it is generally faster than the frame rate, i.e. lower than 0.33 ms.

[6] The order of magnitude of the variations can reach ±20 %.

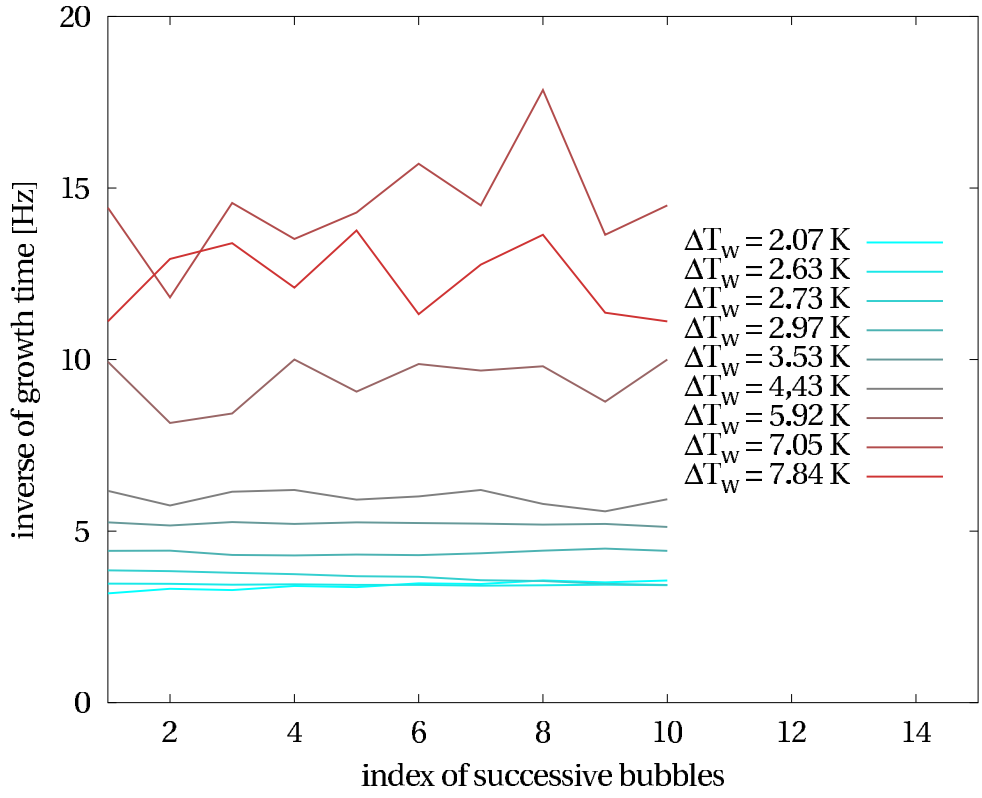

Figure 5.7: Inverse of growth time (i.e. instantaneous frequency) of 10 successive bubbles for different wall superheat

and the volume by the departure volume ($V^* = V/V_d$). A very good similarity between the different normalized curves is observed in Fig. 5.9. Bubble growth, in all the conditions of these experiments, can thus be described by a non-dimensional law that holds true for any wall superheat, as long as no bubble merging occurs.

Bubble growth is usually described by a power law. It is thus considered to fit a curve having the form:

$$V^* = t^{*n} \tag{5.6}$$

with n the only fitting parameter[7]. For a thermal diffusion growth, n is presented as equal to 1.5 in most models in the literature[8] (Plesset and Zwick [154], Forster and Zuber [64], Scriven [164], Griffith [70], Zuber [202], Han and Griffith [73], Cooper [43], Mikic *et al.* [131],Cooper and Vijuk [45], Dzakowic and Frost [58], Cooper and Merry [44], Theofanous and Patel [183], Fyodorov and Klimenko [66], Buyevich and Webbon [21], etc.).

The entire data set from Fig. 5.9 is used to plot the ratio of ($\ln V^*/\ln t^*$) versus the non dimensional time in Fig. 5.10. It is observed that this ratio is not constant for $0 < t^* < 0.2$; the ratio is rather constant and equal to 0.6 for $0.2 < t^* < 0.8$; the ratio values are very scattered around 0.6 for $0.8 < t^* < 1$ as both ($\ln V^* \to 0$) and ($\ln t^* \to 0$).

[7] As the growth is normalized, $V^*(0) = 0$ and $V^*(1) = 1$.
[8] usually presented as a function of the bubble radius, i.e. $R_{eq} \propto t^{0.5}$

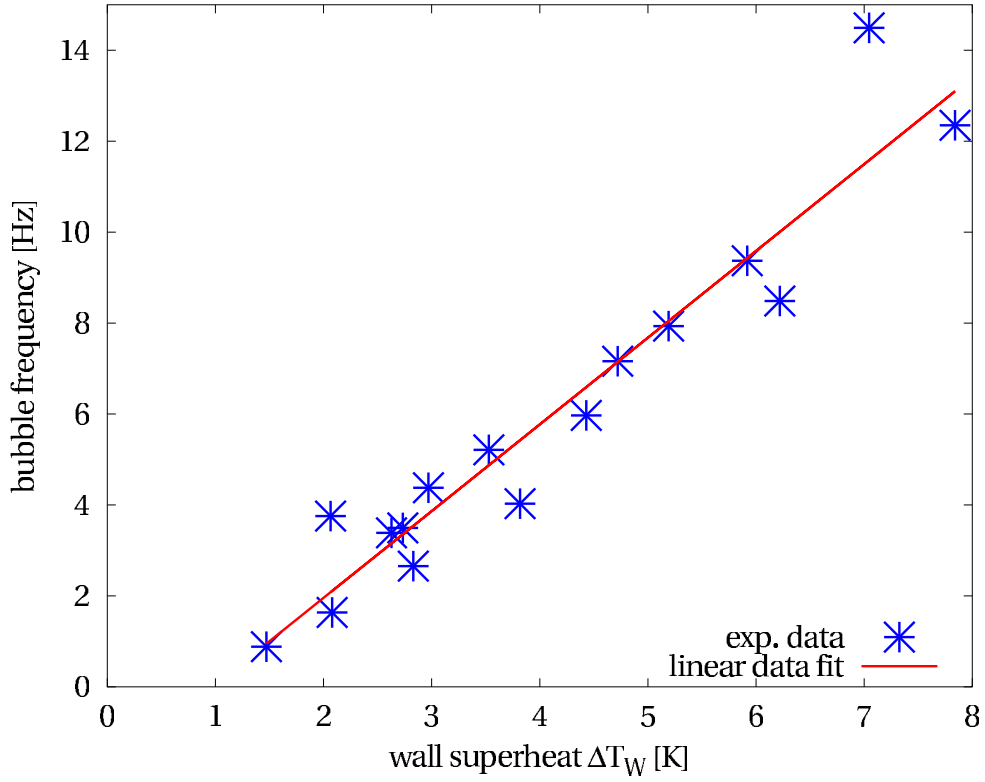

Figure 5.8: Influence of the wall superheat on bubble departure frequency

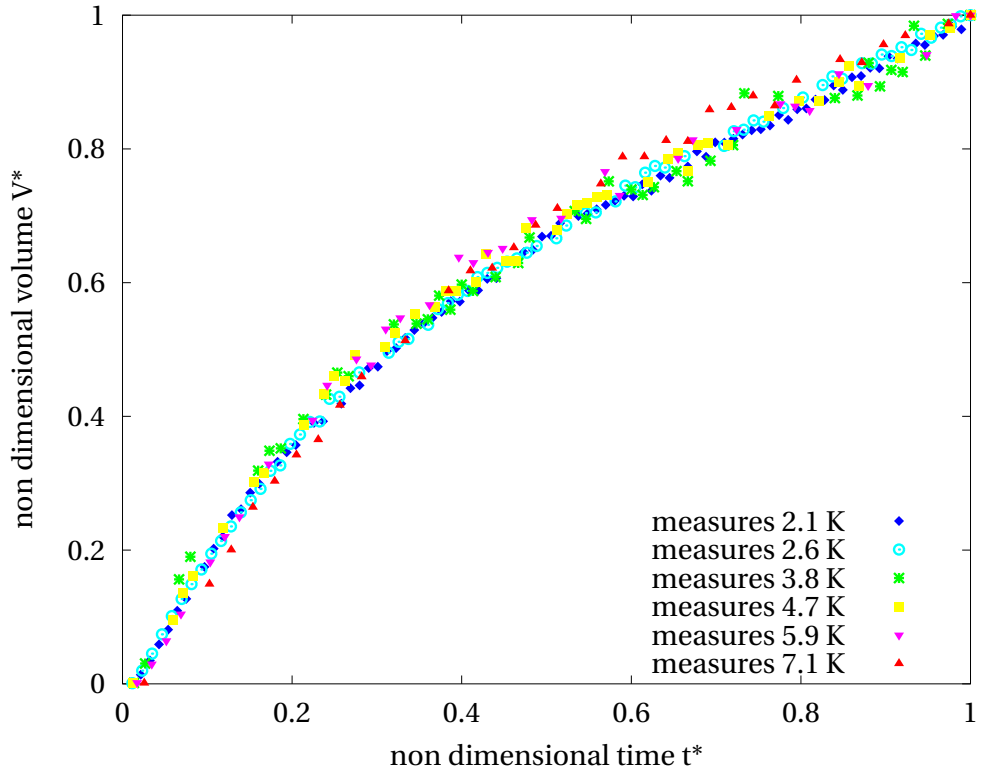

Figure 5.9: Comparison between growth curves for different wall superheats

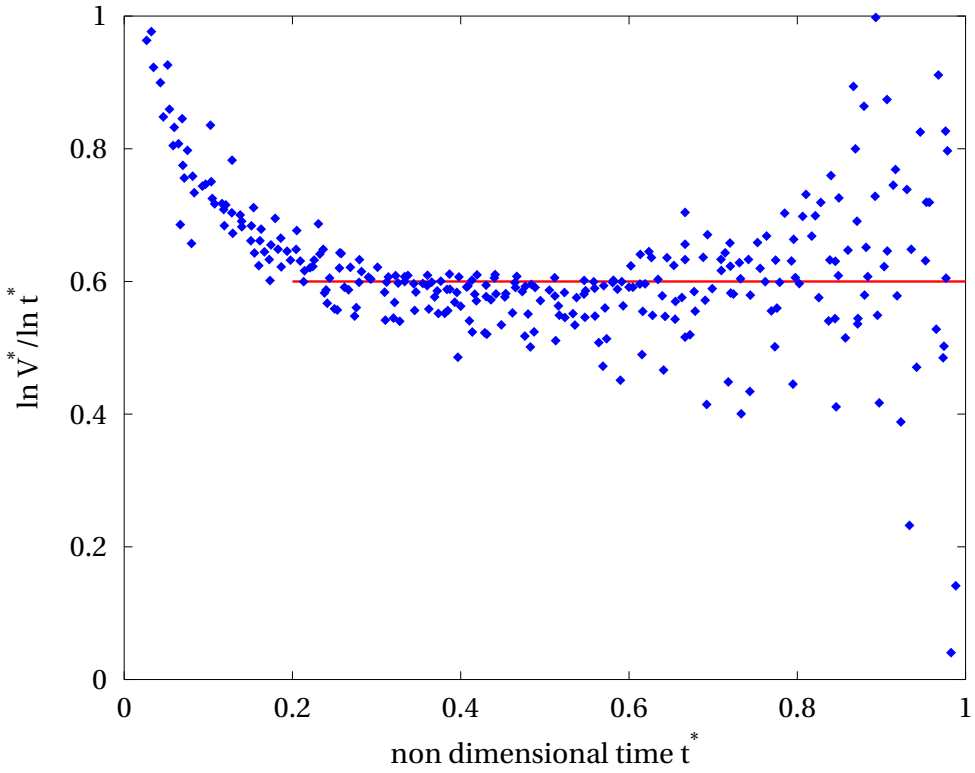

Figure 5.10: Logarithms ratio used to fit a power law.

A power law with a coefficient of 0.6 does describe properly the non-dimensional bubble growth for $0.2 < t^* < 1$, and another equation must be found for the beginning of the bubble growth. It can be observed in Fig. 5.9 that the volumetric growth is initially rather linear. The following relation is suggested:

$$\begin{aligned} V^* &= 2 \times t^* \quad \text{for} \quad 0 < t^* < 0.2 \\ V^* &= t^{*0.6} \quad \text{for} \quad 0.2 < t^* < 1 \end{aligned} \tag{5.7}$$

The experimental volumetric growth law from Eq. 5.7 is illustrated in Fig. 5.11 together with the data set and the conventional growth law predicting $V \propto t^{1.5}$.

Three facts are to be pointed out from Fig. 5.11:

- The experimental growth law suggested agrees with the experimental data.
- Several other growth laws could describe the data set once the growth is segmented into several sections. The first part of the growth is indeed quite linear, so there is no need to use a power law. Moreover, the first instant of the growth can not be properly represented by a power law as the derivative (i.e. the volumetric flow rate) is either 0 for $n > 1$ or ∞ for $n < 1$.
- An essential difference between these experiments and the conventional models is the curvature of the growth. The present growth curve is convex, whereas the literature predict a concave growth curve.

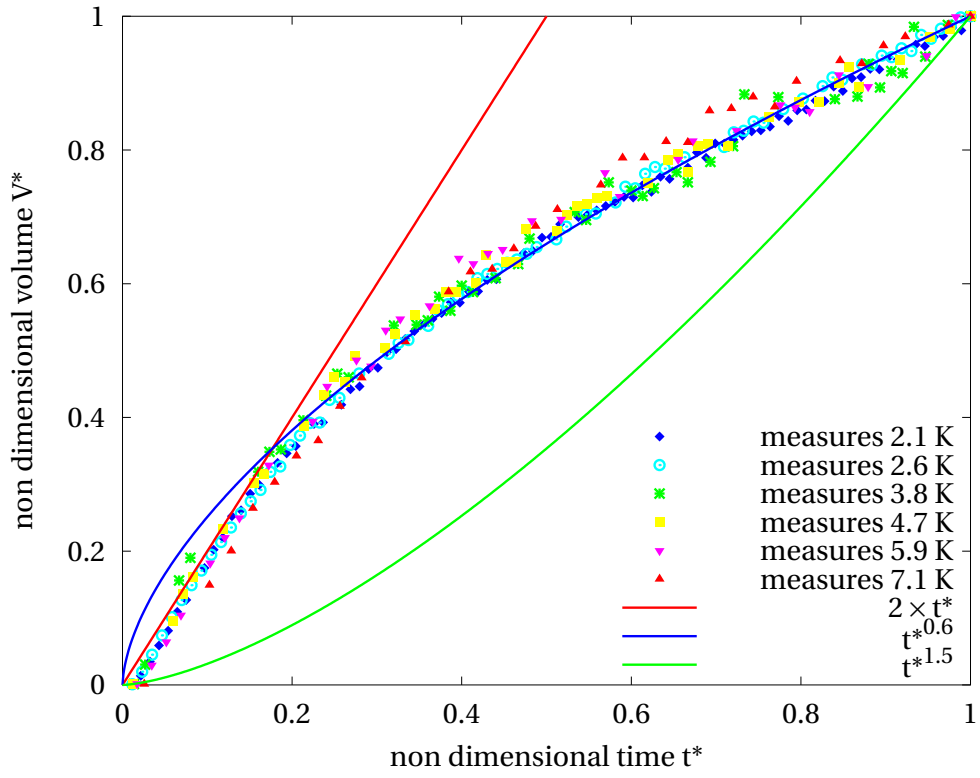

Figure 5.11: Experimental volumetric growth law compared to experimental data and literature power law.

The characteristics of the growth curve and the main differences with most conventional models need to be described in terms of vapour production using the time derivative of the bubble volume.

5.1.4 Vapour production rate

The vapour production rate during bubble growth has been obtained by fitting the volumetric growth by a 7^{th} order polynomial function and by calculating its derivative[9]. The vapour production rate has been normalized using the non-dimensional time and bubble's volume. The function obtained is plotted in Fig. 5.12, together with the time derivative of the experimental growth law proposed in Eq. 5.7.

The most surprising result is the observation of a decreasing vapour production rate while the interface area is increasing. This is a major difference with the conventional analytical models, and this gives new insight into the temperature field around the bubble during its growth. It reveals that the phase change rate is very high after bubble inception, meaning that the new bubble is surrounded by highly superheated liquid. As the waiting time is

[9]The result of the derivative varies with the order of the polynomial function, especially close to the ends. A parametric study has been performed in order to find a acceptable order. For any order between 3 and 11, the overall shape and the values are similar.

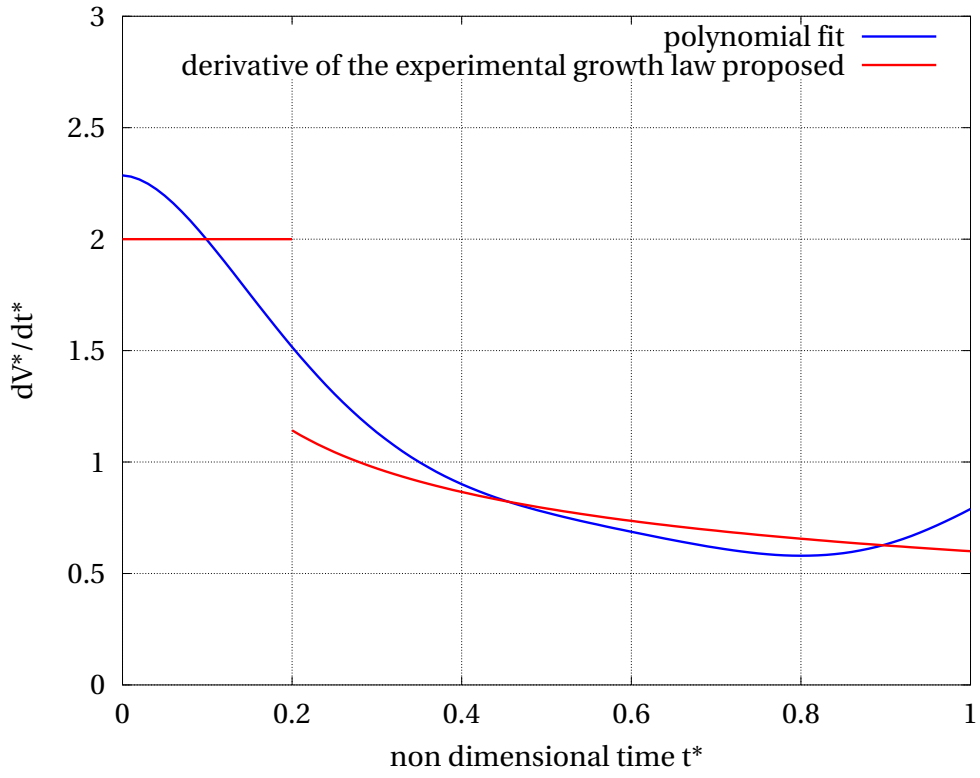

Figure 5.12: Non dimensional vapour production rate during bubble growth

close to zero, the liquid displaced by the detachment of the previous bubble must already be superheated. This is in contradiction with a commonly presented assumption that the thermal boundary layer is *removed* by the detaching bubble (see Fig. 5.13) and replaced by bulk liquid at saturation.

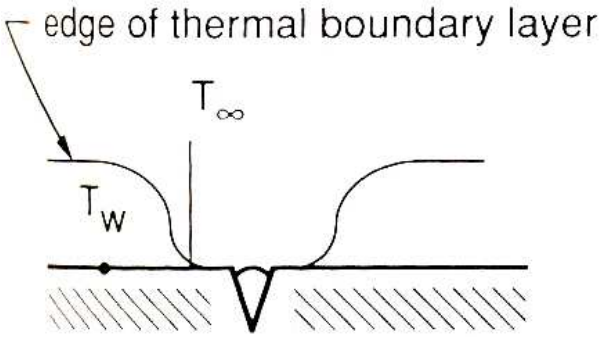

Figure 5.13: Van P. Carey description of the thermal boundary layer after bubble departure ([23], page 199)

The presence of highly superheated liquid around the new growing bubble can be explained by two different mechanisms:

- As described by Siedel *et al.* [168], it is noticed from the interferometry experiments of Beer [15, 176] that the departing bubble tends to draw in its wake the liquid layers that

are close to the wall. This is illustrated in Fig. 5.14, showing the comparison between Beer's experiment and the present analysis.

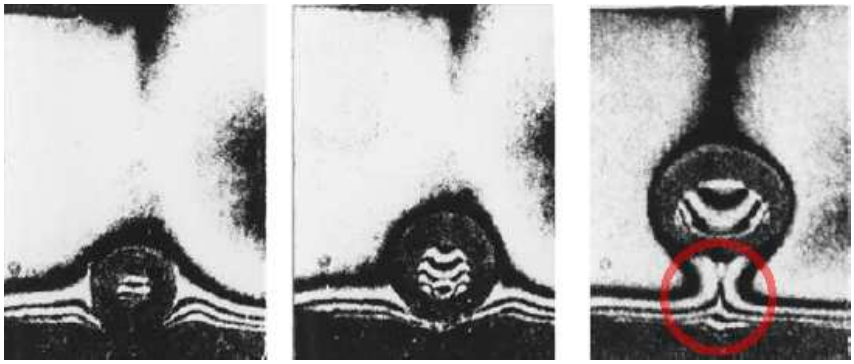

(a) Interferometry images from Beer [15]

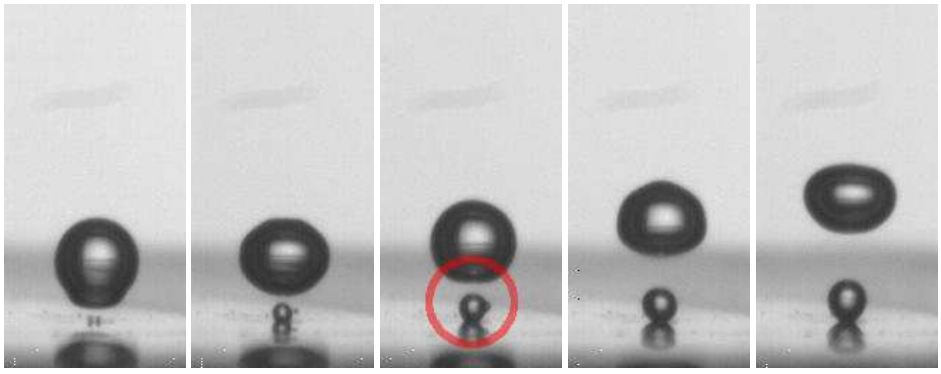

(b) Present study experimental images

Figure 5.14: Superheated liquid drawn in the wake of a departing bubble

- The liquid motion, and thus the temperature field and shape of the thermal boundary layer is highly influenced by the convective structures and flow. From the numerical simulations of Section 4.2.2, it has been determined that convection tends to bring superheated liquid above the center of the plate (i.e., where the bubbles grow).

The vapour production rate can also be analysed through an energy balance. Considering the bubble as a control volume, this energy balance relates the latent heat transported into the bubble to the overall heat transfer into the bubble by conduction within the liquid phase and, for a constant vapour density, can be expressed as:

$$\rho_v h_{fg} \frac{\mathrm{d}V}{\mathrm{d}t} = \oint_S \lambda_l \left(\overrightarrow{\mathrm{grad}}T\right).\vec{n}\ \mathrm{d}S \tag{5.8}$$

where S is the instantaneous bubble surface area and $\left(\overrightarrow{\mathrm{grad}}T\right).\vec{n}$ is the local temperature gradient normal to the interface. Thus, the rate of change of the bubble volume is an important parameter in the sense that it provides rich information regarding the time history of the rate of energy transfer into the bubble. For instances in which $V \propto t^n$ and $n > 1$, this implies that the rate of change of the volume, and thus the rate of energy transfer, continually increases. However, once a bubble nucleates it continually depletes the sensible energy

stored within the liquid surrounding it. Thus, for the rate of energy transfer to increase, it must be that the volumetric growth rate is large enough that the surface area available for heat transfer increases at a rate which is more than sufficient to offset the fact that the local heat flux levels are decreasing. For the case here, where $V \propto t^n$ and $n < 1$, the rate of change of the volume and thus the rate of energy transfer continually decrease, as depicted in Fig. 5.12. Thus, for these low Jakob numbers, possibly in combination with the negligibly small waiting times, the volumetric growth rate is not sufficient to sustain vapour production as the energy in the surrounding liquid is depleted. During early growth, $t^* < 0.2$, the relatively high rate of heat transfer/vapour generation is maintained with $\frac{dV}{dt} \approx 2$. For $t^* \approx 0.2$ it decreases steeply and begins to plateau to a near constant value of $\frac{dV}{dt} \approx 0.6$.

5.1.5 Bubble shape and oscillations

The bubble volumetric growth description does not take into account the shape of the bubble. The shape plays a key role in:

phase change — the area offered to the liquid is determined by the shape
liquid motion — bubble motion is coupled with its shape
bubble detachment — the forces involved strongly rely on the bubble shape

The bubble shape is a *3D* and time-dependant parameter which is difficult to describe with appropriate parameters. The usual parameters of bubble height and width are developed in Section 5.1.5.1, the height of the center of gravity is investigated in Section 5.1.5.1 and a new parameter introduced by Siedel *et al.* [169] is presented in Section 5.1.5.3.

5.1.5.1 Bubble height and width

Bubble height and width, and especially the ratio of the height to width[10] are usual parameters to describe the bubble shape, especially to describe the deformation of a bubble caused by electrohydrodynamic effects (e.g. [29, 35, 54, 86, 101, 151]). These parameters are sometimes directly measured on the bubble contour, or are determined by the minor and major axes of an ellipsoid fitting the contour.

The advantage of this description is that it simply describes what is seen. If the bubble height is larger than the width, the bubble is elongated in the vertical direction, and vice versa. Figure 5.15 shows the height and width evolution for two different wall superheats: a low superheat of 2.1 K and a moderate superheat of 4.7 K.

Figure 5.15a shows a very regular evolution of the two parameters during a bubble growth at low heat flux. During the first 10 % of the growth, the bubble remains spherical. For the rest of the growth, the bubble height increases faster than the bubble width. The bubble hence

[10] commonly called aspect ration AR

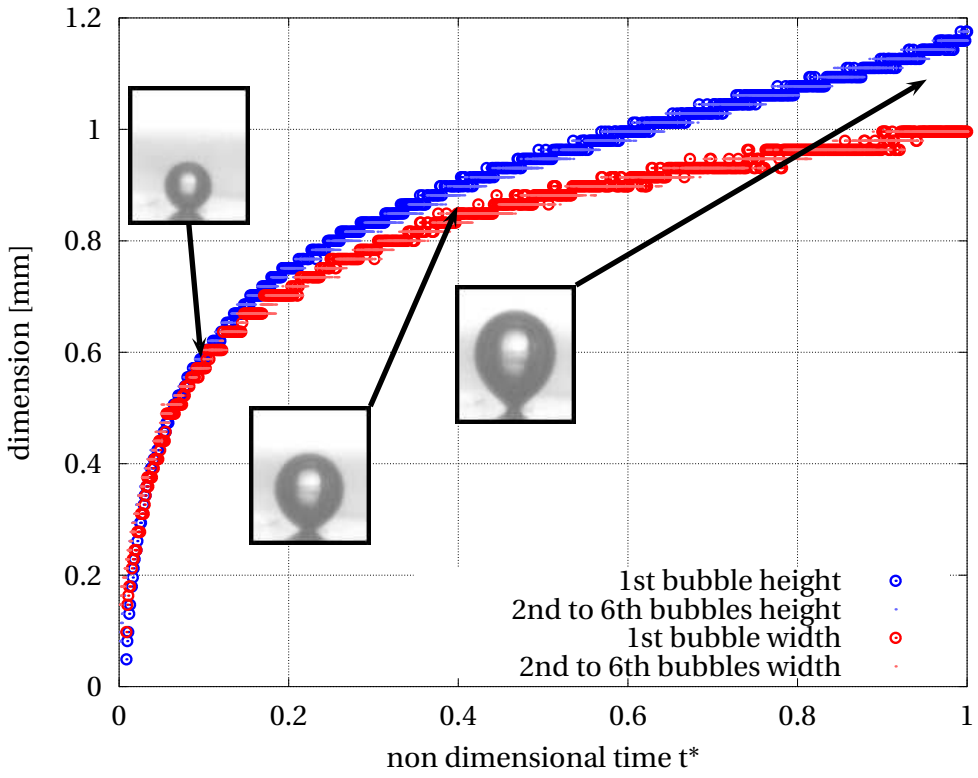

(a) $\Delta T_W = 2.1$ K

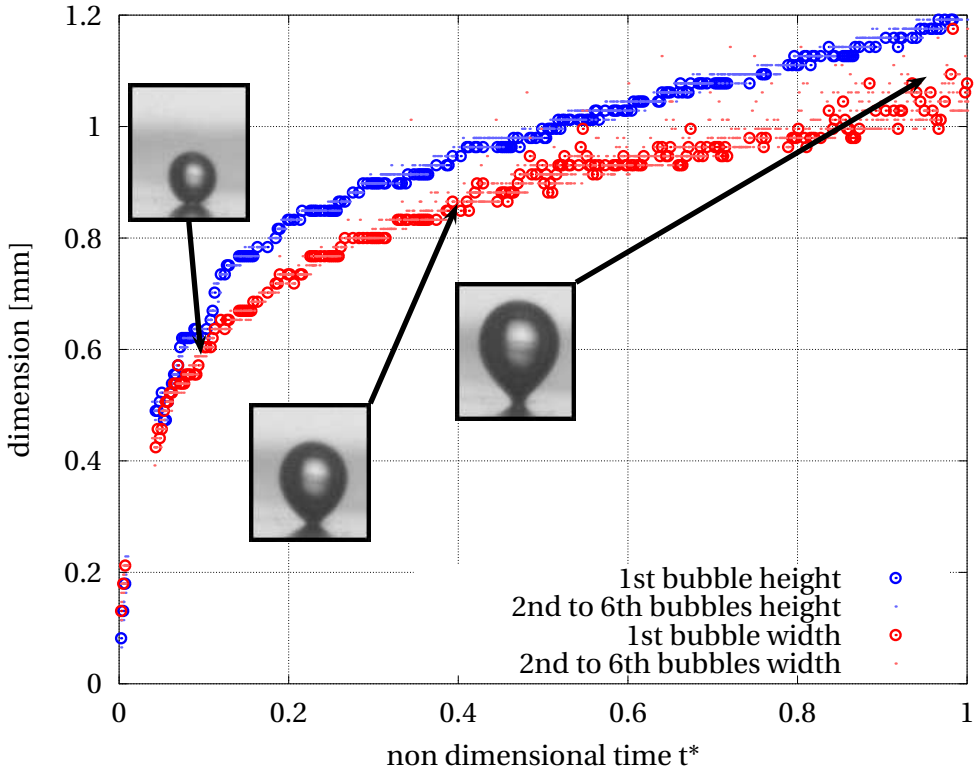

(b) $\Delta T_W = 4.7$ K

Figure 5.15: Bubble height and width, plotted for 6 successive bubbles in the same conditions

forms a neck. It is to be noted that the resolution of the length and width is determined by the size of a pixel[11], leading to rough steps in both curves. It can also be observed on the figure that the growth is very reproducible for different bubbles at the same wall superheat.

Figure 5.15b shows a less regular evolution of the two parameters during a bubble growth at moderate heat flux. Clear oscillations of the shape of the bubble can be observed during the first 40 % of the growth, and the data afterwards are somewhat scattered[12]. Because of the initial oscillations, the bubble height seems to diverge sooner from the bubble width.

Figure 5.16 presents a comparison between the height and width evolution for different wall superheats. The bubble width evolutions are quite similar, even though it is much more scattered at high wall superheats. At a high wall superheat, the width tends to be slightly larger at departure.

Concerning the evolution of the height, more differences appear, as oscillation are clearly observable at moderate and high heat fluxes whereas the evolutions are very regular at low heat fluxes. The same tendency of the height to be larger at high heat flux is observed, but the difference is very small[13].

Figure 5.17 shows the height to width ratio for a low wall superheat of 2.1 K and a moderate superheat of 4.7 K. The poor resolution of this ratio is a result of the pixel resolution of both the height and the width measurement. This ratio starts very low as the bubble is initially hemispherical. For $t^* > 0.1$, the ratio is greater than 1 because of the neck formation. The final aspect ratio is between 1.1 and 1.2. The scatter of the values of the ratio do not allow a deeper description or comparison of the bubble shapes.

5.1.5.2 Height of the center of gravity

As detailed in Section 3.3.2, the height of the center of gravity of the bubble is measured. The evolution of the height of the center of gravity is shown in Fig. 5.18 for 6 successive bubbles at two different wall superheat. With a low superheat, bubble growth seems very repeatable, and no major differences are observed. The evolution of the height of the center of gravity is smooth and of similar shape as the evolution of the bubble's volume. An inflexion is yet noticeable just before departure, revealing a slight vertical acceleration of the bubble before the rupture of its neck.

Figure 5.18b shows the evolution of the height of the center of gravity at a moderate wall superheat. The overall shape of the figure strongly differs from Fig. 5.18a because of the oscillations of the bubble. Quickly after nucleation, several images are not processed by the image processing program owing to the difficulty of distinguishing the new bubble from the

[11] The pixel size is here $\Delta z = 16.3\,\mu m$.

[12] This might be due to non optimal image processing. The bubble is sometimes difficult to identify from its background.

[13] The order of magnitude of the height difference is $\pm 30\,\mu m$ around a mean value, i.e. 2 pixels.

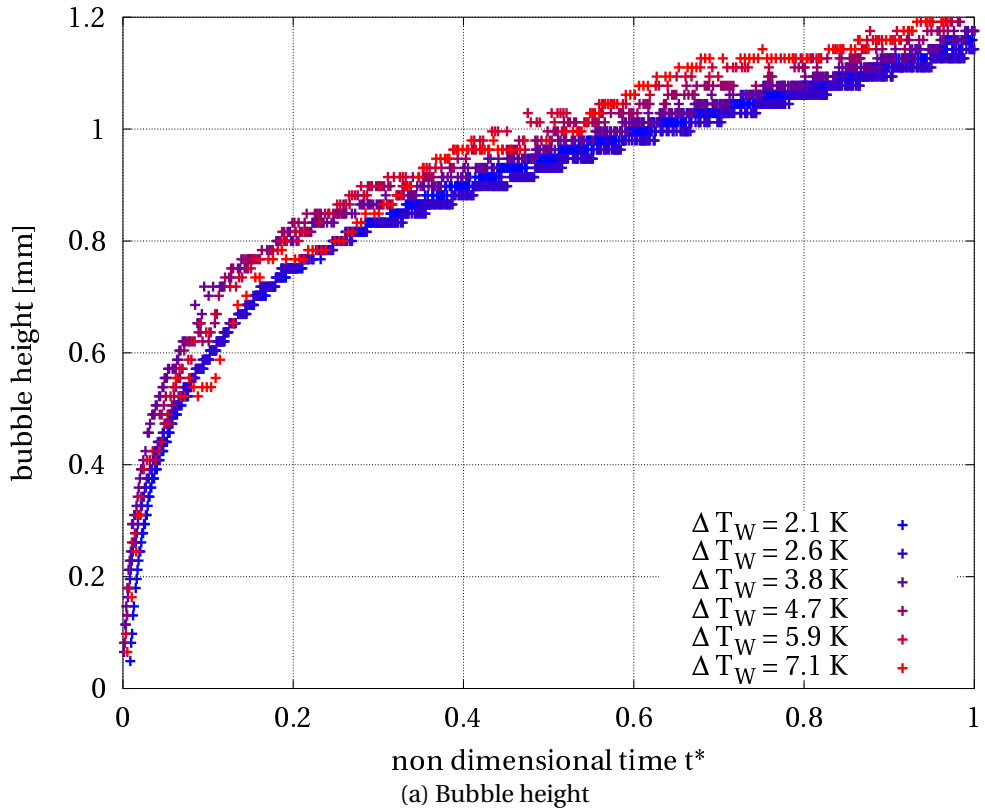

(a) Bubble height

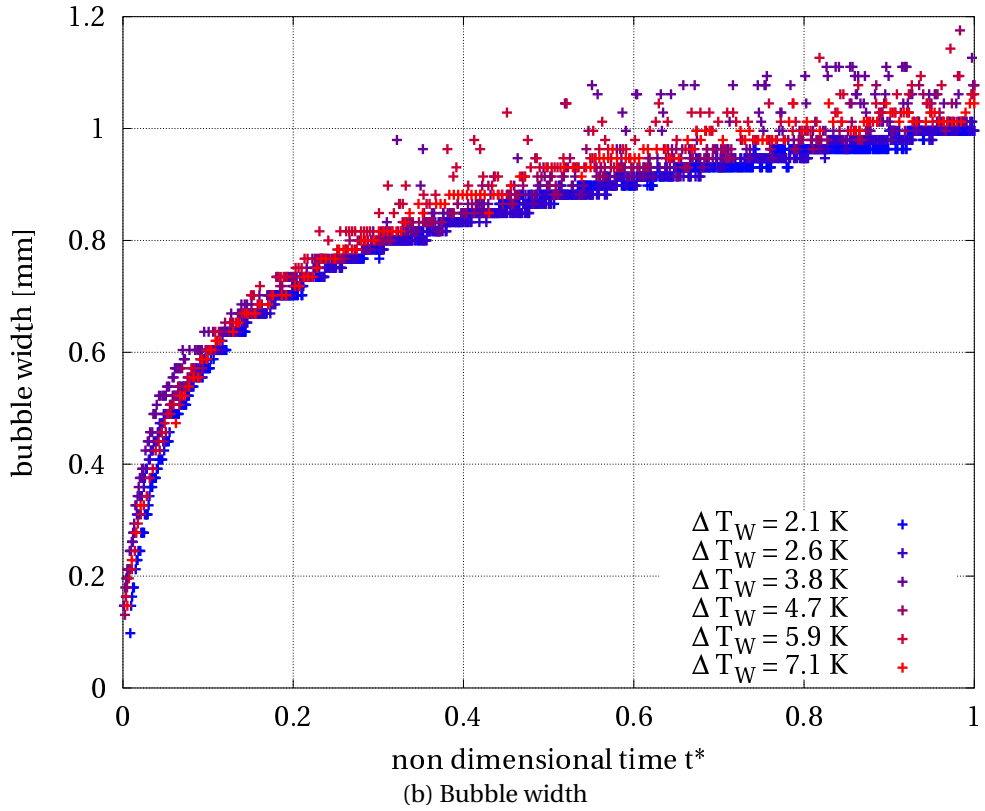

(b) Bubble width

Figure 5.16: Bubble height and width for several wall superheat

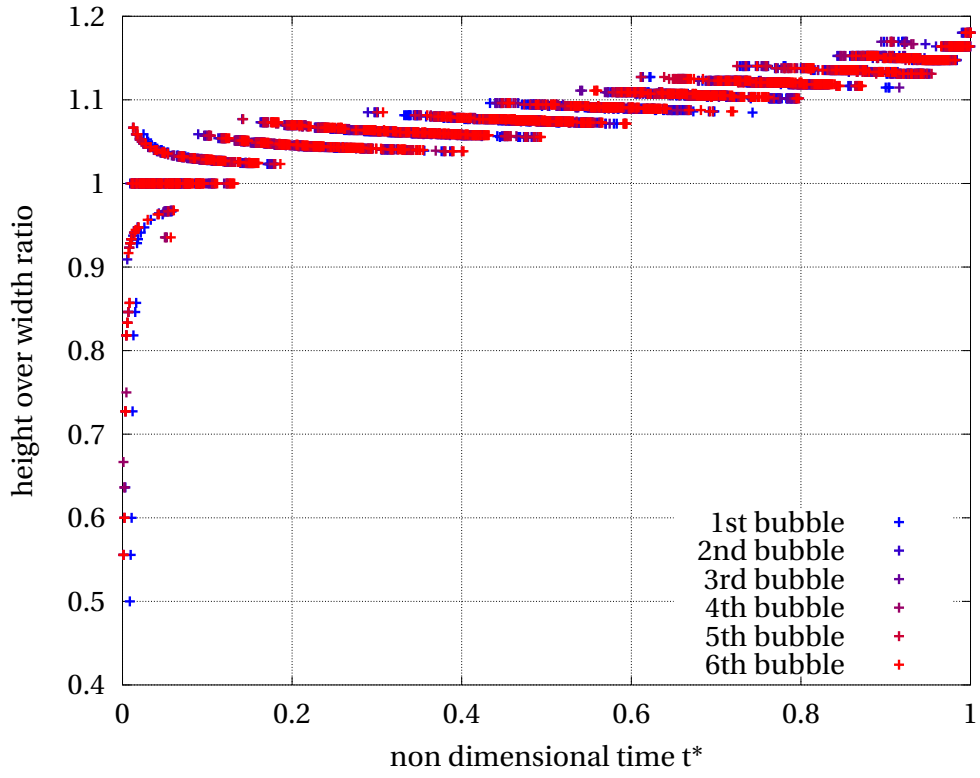

(a) $\Delta T_W = 2.1\,\mathrm{K}$

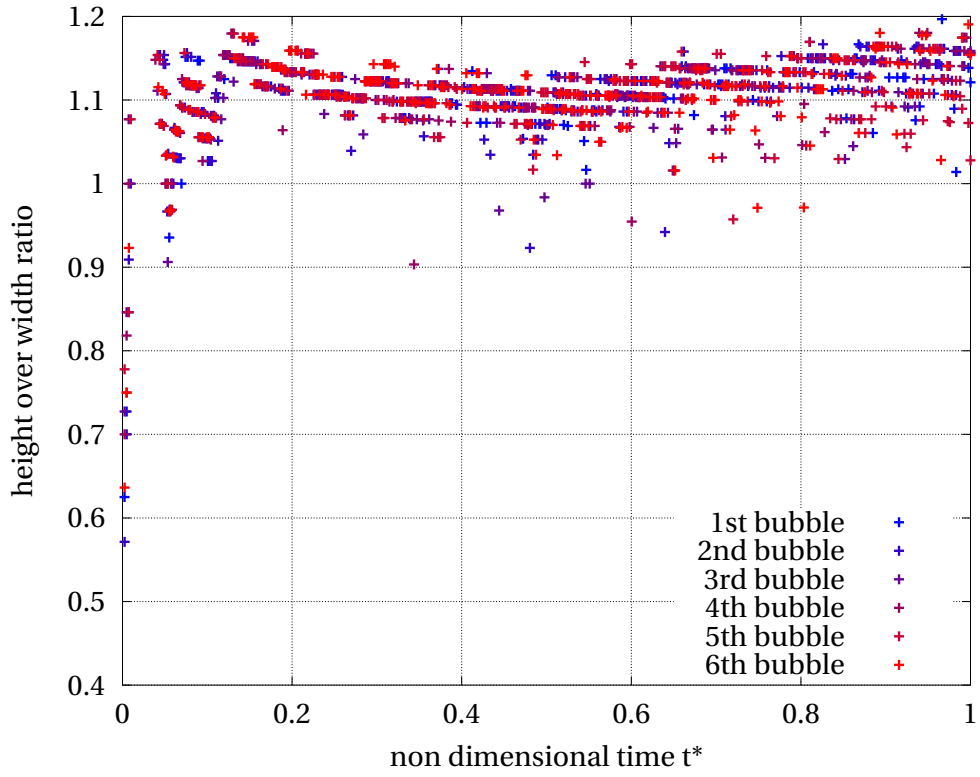

(b) $\Delta T_W = 4.7\,\mathrm{K}$

Figure 5.17: Ratio of bubble height to bubble width

preceding bubble[14]. After this interaction event, the new bubble oscillates vertically during the entire growth, the oscillation being progressively damped. It is noticed that the oscillations are repeatable between successive bubble events.

Figure 5.19 shows the evolution of the height of the gravity center for bubbles at various wall superheat conditions. Two observations can be made:

- The oscillations amplitude increases with the wall superheat.
- The height of the center of gravity at departure seems to increase with the wall superheat as well. This difference is nevertheless relatively small, and the uncertainty on the absolute height depends on the determination of the base of the bubble which is determined to be within a pixel size uncertainty[15].

The height of the center of gravity of the bubble better describes the bubbles oscillations than the respective height and width of the bubble, but does not give information about the shape of the bubble. Another parameter should be used to simultaneously describe the shape and the oscillations.

5.1.5.3 Non dimensional description of the oscillations

A new non-dimensional parameter has been introduced by Siedel *et al.* [169]. It aims at describing together the shape of the bubble, by comparison to a sphere, and its oscillations. This parameter A_S is defined as follows:

$$A_S = \frac{h_{cg}}{R_{eq}} \tag{5.9}$$

with h_{cg} being the height of the center of gravity and using the equivalent radius R_{eq}:

$$R_{eq} = \left(\frac{3V}{4\pi}\right)^{\frac{1}{3}} \tag{5.10}$$

From this definition:

- If the bubble is a sphere, $A_S = 1$.
- If it is a truncated sphere, $A_S < 1$.
- If a neck forms, $A_S > 1$.
- If an oscillation elongates the bubble in the vertical direction, $\frac{dA_S}{dt} > 0$.
- If an elongation tends to flatten the bubble, $\frac{dA_S}{dt} < 0$.

[14] As it can be seen in Fig. 5.21, when the wall superheat is moderate or high, the new growing bubble grows fast enough to reach the previous bubble which did not have the time to move from above the surface. It sometimes results in vertical coalescence events, or may also only distort the interface of both bubbles at the *contact* area.

[15] i.e. 17 µm

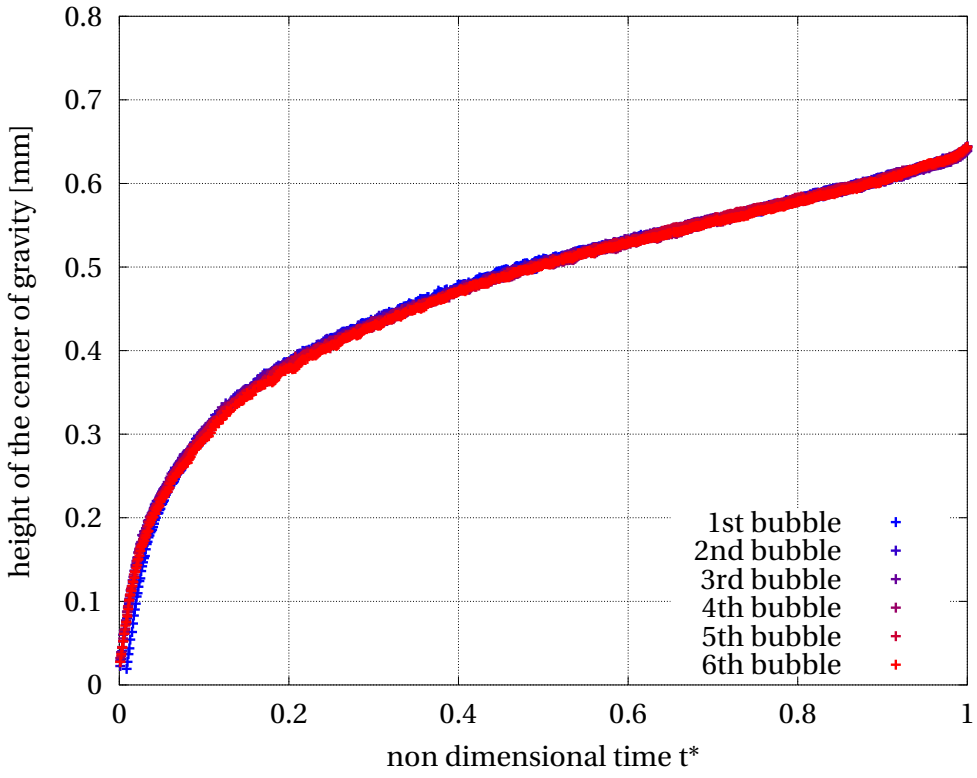

(a) $\Delta T_W = 2.1$ K

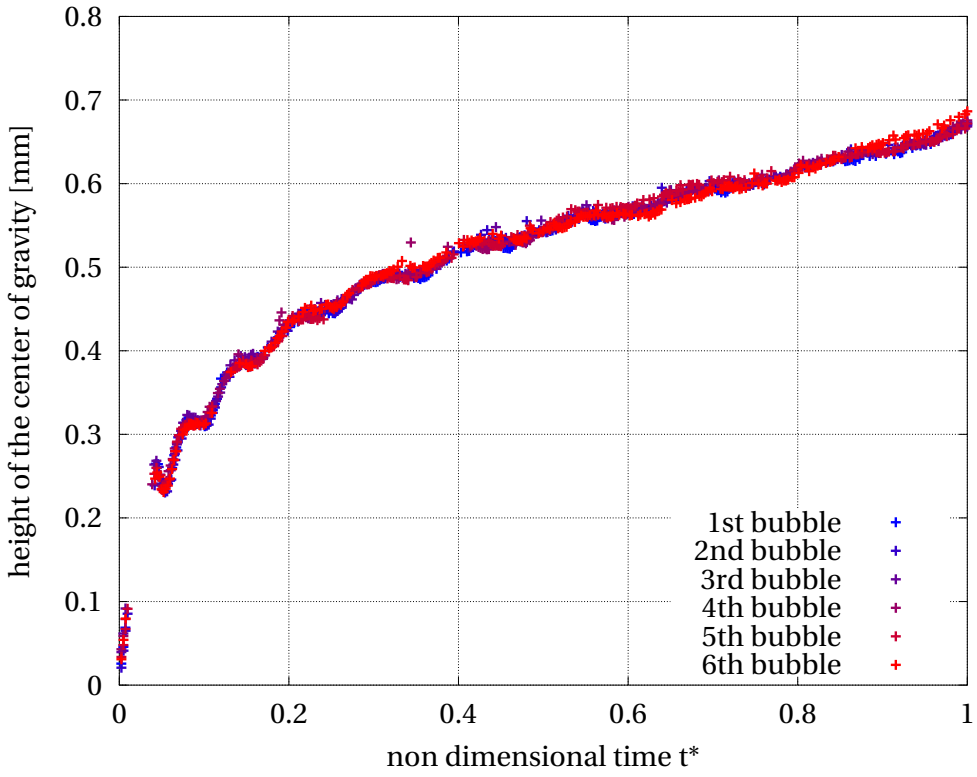

(b) $\Delta T_W = 4.7$ K

Figure 5.18: Height of the center of gravity

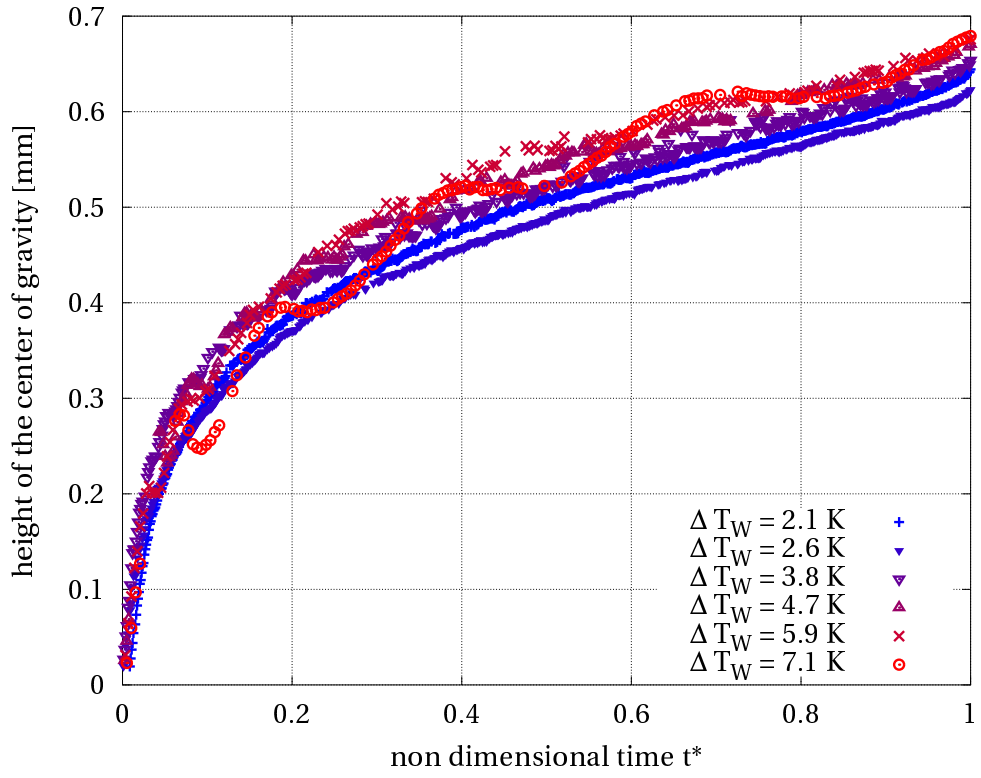

Figure 5.19: Height of the center of gravity for various wall superheat

The equivalent radius and the height of the centre of gravity have been chosen because they reflect the inertia of the bubble and of the surrounding liquid. For example, if the height of the bubble suddenly noticeably increases because of forming *horns* or *tails* (e.g. as described in Section 5.3, when shape oscillations are caused by a coalescence event), the height of the centre of gravity will not change significantly with respect to the whole bubble actual motion.

Figure 5.20 shows the evolution of A_S for several wall superheat conditions. For low wall superheat, the curves exhibit oscillations that reflect oscillations of the bubbles during their growth. These oscillations are caused by the preceding bubble at departure: in some situations, the departing bubble touches the new bubble, particularly when the latter is growing very fast. In some other cases, the departing bubble draws the next bubble up when rising in the liquid.

The oscillations are more significant when the wall superheat is high: the bubble growth velocity is much higher, so that the new bubble is more likely to reach the preceding one or to be influenced by it. Furthermore, since the rising velocity of the preceding bubble is independent of the wall superheat while the growth time is decreasing with an increasing superheat, the ratio of bubbles interaction to the total growth time is larger when the superheat is high.

Figure 5.21 shows the details of the evolution of A_S for a wall superheat of 4.7 K. Data points are missing for $0.02 < t^* < 0.06$ because of the proximity of the preceding bubble

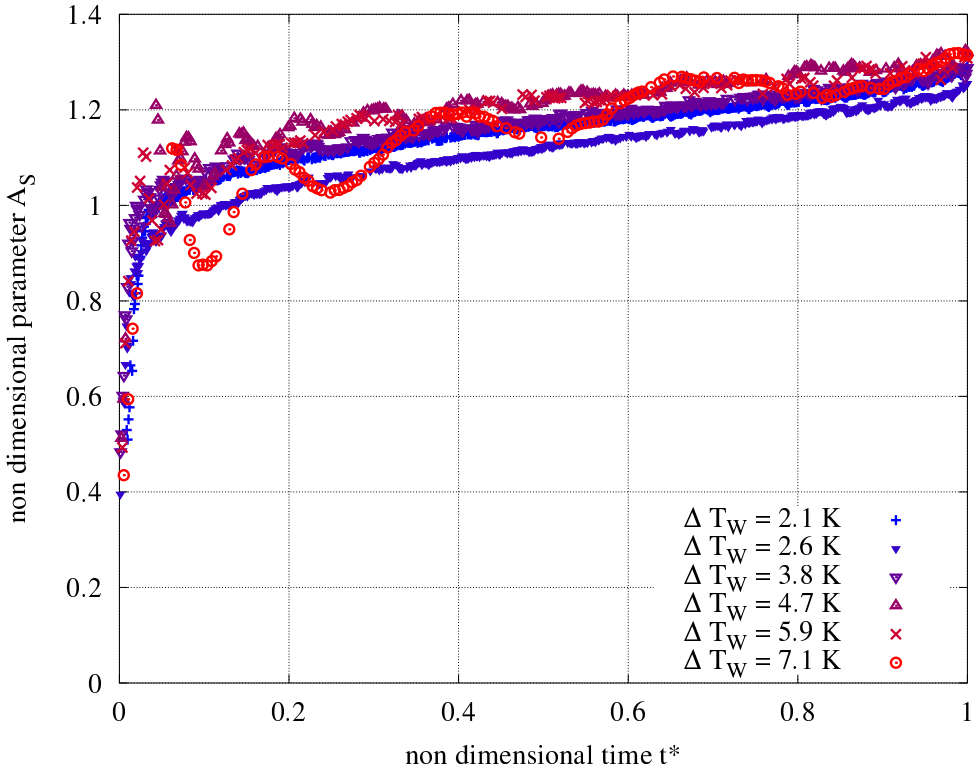

Figure 5.20: Non dimensional parameter A_S for various wall superheat

that prevents a clear determination of the contour of the bubble[16]. As the detached bubble is accelerating and rising in the bulk liquid, it draws up the liquid in its wake and thus the new growing bubble. However, the new bubble is firmly attached by adhesion forces at the triple line. The bubble is thus elongated in the vertical direction until having an A_S-ratio of more than 1.2. Once the preceding bubble is far enough from the new bubble, its influence become negligible. This latter flattens towards the equilibrium shape of a sphere with a neck, and oscillates around this shape. The oscillations are damped by the viscous stress, and the evolution of A_S is eventually smooth.

It is noticed that even at a low wall superheat, the bubble very quickly forms a neck. Once $t > 0.1$, the equilibrium value of A_S is more than unity. The neck continually grows, leading to an A_S-ratio of about 1.3 just before detachment.

As the oscillations are damped, no effect has been measured or observed concerning the bubble size at departure. However, the oscillations might play a significant role in local convective heat transfer enhancement has the bubble oscillation simply reflects the motion of the liquid around the bubble.

Another possible consequence of the oscillations is an augmentation of the interactions between neighbouring bubbles when boiling on a natural surface. The liquid motion may modify the behaviour of other bubbles or may tend to move the bubbles towards each other.

[16]This can be observed on the first picture of the figure.

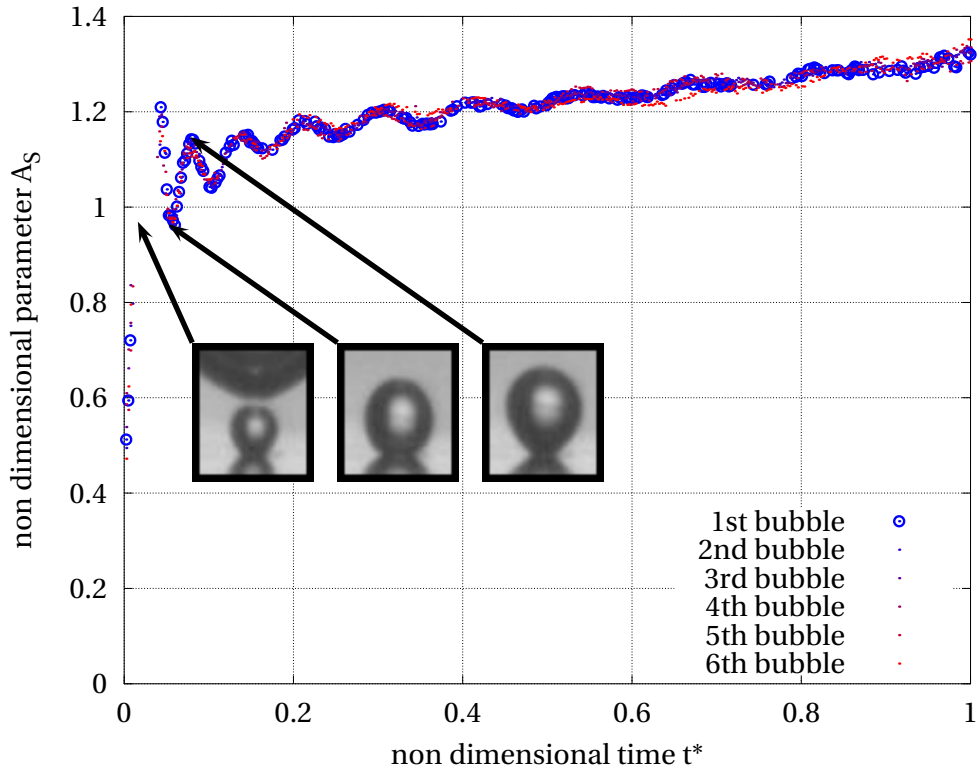

Figure 5.21: Non dimensional parameter A_S with $\Delta T_W = 4.7\,\mathrm{K}$

This latter case would favour coalescence events and strongly modify liquid flow around the bubbles.

5.2 Forces acting on the bubble

The forces acting on the bubble during its growth dictate its shape evolution and its motion, and therefore the conditions of departure from the surface. An analysis of the forces acting on the bubble during its growth has thus been performed [172] in order to bring a better understanding of the bubble dynamics, and hopefully of the bubble detachment which plays a prominent role in boiling heat transfer.

The control volume used for the force analysis is described in Fig. 5.22b. The bubble contour is obtained by image processing from the experimental images. The control volume is defined by the bubble's volume excluding the volume of the nucleation site. The boundaries of the control volume are:

the liquid side of the *liquid-vapour* interface between the vapour bubble and the surrounding liquid.

the contact line between the vapour, the liquid and the solid phases. In our experiments, the contact line does not move during bubble growth, resulting in a constant contact line length.

the *vapour-vapour* interface between the bubble and the nucleation site. This boundary has a fixed area as the contact line does not move appreciably.

A specific subdivision of the control volume will be used for the resolution of the momentum equation. The different volumes, surfaces and lines involved are described in Fig. 5.22c.

5.2.1 Momentum equation

The momentum conservation law states that within a control volume, the variation of momentum is equal to the sum of the external forces applied to this control volume. It is necessary to emphasize the fact that the momentum variation is an integral value. It gives information about a change of mass of the control volume or a motion of its center of gravity, but does not indicate a change of shape as long as the center of gravity is held constant.

The formulation of the momentum equation strongly depends on the hypotheses chosen and on the forces taken into account. Indeed, a full resolution of the most general momentum equation would require an exact knowledge of the instantaneous velocity field, temperature field and local rate of heat transfer, which is not possible to know with certainty.

The force expressions are compiled from various publications among which are Zeng *et al.* [199], Kandlikar and Stumm [88], Duhar [55], Buyevich and Webbon [21], Chen *et al.* [33] and Ginet [67]. The integral form of the momentum equation considered is:

$$\frac{\mathrm{d}}{\mathrm{d}t}\iiint_V \rho_v \overrightarrow{u_v}\,\mathrm{d}V = \overrightarrow{F}_{LI} + \overrightarrow{F}_{buoy} + \overrightarrow{F}_{\sigma} + \overrightarrow{F}_{vs} + \overrightarrow{F}_{vf} \tag{5.11}$$

with $\overrightarrow{F}_{LI}$, $\overrightarrow{F}_{buoy}$, $\overrightarrow{F}_{\sigma}$, $\overrightarrow{F}_{vs}$ and $\overrightarrow{F}_{vf}$ respectively the resultant of the liquid inertia, the buoyancy, surface tension, viscous stress and viscous forces. All these forces are detailed in the subsequent subsections.

The hypotheses considered are detailed in each subsection and are summarized in section 5.2.2.

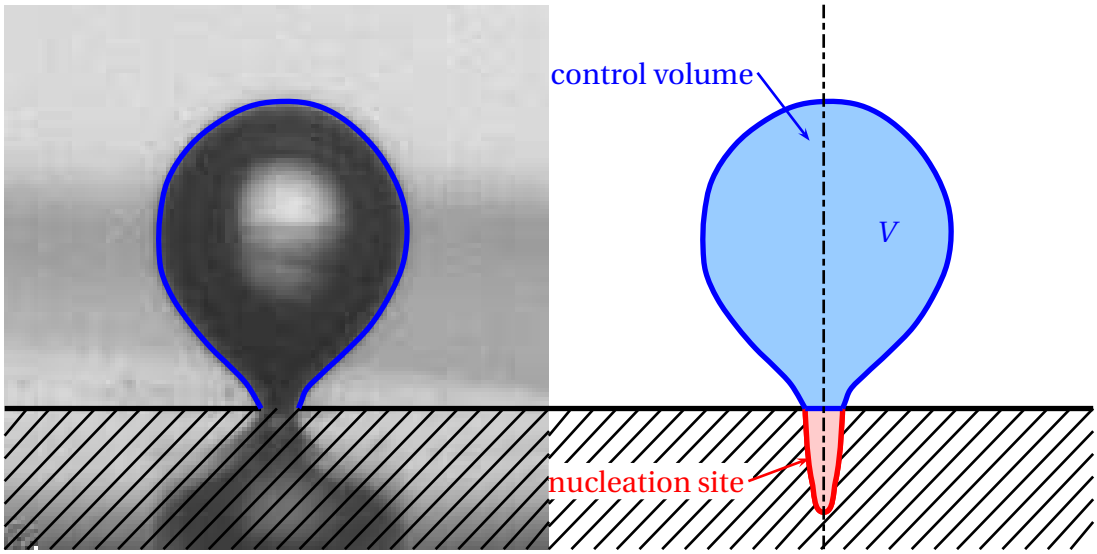

(a) Image with bubble contour

(b) Schematic of the control volume

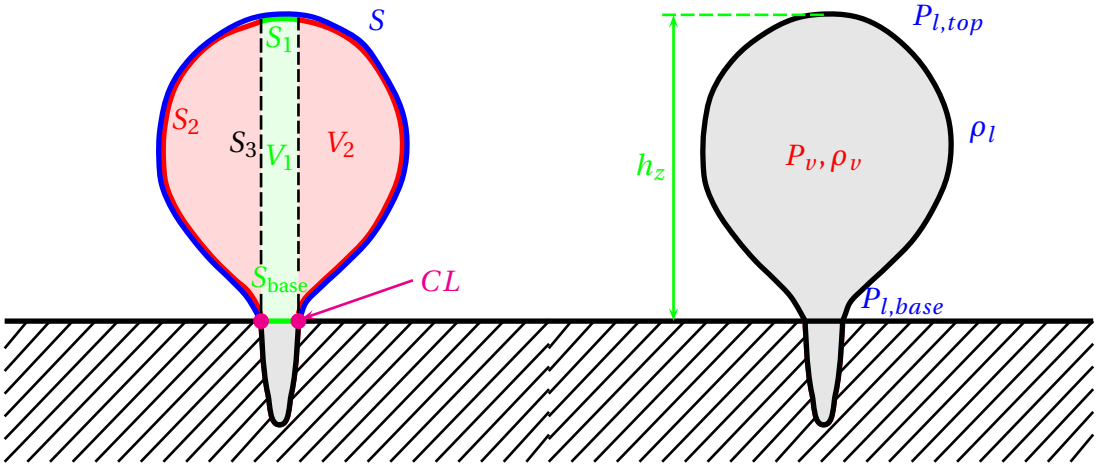

(c) Volumes, surfaces and lines involved

(d) Thermodynamic variables involved

Figure 5.22: Schematic of the control volume for the momentum balance

5.2.1.1 Momentum variation

The momentum derivative with time can be considered as the resultant of the dynamic forces[17]:

$$\overrightarrow{F}_{mom} = \frac{\mathrm{d}}{\mathrm{d}t} \iiint_V \rho_v \overrightarrow{u}_v \, \mathrm{d}V \tag{5.12}$$

The integration of the velocity vector is equal to the velocity of the center of gravity $\overrightarrow{u}_{cg}$.

$$\overrightarrow{F}_{mom} = \frac{\mathrm{d}}{\mathrm{d}t} \left(\rho_v \overrightarrow{u}_{cg} \times \iiint_V \mathrm{d}V \right) \tag{5.13}$$

$$= \frac{\mathrm{d}}{\mathrm{d}t} \left(\rho_v \overrightarrow{u}_{cg} \times V \right) \tag{5.14}$$

$$= \rho_v \overrightarrow{u}_{cg} \frac{\mathrm{d}V}{\mathrm{d}t} + \rho_v V \frac{\mathrm{d}\overrightarrow{u}_{cg}}{\mathrm{d}t} \tag{5.15}$$

Considering h_{cg} the height of the center of gravity[18], and $\overrightarrow{k}$ the unit vertical vector in the upward direction:

$$\overrightarrow{F}_{mom} = \rho_v \frac{\mathrm{d}h_{cg}}{\mathrm{d}t} \frac{\mathrm{d}V}{\mathrm{d}t} \overrightarrow{k} + \rho_v V \frac{\mathrm{d}^2 h_{cg}}{\mathrm{d}t^2} \overrightarrow{k} \tag{5.16}$$

As $h_{cg}(t)$ and $V(t)$ are measured from the recorded images, the resultant of the momentum derivative with time can be computed.

5.2.1.2 Liquid inertia and added mass force

The liquid inertia and added mass force is the liquid reaction to its acceleration caused by the motion of the interface. Its expression is similar to the momentum variation except for two differences:

- The density considered is now the liquid density.
- Each term is weighted by an coefficient usually refered to as *added mass coefficients*.

$$\overrightarrow{F}_{LI} = K_1 \rho_l \frac{\mathrm{d}h_{cg}}{\mathrm{d}t} \frac{\mathrm{d}V}{\mathrm{d}t} \overrightarrow{k} + K_2 \rho_l V \frac{\mathrm{d}^2 h_{cg}}{\mathrm{d}t^2} \overrightarrow{k} \tag{5.17}$$

The value of the added mass coefficients depends on the shape of the bubble and on its proximity to the wall. In the present case, the exact value of each coefficient varies with time and can not be easily estimated. The coefficients can however be bounded by extremum values obtained for simple case by numerical simulation. Duhar [55], citing Magnaudet *et al.* [121] indicates coefficients both equal to 0.5 for the case of a spherical bubble growing in an infinite liquid. For the case of a hemisherical bubble growing on a wall, Klausner *et al.*

[17] As the momentum variation is analogous to a force, it is chosen for the sake of a better readability to refer to it as $\overrightarrow{F}_{mom}$.

[18] The bubble being roughly axisymmetric, the velocity of the center of gravity $\overrightarrow{u}_{cg}$ only presents a vertical component. Consequently, only the height of the center of gravity is considered.

[96] and Legendre *et al.* [111] give $K_1 = 2$ and $K_2 = 4$. The actual coefficients for the present experimental bubble growth are considered to be within this range. More details about the determination of the coefficients can be found in Appendix C.

It can be noted that the difference between the momentum force and the liquid inertia force is of the order of the density ratio, ρ_l/ρ_v. This ratio is usually high, and is equal to 206 in the specific case of this study. The momentum force can thus be neglected in most cases. This inertia argument was also stated by Robinson and Judd [160].

5.2.1.3 Buoyancy

The buoyancy force can be considered as the resultant of the hydrostatic pressure forces on the bubble surface. This force is due to the vertical pressure gradient caused by gravity. The pressures involved are the hydrostatic liquid pressure on the outward surface S, the hydrostatic vapour pressure on the inward surface S (which is equal to the weight of the bubble) and the vapour pressure on both sides of the surface S_{base}. A hypothesis in the calculation of the buoyancy force is to consider a homogeneous vapour and liquid density[19]. The following hydrostatic law thus holds true with a constant liquid density ρ_l:

$$\overrightarrow{\text{grad}}\,(P_l) = \rho_l \overrightarrow{g} \tag{5.18}$$

5.2.1.3.1 Buoyancy of a totally immersed object

In order to provide adequate understanding of the bubble buoyancy and of the simplification hypotheses, the full demonstration of the Archimedes' principle is proposed.

Considering a bubble totally immersed in a stagnant, isothermal liquid; the formal expression of its buoyancy[20] is:

$$\overrightarrow{F}_{buoy} = \oiint_S P_v \, \overrightarrow{\mathrm{d}S} - \oiint_S P_l \, \overrightarrow{\mathrm{d}S} \tag{5.19}$$

$$\overrightarrow{F}_{buoy} = \overrightarrow{F}_{P,vap} + \overrightarrow{F}_{P,liq} \tag{5.20}$$

where $\overrightarrow{F}_{P,vap}$ and $\overrightarrow{F}_{P,liq}$ correspond respectively to the integral of the vapour and liquid pressure forces on the bubble interface. $\overrightarrow{\mathrm{d}S}$ is a infinitesimal element of the surface directed outwards normally to the interface. P_v and P_l are the local vapour and liquid pressures.

$\overrightarrow{F}_{P,liq}$ can be determined as a function of the bubble volume and liquid density as follows. For the sake of the mathematical demonstration, an arbitrary uniform vector field $\overrightarrow{u}$ is

[19] The local hydrostatic liquid pressure depends on the weight of the liquid above, which depends on the liquid density. This later varies with the local temperature. However, the temperature field in the liquid phase is not known.

[20] The buoyancy of a bubble is sometimes considered as only the resultant of the liquid pressure forces, and sometimes also includes the resultant of the vapour pressure forces. Here, the second approach is retained.

introduced.

$$\overrightarrow{F}_{P,liq}.\overrightarrow{u} = -\left(\oiint_S P_l \,\overrightarrow{\mathrm{d}S}\right)\cdot\overrightarrow{u} \tag{5.21}$$

$$= -\oiint_S P_l\,\overrightarrow{u}\cdot\overrightarrow{\mathrm{d}S} \tag{5.22}$$

using the Ostrogradsky's theorem, with V being the bubble's volume:

$$\overrightarrow{F}_{P,liq}\cdot\overrightarrow{u} = -\iiint_V \mathrm{div}\left(P_l\,\overrightarrow{u}\right)\,\mathrm{d}V \tag{5.23}$$

$$\mathrm{div}\left(P_l\,\overrightarrow{u}\right) = \overrightarrow{\mathrm{grad}}\,(P_l)\cdot\overrightarrow{u} + P_l \times \mathrm{div}\left(\overrightarrow{u}\right) \tag{5.24}$$

$\overrightarrow{u}$ being a uniform vector field, $\mathrm{div}\,\overrightarrow{u} = 0$.

$$\mathrm{div}\left(P_l\,\overrightarrow{u}\right) = \overrightarrow{\mathrm{grad}}\,(P_l)\cdot\overrightarrow{u} \tag{5.25}$$

$$\overrightarrow{F}_{P,liq}.\overrightarrow{u} = -\iiint_V \overrightarrow{\mathrm{grad}}\,(P_l)\cdot\overrightarrow{u}\,\mathrm{d}V \tag{5.26}$$

$$= -\left(\iiint_V \overrightarrow{\mathrm{grad}}\,(P_l)\,\mathrm{d}V\right)\cdot\overrightarrow{u} \tag{5.27}$$

$$\overrightarrow{F}_{P,liq} = -\iiint_V \overrightarrow{\mathrm{grad}}\,(P_l)\,\mathrm{d}V \tag{5.28}$$

Considering the hydrostatic pressure around the object:

$$\overrightarrow{\mathrm{grad}}\,(P_l) = \rho_l\,\overrightarrow{g} \tag{5.29}$$

$$\overrightarrow{F}_{P,liq} = -\iiint_V \rho_l\,\overrightarrow{g}\,\mathrm{d}V \tag{5.30}$$

Considering a homogeneous liquid density ρ_l:

$$\overrightarrow{F}_{P,liq} = -\rho_l\,\overrightarrow{g}\iiint_V \mathrm{d}V \tag{5.31}$$

Eventually, the famous Archimedes' principle is found:

> Any object, wholly or partially *immersed* in a fluid, is buoyed up by a force equal to the weight of the fluid displaced by the object.
>
> *Archimedes of Syracuse*, 212 B.C.

$$\overrightarrow{F}_{P,liq} = -\rho_l V\,\overrightarrow{g} \tag{5.32}$$

Similarly, the same reasoning can be applied for the vapour pressure forces on the interface:

$$\overrightarrow{F}_{P,vap} = \rho_v V\,\overrightarrow{g} \tag{5.33}$$

And finally, the buoyancy force for a wholly immersed bubble in a stagnant, isothermal fluid can be expressed as:

$$\overrightarrow{F}_{buoy} = -(\rho_l - \rho_v) V \overrightarrow{g} \tag{5.34}$$

The resultant of the buoyancy forces is thus a vertical force, opposite to the gravity acceleration[21]. Introducing the vertical upward unit vector $\overrightarrow{k} = -\overrightarrow{g}/g$:

$$\overrightarrow{F}_{buoy} = (\rho_l - \rho_v) V g \overrightarrow{k} \tag{5.35}$$

A bubble attached to a surface has a higher buoyancy than a bubble of equivalent volume entirely embedded in a liquid, due to the contact area with the surface. The pressure applied on the bubble on this area is stronger than the liquid pressure. This is commonly called contact pressure.

Two different approaches are found in the literature to take into account the presence of the contact area.

5.2.1.3.2 Contact area causing a contact pressure

The first approach is to consider the buoyancy that the bubble would have if it were totally immersed, to subtract from this force the lack of liquid pressure at the contact area and to add to this force the resultant of the vapour pressure[22] on the same area.

The buoyancy can thus be computed as follows:

$$\overrightarrow{F}_{buoy} = (\rho_l - \rho_v) V g \overrightarrow{k} - \iint_{S_{base}} P_v \, \overrightarrow{\mathrm{dS}} + \iint_{S_{base}} P_l \, \overrightarrow{\mathrm{dS}} \tag{5.36}$$

$$\tag{5.37}$$

using $\overrightarrow{\mathrm{d}S}$ as an infinitesimal element of the surface directed outwards of the bubble, normally to the interface, even for an open surface;

$$\overrightarrow{F}_{buoy} = (\rho_l - \rho_v) V g \overrightarrow{k} - \iint_{S_{base}} (P_v - P_l) \, \overrightarrow{\mathrm{dS}} \tag{5.38}$$

$$= (\rho_l - \rho_v) V g \overrightarrow{k} - \left(P_v - P_{l,base}\right) \iint_{S_{base}} \overrightarrow{\mathrm{dS}} \tag{5.39}$$

$$= (\rho_l - \rho_v) V g \overrightarrow{k} + \left(P_v - P_{l,base}\right) S_{base} \overrightarrow{k} \tag{5.40}$$

The main issue with this approach is the determination of $\left(P_v - P_{l,base}\right)$. By considering the same hypotheses as previously, $P_{l,base} = P_{l,top} + h\rho_l g$ and $P_{v,base} = P_{v,top} + h\rho_v g$. The pressure difference at the tip of the bubble can then be estimated using the Laplace-Young relation[23].

[21] The liquid density ρ_l is always much bigger than the vapour density ρ_v.

[22] or the wall reaction if the control volume was limited by the solid side of a *vapour-solid* interface

[23] However, as it can be observed in Section 5.2.3, it seems unaccurate to consider the Laplace-Young equilibrium and uniquely the hydrostatic pressure gradients near the base of the bubble.

5.2.1.3.3 Separation of the totally immersed and the contact volumes

A second approach with regard to the influence of the presence of the contact area is to divide the bubble into separate volumes and areas, as in Fig. 5.22c. The volume V_1 is axisymmetric, with S_1 being the projection of the circular base area V_{base} on the top of the bubble and S_3 being a vertical cylinder linking S_{base} and S_1. V_2 is the annular part of the bubble and is limited on the outside by the surface S_2. Let the infinitesimal surface element $\overrightarrow{dS}$ of the open surfaces be defined as follows:

- On the surface S_1 and S_2, $\overrightarrow{dS}$ is directed towards the liquid.
- On the surface S_{base}, $\overrightarrow{dS}$ is directed towards the heated wall.
- On the surface S_3, dS is directed towards the symmetry axis.

The buoyancy can be computed as follows:

$$\overrightarrow{F}_{buoy} = \iint_{S_2} (P_v - P_l)\ \overrightarrow{dS} + \iint_{S_{base}} (P_v - P_v)\ \overrightarrow{dS} + \iint_{S_1} (P_v - P_l)\ \overrightarrow{dS} \tag{5.41}$$

$$\overrightarrow{F}_{buoy} = \iint_{S_2} (P_v - P_l)\ \overrightarrow{dS} + \iint_{S_1} (P_v - P_l)\ \overrightarrow{dS} \tag{5.42}$$

Introducing artificially the liquid pressure that would be exerted on S_3 if V_2 was totally immersed:

$$\begin{aligned}\overrightarrow{F}_{buoy} &= \iint_{S_2} (P_v - Pl)\ \overrightarrow{dS} + \iint_{S_3} (P_v - P_l)\ \overrightarrow{dS} - \iint_{S_3} (P_v - P_l)\ \overrightarrow{dS} \qquad (5.43)\\ &\quad + \iint_{S_1} (P_v - P_l)\ \overrightarrow{dS}\\ &= (\rho_l - \rho_v) V_2 g\ \overrightarrow{k} - \iint_{S_3} (P_v - P_l)\ \overrightarrow{dS} + \iint_{S_1} (P_v - P_l)\ \overrightarrow{dS} \qquad (5.44)\end{aligned}$$

The resultant of the pressure on the surface S_3 is vertical as S_3 is axisymmetric. However, as the surface is totally vertical, the resultant of the pressure forces is equal to zero:

$$\iint_{S_3} (P_v - P_l)\ \overrightarrow{dS} = \overrightarrow{0} \tag{5.45}$$

$$\overrightarrow{F}_{buoy} = (\rho_l - \rho_v) V_2 g\ \overrightarrow{k} + \iint_{S_1} (P_v - P_l)\ \overrightarrow{dS} \tag{5.46}$$

Considering S_1 as a portion of sphere of radius equal to R[24], and introducing the Laplace-Young equation, one gets:

$$(P_v - P_l) = \frac{2\sigma}{R} \tag{5.47}$$

$$\begin{aligned}\overrightarrow{F}_{buoy} &= (\rho_l - \rho_v) V_2 g\ \overrightarrow{k} + \iint_{S_1} \frac{2\sigma}{R}\ \overrightarrow{dS} \qquad (5.48)\\ &= (\rho_l - \rho_v) V_2 g\ \overrightarrow{k} + \frac{2\sigma}{R} \iint_{S_1} \overrightarrow{dS} \qquad (5.49)\\ &= (\rho_l - \rho_v) V_2 g\ \overrightarrow{k} + \frac{2\sigma}{R} S_{base}\ \overrightarrow{k} \qquad (5.50)\end{aligned}$$

[24] which is realistic at the top of the bubble

It is also possible to introduce the total volume of the bubble. The relation will now be:

$$\overrightarrow{F}_{buoy} = (\rho_l - \rho_v) V g \overrightarrow{k} - (\rho_l - \rho_v) V_1 g \overrightarrow{k} + \frac{2\sigma}{R} S_{base} \overrightarrow{k} \tag{5.51}$$

This expression of the buoyancy will be further used for the resolution of the momentum equation. The three different terms of the buoyancy will be named as follows:

$$\overrightarrow{F}_{buoy,1} = (\rho_l - \rho_v) V g \overrightarrow{k} \tag{5.52}$$

$$\overrightarrow{F}_{buoy,2} = -(\rho_l - \rho_v) V_1 g \overrightarrow{k} \tag{5.53}$$

$$\overrightarrow{F}_{buoy,3} = \frac{2\sigma}{R} S_{base} \overrightarrow{k} \tag{5.54}$$

5.2.1.4 Surface tension and adhesion forces

5.2.1.4.1 Liquid-vapour surface tension

The surface tension represents the molecular interaction at the border of two separate phases. It can be seen either as an energy per unit area, or as a force per length [50, 23]. The surface tension force between two phases is a tangential stress which tends to stretch the interface in order to minimize the interface area.

First case of study In this paragraph, we will reason – as a case of study – on a bubble will an ellipsoid shape, totally immersed in a stagnant liquid, without gravity. Fig. 5.23 illustrates the actions of the surface tension forces acting on this bubble.

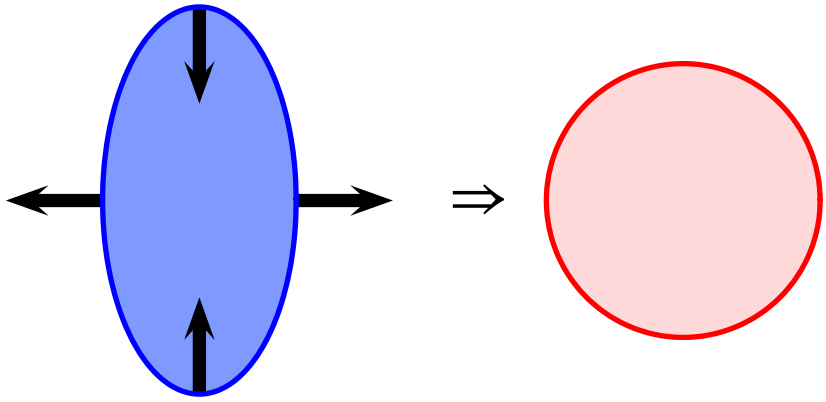

Figure 5.23: Surface tension actions on a totally immersed ellipsoid in absence of gravity

The surface tension forces tend to reduce the surface area [161] to transform the ellipsoid into a sphere. This phenomenon can be described from several points of view:

- Considering the surface tension as the surface derivative of the Helmoltz free energy at constant temperature, volume and number of moles [50],

$$\sigma = \left[\frac{\partial A}{\partial S}\right]_{T,V,n} \tag{5.55}$$

The excess of Helmholtz free energy provided by the excess of surface area of the ellipsoid compared to a sphere of equivalent volume can be considered as a potential energy. This potential energy will be transformed into motion of the interface (i.e. motion of the gas and liquid phases in and around the bubble) that will dissipate through viscosity as heat. This energy dissipation can be observed as a dampening of the bubble oscillation. The equilibrium shape when all the potential energy is dissipated is a sphere, as the interface surface cannot be reduced. This conception of the surface tension indicates the initial and final states, but does not describe the motion of the interface between the non-equilibrium and the equilibrium state. It is not sufficient to describe the forces induced by the interface, and therefore the way a given non-equilibrium state will converge towards an equilibrium one.

- A new interpretation of the local tension surface forces is now proposed. It should be noted first that the common Laplace-Young equation, formulated as:

$$P_v - P_l = \sigma C \tag{5.56}$$

with $C = \frac{1}{R_1} + \frac{1}{R_2}$ the local curvature of the interface, cannot be applied in such a case. This equation describes only a mechanical equilibrium condition, which is not the case for the case of study of interest in this section. Indeed, the hydrostatic pressure field is homogeneous in both the vapour and liquid phases as there is no gravity field nor velocity field, leading to a constant $P_v - P_l$ difference. However, the σC product is not homogeneous around the ellipsoid bubble.

The new interpretation proposed is as follows. The hypothesis that the vapour pressure is homogeneous is justified by the following reasoning: the density and viscosity of the vapour phase being very low compared to the liquid phase, the forces concerned in the motion of the vapour phase are negligible compared to the forces implied in the liquid motion. The vapour pressure homogeneity is therefore achieved much faster[25].

The non-equilibrium shape of the interface results in a force that can be described as an unbalance pressure gradient that *pumps* the liquid from the minor axis region, tangentially along the surface to the major axis region. Let us break up the liquid pressure into two different terms, namely the hydrostatic liquid pressure $P_{l,stat}$ and the unbalance liquid pressure $P_{l,unb}$:

$$P_l = P_{l,stat} + P_{l,unb} \tag{5.57}$$

Let us now consider the hydrostatic liquid pressure and the unbalance liquid pressure in the Laplace-Young equation, generalizing this expression to non-equilibrium conditions:

$$P_v - P_{l,stat} - P_{l,unb} = \sigma C \tag{5.58}$$

[25] Note that in the presence of gravity, the hydrostatic vapour pressure gradient is very little compared to the hydrostatic liquid pressure gradient due to the high ρ_l/ρ_v density ratio which corroborates this assumption.

If the bubble volume is kept constant, the vapour pressure P_v is also constant and considered as homogeneous. The hydrostatic liquid pressure $P_{l,stat}$ is also constant and homogeneous as there is no gravity. The local unbalance liquid pressure $P_{l,unb}$ can thus be directly expressed as a function of the local curvature:

$$P_{l,unb} = P_v - P_{l,stat} - \sigma C \tag{5.59}$$

The unbalance liquid pressure is thus higher in the region of the minor axis than in the region of the major axis. The unbalance pressure gradient is the source of a local volumetric force applied on the liquid particles at the vicinity of the interface causing the liquid (and thus the interface) acceleration, as described in Fig. 5.24. The acceleration of the liquid particles around the interface can be expressed (neglecting the viscous term[26]):

$$\rho_l \frac{\mathrm{D}\vec{u}}{\mathrm{D}t} = -\overrightarrow{\mathrm{grad}}\left(P_{l,unb}\right) \tag{5.60}$$

The static liquid pressure and the vapour pressure being taken as constant, the equation can be simplified into:

$$\rho_l \frac{\mathrm{D}\vec{u}}{\mathrm{D}t} = -\overrightarrow{\mathrm{grad}}\left(\sigma C\right) \tag{5.61}$$

This term is the common Eulerian formulation of the momentum term of the Navier-Stokes equations when neglecting the viscous and gravity effects. It can be found when studying the two-phase unsteady flow in a microgroove where gravity is neglected [179]. The (σC) product is commonly called the capillary pressure.

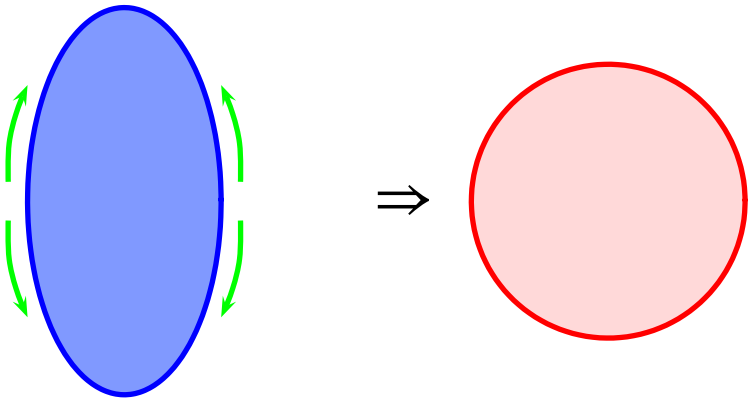

Figure 5.24: Unsteady pressure gradient causing liquid motion around the ellipsoid

It should be noted that the integral of the surface tension forces over the entire contour of the ellipsoid is equal to zero. Indeed, the integral form of the momentum variation is equal to zero as neither the mass nor the position of the center of gravity is changing. It should be kept in mind that a momentum balance inside a control volume does not describe a change of shape.

[26] which is realistic when the velocity is low and even true at initial time as the velocity is zero

Second case of study Let us now consider another non-equilibrium case as a second case of study. A spherical bubble is immersed inside a liquid within a gravity field. Once again, because it is a non-equilibrium case, the classical Laplace-Young equation cannot be applied. Indeed, the σC product is homogeneous around the spherical bubble, but the hydrostatic pressure difference $P_v - P_l$ is varying with the depth, as the vapour and liquid phases have significantly different densities.

Applying the generalized Laplace-Young equation 5.58, a constant vertical unbalance pressure gradient is found around the interface, decreasing from the apex to the bottom of the bubble. A volumetric force field is thus applied on the liquid particles around the bubble that tends to displace to liquid from the appex to the bottom. This is another description of the buoyancy described in section 5.2.1.3.

As a static bubble totally immersed in a stagnant liquid in a gravity field cannot be in equilibrium (it will always be buoyed up), it is impossible to create a surface respecting the Laplace-Young equation without unbalance pressure term (cf. Eq. 5.56) and respecting the constant vertical gradient of the hydrostatic pressure. The hydrostatic pressure between the vapour and the liquid being higher at the top of the bubble than at the bottom, the curvature C should be higher at the top as well. The connection between the top and the bottom of the bubble is then impossible if one wants to respect a vertical linear curvature profile (see Fig. 5.25a). The same dilemma is illustrated in Fig. 5.25b. Using pentane properties at 1 bar, the bubble contour is calculated from the base, with an arbitrary base curvature radius, respecting the bubble axisymmetry and the hydrostatic pressure profile. The upper side of the contour does not connect on the symmetry axis, revealing that the problem cannot be solved in these conditions. The profile found is in fact the profile of a sessile bubble in contact with a upward surface [113]. It can be noted that the critical base radius at which the bubble would move away from a spherical shape corresponds to the capillary length (that is: 1.56 mm for pentane at 1 bar).

Third case of study Let us now consider as the third case of study a bubble attached to a surface. Some more difficulties are added to the description of the surface tension forces. Two different kinds of forces are linked to the surface tension. A tangential force at the *liquid-vapour* interface, and another force at the triple line which is also related to the adhesion force between the solid and liquid phases (detailed in paragraph 5.2.1.4.2). The first force is the one described earlier in this section and is typically a force that tend to reduce the interface area. Figure 5.26 describes the surface tension forces that tends to transform an ellipsoid attached on a wall into a spheroid. These forces are very seldom taken into account in the literature about forces analysis on a bubble as one of the major hypothesis which is usually made is that the bubble shape is approximated as a truncated sphere (e.g. [21, 30, 109, 110]). Yet, this assumption cannot be assessed in most cases, as it is observed in the present study and noted by several authors ([31, 181, 141] to cite a few). The illustration from Fig. 5.26 shows that (without considering the gravity forces) an oblate bubble tends to transform into a sphere keeping the same center of gravity, and this force can lead towards a

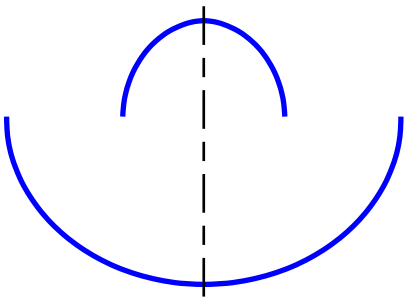

(a) Higher curvature at the top than at the bottom - impossible connexion

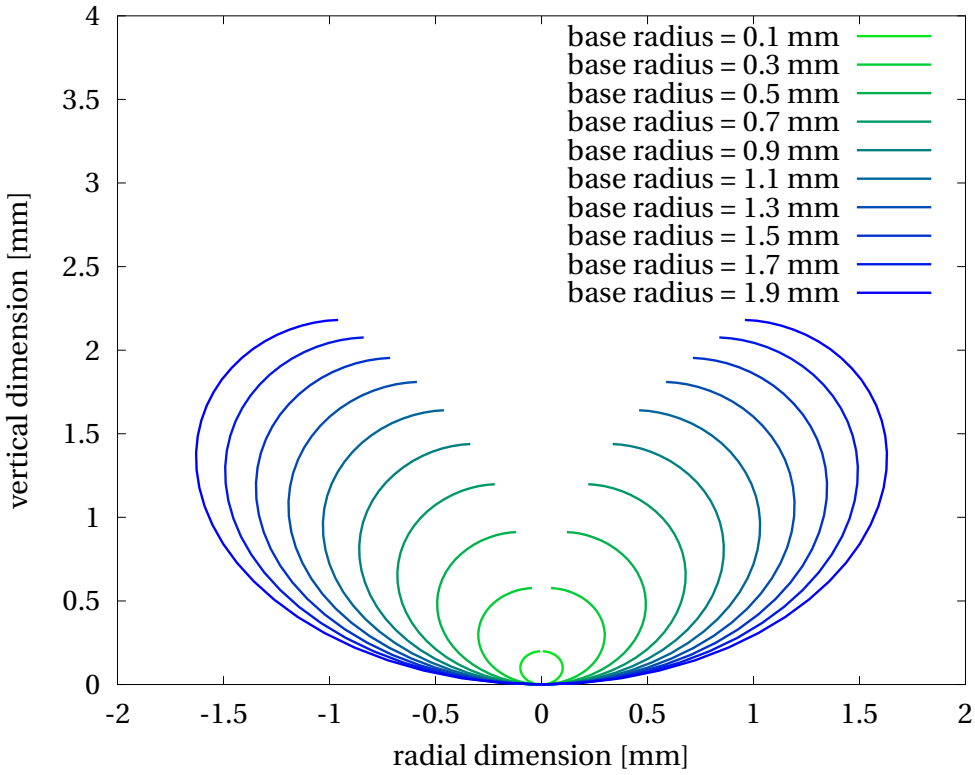

(b) Contour curvature evolution for pentane at 1 bar considering no dynamic pressure and starting from the base of the bubble with various arbitrary curvature radii

Figure 5.25: Impossible equilibrium of the bubble with a stagnant liquid in a gravity field

motion of the triple line[27] or even to its detachment from the heated surface.

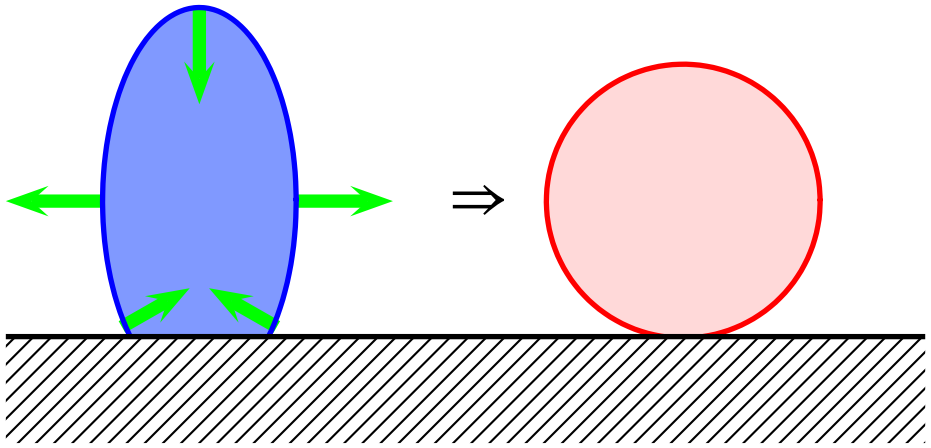

Figure 5.26: Surface tension forces acting on an ellipsoid attached on a surface

Figure 5.27 shows an example of the *liquid-vapour* surface tension forces effect on the shape of a bubble attached by a foot to the heated wall[28]. The surface area tends to minimize, i.e. a dynamic pressure gradient will press the liquid towards the neck, provoking its breakage.

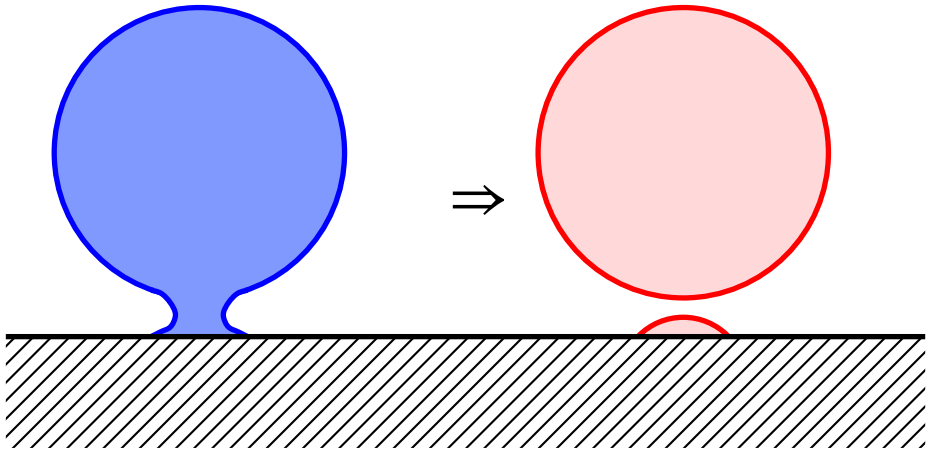

Figure 5.27: Surface tension forces acting on a bubble with a foot

To conclude about the effects of the *liquid-vapour* surface pressure forces, its resultant[29] is strongly related to the buoyancy and has to be taken into account in the calculation of the contact pressure (see paragraphs 5.2.1.3.2 and 5.2.1.3.3). The effect on the shape of the bubble, that cannot be estimated using the integral form of the tension surface forces, should not be neglected and can be the cause of bubble detachment. The local unbalance pres-

[27] either reducing or increasing the contact area depending on the direction of the bubble elongation, as noted by Chen and Groll [31]

[28] This example is somehow representative of the experimental observation of a bubble near departure presented in Fig. 5.22a.

[29] i.e. the integral over the entire contour

sure around the bubble will be investigated in section 5.2.3 and a very good overview of the subject can be found in Chen et Groll [31].

5.2.1.4.2 Triple line surface tension and adhesion forces

The effects of the forces involved at the contact area between 3 different phases are very complex. The geometry and forces of the triple line are governed by both the surface tension between the liquid and vapour phases and the wettability of the liquid over the solid surface. The wettability, usually characterized by a contact angle θ (see Section 5.1.1.2), results from the competition of molecular and capillary forces ([50], p. 24). The resultant of the triple line forces, commonly named simply the "surface tension force", is expressed as follows:

$$F_\sigma . \vec{k} = \int_{CL} \sigma \vec{t} \, \mathrm{d}l \tag{5.62}$$

with $\vec{t}$ the unit vector tangential to the interface in the meridian plane and at the contact line.

If the bubble or at least the base of the bubble is axisymmetric, this term can be expressed as follows [32, 50, 67]:

$$F_\sigma = -2\pi R_{base} \sigma \sin\alpha \tag{5.63}$$

with $2\pi R_{base}$ the perimeter of the triple line of radius R_{base}, and α the angle between the interface at the triple line and the horizontal plane. This angle is defined in the liquid phase.

As most models describe bubble growth on a plane surface, α is generally simply taken as the contact angle θ. However, in the case of this study, these angles may be very different. As an illustration, Fig. 5.28 shows schematically two different positions of the triple line, both located on the rim of the nucleation site. A large variation on the contact angle θ for a small displacement of the triple line. Yet, the angle α is the same in both cases and is equal to θ_2.

In order to calculate the adhesion force, the value of the contact angle α is measured from the processing of the images. More details on the processing of the images to determine α is given in Section 5.2.2.2.1.

5.2.1.5 Viscous stress due to surface tension gradient

The surface tension is a *liquid-vapour* property of the fluid used that describes the force equilibrium at the interface. This property varies with several parameters:

- Surface tension gradients may be due to chemical or concentration gradients at the interface. This is the case when boiling mixtures [26, 65, 180] or when using surfactants [80, 193]. None of these cases are involved in this experimental study as a particular care has been given to employ a perfectly pure pentane in the experiments (see Section 3.2).

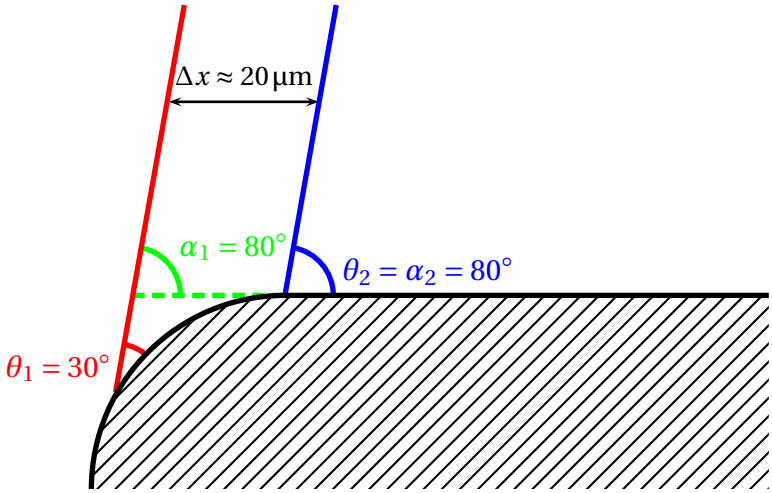

Figure 5.28: Evolution of the contact angle θ and of the angle α for a small change in the triple line location close to the nucleation site edge.

- Surface tension gradients may also be caused by temperature gradients. Surface tension is indeed varying with temperature, which is never homogeneous in a heat transfer process. The surface tension is generally decreasing with temperature. This is the case for pentane. In saturated condition at $P = 1$ bar, $\frac{d\sigma}{dT} \approx -9.98 \times 10^{-5}\,N{\cdot}m^{-1}{\cdot}K^{-1}$.

Similarly to curvature gradients (see Section 5.2.1.4), surface tension gradients can be the driving force for fluid motion. This phenomenon is often referred to as the Marangoni effect, or as the thermocapillary effect when the surface tension gradient is due to a temperature gradient. For the case of an air bubble attached upwardly on a heated surface, the Marangoni flow is represented schematically in Fig. 5.29.

The Marangoni number is a dimensionless number used in order to characterize the relative effects of surface tension and viscous forces. Several expressions of the Marangoni number are found in the literature. For the case of a bubble, the Marangoni number Ma can be defined as follows [153]:

$$\mathrm{Ma} = \frac{d\sigma}{dT}\frac{dT}{dz}\frac{R_{eq}^2}{\mu_l \alpha_l} \tag{5.64}$$

with z the vertical dimension chosen in the direction so that $\mathrm{Ma} > 0$.

Marangoni flows affect the momentum balance by causing a shear viscous stress at the interface. The liquid viscosity being much larger than that of vapour, the viscous stress is mostly applied on the liquid side of the interface. Calculating the shear stress is difficult mainly because the temperature gradient needs to be known on the interface. The temperature gradient within the liquid phase is already unknown in the presence of the bubble, and the temperature on the interface is even harder to determine because of the occurrence of phase change at the interface.

Thermocapillary effects are usually taken as negligible for low wall superheat conditions and presence of gravity [77]. Marangoni flows are known to play a prominent role in the

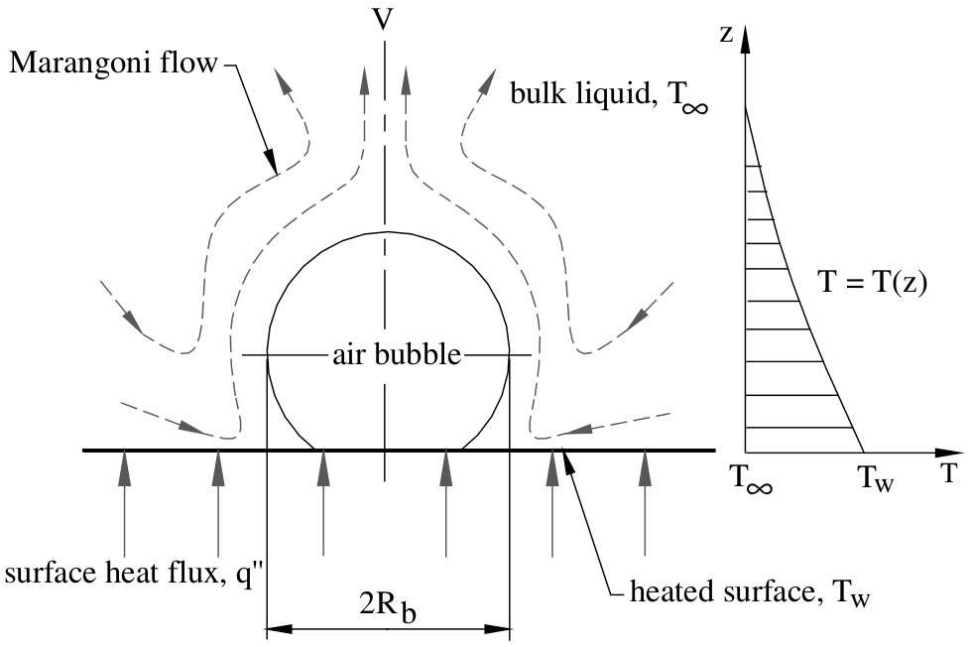

Figure 5.29: Marangoni flow around an air bubble – Figure extracted from Petrovic *et al.* [153].

following conditions:

- In micro-gravity conditions [77, 81, 112, 143, 186]. Buoyancy forces become negligible in micro-gravity, thermocapillary effects can be the main cause of fluid motion.
- In the case of downward facing bubbles [105, 159]. Indeed, no natural convection occurs bellow a downward facing heated plate. Thermocapillary effects are thus prominent.
- In the case of highly subcooled boiling [14, 36, 153]. Temperature gradients can indeed be very high in such cases.
- In the presence of surfactant or when boiling fluid mixtures.

The forces due to the viscous stress induced by thermocapillary effects will thus be neglected in the present momentum balance analysis.

5.2.1.6 Viscous forces

Viscous forces are applied on the bubble due to its motion or due to the surrounding liquid motion. These forces can be detailed as follows:

- A shear lift force is applied on the bubble due to the convective motion of the surrounding liquid. The superheated liquid is naturally rising and forming a plume at the center of the heated plate (see Chapter 4). The viscous liquid flow shears the bubble and the resultant viscous force applied on the bubble is in the flow direction. This

force is similar to that of a convective flow [56, 99, 129], except that convective flows are usually tangential to the heated wall. However, the liquid velocities implied in natural convection are at least an order of magnitude below the flow velocities of a shear flow[30]. This shear flow forces can thus be neglected.

- Viscous forces are caused by the motion of the bubble itself. The *liquid-vapour* interface is moving due to bubble translation and expansion. Similar to the shear lift force due to convective liquid motion, the velocities are very low. In accordance with the literature studies on forces applied on a growing bubble [21, 33, 55, 67, 88, 199], this force will be neglected during bubble growth.
- A rising bubble is drawing liquid in its wake. This flow field can impact the next growing bubble if the latter is close enough. The resultant of this force would be a vertical lift force that tends to detach the new bubble from the wall. Zeng *et al.* [199] have established an approximate expression of this force. For a spherical bubble of radius R rising over a hemispherical bubble of identical radius R at a velocity of U, L being the distance between the center of each bubble, the resultant of the lift force applied on the hemi-spherical bubble is:

$$F_{lift} = \frac{75}{16}\rho_l U^2 R^2 \left(\frac{R}{L}\right)^8 \tag{5.65}$$

It is noticeable that the force is proportional to L^{-8}. This indicates that the force is non negligible only when both bubbles are very close to each other. This was observed in this study for moderate to high wall superheats when the new growing bubble almost *reached* the preceding bubble at the beginning of its growth (see Section 5.1.5). This phenomenon being a particular case encountered, this force will not be taken into account in the present momentum balance.

5.2.2 Computation of the momentum balance

5.2.2.1 Forces considered in the momentum balance

Recall from the detailed force analysis of Section 5.2.1 that the following momentum equation will be considered and solved in the case of the present experiments:

$$\frac{\mathrm{d}}{\mathrm{d}t}\iiint_V \rho_v \overrightarrow{u_v}\,\mathrm{d}V = \overrightarrow{F}_{LI} + \overrightarrow{F}_{buoy,1} + \overrightarrow{F}_{buoy,2} + \overrightarrow{F}_{buoy,3} + \overrightarrow{F}_{\sigma} + \overrightarrow{\varepsilon}_{res} \tag{5.66}$$

The exact formulation of the momentum variation[31] is written as follows:

$$\overrightarrow{F}_{mom} = \rho_v \frac{\mathrm{d}h_{cg}}{\mathrm{d}t}\frac{\mathrm{d}V}{\mathrm{d}t}\overrightarrow{k} + \rho_v V \frac{\mathrm{d}^2 h_{cg}}{\mathrm{d}t^2}\overrightarrow{k} \tag{5.67}$$

[30] As depicted in Section 4.1.4, velocities implied in the plume are of the order of 5 to 10 mm·s^{-1}.

[31] The momentum variation is analogous to a force. For a better readability, is was consequently chosen to refer to it as $\overrightarrow{F}_{mom}$.

with $\overrightarrow{k}$ the upward vertical unit vector. The height of the center of gravity of the bubble h_{cg} is measured from the recorded images, and the velocity and acceleration of the center of gravity are obtained by calculating the first and second derivatives of a regression fit of the height of the center of gravity. Details about the momentum variation computation can be found in Section 5.2.2.2.2.

The liquid inertia and added mass force formulation is very similar to the momentum variation formulation:

$$\overrightarrow{F}_{LI} = K_1 \rho_l \frac{\mathrm{d}h_{cg}}{\mathrm{d}t} \frac{\mathrm{d}V}{\mathrm{d}t} \overrightarrow{k} + K_2 \rho_l V \frac{\mathrm{d}^2 h_{cg}}{\mathrm{d}t^2} \overrightarrow{k} \tag{5.68}$$

Details on the liquid inertia calculation can be found in Section 5.2.2.2.2.

The buoyancy has been divided into three different terms. The first term is considering the buoyancy of the bubble as if it was totally immersed in the liquid:

$$\overrightarrow{F}_{buoy,1} = (\rho_l - \rho_v) V g \overrightarrow{k} \tag{5.69}$$

The second term corrects the buoyancy by subtracting the volume located above the bubble contact area with the heated wall:

$$\overrightarrow{F}_{buoy,2} = -(\rho_l - \rho_v) V_1 g \overrightarrow{k} \tag{5.70}$$

The last term of buoyancy takes into account the pressure difference on the interface portion located vertically above the contact area:

$$\overrightarrow{F}_{buoy,3} = \frac{2\sigma}{R} S_1 \overrightarrow{k} \tag{5.71}$$

R being the curvature radius at the tip of the bubble. R is calculated from the tip curvature obtained in the bubble contour analysis (see Section 5.2.3.3). The tip of the bubble being located on the symmetry axis, both main radii of curvature are equal. More details about the calculation of the buoyancy terms can found in Section 5.2.2.2.3.

The resultant of the triple line surface tension and adhesion forces is expressed as follows:

$$\overrightarrow{F}_{\sigma} = -2\pi R_{base} \sigma \sin\alpha \overrightarrow{k} \tag{5.72}$$

with α being the angle between the interface at the triple line and the horizontal plane in the liquid phase and R_{base} the radius of the nucleation site. More details on the determination of α and on the computation of F_σ can be found in Section 5.2.2.2.1.

The last term, $\overrightarrow{\varepsilon}_{res}$, represent the residual error that can be due to measurement uncertainty, to approximations in the calculation and to non-negligible forces that were not taken into account in this momentum balance.

For the sake of readability, only the norm of the forces will be computed. As the problem considered presents an axial symmetry, the norm will be expressed in the vertical direction and upwards:

$$F = \overrightarrow{F} \cdot \overrightarrow{k} \tag{5.73}$$

The forces considered are in fact the resultant of pressures or of linear forces integrated over a surface or a contour. In the following section, the *resultant* will refer either to the integrated vectorial force considered or to its norm.

5.2.2.2 Measurement and computation of the forces

5.2.2.2.1 Computation of the angle α and of the resultant of the adhesion forces

The angle α is the angle between the interface at the triple line and the horizontal plane. This angle is defined in the liquid phase. The value is obtained using the image processing method described in Section 5.2.3.

The smoothed interface of a sample bubble at a wall superheat of 2.1 K and at $t^* = 0.5$ is shown in Fig. 5.30. For a better understanding, the contour is rotated and the vertical axis origin is set at the wall in Fig. 5.31. The angle α is defined at the base of the bubble, between the wall and the interface of the bubble, as depicted in Fig. 5.31. α is calculated from the two data points of the smoothed interface that are located the closest to the wall[32].

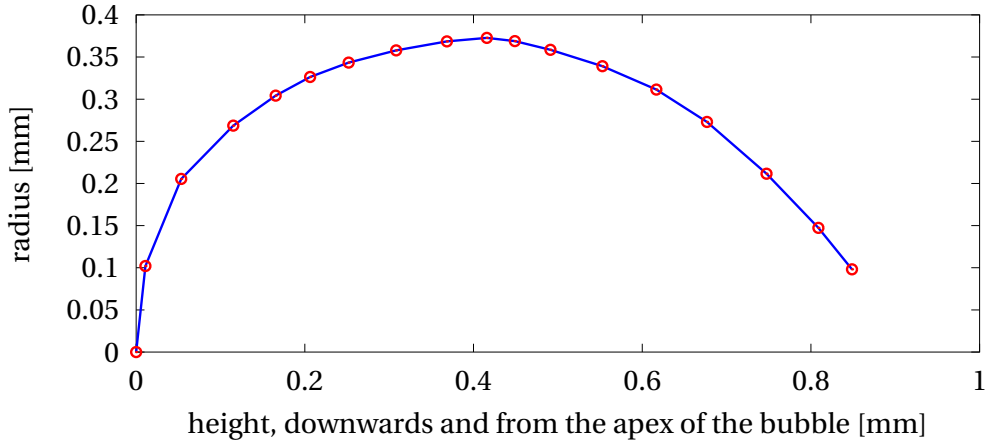

Figure 5.30: Smoothed interface of a bubble at a wall superheat of 2.1 K and at $t^* = 0.5$.

[32] Because the interface has been smoothed, very similar results are found when using a linear interpolation and a second order polynomial interpolation.

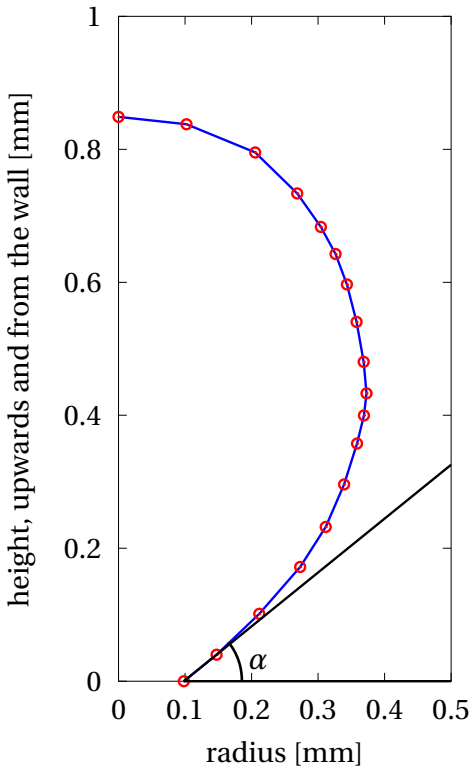

Figure 5.31: Definition of α on the contour.

The angle α is measured at different time-steps during bubble growth, as shown in Fig. 5.32. It should be noticed that for $t^* < 0.05$, it is not possible to correctly capture the bubble contour due to the small size of the bubble. The angle α is thus not measured at the beginning of the growth.

The measured angles obtained are then fitted with an appropriate[33] polynomial function (see Fig. 5.32). This function is used to compute the adhesion force acting on the bubble during its growth. As a recall from Section 5.2.1.4.2, this force is expressed as follows:

$$F_\sigma = -2\pi R_{base}\sigma \sin\alpha \tag{5.74}$$

The base diameter and the surface tension being taken as constant with $R_{base} = 90\,\mu m$ and $\sigma = 0.014\,506\,N{\cdot}m^{-1}$, the resultant of the adhesion forces is calculated and plotted in Fig. 5.33.

As an illustration of the sensitivity of this force to the measurement of α, Fig. 5.34 shows its evolution using the measured value of α and a *fictive* underestimation of α decreased by 10 degrees. Such a difference in the angle results in an offset in the force calculation by about $1\,\mu N$.

A error of a 10° in the determination of α is possible for two reasons:

[33] See Appendix D for details about polynomial fitting of the evolution of α.

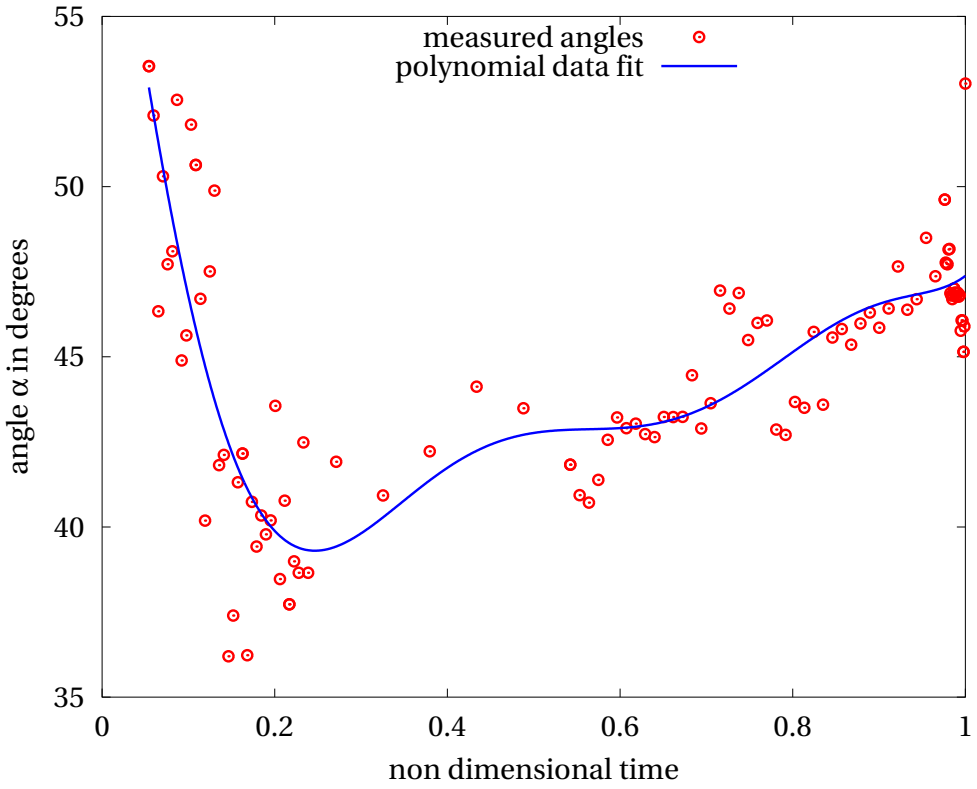

Figure 5.32: Angle α during bubble growth at a wall superheat of 2.1 K.

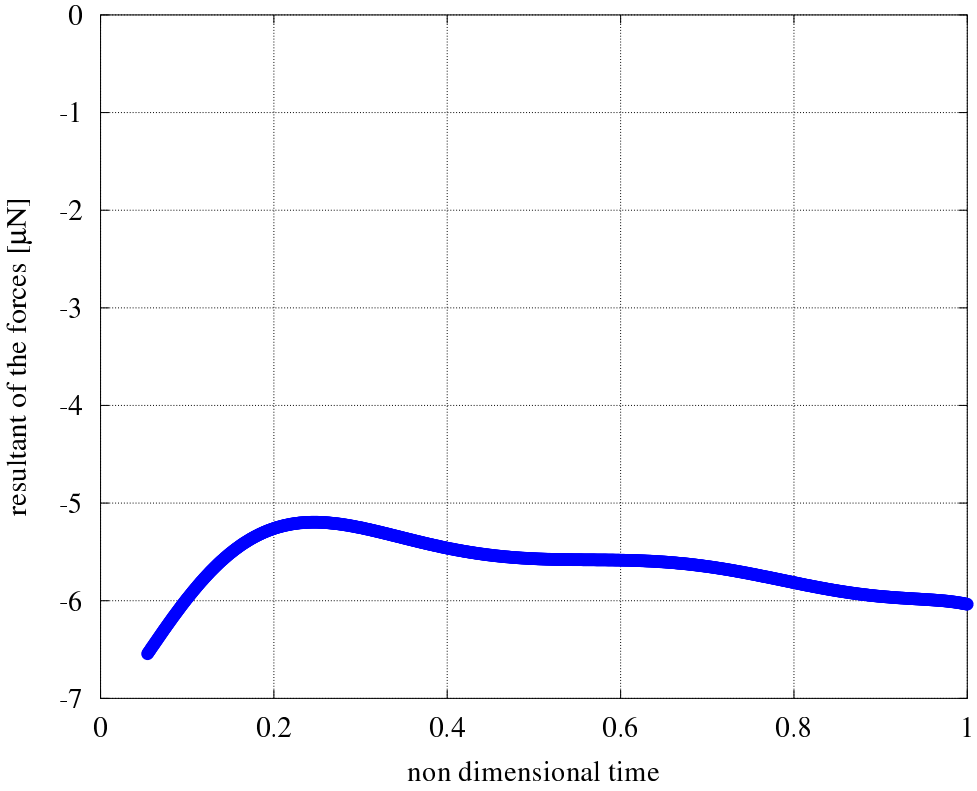

Figure 5.33: Resultant of the adhesion forces acting on a bubble at a wall superheat of 2.1 K.

- As detailed in Section 3.2.2, the recorded angle was slighly modified to allow a 3° angle with the horizontal plane, in order to avoid mirage effects.
- With the strong temperature gradients caused by the heated surface and by phase change at the triple line, the location where α is measured is the zone of the recorded images which can be the most distorted by mirage effects [42]. If the occurrence of mirage effect were not totally avoided in the present experiments, they would result in an over-prediction of the angle α.

As a conclusion for the computation of the surface tension and adhesion forces, the calculated resultant of the forces is very sensitive to the measurement of the angle α, and its absolute value might be over-predicted.

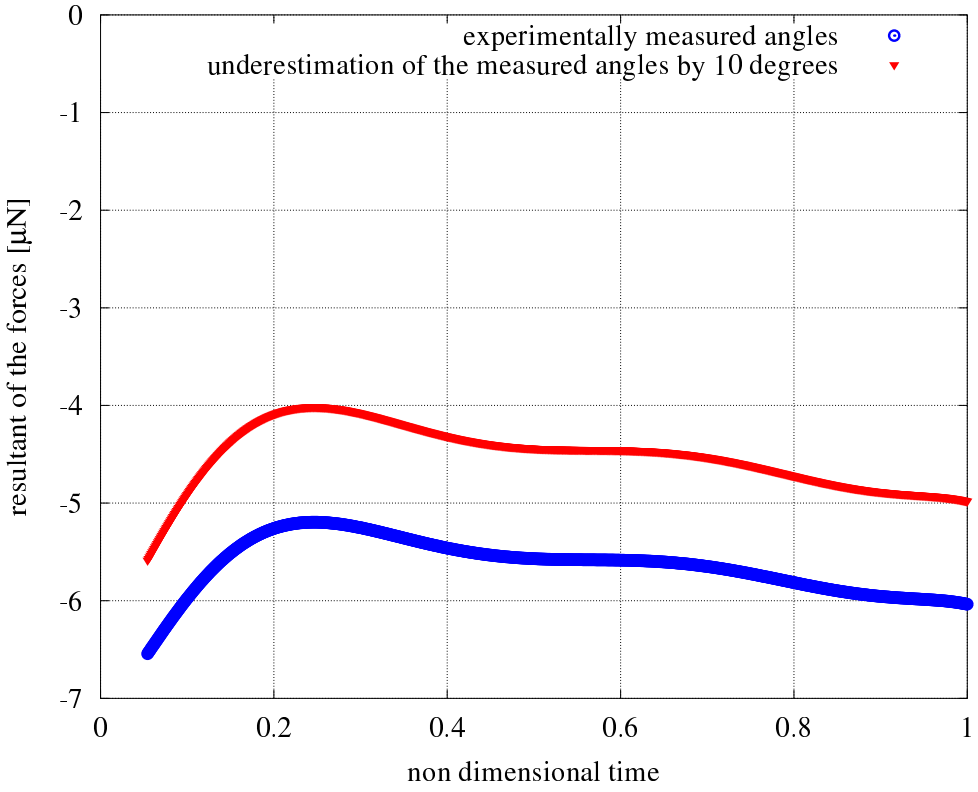

Figure 5.34: Resultant of the adhesion forces acting on a bubble, using the measured angle α and an underestimation of the angle by 10 degrees.

5.2.2.2.2 Computation of the momentum variation and of the resultant of the liquid inertia forces

Momentum variation For the computation of the momentum balance in Section 5.2.1, the exact formulation of the momentum variation is expressed as follows (see Section 5.2.1.1):

$$\vec{F}_{mom} = \rho_v \frac{dh_{cg}}{dt} \frac{dV}{dt} \vec{k} + \rho_v V \frac{d^2 h_{cg}}{dt^2} \vec{k} \tag{5.75}$$

with $\vec{k}$ the unit vertical vector in the upward direction and h_{cg} the height of the center of gravity.

The height of the center of gravity is measured through the processing of the recorded images (see Section 3.3.2) and shown in Fig. B. The measured height is fitted with an appropriate[34] polynomial function. Its first and second derivative are the computed, and are shown in Fig. 5.36 and 5.37.

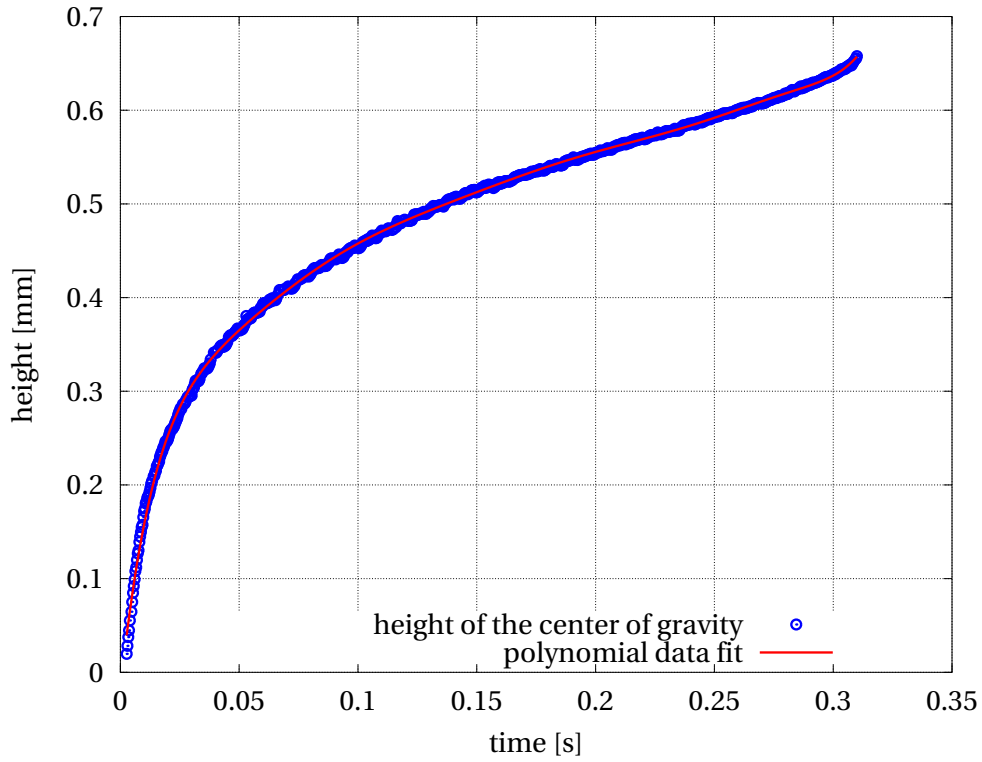

Figure 5.35: Height of the center of gravity of a bubble at a wall superheat of 2.1 K.

From the same manner, the volumetric growth is fitted with an appropriate polynomial function (see Fig. 5.38). This first time derivative of the function approximates the volumetric growth rate (see Fig. 5.39).

The momentum variation is calculated using the thermodynamic properties of pentane, the first and second time derivative of the height of the center of gravity, the volume of the bubble and its first time derivative. The momentum variation obtained is shown in Fig. 5.40. It is computed only for $t^* > 0.05$ as the uncertainty is very high at the beginning and other forces cannot be computed for $t^* < 0.05$.

It can be noticed on Fig. 5.40 that the momentum variation is lower than 0.4 nN. This value is negligible compared to other forces, and this was already expected by comparison to the liquid inertia force in Section 5.2.1.2.

[34] Appendix E presents an analysis of the time derivation of the height of the center of gravity of the bubble and of its volume. The impact of the fitting function on the force computation is estimated.

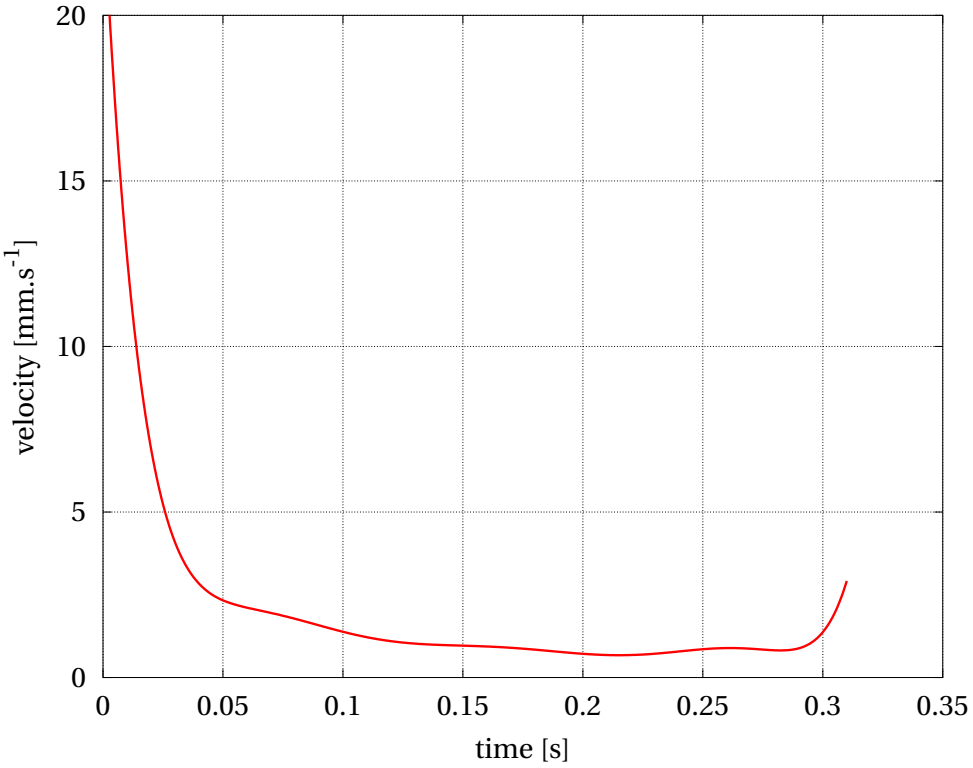

Figure 5.36: Time first derivative of the height of the center of gravity of a bubble at a wall superheat of 2.1 K.

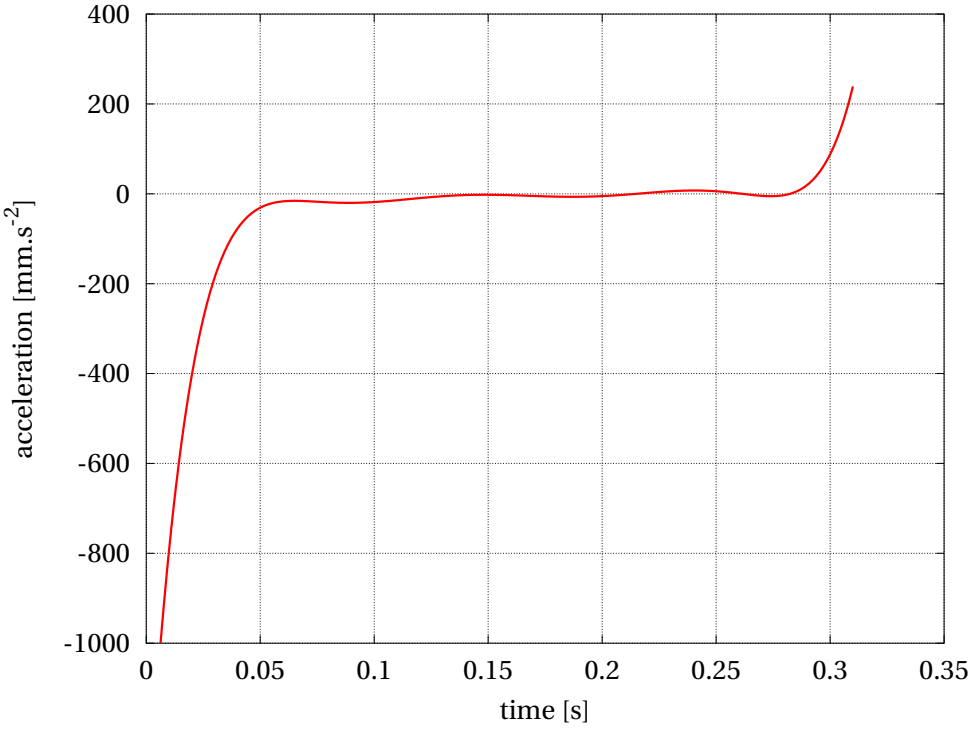

Figure 5.37: Time second derivative of the height of the center of gravity of a bubble at a wall superheat of 2.1 K.

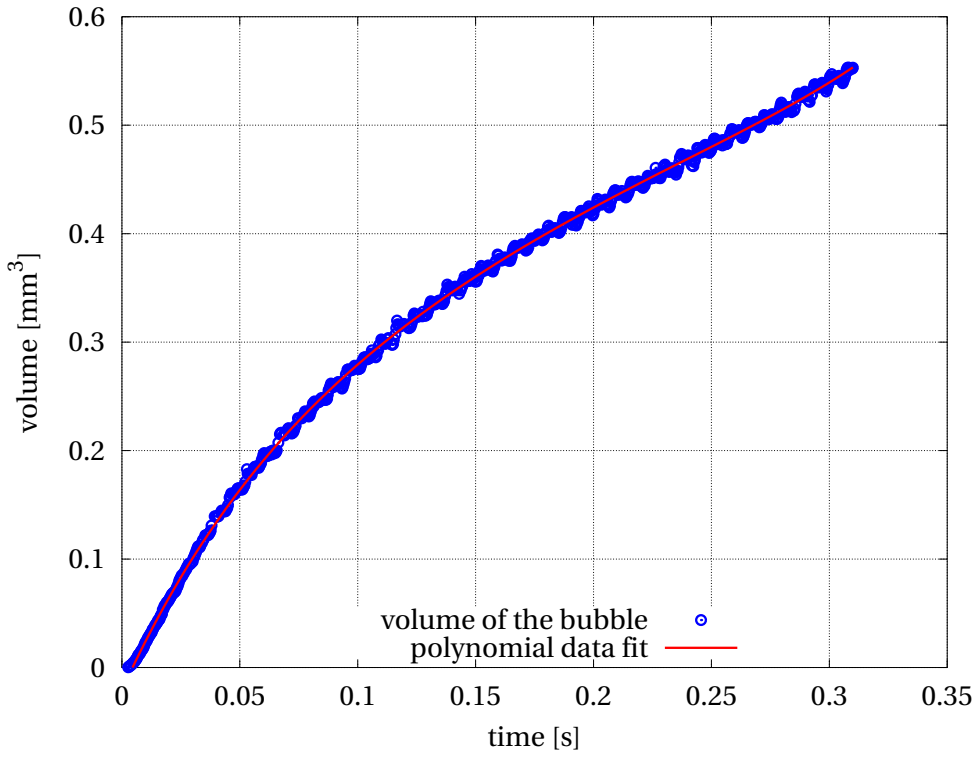

Figure 5.38: Volume of a bubble at a wall superheat of 2.1 K.

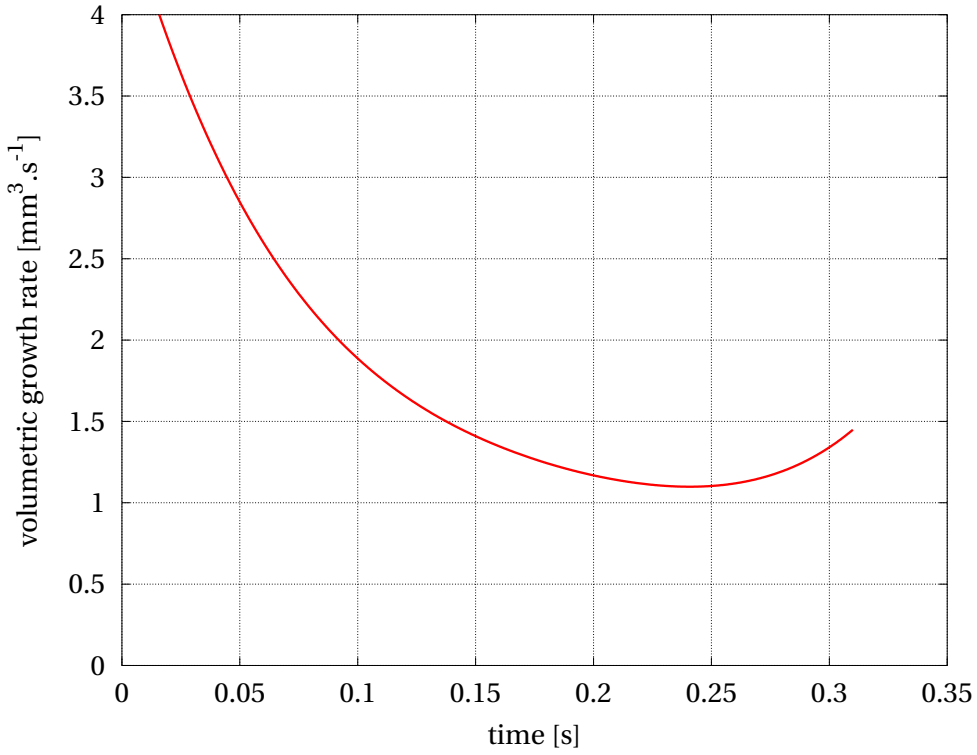

Figure 5.39: Volumetric growth rate of a bubble at a wall superheat of 2.1 K.

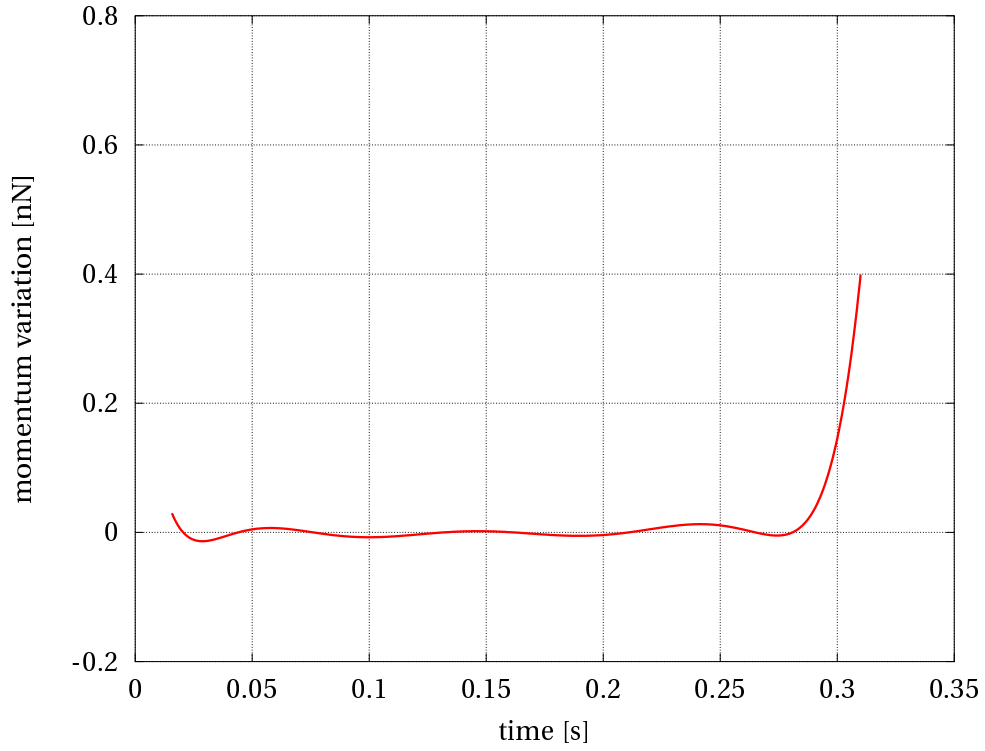

Figure 5.40: Momentum variation of a growing bubble at a wall superheat of 2.1 K.

It should also be noticed that the determination of the first and second derivative of measured data causes high uncertainty. This uncertainty does not impact the momentum balance as the momentum variation is negligible.

Liquid inertia forces The liquid inertia force is the resultant of the forces induced by the displacement of liquid due to the bubble motion and growth. Similarly to the momentum variation, the resultant of the liquid inertia forces can be expressed as a function of the thermodynamic properties of pentane, the first and second time derivative of the height of the center of gravity, the volume of the bubble and its first time derivative and two added mass coefficients (see Section 5.2.1.2 and Appendix E):

$$\overrightarrow{F}_{LI} = K_1 \rho_l \frac{\mathrm{d}h_{cg}}{\mathrm{d}t} \frac{\mathrm{d}V}{\mathrm{d}t} \overrightarrow{k} + K_2 \rho_l V \frac{\mathrm{d}^2 h_{cg}}{\mathrm{d}t^2} \overrightarrow{k} \tag{5.76}$$

The value of the added mass coefficients is not known but considered as bounded by $K_1 = K_2 = 0.5$ and $K_1 = 2$ and $K_2 = 4$ (see Section 5.2.1.2 and Appendix C).

Using the results of Section 5.2.2.2.2, the resultant of the liquid inertia forces is computed and plotted in Fig. 5.41 using the two previously mentionned sets of added mass coefficients. Its value is always below 0.4 µN. This is an order of magnitude below other forces as the buoyancy force and the adhesion forces (see Section 5.2.2)[35]. This was expected as the bubble

[35]The early stage of bubble growth is usually considered to be inertially controlled. As detailed in Section

shape and volume at departure was similar for any wall superheat whereas the growth rate was varying.

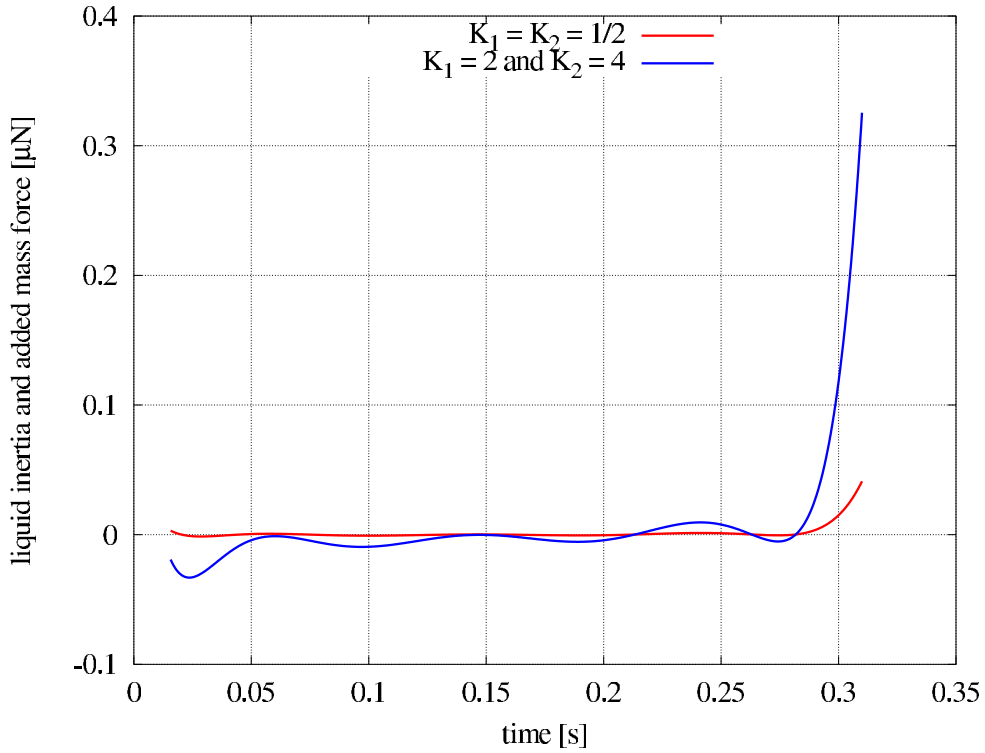

Figure 5.41: Resultant of the liquid inertia forces acting on a growing bubble at a wall superheat of 2.1 K, using two different sets of added mass coefficients.

5.1.1.5, the inertia controlled stage is very short at the scale of the growth time. As the forces are not computed during the first 5 % of the growth, this stage is not observed in the results.

5.2.2.2.3 Computation of the buoyancy forces

First and second buoyancy term As a recall from Section 5.2.1.3, the two first buoyancy terms considered are expressed as follows:

$$\overrightarrow{F}_{buoy,1} = (\rho_l - \rho_v) V g \overrightarrow{k} \tag{5.77}$$

$$\overrightarrow{F}_{buoy,2} = -(\rho_l - \rho_v) V_1 g \overrightarrow{k} \tag{5.78}$$

with V the total volume of the bubble and V_1 the vapour volume located above the nucleation site, as described in Fig. 5.22c. The first term of buoyancy represents the buoyancy of the bubble as if it was totally immersed in the liquid, and the second term is correcting the volume in order to take into account only the vapour volume which is surrounded by liquid as well from above as from below. The third buoyancy term, detailed in the next section, is accounting for the pressure difference through the interface located above the nucleation site.

The volume V and V_1 are obtained by processing the recorded images, as detailed in Section 3.3.2. If expressed in terms of non-dimensional time, the evolutions of the volumes are very similar for different wall superheat conditions, as the non-dimensional growth curve is identical and the departure volume is constant. These evolutions are shown for a bubble at a wall superheat of 2.1 K in Fig. 5.42. It can be noticed that V_1 is small compared to V.

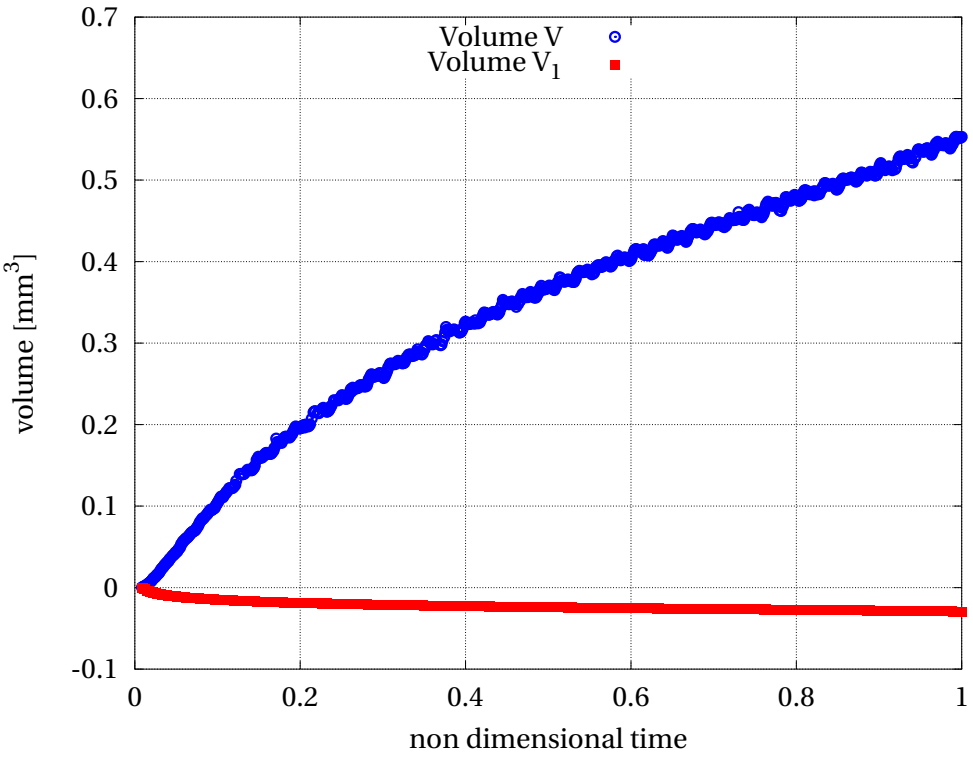

Figure 5.42: Growth of the volume V and V_1 of a bubble at a wall superheat of 2.1 K.

Figure 5.43 shows the resultant of these two buoyancy terms. The first buoyancy term is directly proportional to the volumetric growth rate of the bubble.

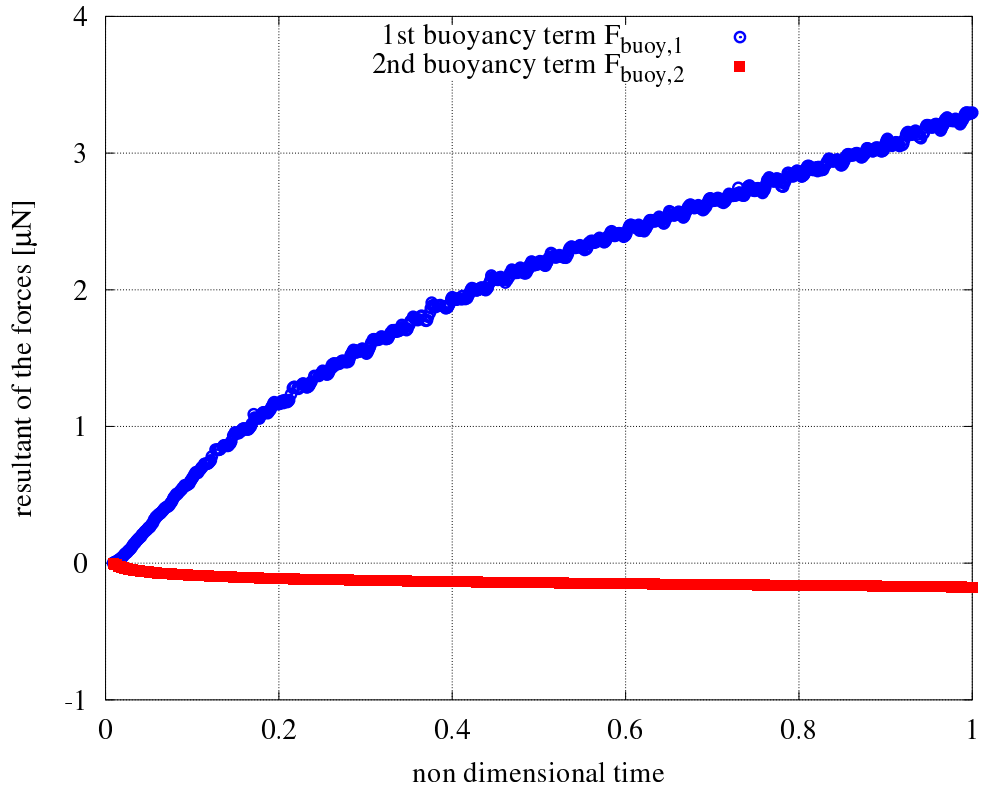

Figure 5.43: Resultant of the first and second buoyancy terms acting on a bubble at a wall superheat of 2.1 K.

5.2.2.2.4 Third buoyancy term

The third considered buoyancy term is taking into account the pressure difference through the interface located above the nucleation site. For the computation of this term, the Laplace-Young equation is used in order to calculate the pressure difference from the curvature of the bubble at its apex. This buoyancy term is expressed as follows (see Section 5.2.1.3):

$$\overrightarrow{F}_{buoy,3} = \frac{2\sigma}{R} S_{base} \overrightarrow{k} \tag{5.79}$$

with S_{base} the surface of the base of the bubble, as described in Fig. 5.22c and R the radius of curvature at the apex of the bubble. As it is located on the axis of symmetry of the bubble, both main radii of curvature are equal. The curvature is taken as homogeneous on the surface considered, which is consistent with curvature measurements shown in Fig. 5.54 to Fig. 5.61.

As the total curvature C is measured from this recorded images (see Section 5.2.3), the third buoyancy term can also be expressed as follows:

$$\overrightarrow{F}_{buoy,3} = \sigma C_{tip} S_{base} \overrightarrow{k} \tag{5.80}$$

with C_{tip} the curvature at the apex of the bubble. The evolution of the curvature at the apex is shown in Fig. 5.44.

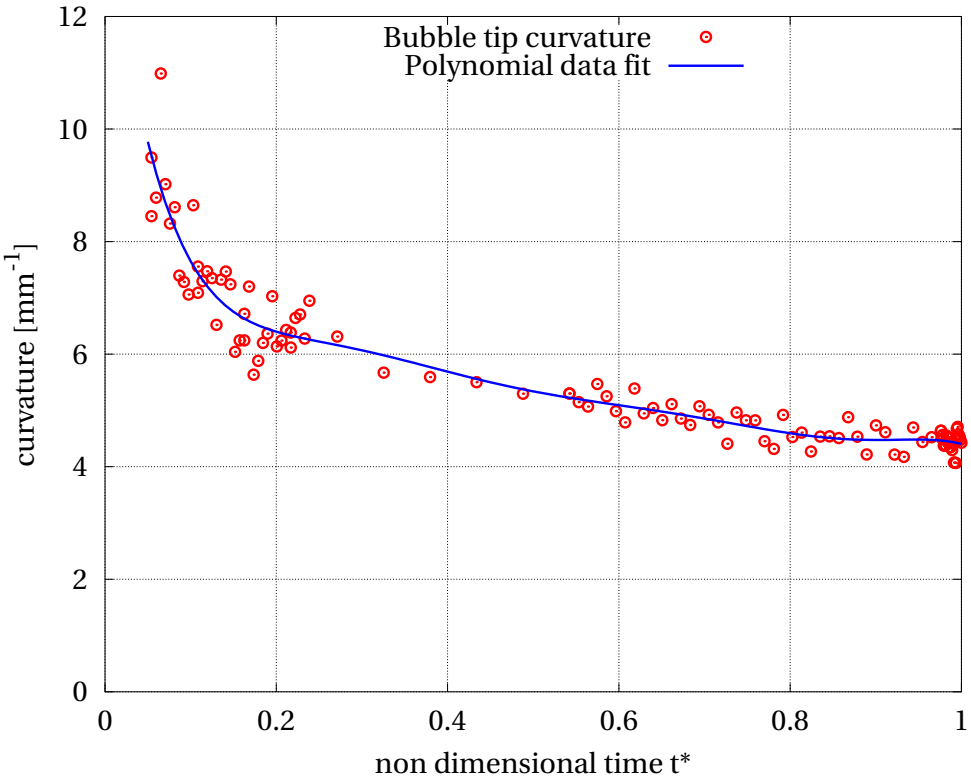

Figure 5.44: Curvature at the apex of a bubble at a wall superheat of 2.1 K.

For the same reasons as for the forces evoked previously, it is not possible to correctly capture the bubble contour for $t^* < 0.05$. The curvature is thus not measured at the beginning of the growth. Here again, the measured curvature data are fitted with an appropriate polynomial function which is used to calculate the resultant of the third buoyancy term (see Fig. 5.45).

The resultant of the first buoyancy term strongly depends on the base area, the uncertainty for which may be relatively high. As an illustration of the sensitivity of this force to the value of the base radius, Fig. 5.46 shows its time evolution for two close values of R_{base} (namely 90 µm and 100 µm). Decreasing the radius by 10 % reduces the force by up to 20 %.

5.2.2.3 Results of the momentum balance

Figure 5.47 shows the evolution of all the forces considered during a bubble growth with a wall superheat of 2.1 K. Similar results were obtained at a wall superheat of 4.7 K and are shown in Fig. 5.48. As explained before, the momentum balance has been computed only for $t^* > 0.05$ as several forces were impossible to compute for $t^* < 0.05$.

As can be seen on Figure 5.47, the momentum variation is negligible. As $\rho_l \gg \rho_v$, the momentum variation is very small compared to the liquid inertia.

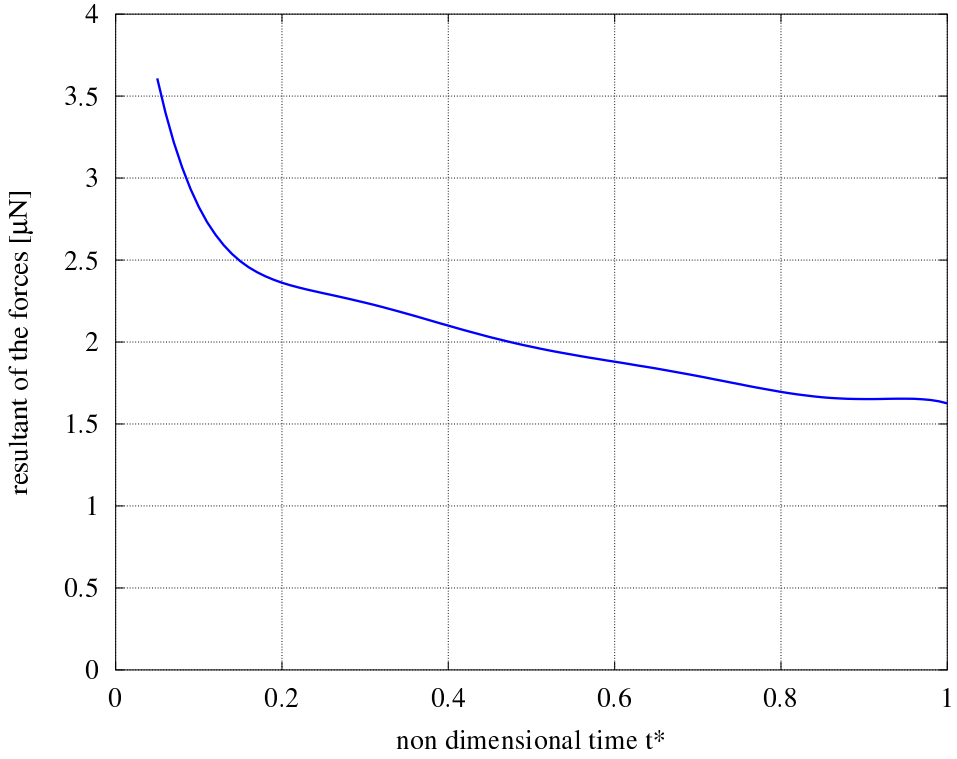

Figure 5.45: Resultant of the third buoyancy term acting on a bubble at $\Delta T_W = 2.1\,\mathrm{K}$.

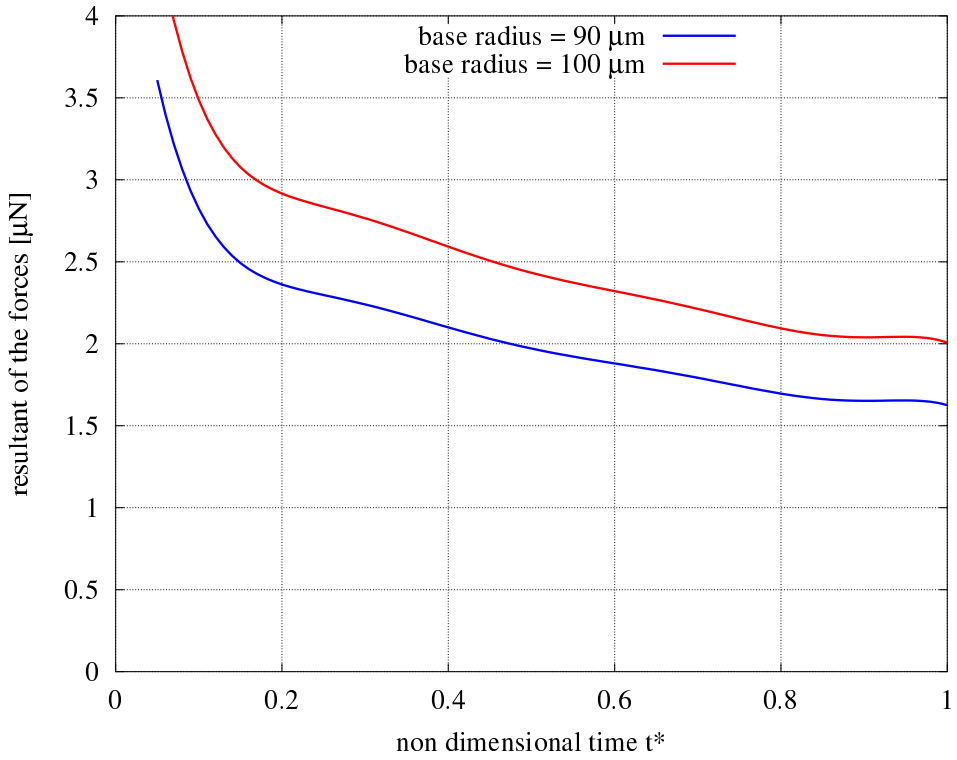

Figure 5.46: Resultant of the third buoyancy term acting on a bubble at $\Delta T_W = 2.1\,\mathrm{K}$, for two different base radii.

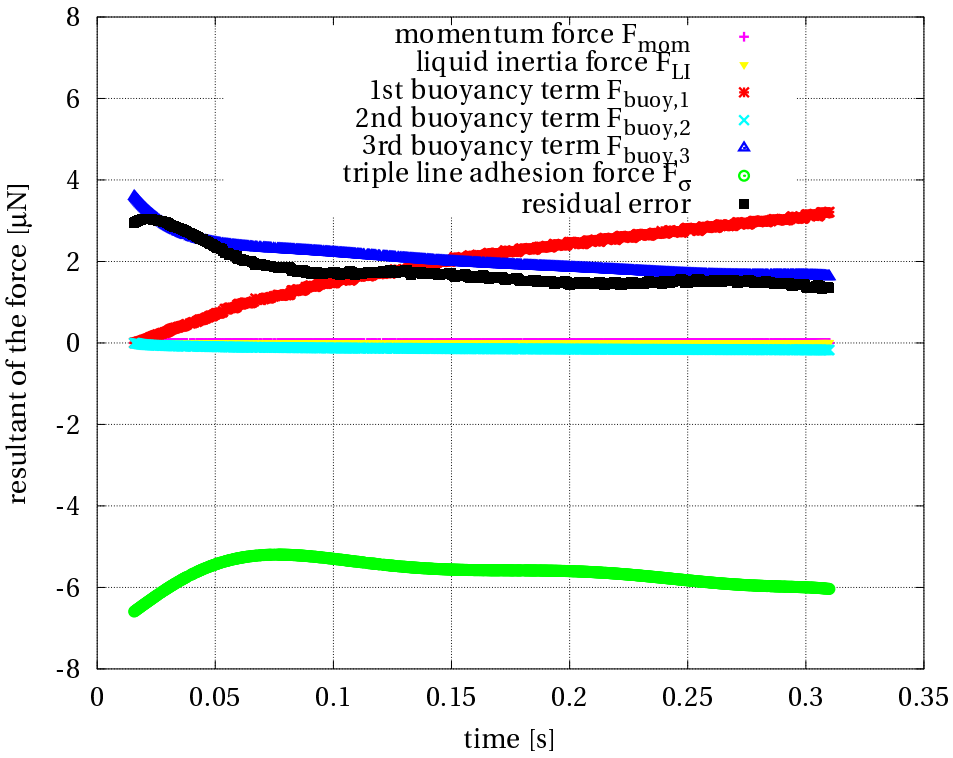

Figure 5.47: Momentum balance for a bubble growing at a wall superheat of $\Delta T_W \approx 2.1$ K.

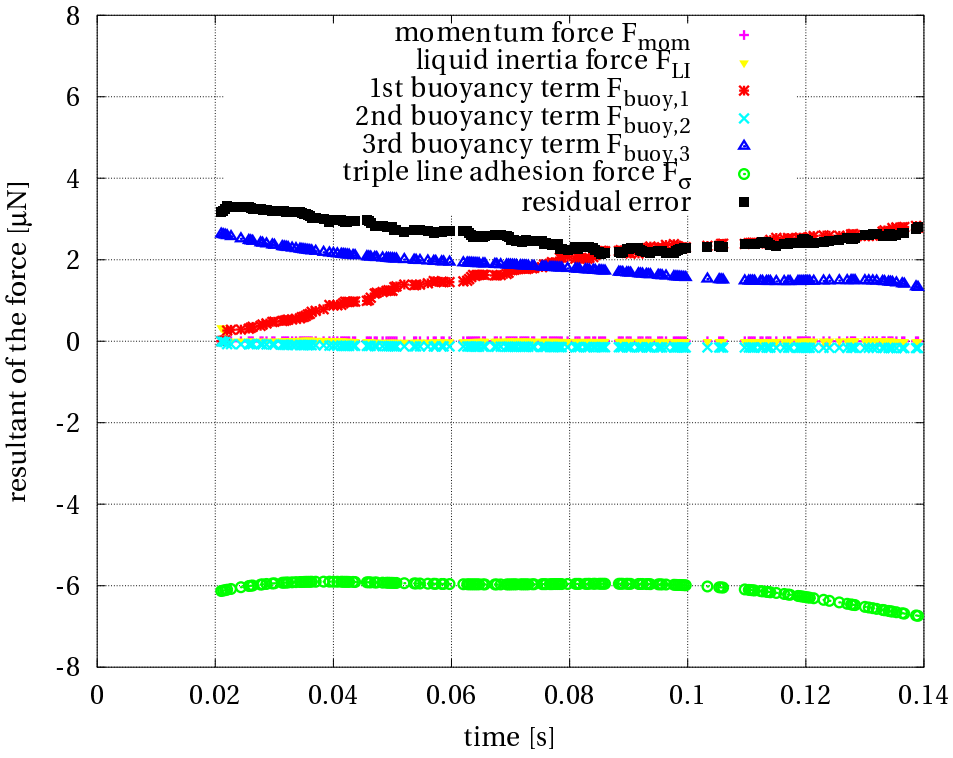

Figure 5.48: Momentum balance for a bubble growing at a wall superheat of $\Delta T_W \approx 4.7$ K.

The liquid inertia force is also negligible. It was also expected because no real influence of the wall superheat was observed on the departing diameter of bubble aspect. All dynamic forces are thus negligible compared to static forces.

The separation of buoyancy into three different terms highlights the role of each mechanism. The buoyancy due to the vapour volume $F_{buoy,1}$ corrected by $F_{buoy,2}$ increases monotonically, until being the dominant force that tends to detach the bubble. The so-called *contact pressure* term $F_{buoy,3}$ begins very high. Indeed, the curvature at the tip of the bubble is very low when the bubble is small, leading to a high vapour pressure at the beginning of the growth. This buoyancy term then decreases until being about half of the first buoyancy term.

The triple line surface tension and adhesion forces are the only forces keeping the bubble attached to the heated wall. These forces depend on the angle α which varies from 40 to 55 degrees.

A non-negligible residual error is found. Its value is close to the third buoyancy term, and it is directed upwards. This error might be due to uncertainties in the computation of the forces, especially the contact pressure force and the triple line adhesion force. As it has been detailed previously, the contact pressure force is very sensitive to the radius of the base area, and the triple line adhesion force is very sensitive to the measurement of the angle α. As an illustration, Fig. 5.49 shows the momentum balance when underestimating the angle α by 10°. It is shown that this error can almost compensate in itself the residual error.

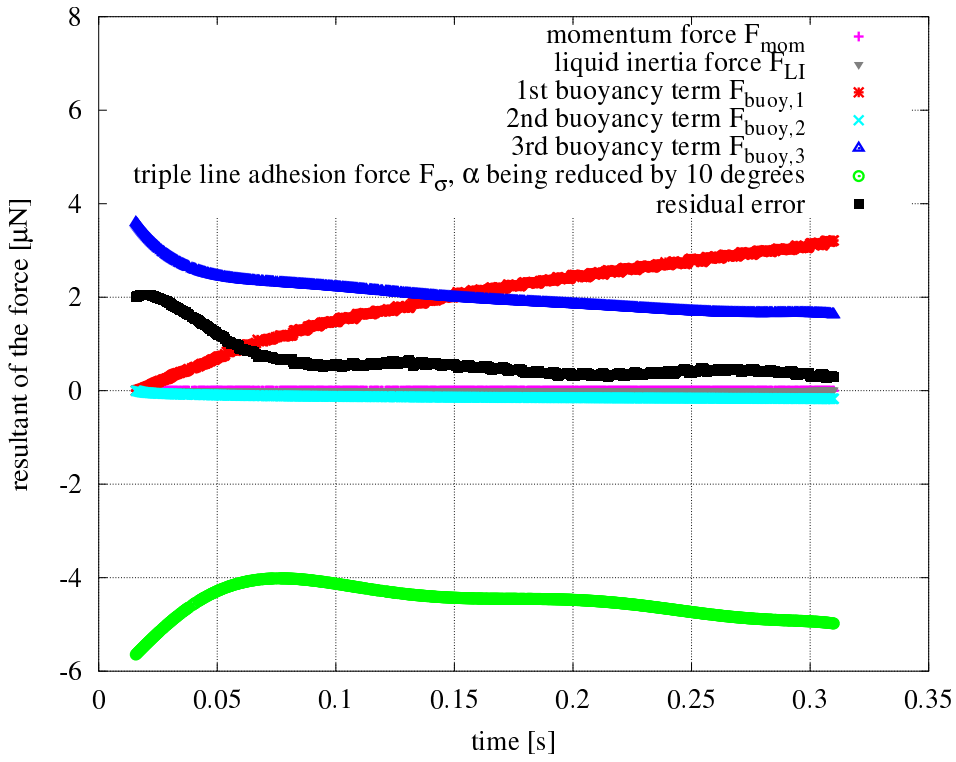

Figure 5.49: Momentum balance for a bubble growing at a wall superheat of $\Delta T_W \approx 2.1$ K. The angle α has been reduced by 10° in the computation of the triple line adhesion force.

The analysis of the forces acting on the bubble during its growth performed in this section provides new elements of understanding of the bubble dynamics, and give a clear explanation of the similarity between the growth curves for different wall superheat due to negligible dynamic forces. However, this analysis does not explain the mechanism of bubble detachment. Detachment is likely due to local forces which are not noticeable in such an integral momentum analysis. It is therefore necessary to investigate the local bubble curvature around the bubble contour during its growth.

5.2.3 Bubble curvature and local liquid pressure around the bubble

As the resultant of the forces acting on the bubble only refers to the bubble as a whole, another analyse of the forces is needed in order to describe the bubble shape. Moreover, if the bubble detachment is caused by a change of shape, only a study of the local forces can lead to its understanding.

The local forces involved on the interface are closely related to the local curvature of the interface, as described in subsection 5.2.1.4. The local curvature of the bubble during its growth is thus investigated in this section [167].

The author wishes to cheerfully thank Dr. Sergio Di Bari [11, 12] and Dr. Tony Robinson (University of Dublin, Trinity College – Ireland) who gratefully shared their image processing code and gave us the right to use and modify the code. Part of this code has been used in this section.

5.2.3.1 Image processing and definition of the curvature

The bubble contour is preprocessed in order to measure the curvature. The bubble, described as a stack of 1 pixel high cylinders (see section 3.3.2), is first made symmetric by setting the axis of each cylinder on the bubble symmetry axis. A Butterworth filter is then used to smooth the interface.

Once the bubble is symmetric, only half of the bubble is used for the calculation. The vertical axis is redefined and normalized by setting the origin of the axis on the tip of the bubble and the direction downwards, and by dividing the size by the bubble height. The new non-dimensional distance z^* is used, as described in Fig. 5.50.

In order to define the two major axes of curvature of the interface, the three dimensions are set as follows:

- The visualization direction is the y-axis.
- The axis of symmetry is the z-axis.
- The plane of the bubble contour, perpendicular to the visualization axis, is the x-z plane.

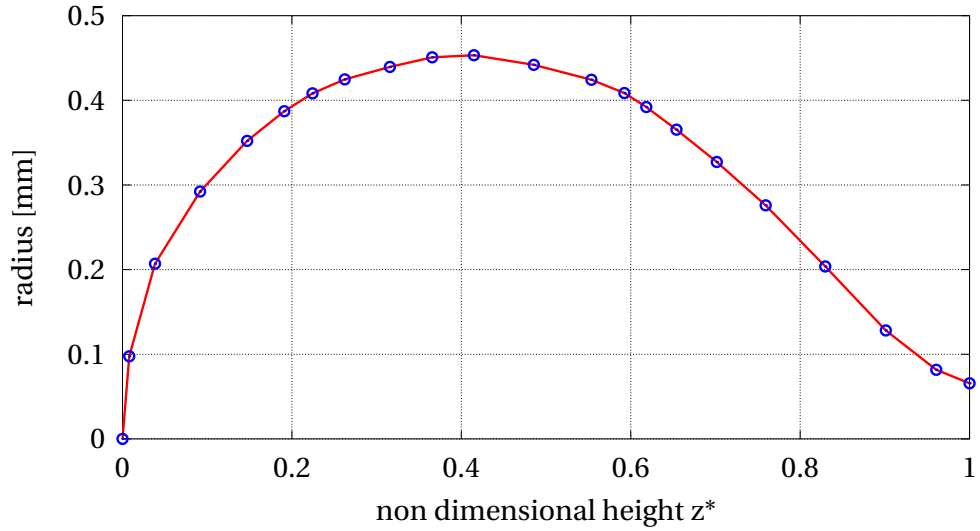

Figure 5.50: Smoothed interface with non dimensional height

Using these coordinates, the direction normal to the interface $\vec{n}$ belongs to the x-z plane. The curvature of the interface, at each point of the contour can be determined with two curvature radii, in two different planes including $\vec{n}$. The first radius of curvature R_1 is defined in the x-z plane, and the second radius of curvature R_2 is defined in the plane that is perpendicular to the x-z plane and that includes $\vec{n}$.

R_1 and R_2 are defined as positive when the curvature is directed toward the vapour phase, and negative otherwise. Both radii of curvature are illustrated in Fig. 5.51 for a *quasi*-spherical curvature near the tip of the bubble and in Fig. 5.52 for a *convex-concave* curvature at the neck of the bubble. R_1 is drawn in red while R_2 is in blue.

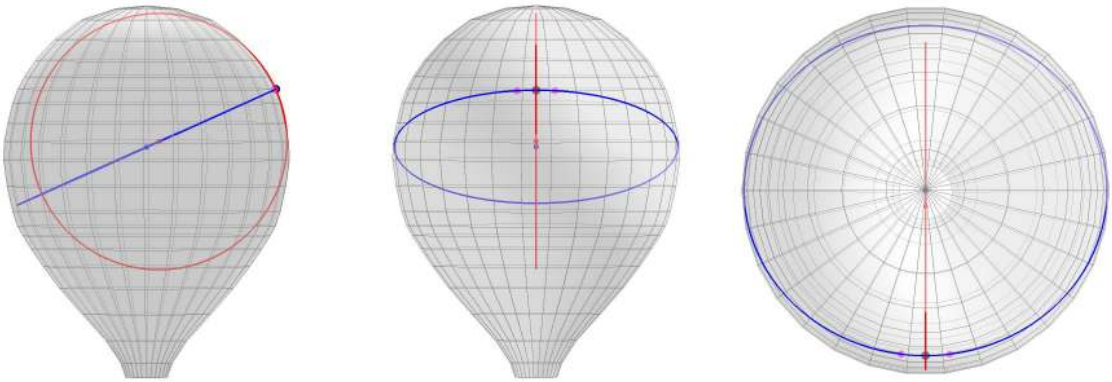

(a) Front view – x-z plane (b) Right view – y-z plane (c) Top view – x-y plane

Figure 5.51: Illustration of the curvature radii on the top part of the bubble

The curvature value is defined as the reverse of the curvature radius. Both curvatures are

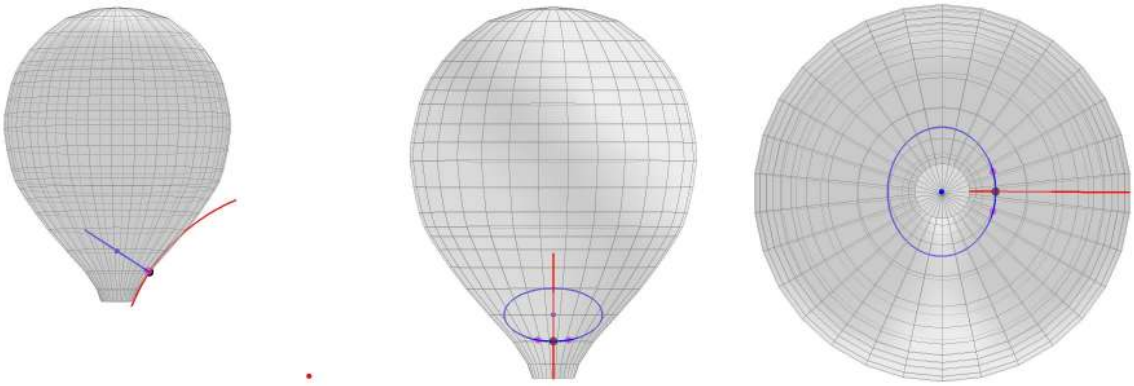

(a) Front view – x-z plane (b) Right view – y-z plane (c) Bottom view – x-y plane

Figure 5.52: Illustration of the curvature radii on neck of the bubble

thus defined as follows:

$$C_1 = \frac{1}{R_1} \text{ and } C_2 = \frac{1}{R_2} \tag{5.81}$$

The total curvature C is simply the sum of both curvatures and is expressed in m^{-1}:

$$C = C_1 + C_2 \tag{5.82}$$

In order to estimate the curvature at the tip of the bubble, the axisymmetry is used to define ghost points at the other side of the bubble profile depicted in Fig. 5.50. For the case of the curvature at the base of the bubble[36], the symmetry to the plane which is normal to the bubble profile in $z^* = 1$ is used in order to define ghost points.

5.2.3.2 Curvature evolution during bubble growth

The bubble shape, and thus the local bubble curvature, does change during the successive steps of bubble growth. Four significant instants have been chosen to illustrate this evolution (Figure 5.53):

- 10 % of the growth, which corresponds to the initial linear stage of the volumetric growth, while the bubble volume is still less than a fifth of the departure volume.
- 50 % of the growth, which corresponds to an early instant of the slow growth. The bubble already measures two thirds of the departure volume.
- 90 % and 99.9 %, which describes the particular shape evolutions leading the detachment of the bubble.

For two different wall superheat of 2.1 K and 4.7 K, both main radii of curvature C_1 and C_2 as well as the total curvature C are computed and plotted for each of the four steps. The same trends are observed for both superheat conditions.

[36] i.e. close to the triple line

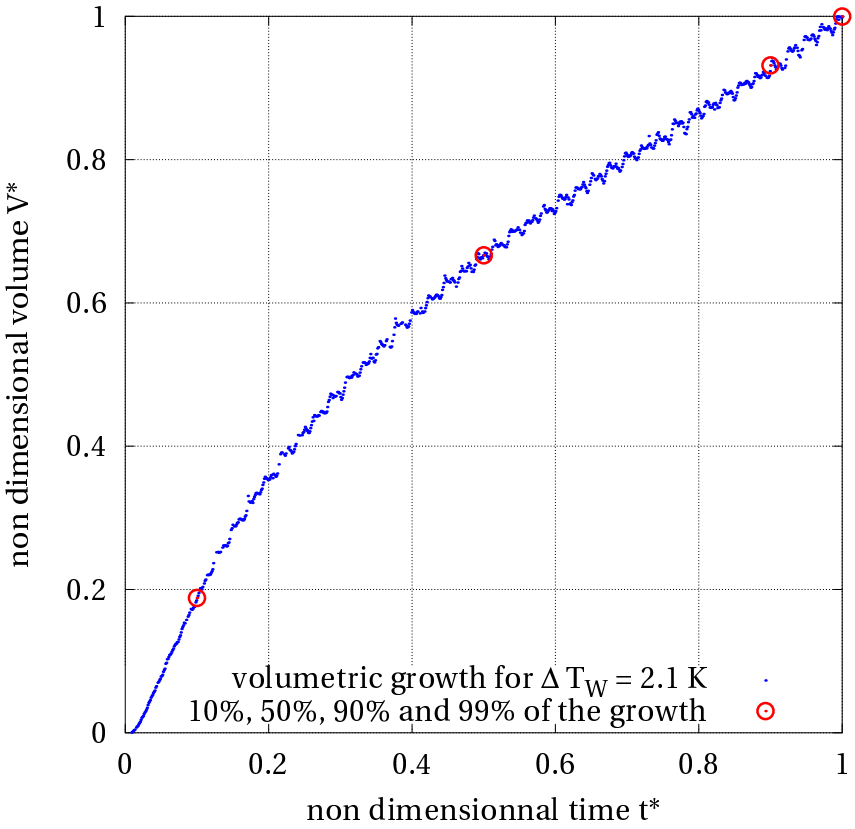

Figure 5.53: Respective positions of the images used further on the growth curve.

At the beginning of the bubble growth (Fig. 5.54 and 5.55), the bubble appears quasi-spherical, and slightly elongated near the base. Both curvature are thus constant and equal for the top half of the bubble. The total curvature is quite high ($C \approx 8\,\mathrm{mm}^{-1}$) because of the small size of the bubble. Concerning the base of the bubble, C_1 is decreasing whereas C_2 is increasing. The total curvature, sum of C_1 and C_2 remains constant. It should be noted that as the bubble is small, the resolution of the contour is poor and the uncertainty on the curvature calculation is high. Nevertheless, the same trends and values are observed for both conditions.

At the middle of the growth (Fig. 5.56 and 5.57), the growth rate has already decreased and a neck has started to form. The two thirds of the top part of the bubble are spherical, with a constant value of both curvature radii. At the base, the formation of the foot is clear with an increasing C_2 and the elongation of the neck leads to a decreasing C_1. The total curvature is increasing near the base as the C_2 evolution is much more important than the C_1 decrease.

Close to detachment, the neck gets tighter. The first curvature C_1 decreases to negative values close the base, revealing the inflexion and the change of curvature direction, as in Fig. 5.52. The second curvature C_2 increases to values close to the curvature of the bubble nucleation site of about $11\,\mathrm{mm}^{-1}$. The total curvature is thus increasing too, and seems to show more noticeable changes just before detachment between respectively Fig. 5.58 and 5.59 and Fig. 5.60 and 5.61.

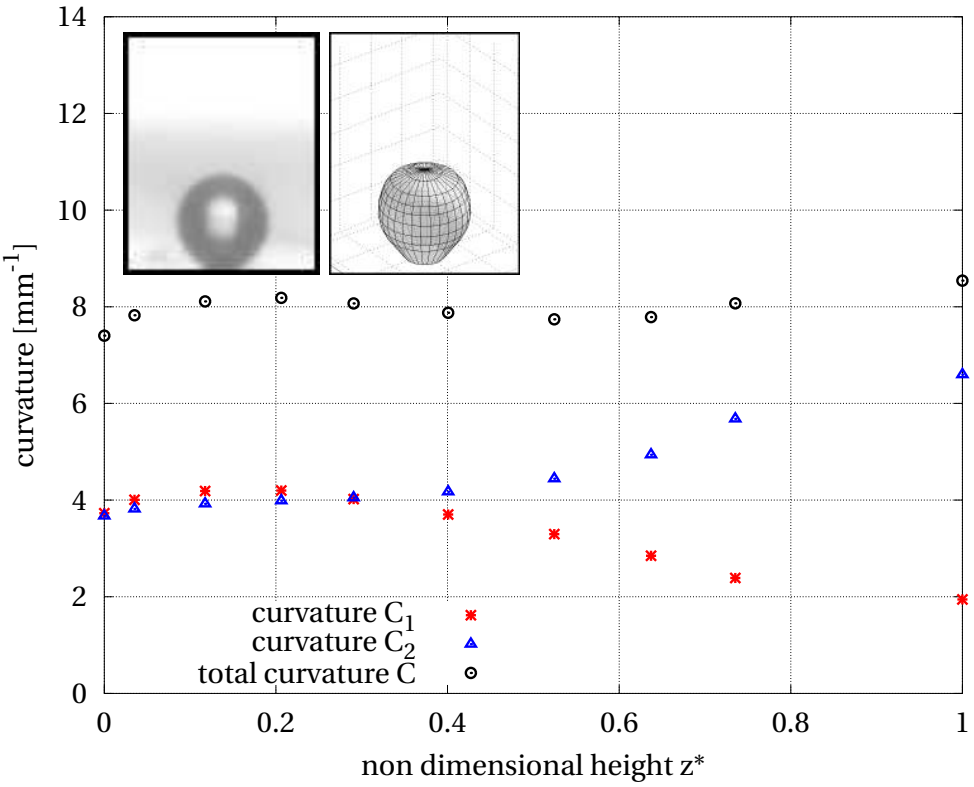

Figure 5.54: Curvature of the interface with $\Delta T_W = 2.1\,\mathrm{K}$ and $t^* = 10\,\%$.

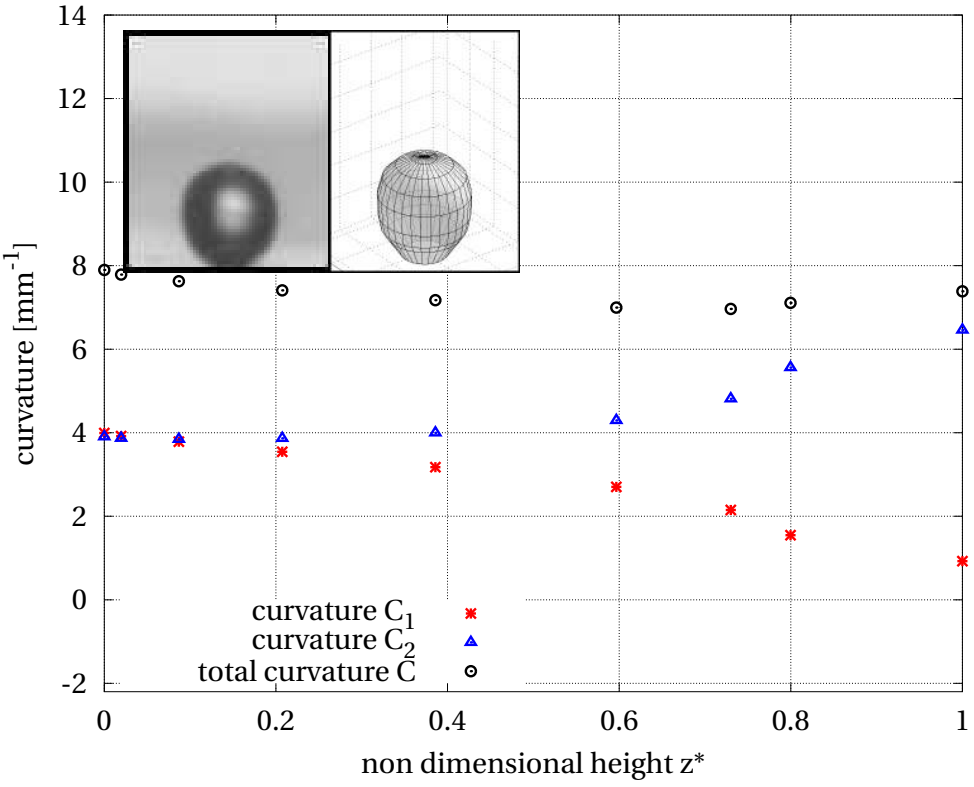

Figure 5.55: Curvature of the interface with $\Delta T_W = 4.7\,\mathrm{K}$ and $t^* = 10\,\%$.

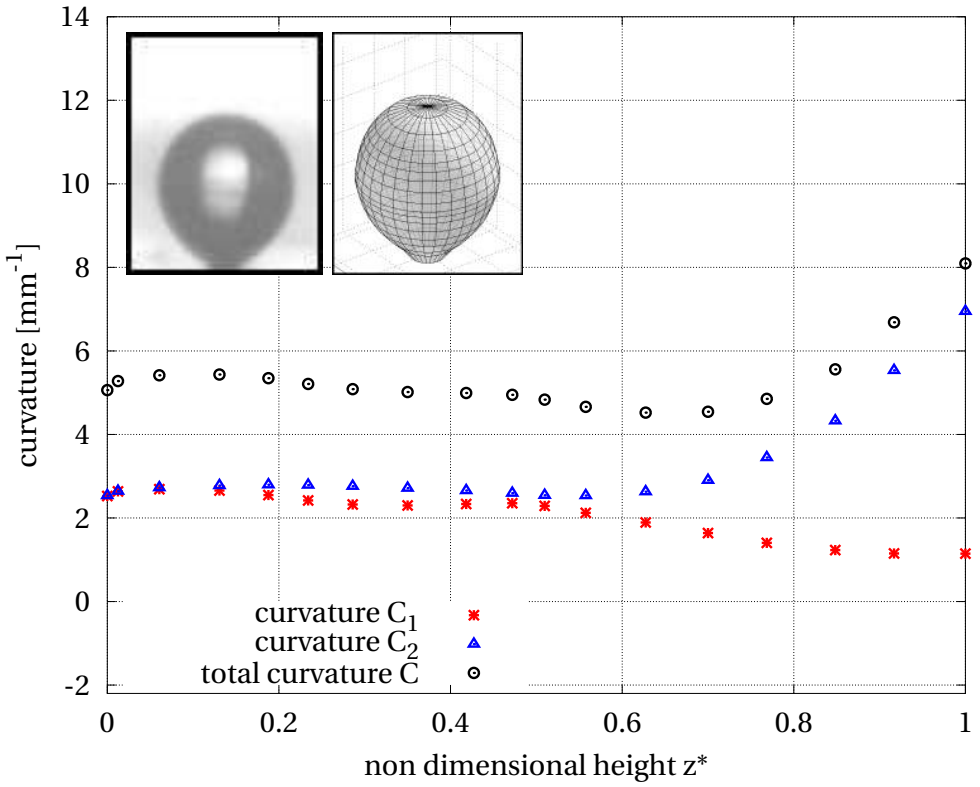

Figure 5.56: Curvature of the interface with $\Delta T_W = 2.1\,\mathrm{K}$ and $t^* = 50\,\%$.

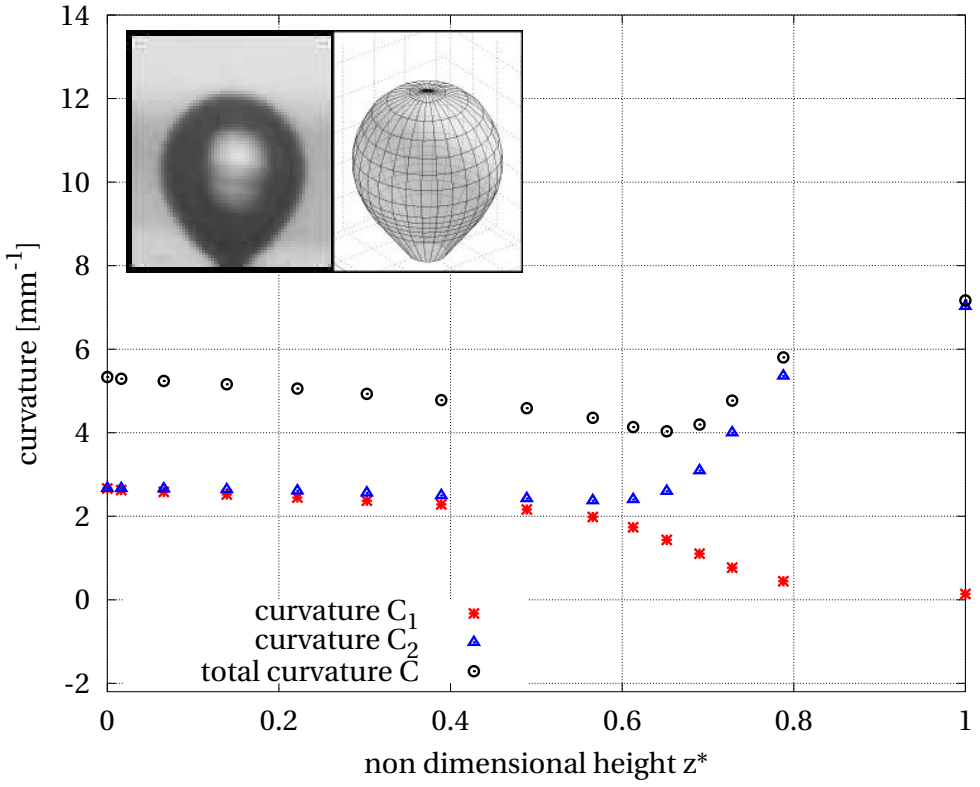

Figure 5.57: Curvature of the interface with $\Delta T_W = 4.7\,\mathrm{K}$ and $t^* = 50\,\%$.

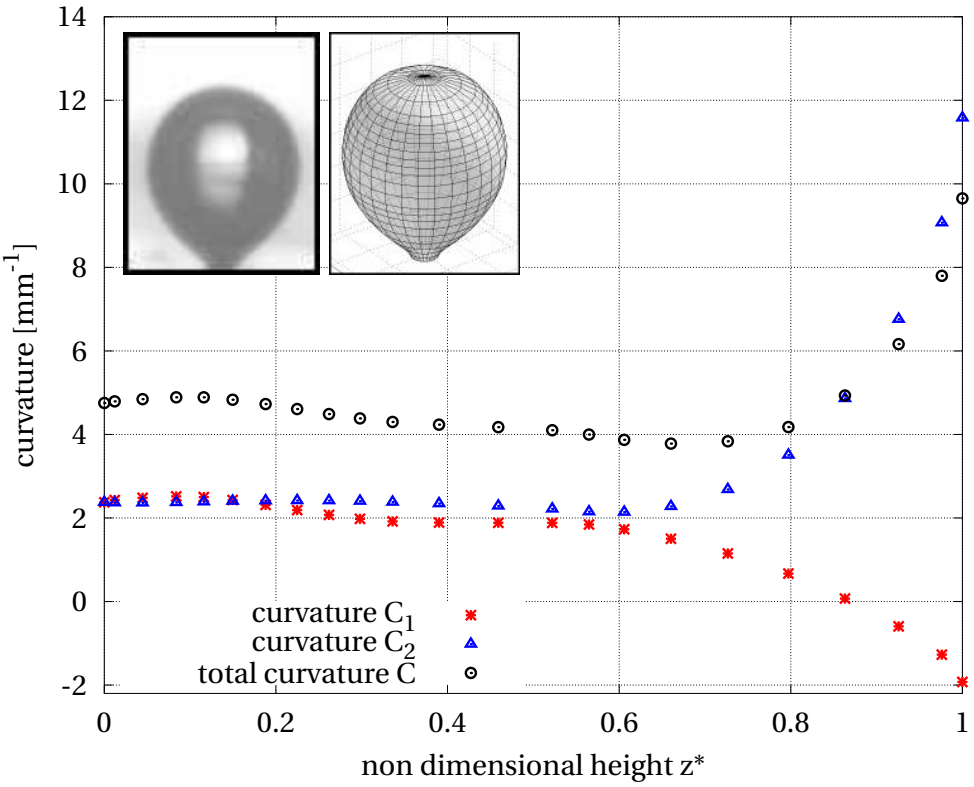

Figure 5.58: Curvature of the interface with $\Delta T_W = 2.1\,\mathrm{K}$ and $t^* = 90\,\%$.

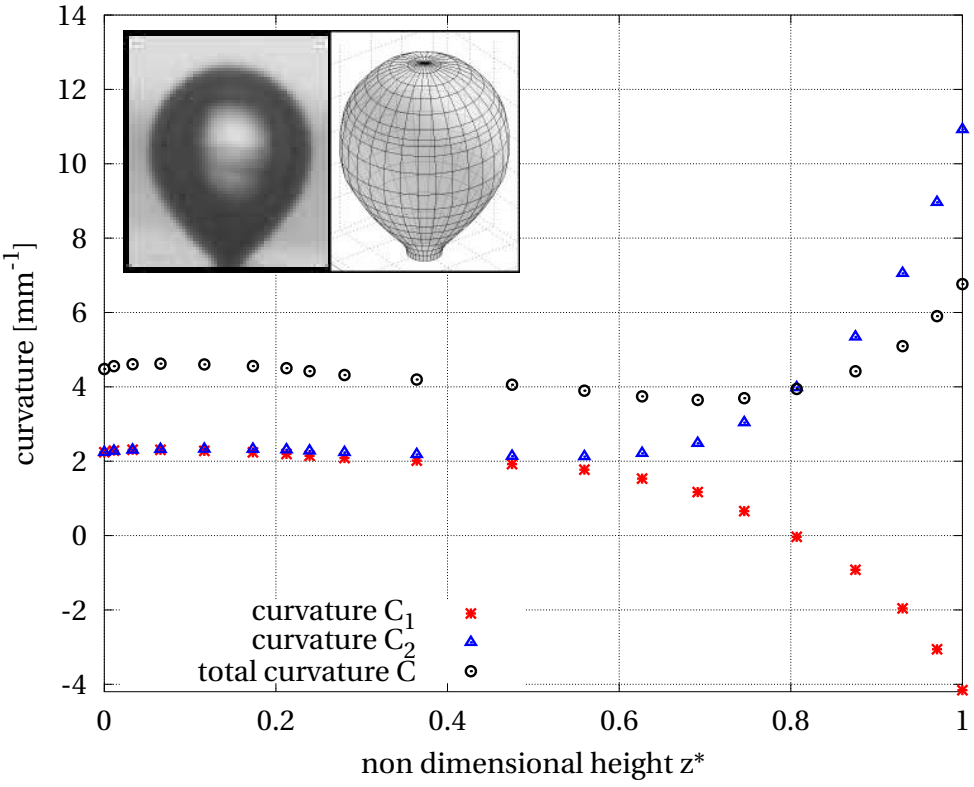

Figure 5.59: Curvature of the interface with $\Delta T_W = 4.7\,\mathrm{K}$ and $t^* = 90\,\%$.

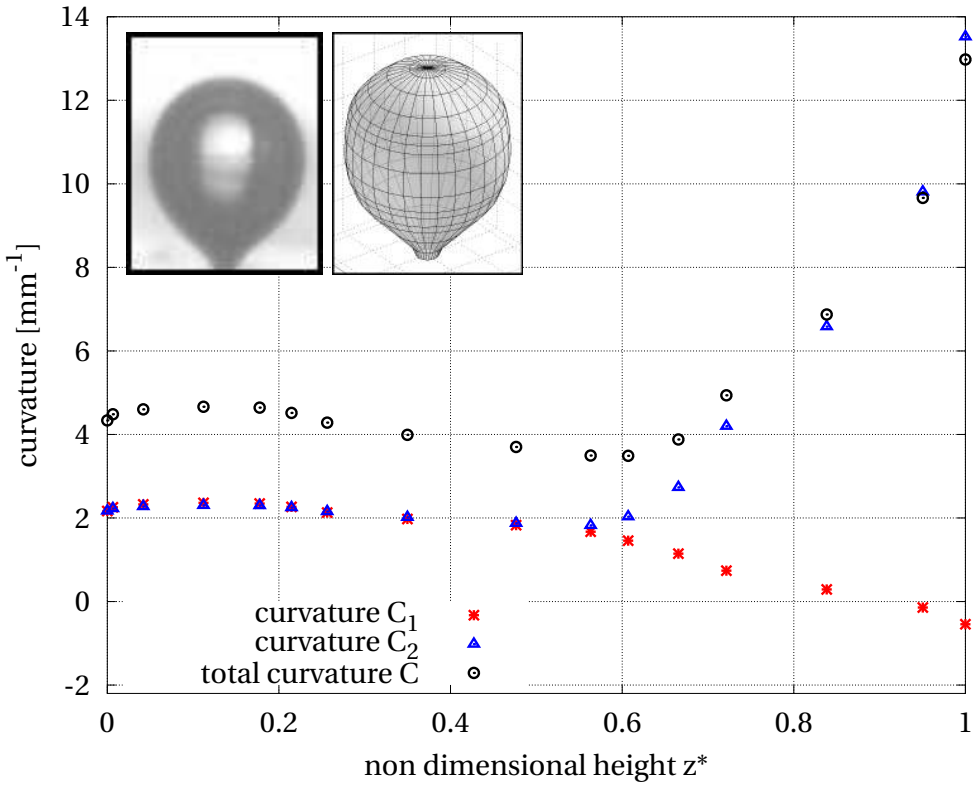

Figure 5.60: Curvature of the interface with $\Delta T_W = 2.1\,\mathrm{K}$ and $t^* = 99.9\,\%$.

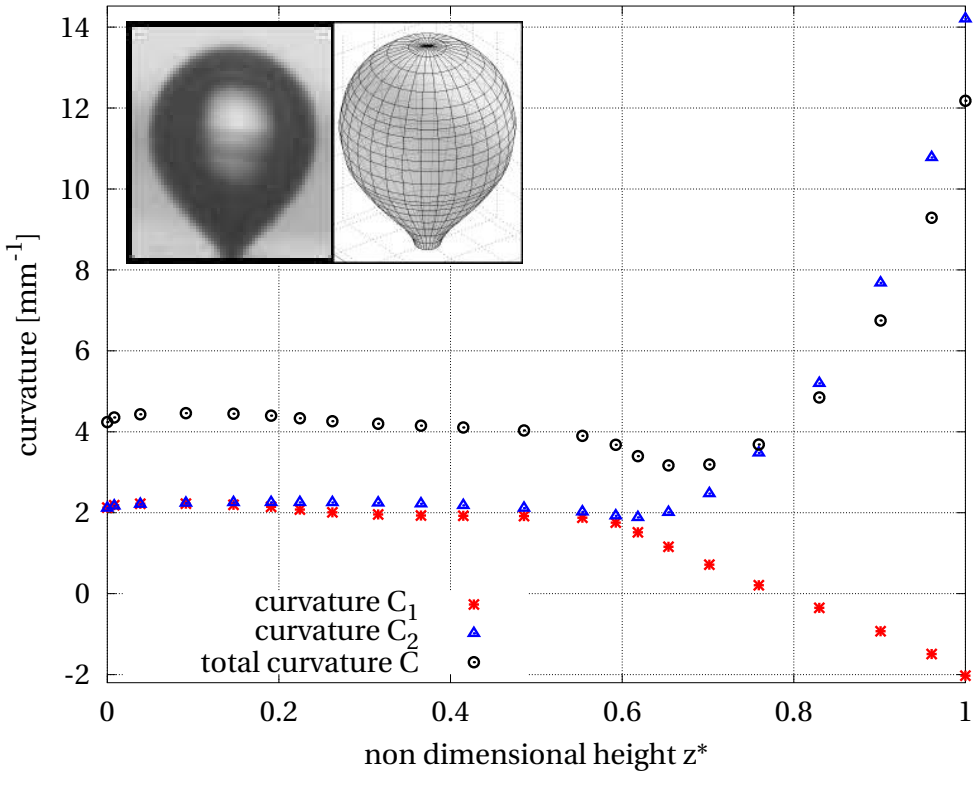

Figure 5.61: Curvature of the interface with $\Delta T_W = 4.7\,\mathrm{K}$ and $t^* = 99.9\,\%$.

It is interesting to compare the total curvature along the interface to the steady shape which would result from the Laplace-Young equation and the hydrostatic law in the liquid and vapour phases. The theoretical curvature C_{th} respects the following relation, considering constant thermodynamic properties:

$$\sigma C_{th}(z^*) = P_v(z^*) - P_l(z^*) \tag{5.83}$$

Using the hydrostatic law and the bubble height h:

$$\begin{aligned} \sigma C_{th}(z^*) &= P_v(0) + \rho_v g z^* h - P_l(0) - \rho_l g z^* h & (5.84)\\ &= [P_v(0) - P_l(0)] - (\rho_l - \rho_v) g z^* h & (5.85)\\ &= \sigma C_{th}(0) - (\rho_l - \rho_v) g z^* h & (5.86) \end{aligned}$$

$$C_{th}(z^*) \approx C_{th}(0) - \frac{5950}{\sigma} \times z^* h \tag{5.87}$$

The theoretical curvature has a linear and decreasing profile along the z-axis (directed downward).

Just before detachment, the bubble height is about 1.2 mm. The curvature difference between the tip and the base would theoretically be:

$$\begin{aligned} C_{th}(0) - C_{th}(1) &\approx 490\,\mathrm{m}^{-1} & (5.88)\\ &\approx 0.49\,\mathrm{mm}^{-1} & (5.89) \end{aligned}$$

Compared to the scale of Fig. 5.54 to 5.61, even with the bubble showing the largest height (i.e. at detachment), the theoretical curvature would appear almost constant along the z^* axis.

As a matter of fact, when the bubble is small and thus relatively spherical, the actual curvature is relatively constant (Fig. 5.54 and 5.55). But after the formation of the neck[37], the curvature appears to be constant over only a portion of the bubble height, namely $0 < z^* < 0.6$. The top part of the bubble is spherical and respects the theoretical curvature profile. On the contrary, the lower part of the bubble, for $z^* > 0.6$, shows an increase of the curvature. The neck, closely related to adhesion forces can therefore not be described only in terms of capillarity and hydrostatic gravity forces.

5.2.3.3 Tip curvature evolution and growth regime

The bubble tip curvature evolution has been computed for a bubble growth with $\Delta T_W = 2.1$ K and plotted in Fig. 5.62. The bubble curvature was not possible to compute while the bubble size was of the order of magnitude of the nucleation site[38] as the image resolution was too poor.

[37] that corresponds about to $t^* > 0.2$

[38] i.e. while $t^* < 0.05$

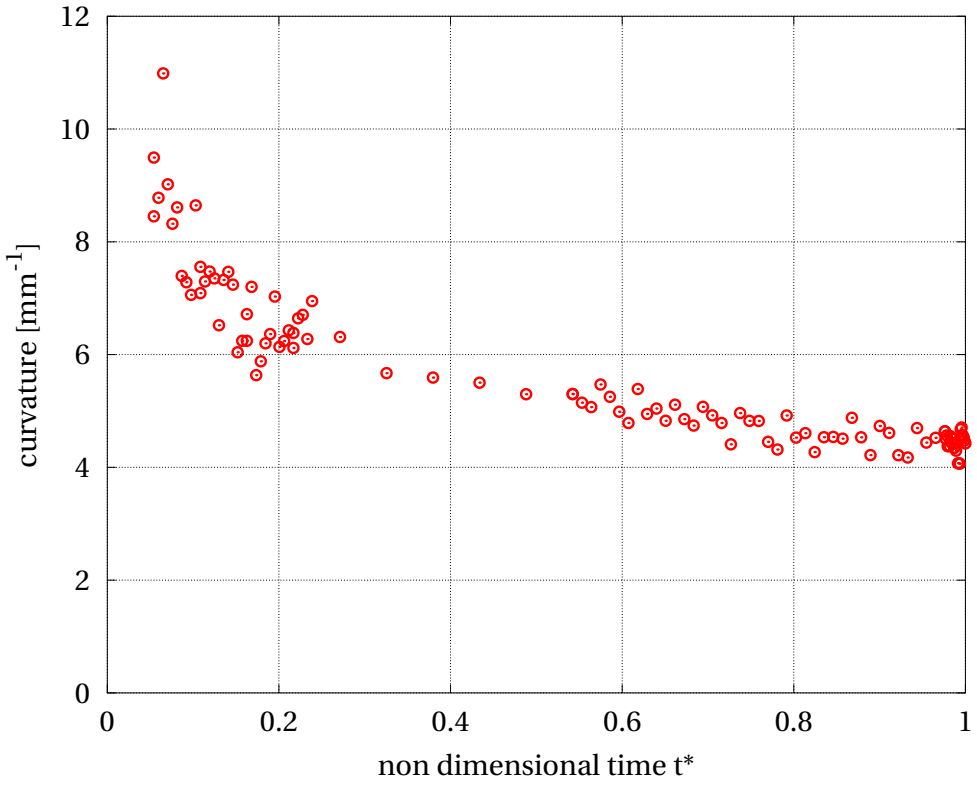

Figure 5.62: Bubble tip curvature during bubble growth with $\Delta T_W = 2.1\,\mathrm{K}$

It can be observed that the curvature begins high due to the small size of the bubble and decreases sharply until $t^* \approx 0.2$. The tip curvature then decreases much more gradually around a value of $5\,\mathrm{mm}^{-1}$. It is interesting to note that this change of behaviour corresponds to the critical change in the bubble growth curve (see Fig. 5.10 and 5.11).

The bubble curvature is related to the equilibrium pressure difference between the vapour and liquid phases by the Laplace-Young equation. This equilibrium cannot be assessed all around the bubble during its growth but is most probable at the tip of the bubble, as it is on the axis of symmetry and the distance from the triple line lessens the probability of an interaction between the liquid-vapour interface and the heated wall.

The maximum measured curvature at the tip of the bubble is about $11\,\mathrm{mm}^{-1}$. When the bubble is even smaller, the theoretical maximum curvature is achieved with a hemispherical bubble of the nucleation site diameter. The tip curvature in this case is:

$$C_{tip} = \frac{2}{R_{nc}} \tag{5.90}$$

$$\approx 22.2\,\mathrm{mm}^{-1} \tag{5.91}$$

The equilibrium pressure difference can then be computed too:

$$P_v - P_l = C_{tip} \times \sigma \tag{5.92}$$

$$\approx 322\,\mathrm{Pa} \tag{5.93}$$

This pressure difference is very small compared to the ambient pressure, namely $P = 1$ bar during the tests. Moreover, the change of thermodynamic properties due to such a pressure difference is negligible. From this order of magnitude comparison, it is clear that the change of slope in the volumetric growth cannot be explained by the change of slope of the tip curvature, and should on the contrary be explained by a thermal analysis.

5.2.3.4 Base curvature evolution and bubble detachment

Let the curvature at the base of the bubble[39] be named the *base curvature*. The base curvature evolution during bubble growth is plotted in Fig. 5.63. Both main curvatures as well as the total curvature are plotted. The data points are rather scattered because of a certain level of uncertainty in their computations, but their trends are clear. The curvature C_1 begins close to the curvature C_2 and decreases until reaching a plateau around 0 for $t^* \approx 0.3$. C_1 seems to have negative values when the bubble is close to detachment, as described in Fig. 5.52. While C_1 is close to zero, the total curvature more or less equals C_2.

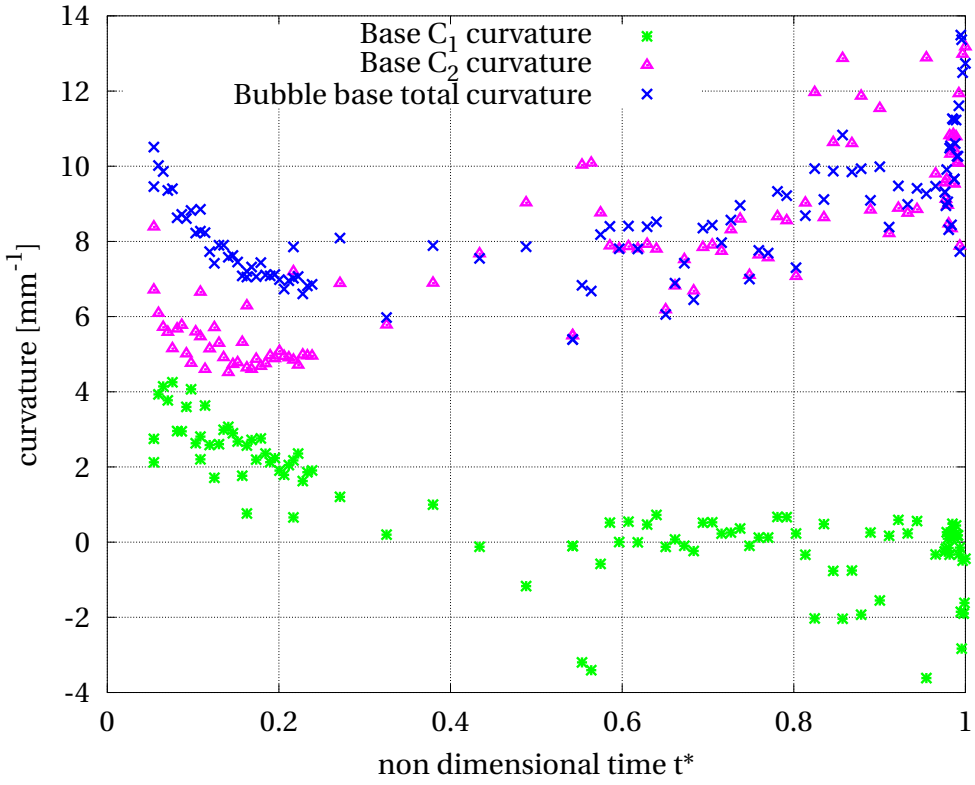

Figure 5.63: Bubble base curvature during bubble growth with $\Delta T_W = 2.1$ K

Figure 5.64 is the plot of the evolution of the tip and the base total curvature. For $t^* < 0.2$, the base and the tip curvature are close, as it was foreseen in Fig. 5.54 and 5.55. The bubble is more or less spherical, and its curvature is decreasing quickly due to the rapid evolution of its diameter. After $t^* \approx 0.2$, the neck is forming, leading to a higher curvature at the base,

[39] for $z^* = 1$

that stays almost constant until close to detachment. Just before departure, with $t^* > 0.95$, the neck constricts and the base curvature diverges towards high values. The bubble detachment seems to be closely related to the hydrodynamic equilibrium of the neck.

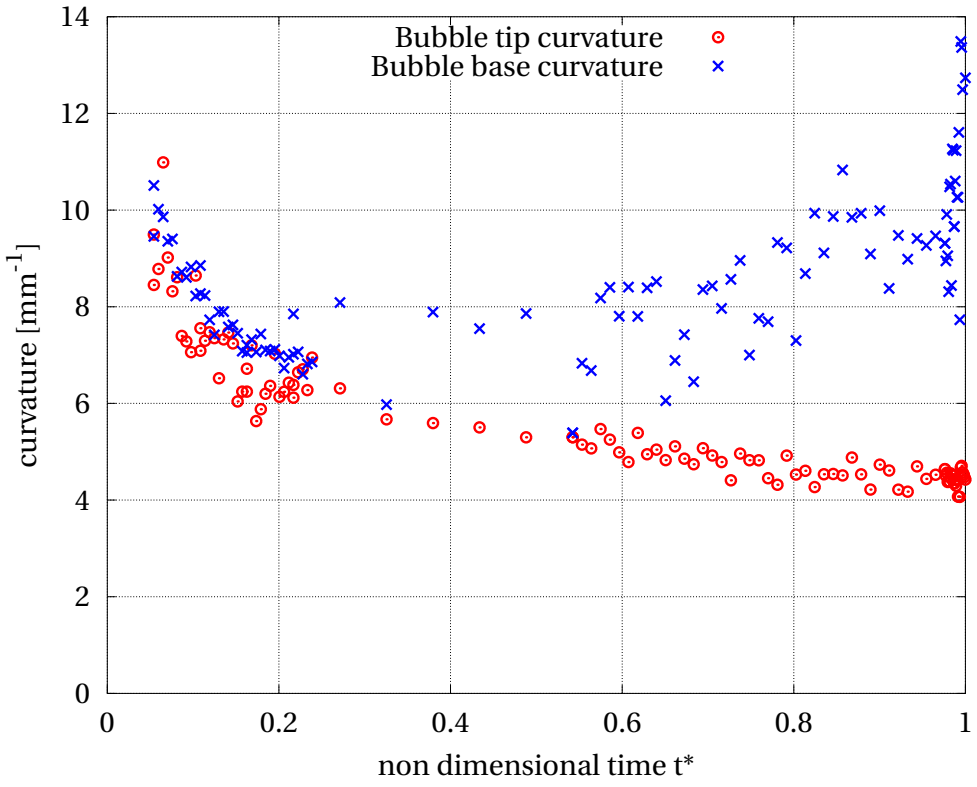

Figure 5.64: Bubble base and tip curvature during bubble growth with $\Delta T_W = 2.1$ K

5.3 Coalescence of bubbles

Coalescence is the main phenomenon which dictates in the upper limit of the isolated bubble regime. The density of bubbles become so high that contact occurs between neighbour bubbles, either because of the density of active nucleation site or because of the high bubble frequency from each nucleation site. As V.P. Carey explains ([23], page 217):

> With increasing surface superheat, more and more sites become active, and the bubble frequency at each site generally increases. Eventually, the active sites are spaced so closely that bubbles from adjacent sites merge together during the final stages of growth and release. Vapor is being produced so rapidly that bubbles merging together form columns of vapor slugs that rise upward in the liquid pool toward its free surface. This higher range of wall superheat [...] is referred to as the *regime of slugs and columns*.

This latter regime is also sometimes referred to as the *fully developed nucleate boiling regime*. It often has associated with it a decrease in the heat transfer coefficient, leading eventually to the critical heat flux (CHF). This decrease in the heat transfer coefficient is closely related to the coalescence phenomenon as the size of merged bubbles becomes large and prevents the liquid phase from moving freely towards the heated surface.

5.3.1 Vertical and lateral coalescence events

Two different types of coalescence events were observed during this study. A first type, illustrated in Fig. 5.65 and called *vertical* coalescence, occurs when the wall superheat exceeds about 4.5 K. Once a bubble is detached from its neck, it quickly accelerates vertically in the liquid due to its buoyancy. However, although the acceleration can be high, the initial velocity of the departing bubble is zero. The characteristics of the rise of the bubble do not depend on the wall superheat (see Section 5.4) as the only significant parameter is the bubble departure volume. As the departing bubble is moving away from the surface, a new bubble nucleates and grows over the artificial nucleation site. The growth rate of the new growing bubble depends on the wall superheat. If the growth is slow enough, the departed bubble has time to leave before the new bubble reaches its interface. On the contrary, if the bubble growth is fast, it reaches the previous bubble and eventually merges with this latter[40].

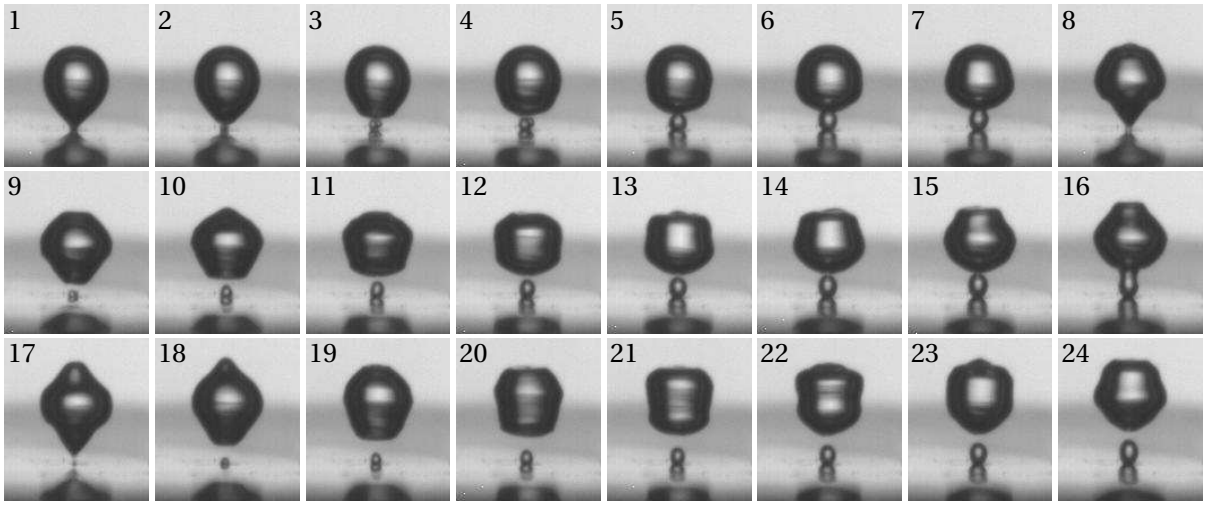

Figure 5.65: Photos of vertical coalescence between successive bubbles coming from the same nucleation site, at a high wall superheat of $\Delta T_W \approx 5.9$ K. Time difference between two photos is $\Delta t \approx 0.33$ ms.

As it is observed in Fig. 5.65, several successive bubbles can merge with the previously departed bubble, which is much very distorted by the multiple coalescence events. The coalescence event itself is very fast, and its duration cannot be evaluated with the time resolution used here.

[40] If both bubble get very close without break up of the separating liquid film, the bubbles do not merge but their shape are modified leading to shape oscillations, as detailed in Section 5.1.5.3.

The second type of coalescence observed, illustrated in Fig. 5.66 and named *horizontal* or *lateral* coalescence, occurs when two neighbouring nucleation sites are active with a moderate or high heat flux[41] and the distance between both sites is less than the departure lateral diameter of the bubbles [18]. In order to observe this phenomenon, a second artificial nucleation site, almost identical to the first one, has been created at a distance of 660 μm (see Section 3.1.3). A few differences on the edge of the nucleation sites, due to the successive polishing processes, result in a poorer stability of the second site (on the left side on Fig. 5.66 and 5.67). The right site being more stable, the bubble preferentially nucleates in that site at low heat flux, deflecting the heat flux in the heated wall towards the active site [18]. When increasing the heat flux, the left nucleation site is also activated but has a significant waiting time. As the left bubble nucleates later than the right bubble, they merge with different sizes (see Fig. 5.67). It is observed that the smaller bubble is sucked inside the bigger one (as predicted by P.G. De Gennes, [50] page 16). This is due to two reasons:

- The vapour pressure inside the smallest bubble is higher, due to a higher curvature of the interface (see Section 5.2.3).
- The bigger bubble needs much more energy to me moved from its place due to the inertia of the surrounding liquid.

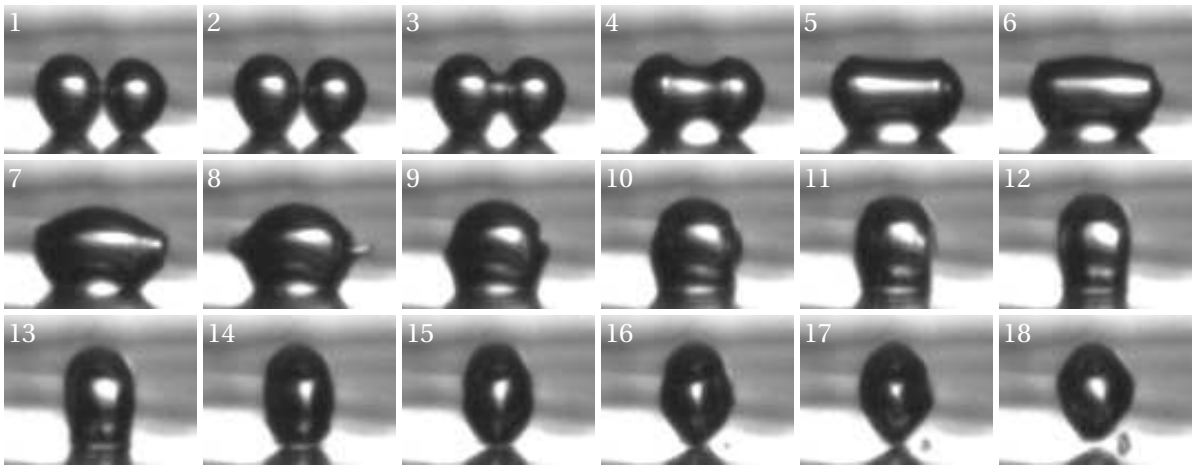

Figure 5.66: Photos of lateral coalescence between adjacent bubbles coming from neighbour nucleation sites, at a high wall superheat of $\Delta T_W \approx 6.5\,\mathrm{K}$. Time difference between two photos is $\Delta t \approx 0.19\,\mathrm{ms}$.

5.3.2 Wave front propagation during lateral coalescence of two bubbles

Figure 5.68 shows the lateral merging of two bubbles with a wall superheat of 8.5 K. A bubble nucleates at the same time at each nucleation site. Both bubbles grow at the same rate. Once the bubble diameters are large enough, both *liquid-vapour* interfaces are very close, so

[41] Lateral coalescence was observed within a superheat range of $6\,\mathrm{K} < \Delta T_W < 9\,\mathrm{K}$. When the superheat was lower than 6 K, one of the sites was not activated, and when the superheat was higher than 9 K, vertical coalescence events were interfering with the phenomenon.

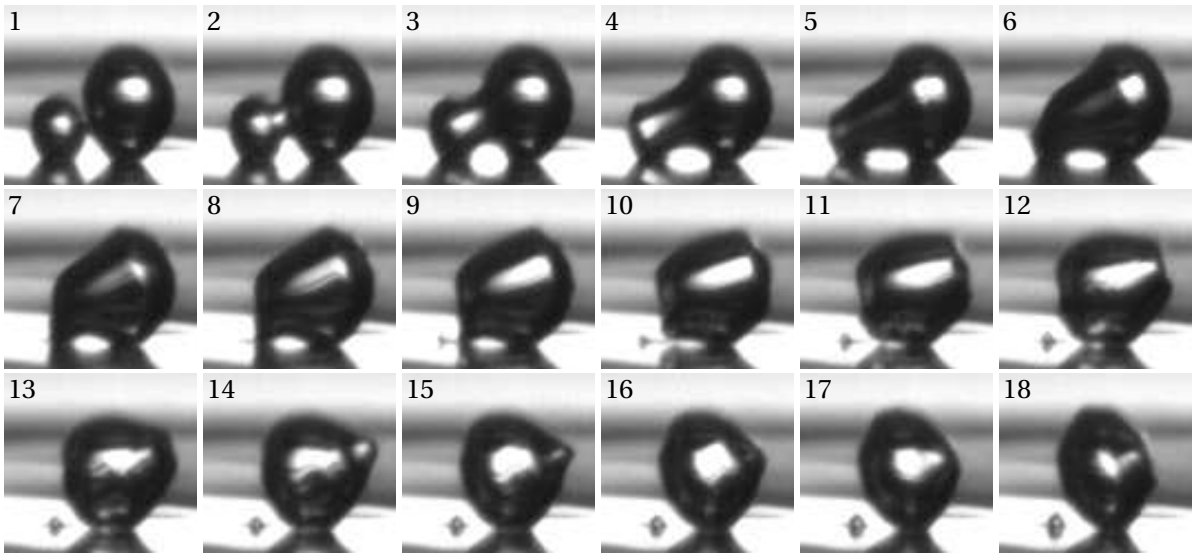

Figure 5.67: Photos of lateral coalescence between adjacent bubbles coming from neighbour nucleation sites, at a moderate wall superheat of $\Delta T_W \approx 6.5\,\mathrm{K}$. Time difference between two photos is $\Delta t \approx 0.15\,\mathrm{ms}$.

that there only remains a thin liquid film between the bubbles. Then, the liquid film breaks up, and coalescence occurs. The circular opening between the bubbles grows rapidly until the vapour forms a single bubble. The liquid *macrolayer* volume between the bubble necks decreases until the *macrolayer* disappears. Both necks then come free, and the resulting bubble forms a new neck that touches the wall just in between the two preceding necks (see Fig. 5.66, image 15-16). Then, the bubble leaves the wall and starts rising in the liquid, and both nucleation sites are almost instantaneously activated again. The coalesced bubble oscillates, and has a higher inertia than a single non coalesced bubble. Therefore, it accelerates slowly, and often vertical coalescence occurs with the next bubbles.

In these experiments, no influence on the phase change was detected during coalescence: indeed, the vapour production is less than $0.01\,\mathrm{mm}^3$ between the time when the bubbles touch each other (just before the breakage of the liquid layer) and the time when the coalesced bubble departs from the wall while the typical volume of a single bubble at detachment is about $1\,\mathrm{mm}^3$. This is due to the quickness of the phenomenon: typically 2 to 3 ms, whereas the growth time range is 70 to 300 ms. These results tend to indicate that the liquid film between the bubbles does not evaporate, but is rather pushed away by capillary effects. This conclusion is also drawn for the liquid macrolayer trapped between the two necks.

The liquid film breakage induces the propagation of two wave fronts[42] (see Fig. 5.68 and Electronic Annex 1 in the online version of Siedel *et al.* [169]) at a velocity of about $63\,\mathrm{cm{\cdot}s^{-1}}$. This front distorts the *liquid-vapour* interface. When the wave fronts reach the ends of the coalesced bubble, tails are created by the distortion of the interface. Such tails have been

[42] This wave front propagations have been observed with an unrivalled accuracy due to a very high recording frame rate of 27 000 fps.

shown by Mukherjee and Dhir [133]. The wave is then reflected and attenuated. This wave can be explained by capillary effects: the Laplace-Young equilibrium is obtained before the film breakage, and as both main curvature radii are large ($R_1 \approx R_2 > 10^{-4}$ m, same order of magnitude as the bubble equivalent diameter), the pressure difference between the liquid and the vapour is low ($P_v - P_l < 3.10^{-3}$ bar). When the film breaks up, its thickness is about 1 to 10 μm [158]. The smallest curvature radius R_1 just after the breakage is of the same order of magnitude. The deficit of pressure of the liquid, compared to the Laplace-Young equilibrium, is then of the order of magnitude of 0.1 bar. The shock that creates the wave front on the interface is caused by this deficit of pressure. For a better understanding of the orders of magnitude of R_1 and R_2, Fig. 5.69 shows schematically half of two bubbles (drawn as two halves of spheres), during the merging process: this schematically shows that R_1 is much smaller than R_2.

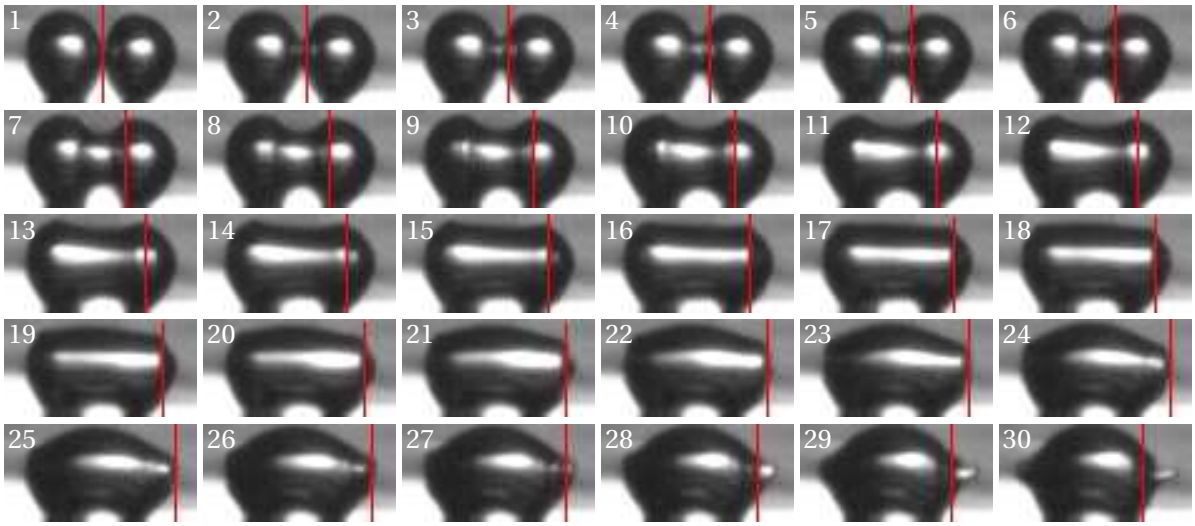

Figure 5.68: Photos of lateral coalescence between adjacent bubbles coming from neighbour nucleation sites, at a high wall superheat of $\Delta T_W \approx 8.5$ K. Time difference between two photos is $\Delta t \approx 37\,\mu$s.

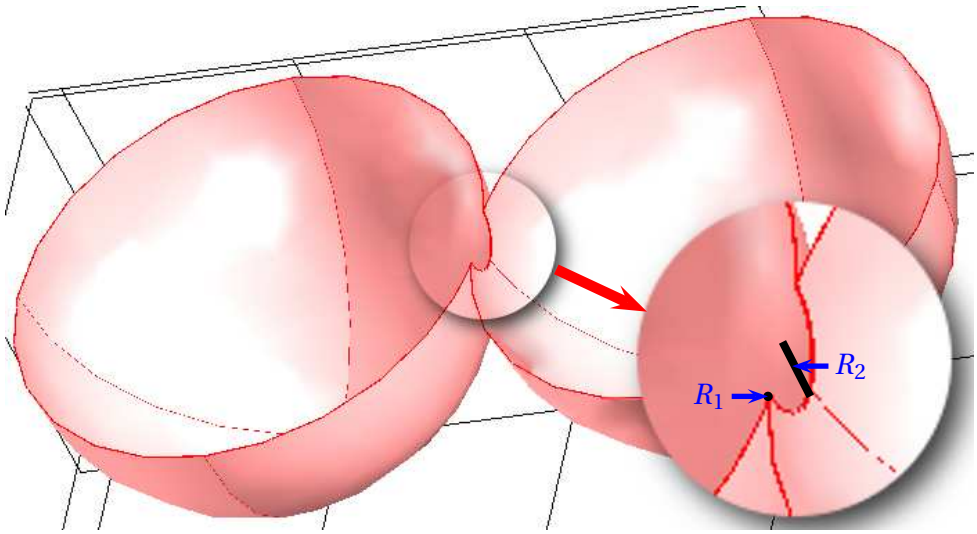

Figure 5.69: Curvature radii at the thin film breakage.

5.4 Bubble departure and rise

The heat transfer mechanisms associated with boiling are detailed in Section 4.1.2. These mechanisms can be divided into two categories:

latent heat transfer which is widely investigated in this chapter through the study of bubble growth and bubble interactions.

sensible heat transfer which is the combination of single phase convection (investigated in Chapter 4) and enhancement of convection due to the liquid motion induced by the bubbles.

The liquid motion is first due to the growth of each bubble. As the liquid to vapour density ratio is equal to more than 200, the vapour produced by means of phase change at the bubble interface will move away. The liquid also moves because of the surface tension forces that tend to minimize the bubble area: even if most of the vapour might be produced close to the base of the bubble, the bubble will grow in size and height over the surface.

A second cause of liquid motion induced by the bubbles is due to the interaction between bubbles and to the occurrence of coalescence events. Two bubbles merging will push away the liquid between them, and the motion of the interface to form a new single bubble is an image of the liquid motion around the bubble.

A third cause of liquid motion induced by the bubbles, maybe the most important, is the motion induced by the rise of the bubbles. After detachment of a bubble from the boiling surface, buoyancy forces tend to accelerate the bubble upwards. Consequently, some liquid is drawn towards the boiling surface and replaces the bubble[43]. The liquid motion induced

[43]This motion has been particularly studied to understand and predict the critical heat flux. Indeed, the resulting vapour drag on the liquid moving toward the surface becomes eventually so severe that liquid is unable

by the motion of the bubbles strongly depends on their acceleration and velocity, and hence on their trajectory. Bubble trajectory is therefore a relevant field of study to better understand the boiling processes.

Bubble rise trajectories have been investigated by Haberman and Morton [72] and of Harmathy [74], in their pioneer work. They described three different kinds of trajectories: linear, helicoidal and zigzag. When the Reynolds number is low, bubbles trajectory is linear. For higher Reynolds number, trajectories are helicoidal or zigzagging, and for even higher Reynolds number corresponding to large bubbles, the trajectories are linear once again.

Keshock and Siegel [92] have shown that when the bubble trajectory is linear, the bubble accelerates suddenly after detachment and then stabilizes at a constant terminal velocity. Harper [75] adds that the drag coefficient differs for a unique bubble or for successive bubbles from the same nucleation site.

Several correlations for the value of the terminal velocity have been suggested, for example by Haberman and Morton [72] or by Harmathy [74]. Peebles and Garber [150] have suggested four different correlations covering a large range of Reynolds number.

The present study focuses on the first millimetres of bubble rise after bubble detachment. These results have been presented at the 7th International Conference on Boiling Heat Transfer [170] as well as at the 2nd Rhône-Alpes/Brazil Meeting on Micro and Nano-Technologies applied to Heat Transfer with Liquid-Vapour Phase Change [38].

5.4.1 Bubble trajectory and vertical velocity

After detachment, no more forces act on the bubble to balance buoyancy. The bubble thus immediately accelerates in the upwards direction. Starting from a very low velocity, the bubble slowly accelerates vertically (see Fig. 5.70 for a typical bubble rise).

The bubbles in these experiments always have the same volume at detachment (see Section 5.1.1.4). The initial conditions of bubble rise are thus very similar for all bubble rise events, even for different wall superheat conditions. The bubble equivalent diameter is $R_{eq} \approx 1\,\text{mm}$. This diameter is slightly lower than the capillary length (which is equal to 1.56 mm for pentane at its normal boiling point). The bubble shape is close to a spherical shape at detachment, except for a neck that detaches or breaks up at the base of the bubble (see Section 5.2.3 for more details on the shape).

Due to the break-up of the neck, the bubble shape oscillates in the vertical direction after detachment (see Fig. 5.71 for instance between image 3 and 11). As some very slight differences might occur between different bubble detachment events, the oscillations observed might also be slightly different[44].

to reach the surface fast enough to keep the surface completely wetted with liquid ([23], page 218)

[44] As for vertical coalescence (see Section 5.3.1), detachment of the bubbles presents some stochastic fea-

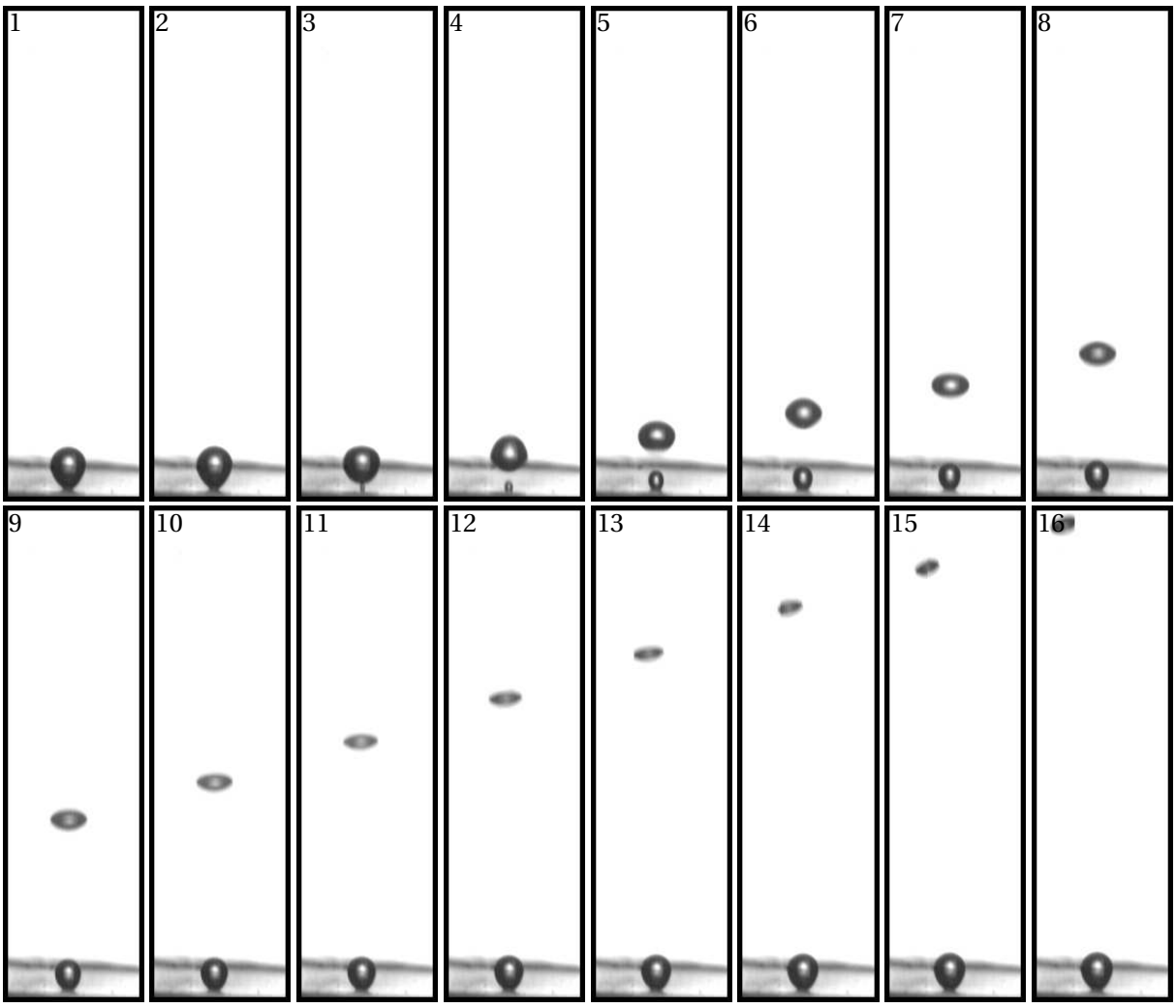

Figure 5.70: Photos of a typical bubble rise, at a wall superheat of $\Delta T_W \approx 3.5\,\mathrm{K}$. Time difference between two photos is $\Delta t = 2.5\,\mathrm{ms}$. Physical height represented is $\Delta z \approx 14\,\mathrm{mm}$.

While the bubble vertical velocity increases, the liquid inertia as well as the viscous stress tend to slow down the bubble and to distort the interface. The bubble is flattened into a distorted oblate spheroid and might even form into a spherical cap shape [184]. It seems from Fig. 5.70 that the bubble volume is decreasing during its rise. This impression is in fact an optical effect: the depth of field is very small[45] and set to have a sharp contour of the attached bubbles. The image is sharp only in the plane perpendicular to the recording direction and passing on the nucleation site. The bubble that is rising often moves slightly from this plane. Its image becomes blurred. Depending on the contrast and brightness settings, the rising bubble will then look larger or smaller.

The height of the center of gravity is computed from the recorded images. It is plotted versus time on Fig. 5.72 for the sample bubble shown in Fig. 5.70. A polynomial function is

tures.

[45] The typical order of magnitude of the field of depth is 0.1 mm.

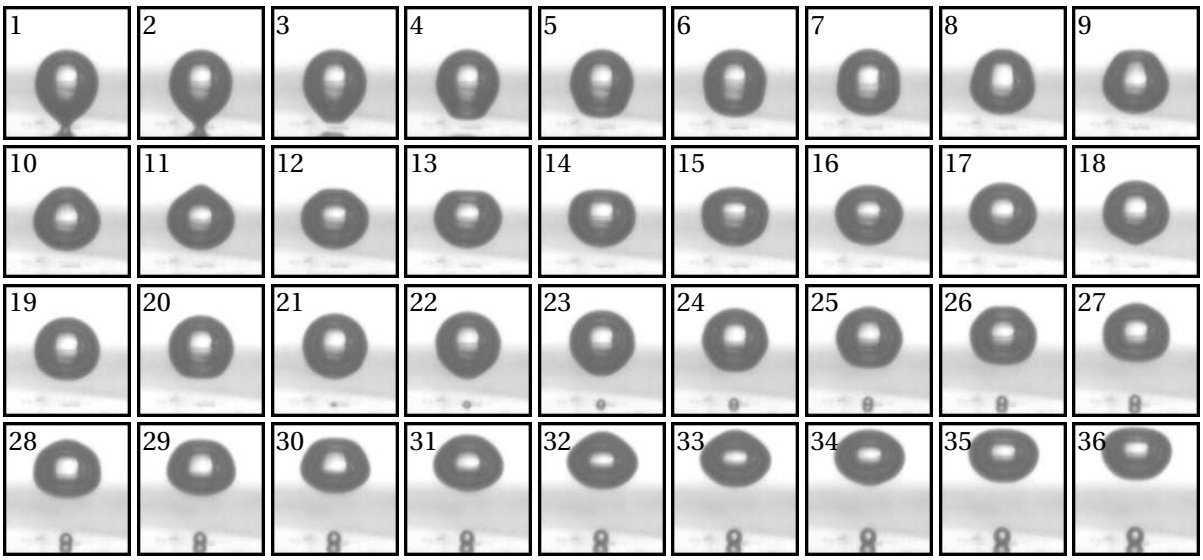

Figure 5.71: Photos of the shape oscillations of a bubble just after its detachment, at a wall superheat of $\Delta T_W \approx 2.1$ K. Time difference between two photos is $\Delta t \approx 333\,\mu$s.

used to fit the calculated data, in order to obtain its derivative with respect to time[46].

The bubble vertical velocity is thus obtained, and plotted versus time together with the lateral position of the bubble on Fig. 5.73. The origin of the lateral position is defined at the initial position of the center of gravity of the bubble. It is observed that the bubble accelerates in the vertical direction until reaching a maximum vertical velocity. This velocity can also be expressed in terms of a critical Reynolds number.

When the critical Reynolds number is reached, the bubble randomly changes its direction. As shown on Fig. 5.73, the horizontal lateral position of the sample bubble remains the same during the acceleration of the bubble and eventually changes at the moment when the maximum vertical velocity is reached. An analogous behaviour was explained by Jenny *et al.* [87] for a free ascending sphere: the sudden change of direction would occur when an instability would break the axisymmetry of the sphere's wake and would impose a plane oblique trajectory.

The transition to zigzag or helical trajectories has been widely observed in bubble rise studies [7, 60, 118, 120, 203]. Ellingsen and Risso [60] pointed out that the primary unstable mode of the bubble rise is the zigzag motion, and that the secondary unstable mode is the helical motion.

[46] i.e. the vertical velocity

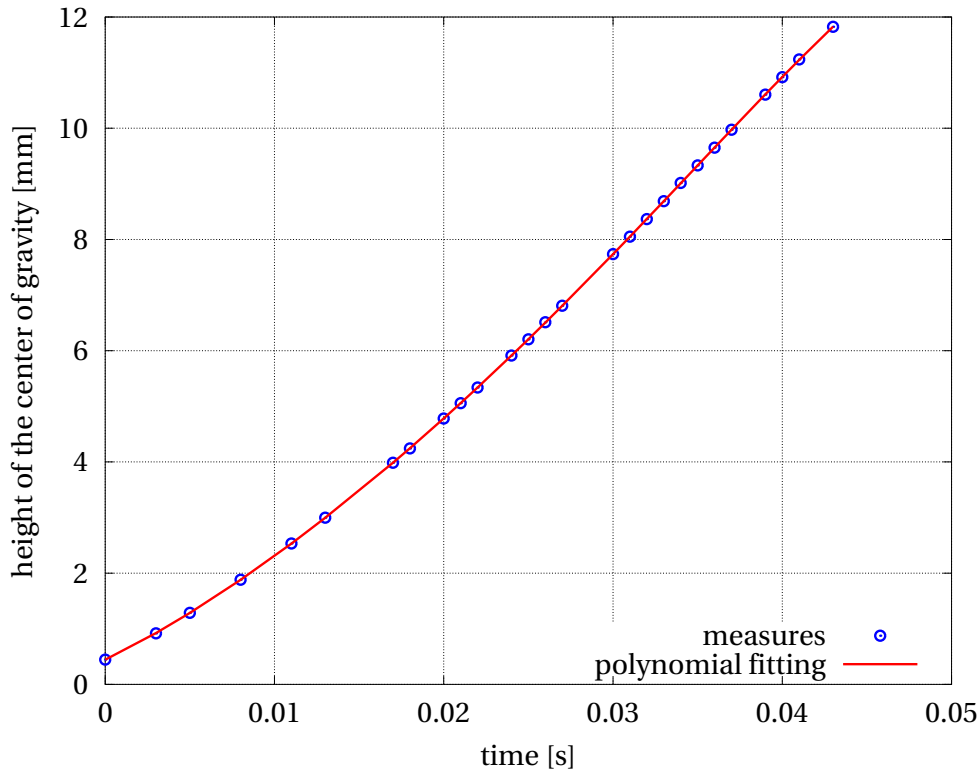

Figure 5.72: Evolution of the height of the center of gravity of the bubble.

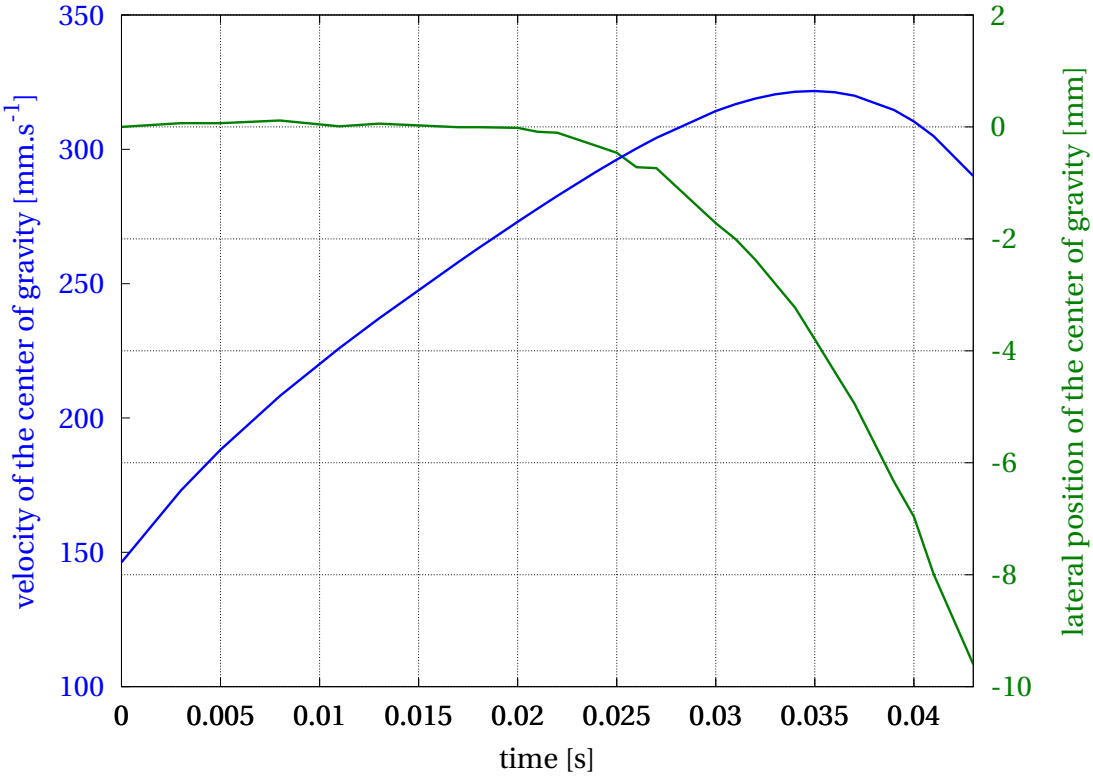

Figure 5.73: Evolution of the vertical velocity and lateral position of the bubble.

5.4.2 Bubble terminal velocity

The bubble rise analysis has been performed for 20 different bubbles for different wall superheats between 1.5 and 8 K. The wall superheat has shown no influence on bubble rise. In all cases, the bubble accelerates until it reaches a maximum velocity in the vertical direction, and then turns to another random direction: sometimes to the left, sometimes to the right, and sometimes the bubbles vertical speed decreases and the bubble seems to be moving toward the direction perpendicular to the picture plane.

The mean maximum velocity[47] has was found to be equal to 331 mm·s^{-1}, with a standard deviation of 12 mm^{-1}. The scattering of the maximum velocities is well explained by Tomiyama *et al.* [184]:

> ...there is a possibility that the scatter of V_T[48] in the surface tension force dominant regime is not caused by the difference in surfactant concentration but by the difference in initial conditions, i.e. the way of bubble releases.

The mean maximum velocity has been compared against the Peebles and Garber [150] model:

$$u_{max} = 0.33 g^{0.76} \left(\frac{\rho_l}{\mu_l} \right)^{0.52} R_{eq}^{1.28} \tag{5.94}$$

With a Reynolds number in the following range:

$$2 \leq \mathrm{Re} \leq 4.02 \left(\frac{\mathrm{We}^3}{\mathrm{Re}^4 \mathrm{Fr}} \right)^{-0.214} \tag{5.95}$$

The characteristic length used for the Reynolds, Weber and Froude numbers calculation in the model is the equivalent radius of the bubble R_{eq}. The maximum velocity calculated with this model is 299 mm·s^{-1} with a Reynolds number of 2.49 . This maximum velocity is of the same order of magnitude as the measured maximum velocity. Beyond the question of the accuracy of the correlation, a difference between the present experiment and that of Peebles and Garber lies in the fact that this experimental work is non adiabatic.

Indeed, the measured velocity is in fact the velocity of the bubble compared to the boiling surface and not to its surrounding liquid. This speed is thus the sum of the bubble's velocity relative to the liquid plus the liquid velocity relative to the boiling surface, assuming that the liquid surrounding the bubble is moving in the same direction as the bubble. This assumption seems to be verified by observing convection images like that of Section 4.1.4.

Another correlation has been compared against the experimental results. An usual correlation for surface tension dominant regimes [128, 130, 185] has been generalized to distorted

[47] This maximum velocity is often referred to as the terminal velocity (e.g. [184]).
[48] i.e. the terminal velocity

oblate spheroid by Tomiyama *et al.* [184]. The usual formulation of the correlation is as follows:

$$u_{max} = \sqrt{\frac{2\sigma}{\rho_l D_{eq}} + \frac{\left(\rho_l - \rho_v\right) g D_{eq}}{2\rho_l}} \tag{5.96}$$

Using the properties of pentane and the geometry of the bubbles of the experiments, the theoretical maximum velocity predicted by this correlation is $u_{max} \approx 227\,\mathrm{mm{\cdot}s^{-1}}$. This value is slightly lower than the experimental value. This might be due to an invalid hypothesis.

The hypothesis of a surface dominant regime states that viscosity forces are small compared to surface tension and inertia forces [184] which is justified if:

$$Re = \frac{\rho_l u_{max} D_{eq}}{\mu_l} \gg 1 \tag{5.97}$$

This is valid in the case of these experiments as $Re \approx 1048$. Other models of bubble maximum rising velocity are reported by Celata *et al.* [25].

To conclude about bubble rise, velocity and trajectory, the experimental observations and measurements are in good agreement with the models and description from the literature. In addition, these results bring new data concerning an unusual fluid[49] and the case of boiling single bubbles[50].

This chapter detailed an original experimental work that presents several important results for the knowledge of the most fundamental phenomena that occurs during pool boiling.

- *After ensuring the repeatability and reliability of the measurements, an experimental bubble growth law was established. This law raises new questions about the mechanisms of phase change and heat transfer during bubble growth, and questions some usual assumptions of many existing growth models and experiments.*
- *Bubble shape and oscillations were investigated, and a new non-dimensional parameter was proposed in order to describe the oscillation. The influence of the previous bubble on the next bubble at moderate wall superheat was brought to the fore.*
- *The different forces implied in the integral form of the momentum conservation equation were deeply investigated. Each term has been described and evaluated, and the equation was solved for each moment of an experimental bubble growth. It is noticeable that the exact solution of the momentum variation has been computed.*
- *The bubble curvature along the interface was divided into two main curvatures and was computed for different time-steps during bubble growth. The evolution of the vapour pressure was interpolated from the curvature along the interface, and the specificity of the curvature close to the triple line was highlighted.*
- *Bubble vertical and lateral coalescence has been described, as well as the occurrence of a wave front propagation during merging of neighbouring bubbles.*

[49] Many experimental works from the literature use water.

[50] Most experimental works are performed adiabatically using gas injection in a liquid.

- *Bubble rise, trajectory and vertical velocity were investigated. Comparison against existing models of the terminal velocity were performed, and showed good agreement.*

Some of the results shown have been published in peer-reviewed journals [169, 171] and some have been presented in international conferences [38, 168, 170] where they were received with great interest. Other results are still waiting for future publication.

Chapter 6

Bubble dynamics in the presence of electric fields

Since boiling heat transfer affords a very effective means to transfer heat, it is implemented in numerous technologies and industries ranging from large power plants to micro-electronics thermal management. No matter what the scale of the technology, industries are continually demanding smarter and smaller heat exchangers. A promising technique for improving and controlling the heat transfer during boiling is the introduction of an electric field. This technique is generally termed electrohydrodynamics (EHD). Whether for pool boiling or flow boiling scenarios, several studies have shown that EHD can considerably augment two phase heat transfer (e.g. [47, 82, 116, 127, 140, 142] and the review on electrohydrodynamic enhancement of heat transfer by Laohalertdecha et al. *[104]).*

Most studies concerning electrohydrodynamics applied to two-phase heat transfer concern boiling on natural surface and associated heat transfer coefficients. However, as the boiling heat transfer coefficient is difficult to predict and is intimately linked to the bubble dynamics, it is prudent to investigate the EHD effects at the scale of a single bubble. A limited number of studies concern the behaviour of single bubbles in the presence of electric fields, among which several are adiabatic (i.e. a gas bubble is injected in a dielectric liquid) [29, 49, 54, 78, 79, 86, 117, 123, 125, 126, 151], in a more or less isolated *bubble regime [100, 119] or approximate numerical or theoretical analyses [61, 198, 200, 201]. The present work aims at being a reference experimental study of electrohydrodynamic effects on bubble dynamics in the case of boiling on an artificial nucleation site.*

The present chapter is organized similarly to Chapter 5 to successively investigate the electrodynamic effects on bubble growth, detachment and shape, on bubble interaction with neighbouring bubbles and on bubble rise. A detailed analysis of the phenomena in the absence of electric fields is provided in Chapter 5 so that only the influence of the electric field will be investigated in depth. The force analysis and momentum balance of the growing

bubble is not included in the present study.

6.1 Bubble growth

Bubble growth dynamics has been widely studied in the absence of electric fields. As described in Section 5.1, many theoretical analyses and experimental studies concern single bubble growth. However, to the author's best knowledge, no published work focuses on the effect of electrohydrodynamics on bubble growth dynamics in the case of boiling. The closest experimental study to the present work has been performed by Cattide *et al.* [24]. These authors investigated boiling on a single artificial nucleation site on a stainless steel sheet with two different well-wetting dielectric fluids[1]. Heat was provided by a micro-heater located below the steel surface. The heated surface was connected to ground and a voltage potential was created by a ring electrode 3 mm above the plate. The influence of electric field on bubble detachment diameter and growing period was investigated and some raw data concerning the evolution of the equivalent diameter with variable heat load is available.

The experimental results presented in this section focus on the effect of electrohydrodynamics on bubble growth dynamics, detachment diameter and frequency and on bubble shape during its growth. These results have been published in 2011 by Siedel *et al.* [171]. The heated surface is connected to ground and the grid mesh electrode above the surface is connected to the high voltage source. For the sake of readability, the potential of the upper electrode is positive when no indications is given or when a positive polarity is mentioned. In all experiments, the grid mesh electrode was located 7 mm above the heated surface. Experiments have been performed by applying 12 kV, 18 kV or 24 kV to the electrode. This corresponds, in the case of a homogeneous dielectric permittivity between the electrodes, to uniform and vertically oriented electric fields of respectively 17.1 kV·cm^{-1}, 25.71 kV·cm^{-1} and 34.3 kV·cm^{-1}. Only the value of the voltage applied to the upper electrode will generally be mentioned in this chapter.

Photo sequences of bubble growth with an applied voltage of 12 kV, 18 kV and 24 kV are presented in Fig. 6.1, 6.2 and 6.3 respectively. Approximately the same wall superheat was imposed[2]. The first observation is that the bubble is elongated in the vertical direction by the electric field. This observation will be discussed further in this section.

[1] namely FC-72 and HFE-7100

[2] 3.6 K < ΔT_W < 4.1 K

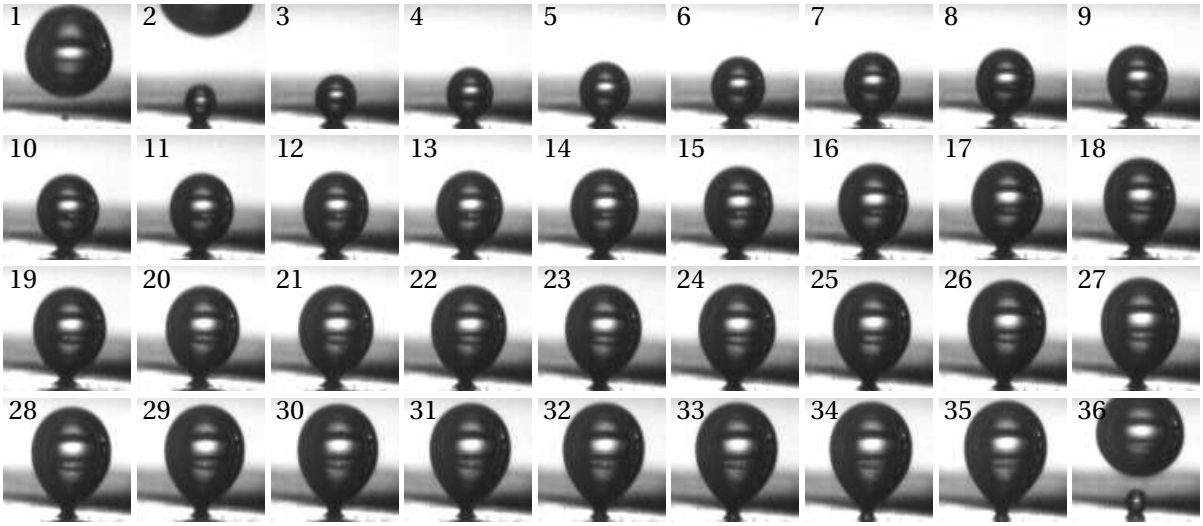

Figure 6.1: Bubble growth at $\Delta T_W \approx 3.6\,\mathrm{K}$, with $\Delta t = 8\,\mathrm{ms}$ between two images. A tension of 12 kV is applied on the electrode.

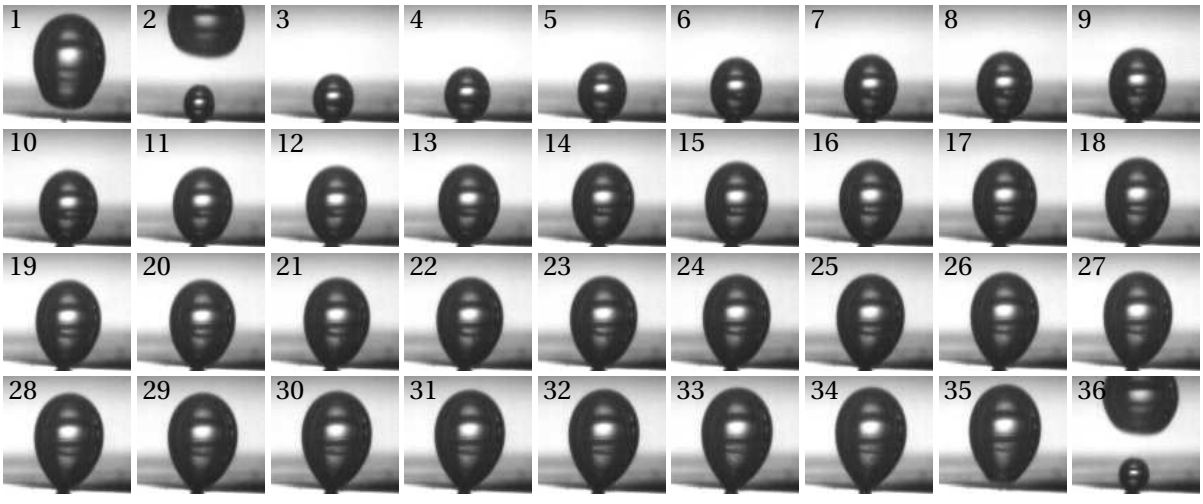

Figure 6.2: Bubble growth at $\Delta T_W \approx 4.1\,\mathrm{K}$, with $\Delta t = 8\,\mathrm{ms}$ between two images. A tension of 18 kV is applied on the electrode.

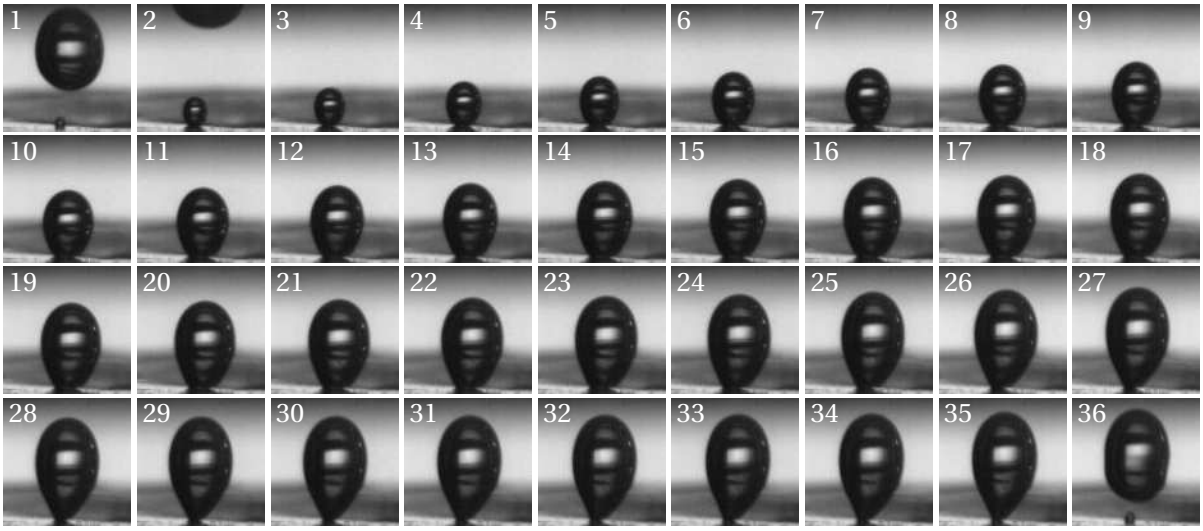

Figure 6.3: Bubble growth at $\Delta T_W \approx 3.7$ K, with $\Delta t \approx 6.33$ ms between two images. A tension of 24 kV is applied on the electrode.

6.1.1 Repeatability and reproducibility

Bubble nucleation, growth, detachment and rise is a cyclic event. As observations and measurements are performed on individual cycles, it is essential to evaluate the repeatability and reproducibility of the event. Although a very good similarity had been found when studying bubble dynamics without electric fields (in Chapter 5), more experimental issues were encountered when studying electrohydrodynamic effects on bubble dynamics:

- With the presence of the mesh grid electrode above the heated surface, adequate illumination of the surface was difficult to achieve. The images recorded were of poorer quality (see for example Fig. 6.1, 6.2 and 6.3), and proper processing of the photos to measure bubble properties was more difficult to define.
- As detailed in Section 4.1.4[3], strong convective movements occur when applying an electric field above the heated surface. These convective movements slightly change the background brightness in the recorded images. This effect sometime prevents the batch processing of images because of varying brightness.
- Because of the time restriction and of the difficulty creating a stable nucleation site on such a test sample, the data originates from a single experimental campaign.
- More parameters and more forces are involved in bubble dynamics with EHD. Less accuracy may be achieved in reproducing experimental conditions. This is likely due to unsteady convective motion above the heated plate that creates a different thermal environment even for two successive bubbles.

[3] This is especially noticeable in Fig. 4.3.

- After several days of use of the experimental facility, some impurities or deposits were sometimes observed in the tank. The sedimentation of these impurities were occurring at the bottom of the tank, far from the heated surface. However, these impurities were polarized by the intensity of the electric fields and were directed towards one of the electrodes during the tests. In was then often necessary to dismantle the whole facility to change the fluid to new, pure pentane.

Figure 6.4 shows the volumetric growth curves of 7 successive bubbles at a wall superheat of 3.7 K with an electrode voltage of 24 kV. The curves show a certain scatter of growth time. The total growth time, in the same conditions, varies from 0.16 to 0.23 s[4]. On the other hand, the departure volume is almost constant with a mean value of 0.51 mm^3 and a standard deviation of 1.6 % on this data sample.

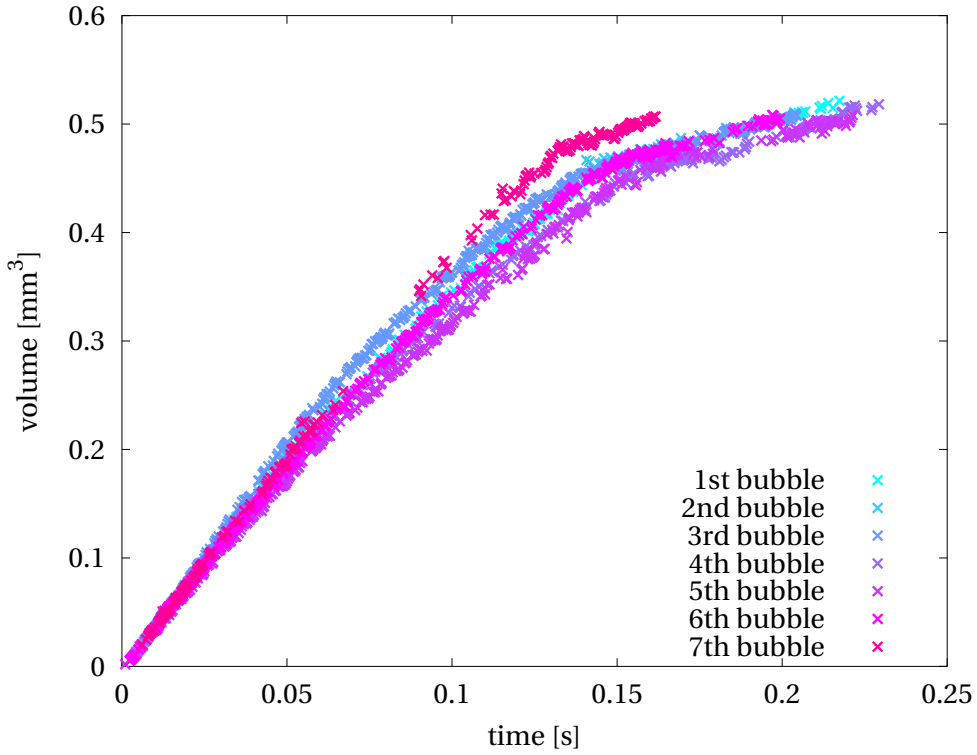

Figure 6.4: Growth curves of 7 successive bubbles at a wall superheat of 3.7 K and with an electrode voltage of 24 kV.

It is noticed that the departure volume is very similar to that obtained in the absence of electric field. However, the growth time seems much more scattered, as one would expect for different superheat conditions. This might indeed be due to different fluid superheat conditions due to the convective movements enhanced by the electric fields.

As a conclusion about repeatability, the results obtained with the presence of electric fields are more scattered than those obtained in the absence of electric fields, presented in

[4] that is ±31 % around a mean value

Chapter 5. Therefore, while qualitative trends can certainly be captured from this study, quantitative measurements should sometimes be taken with a note of caution.

6.1.2 Influence of the wall superheat

In the absence of electric fields, as detailed in Chapter 5, the influence of the wall superheat conditions on bubble dynamics is mainly to modify the vapour production rate. As the dynamic forces acting on the bubble are negligible compared to the static forces, the volume at detachment remains constant. The increase of vapour production rate with the wall superheat causes an increase in the bubble frequency. It was nevertheless observed that the non-dimensional growth curves were similar for all superheats investigated.

With the application of an electric field above the heated surface, the changes in bubble dynamics are investigated including the influence of the wall superheat and the intensity of the electric field. These influences will be discussed in terms of growth curves and of bubble departure frequencies.

6.1.2.1 Bubble growth

Bubble growth curves are presented for different wall superheat conditions with an electrode voltage of 12 kV (Fig. 6.5), 18 kV (Fig. 6.6) and 24 kV (Fig. 6.7). The growth curves of several bubbles with the same wall superheat are shown in some cases.

The growth curves presented here show several different behaviours with the variation of the wall superheat ΔT_W and the electrode voltage U:

- It seems that the bubble departure is sometimes anticipated due to the electric field. For a voltage electrode of 12 kV and 18 kV (Fig. 6.5 and 6.6), the volume at departure is about 0.42 mm^3. This is 20 % lower than the departure volumes observed in the absence of electric field. For an electrode voltage of 24 kV (Fig. 6.7), the departure volume is only reduced for one wall superheat condition. This behaviour is not always repeatable. Such variations were also observed by Cattide *et al.* [24].

- The growth curves present a characteristic change of slope. In the absence of electric field, this change was observed approximately for $0.2 < t^* < 0.3$. This change of slope is observed later when an electric field is applied. This is especially visible for an electrode voltage of 24 kV.

No definitive trend can be determined for the variations of the volume at departure with the voltage. The influence of electric fields on the bubble growth time can be analysed in terms of bubble frequency.

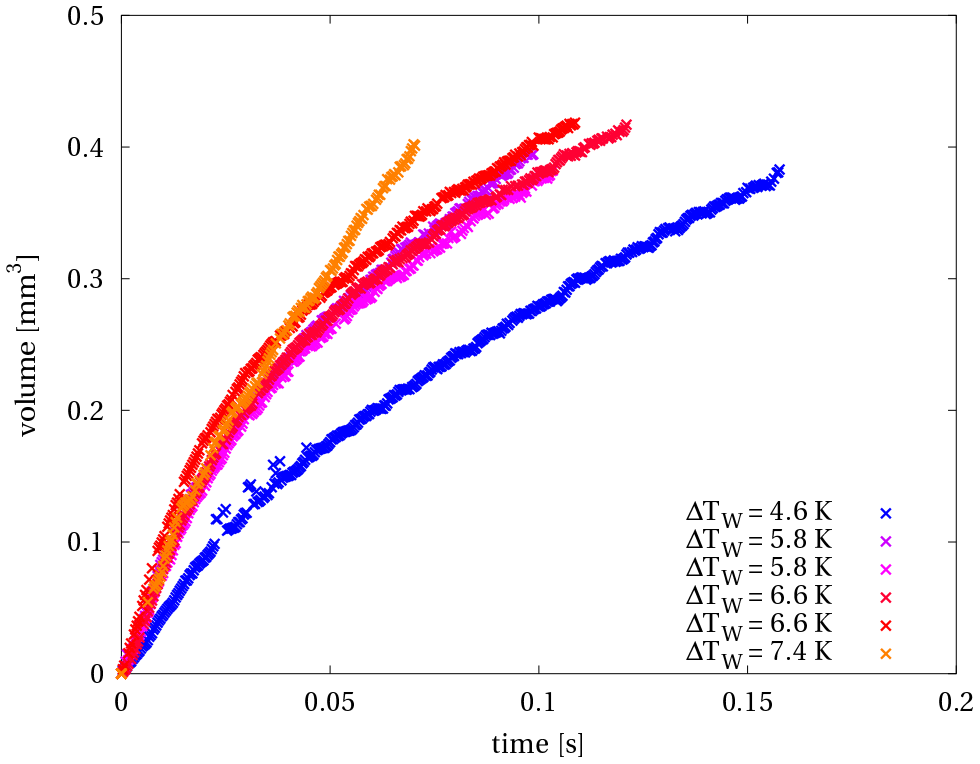

Figure 6.5: Bubble growth for different wall superheats with an upper electrode voltage of 12 kV.

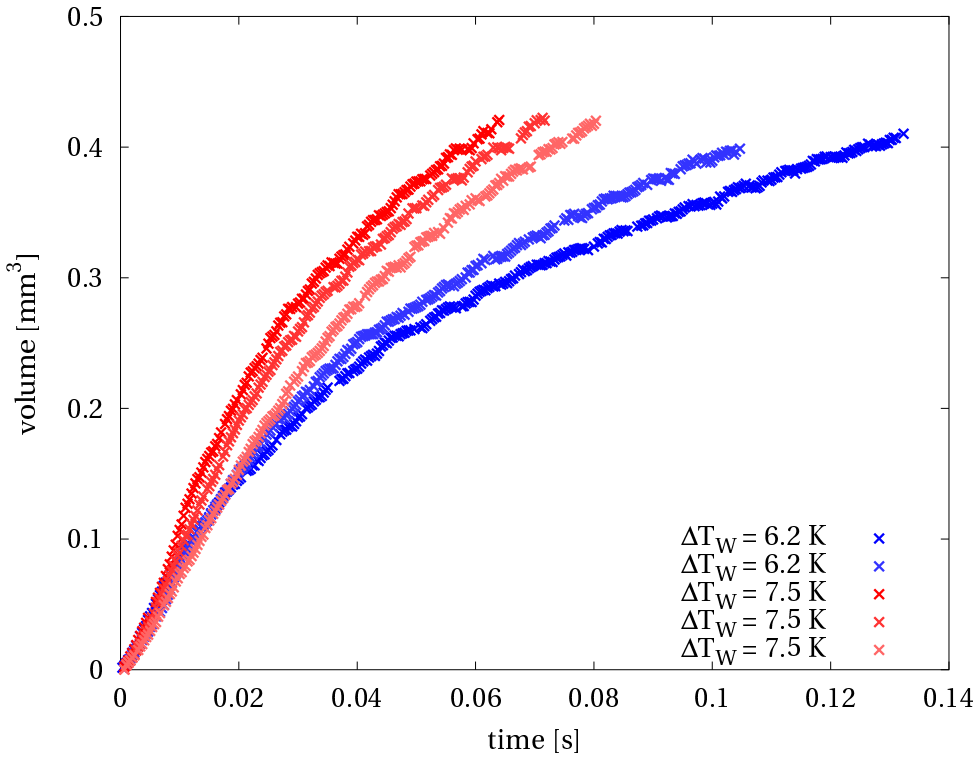

Figure 6.6: Bubble growth for different wall superheats with an upper electrode voltage of 18 kV.

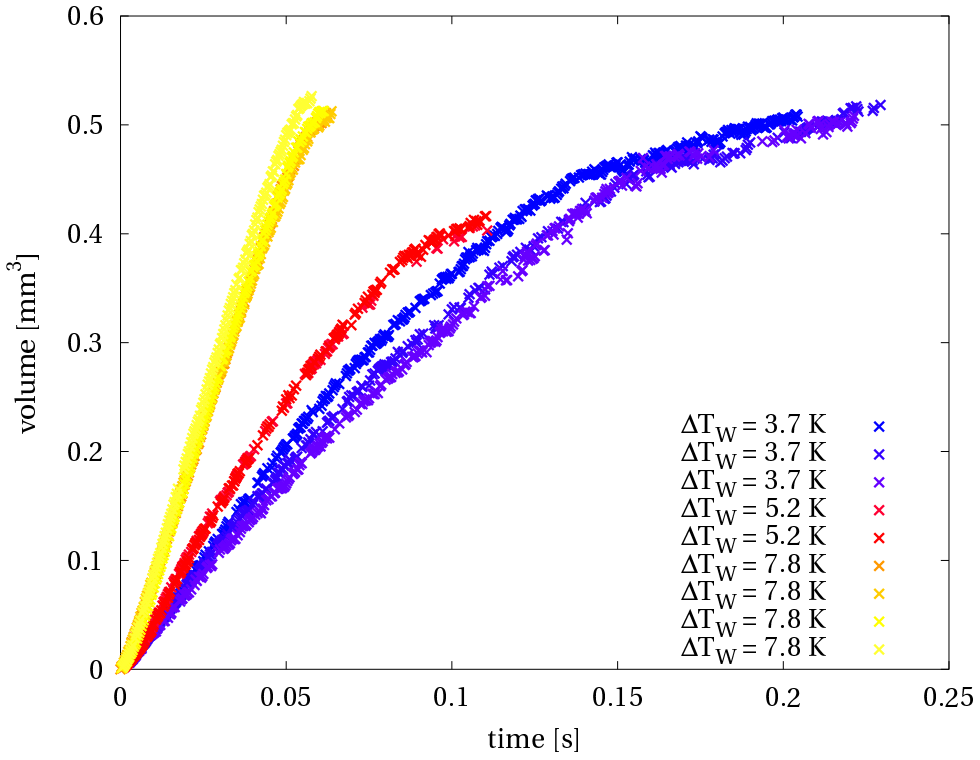

Figure 6.7: Bubble growth for different wall superheats with an upper electrode voltage of 24 kV.

6.1.2.2 Bubble frequency

Like in Chapter 5, the frequency is based on the count of departing bubbles as long as no coalescence occurs, and on the count of departing coalesced bubbles otherwise[5]. Let the instantaneous frequency be defined as the inverse of the growth time of a single bubble event.

Figure 6.8 shows the mean bubble frequency over data samples of 5 successive bubbles, plotted versus the wall superheat for different electrode voltages. No clear influence of the presence of electric fields is observed within the voltage range applied to the electrode.

6.1.3 Non dimensional bubble growth and vapour production rate

As for the study of bubble dynamics without electric fields (see Section 5.1.3), the growth curves have been normalized by dividing the time by the total growth time ($t^* = t/t_d$), and the volume by the departure volume ($V^* = V/V_d$). However, as the growth curves are not similar when varying the wall superheat conditions and the intensity of the electric fields applied, it is more difficult to make meaningful comparisons. Detailed figures showing non-dimensional growth curves for each upper electrode voltage can be found in Appendix G.

[5]It should be noticed that the occurrence of coalescence seems even more stochastic in the presence of electric fields.

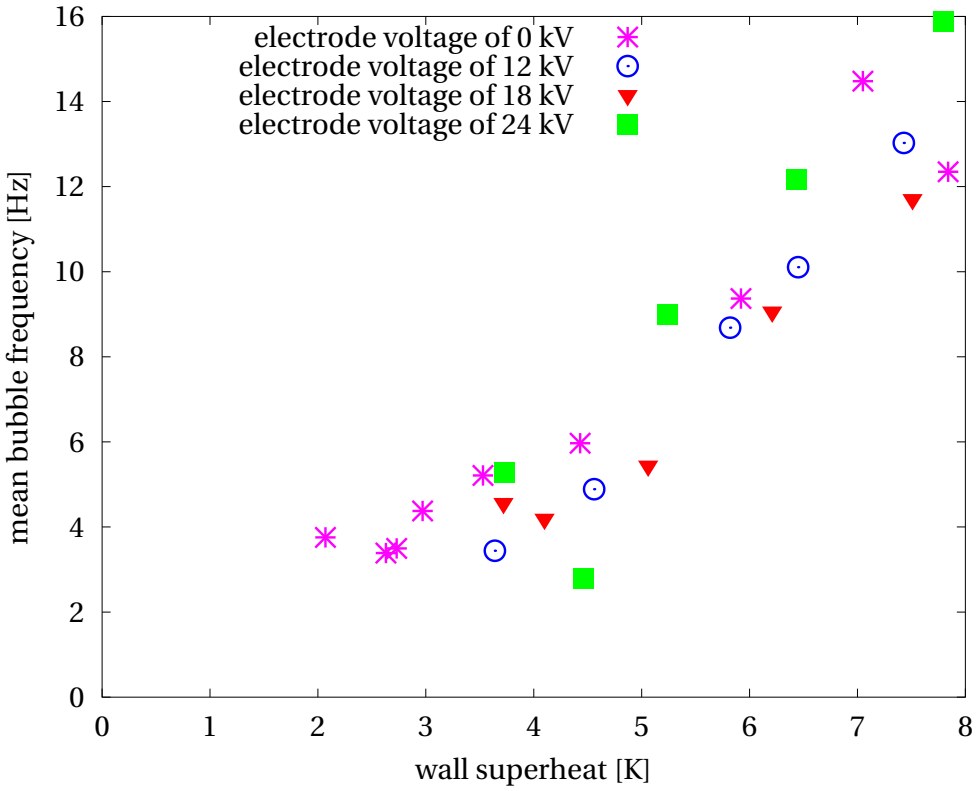

Figure 6.8: Mean bubble frequency vs. wall superheat.

The effects of the voltage on non dimensional bubble growth is shown in Fig. 6.9. It is observed that with high electric fields[6], the bubble growth is more linear. The typical change of slope in the growth curve appear late for $0.6 < t^* < 0.8$.

The effects of the wall superheat on non dimensional bubble growth in the presence of electric fields is shown in Fig. 6.10. No clear trend can be detected.

All growth curves in the presence of electric fields are compared to the experimental data in the absence of electric field and to power laws of $V^* = t^{*0.5}$ and $V^* = t^*$. It can be observed that all growth curves in the presence of electric fields are scattered around the growth curve obtained in the absence of electric field, but stay mostly within the range of power law $V \propto t^{0.5 \to 1}$. The exponent of the power remaining below unity, the volumetric growth rate[7] is decreasing during bubble growth, as it was already observed in the absence of electric field[8].

[6] i.e. for an electrode voltage of 24 kV
[7] that is roughly proportional to the vapour production rate
[8] See Section 5.1.4 for more details in the absence of electric fields.

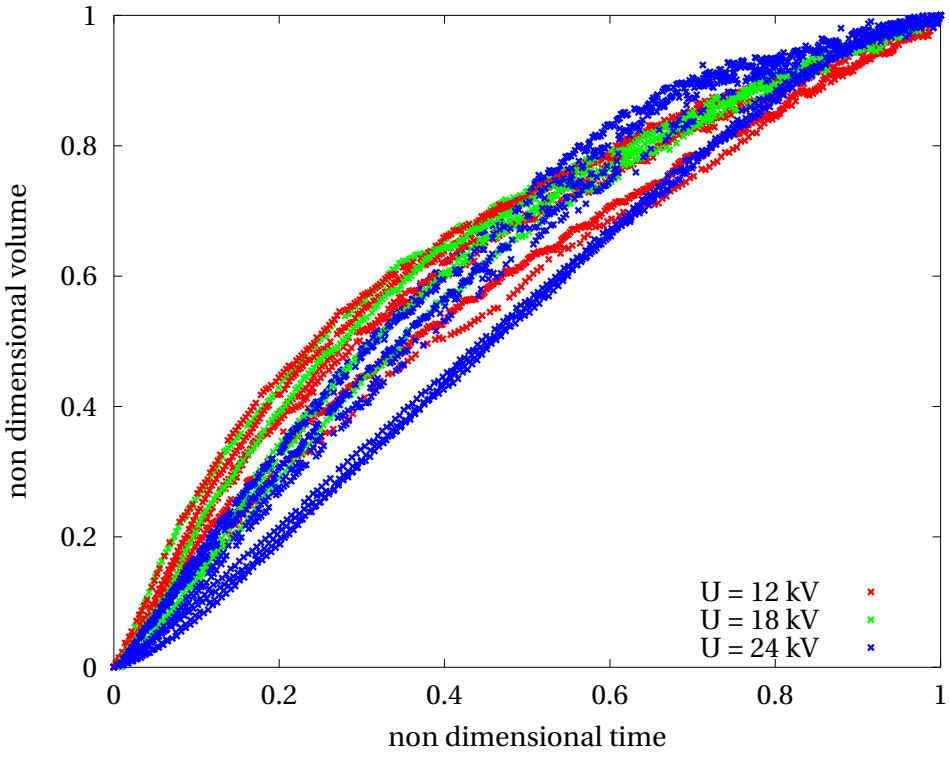

Figure 6.9: Non dimensional bubble growth with different intensities of the electrode voltage.

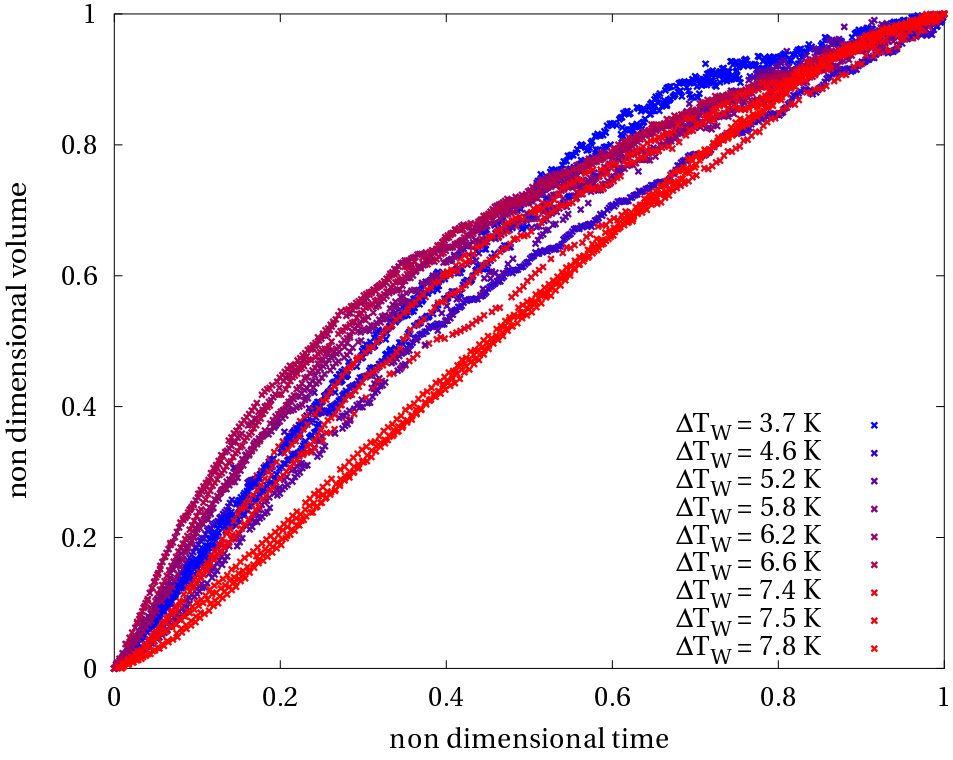

Figure 6.10: Non dimensional bubble growth in the presence of electric fields for different wall superheat conditions.

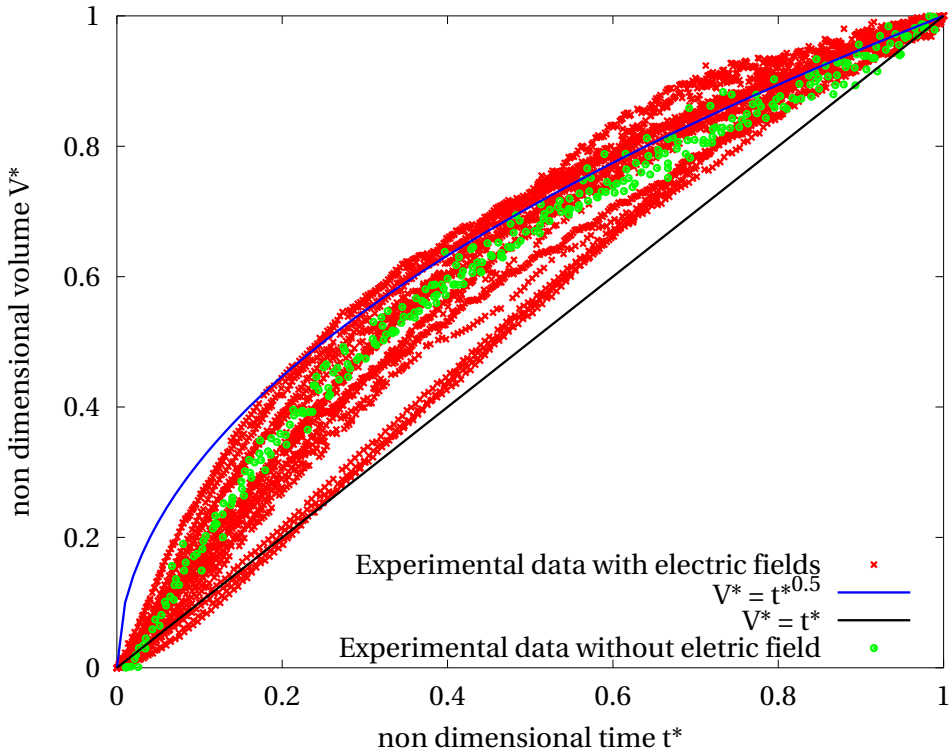

Figure 6.11: Comparison of non dimensional bubble growth in the presence of electric fields with experimental data without electric fields.

6.1.4 Bubble shape and deformation

As discussed in Section 5.1.5, the bubble shape plays a key role in the description and understanding of boiling. Indeed, forces that cause bubble detachment and liquid motion in the vicinity of the bubble are closely related to the shape of the bubble.

Bubble elongation due to the presence of electric fields is the first immediate visual consequence of the application of electric fields, as can be seen in the images of Fig. 6.1, Fig. 6.2 and Fig. 6.3. Bubble height and width, and especially the ratio of the height over the width[9] are parameters often used to describe the deformation of a bubble cause by electrohydrodynamic effects.

The height and width of several bubbles at various wall superheat conditions are shown for a voltage of 12 kV, 18 kV and 24 kV in Fig. 6.12, 6.13 and 6.14 respectively. Despite the oscillations and the scattering of the data, the same trends are observed at all electric fields conditions. Similarly to the observations without electric field (see Section 5.1.5), the height quickly exceeds the width with the formation of the bubble neck. This difference tends to increase with the intensity of the applied electric fields. The bubble width at detachment remains constant with a value of about 0.85 mm, whereas the bubble height at detachment increases from 1.2 mm for an electrode voltage of 12 kV to 1.45 mm for an electrode voltage

[9] commonly referred to as aspect ratio AR

of 24 kV.

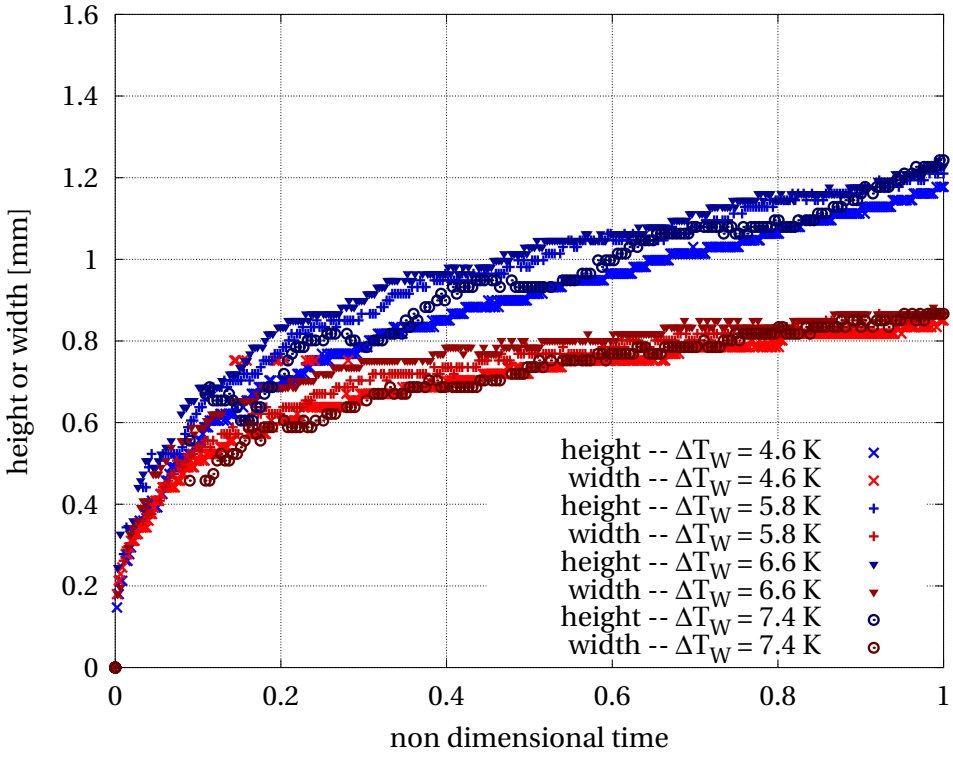

Figure 6.12: Bubble height and width for a voltage electrode of 12 kV.

The height over width ratio, namely the aspect ratio, is plotted for various wall superheat conditions and upper electrode voltages. Detailed figures at each electrode voltages are shown in Appendix H, and a figure with all conditions is shown in Fig. 6.15. The aspect ratio in the absence of electric field is plotted in magenta, and the aspect ratio with electrode voltages of 12 kV, 18 kV and 24 kV are plotted in red, green and blue respectively (i.e. from bottom to top of the figure).

Clears trends can be observed in Fig. 6.15 concerning the evolution of the aspect ratio during bubble growth. At any time of the bubble growth, the higher the voltage, the higher the aspect ratio.

The aspect ratio at detachment has been investigated by Chen *et al.* [29] and by Peng *et al.* [151]. The aspect ratio has been compared to a non-dimensional number, called electric Weber number We_e, that describes the ratio between the electric forces and the surface tension forces. The electric Weber number is expressed as follows:

$$We_e = \frac{\varepsilon_0 \varepsilon_{rl} E_0^2 R_{eq}}{\sigma} \tag{6.1}$$

with ε_0 the void permittivity[10], ε_{rl} the relative permittivity of the liquid phase, E_0 the initial

[10] $\varepsilon_0 = 8.854 \times 10^{-12}$ F·m^{-1}

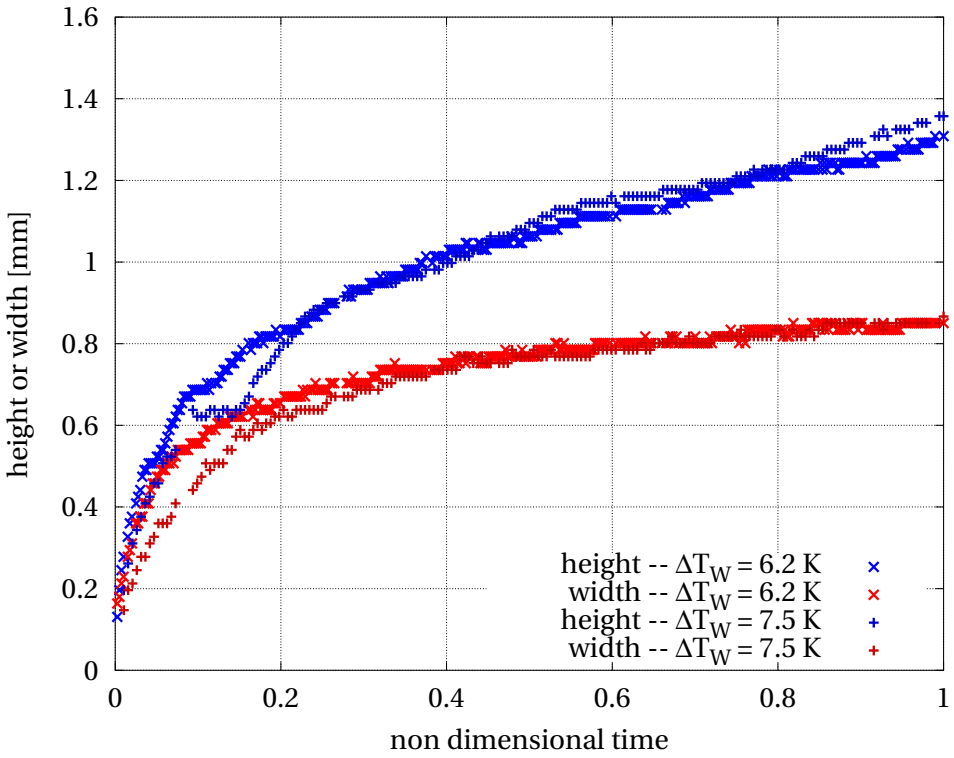

Figure 6.13: Bubble height and width for a voltage electrode of 18 kV.

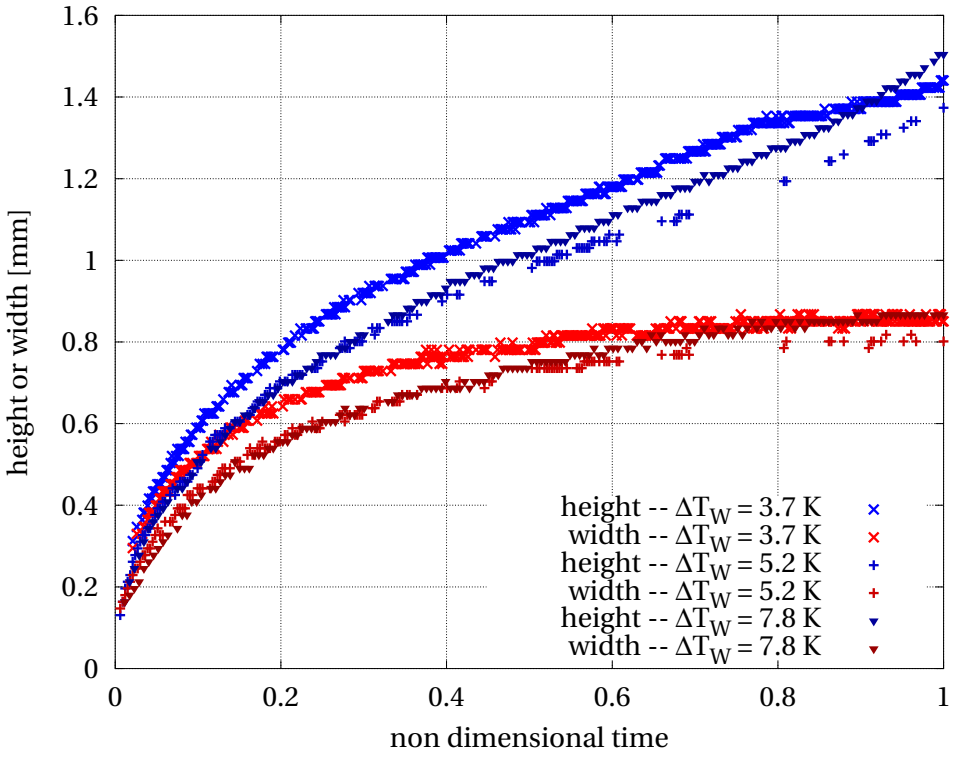

Figure 6.14: Bubble height and width for a voltage electrode of 24 kV.

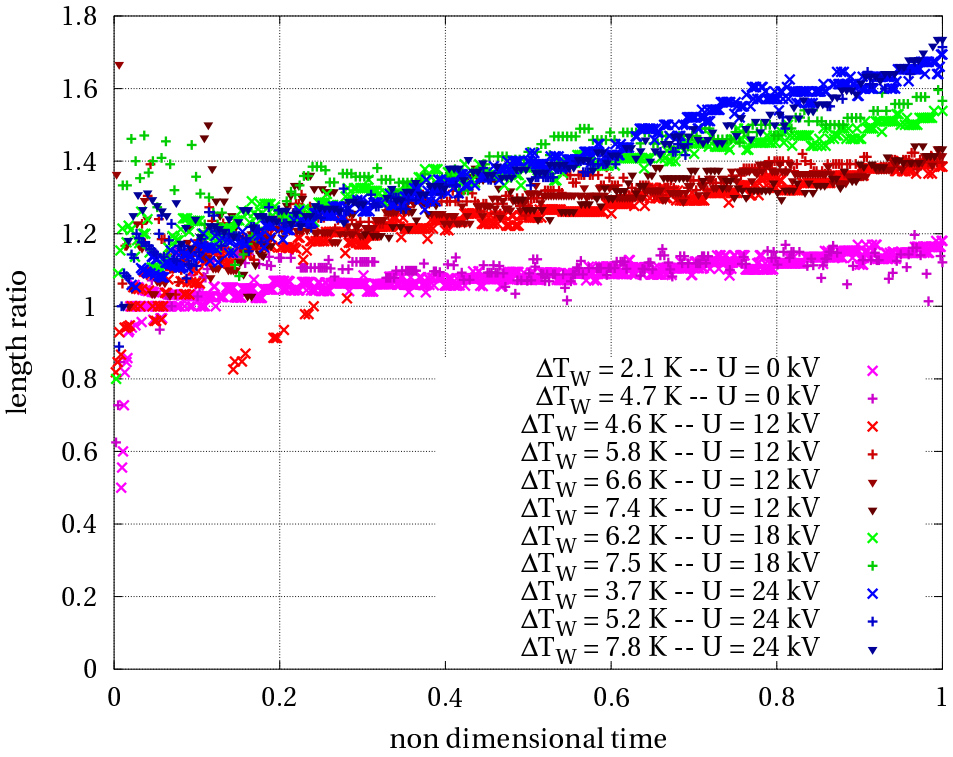

Figure 6.15: Height over width ratio with different electrode voltages.

homogeneous electric field[11], R_{eq} the equivalent radius of the bubble at detachment and σ the surface tension between the liquid and vapour phases.

The mean aspect ratio at detachment in the present experimental conditions is shown in Fig. 6.16 together with experimental data from Chen *et al.* [29] and Peng *et al.* [151]. The same trends are observed with different aspect ratios in the absence of electric fields.

In order to further compare the effects of electric fields on the aspect ratio, the relative increase of the aspect ratio with respect to the case of the absence of electric field is plotted as a function of We_e and shown in Fig. 6.17 together with experimental data from Cho *et al.* [35], Chen *et al.* [29] and Peng *et al.* [151]. The present experiment data are close to the mean values of the experimental data from the literature. The increase of aspect ratio as a function of the electric Weber number is roughly linear.

6.2 Coalescence of bubbles

As detailed in Section 5.3, during boiling in the absence of an electric field, the coalescence phenomenon corresponds to the case where two or more bubbles come so close to each other that they merge to form a single resulting bubble. Coalescence plays a prominent role

[11] That is: in the absence of a bubble. E_0 is then the upper electrode voltage divided by the distance between the electrodes.

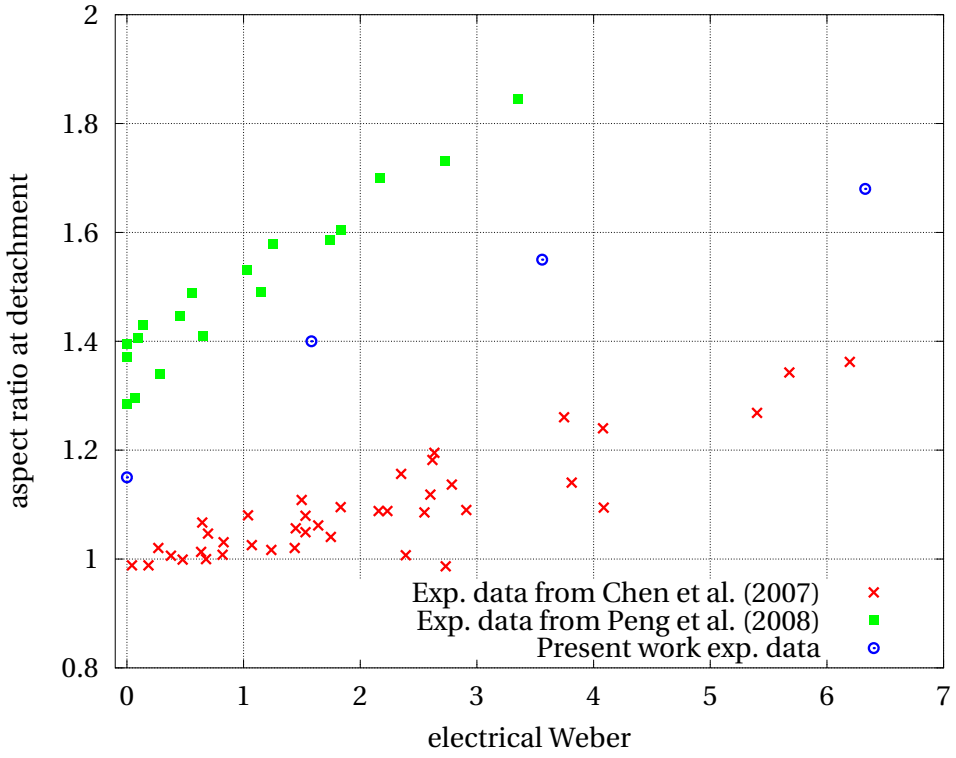

Figure 6.16: Comparison of aspect ratio to experimental data from Chen *et al.* [29] and Peng *et al.* [151].

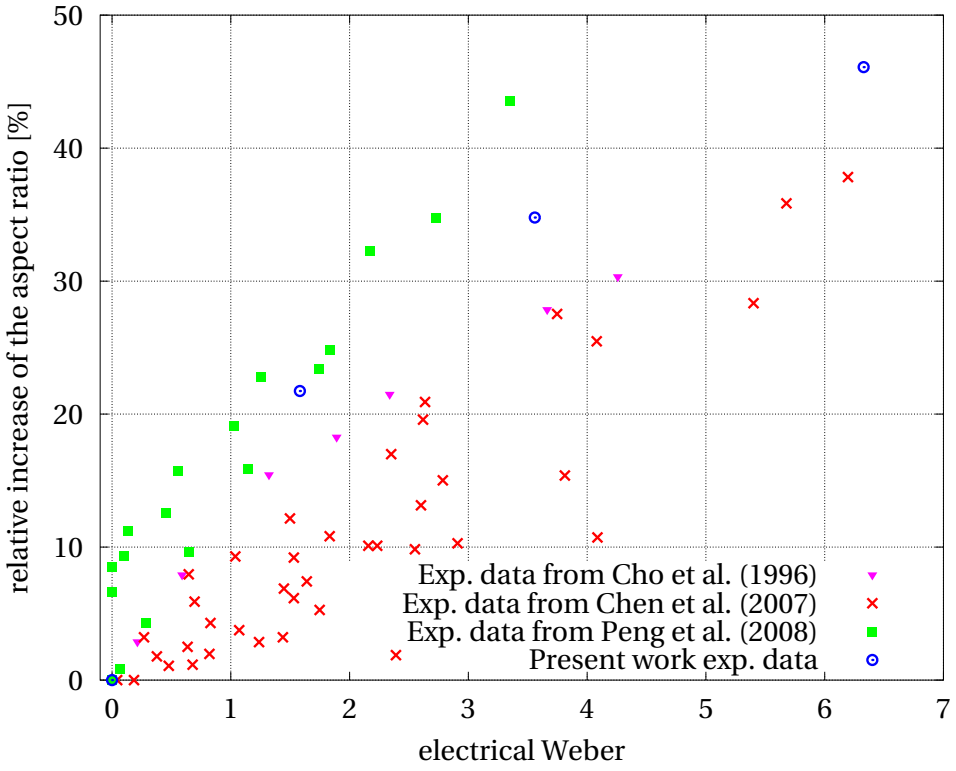

Figure 6.17: Aspect ratio increase with electric field. Comparison to experimental data from Cho *et al.* [35], Chen *et al.* [29] and Peng *et al.* [151].

in boiling heat transfer as it is the source of liquid motion[12] at the vicinity of the merging bubbles but it can also inhibit the liquid motion towards the heated surface[13] as the resulting bubbles have a larger volume and inertia to move away from the boiling surface. Coalescence is thus the key phenomenon that may lead to a maximum heat transfer rate in the early fully developed boiling regime (see Section 2.2 and also Liu *et al.* [117]) and is also a phenomenon that may contribute to the triggering of the critical heat flux by preventing the liquid from rewetting the boiling surface [23].

Even being such an important phenomenon in boiling, coalescence is poorly understood, as it can be inferred from the recent studies focusing on this phenomenon [18, 68, 69]. Coalescence is indeed a stochastic phenomenon as many temporal and spatial parameters related to the occurrence of boiling can usually not be measured or determined.

In the presence of electric fields, the coalescence phenomenon has been rarely investigated at the scale of two neighbouring bubbles. Liu *et al.* [117] have proposed a review on the behaviour of neighbouring bubbles in the absence of electric fields. They have in the same study investigated the influence of a non-uniform electric field on the behaviour of single and neighbouring injected gas bubbles in a dielectric fluid. They have noted that for the single bubble experiments, the detaching bubble is either deformed away or towards the upper electrode. For the case of two bubbles injected simultaneously in neighbouring orifices, their tendency was to repulse each other, which prevents coalescence at moderate volumetric flow rates.

To the author's best knowledge, no past study has investigated the influence of a uniform electric field on the coalescence of bubbles growing in pairs. The following observations and results come from experiments performed using the double nucleation site test sample as described in Section 5.3. Bubble are growing on two identical artificial nucleation sites, located at a distance of 660 µm from each other. A same wall superheat condition between 8.0 and 8.2 K is ensured by adjusting the heat flux supplied to the test sample. The upper electrode, located 8.7 mm above the heated surface, is connected to the high voltage generator. Positive voltages of respectively 0, 6, 12, 18, 24 and 30 kV are imposed to the upper electrode in 6 different experiments.

It should be noted first that in each experiment, the bubbles growing on the artificial nucleation site located on the left side of the photos always grow slightly faster[14]. For low to moderate electrode voltages between 0 and 12 kV, the scenarii are very similar. The bubbles nucleate at about the same time at each nucleation site, and then coalesce after a growing period between 120 and 150 ms (see Fig. 6.18). The resulting bubble immediately detaches from the surface, and new bubbles are instantaneously nucleating at both nucleation sites. Some vertical coalescence events may occur between the new growing bubbles and the previously merged bubble, and a new cycle begins.

[12] and thus enhanced convection

[13] and prevent the rewetting of the surface

[14] As explained by Bonjour *et al.* [18], the heat flux inside the wall may be deflected towards one of the nucleation sites.

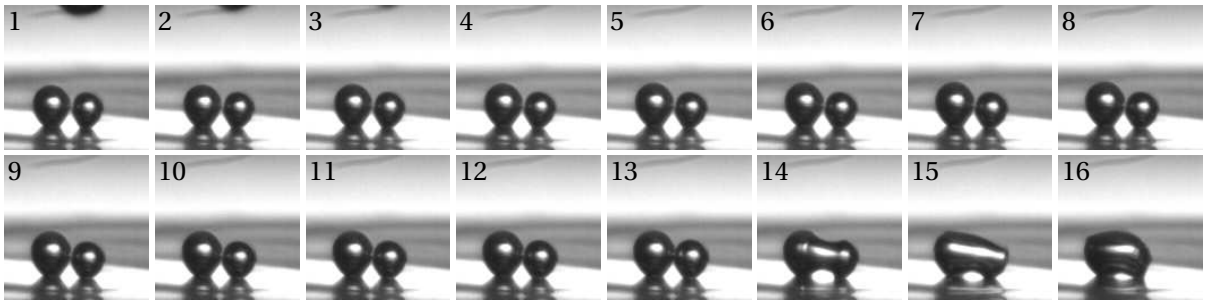

Figure 6.18: Photos of bubble interaction between bubbles from neighbouring nucleation sites, at a high wall superheat of $\Delta T_W \approx 8.1\,\mathrm{K}$ and an upper electrode voltage is 12 kV. Coalescence event occurs after 147 ms of growth. Time difference between two photos is $\Delta t \approx 3.3\,\mathrm{ms}$.

For higher voltages imposed to the upper electrode, the bubbles tend to repulse each other because of the electric forces. Consequently, the coalescence phenomenon occurs later in the growth for an electrode voltage of 18 kV[15] (see Fig. 6.19). For an even higher electrode voltage of 24 kV (see Fig. 6.20), the repulsion between the bubbles prevent them from merging before detachment and the coalescence event occurs after detachment. For the highest electrode voltage of 30 kV, the bubble do not merge at all (see Fig. 6.21).

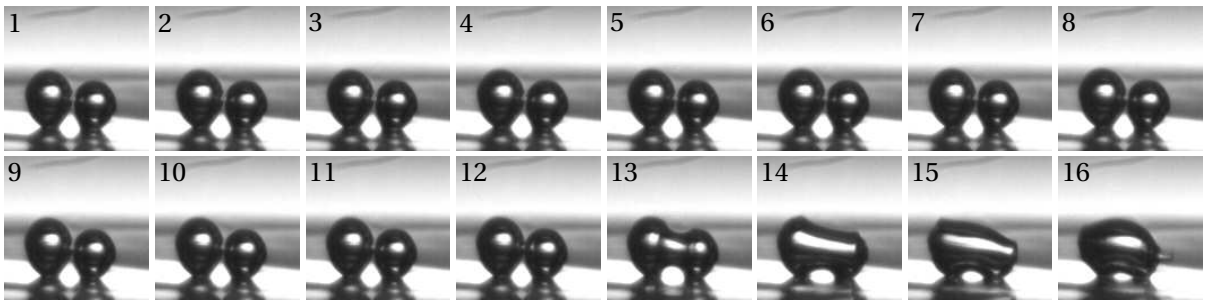

Figure 6.19: Photos of bubble interaction between bubbles from neighbouring nucleation sites, at a high wall superheat of $\Delta T_W \approx 8.1\,\mathrm{K}$ and an upper electrode voltage is 18 kV. Coalescence event occurs after 342 ms of growth. Time difference between two photos is $\Delta t \approx 3.3\,\mathrm{ms}$.

Such a repulsion between bubbles growing side by side can be explained by the loss of axisymmetry of the system. The electric forces acting on the fluid particles for a single bubble injected in a uniform electric field has been calculated by Zu and Yan [201] (see Fig. 6.22). It can be seen in Fig. 6.22b that the electric potential distribution is uniform far from the bubble. However, as the vapour and liquid phases have different dielectric permittivity constants[16], the distribution of the electric potential is distorted by the bubble. At the vicinity of the interface, the distribution is not uniform.

[15] namely approximately 342 ms instead of 147 ms for an electrode voltage of 12 kV

[16] The simulation performed bu Zu and Yan [201] is adiabatic. In the case of boiling, the temperature field also causes a modification of the electric properties distribution.

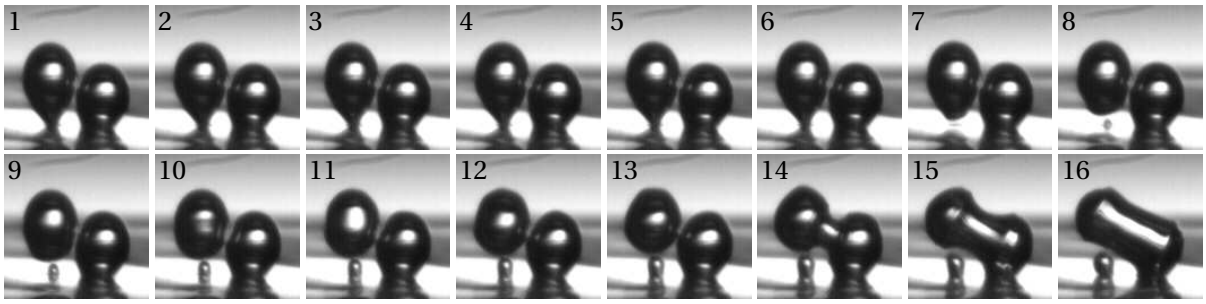

Figure 6.20: Photos of bubble interaction between bubbles from neighbouring nucleation sites, at a high wall superheat of $\Delta T_W \approx 8.1\,\mathrm{K}$ and an upper electrode voltage is 24 kV. Coalescence event occurs after one of the bubbles detached from the surface. Time difference between two photos is $\Delta t \approx 3.3\,\mathrm{ms}$.

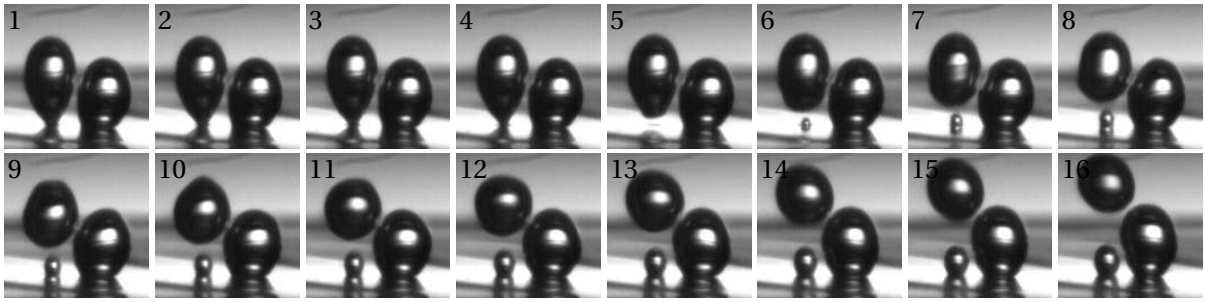

Figure 6.21: Photos of bubble interaction between bubbles from neighbouring nucleation sites, at a high wall superheat of $\Delta T_W \approx 8.2\,\mathrm{K}$ and an upper electrode voltage is 30 kV. No coalescence occurs. Time difference between two photos is $\Delta t = 5\,\mathrm{ms}$.

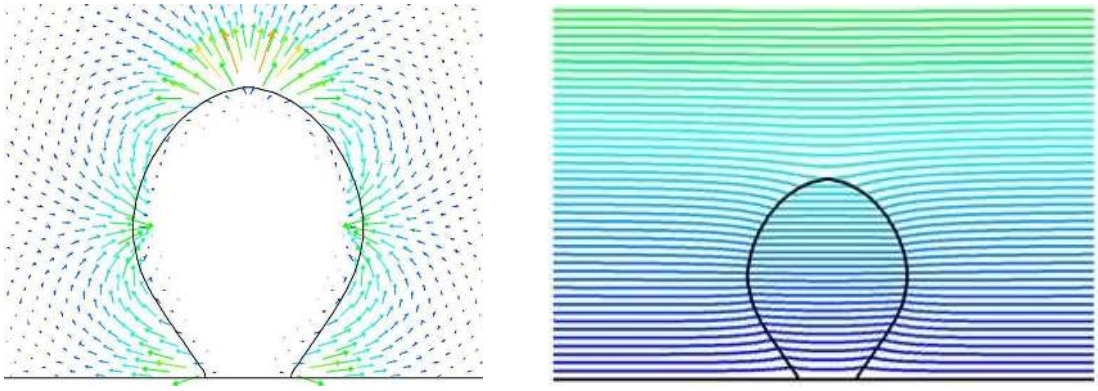

(a) Electric forces on the fluid particles (b) Distribution of constant electric potential

Figure 6.22: Illustration of the electric forces acting on the fluid particles of a single axisymmetric bubble (a) in a *pseudo*-uniform electric field (b), by Zu and Yan [201].

In the case of a single bubble, the non-uniform distribution of the electric potential within the system still presents an axial symmetry. As a consequence, the electric force distribution presents the same symmetry. In the case of two bubbles growing side by side, the axisymmetry of the electric potential distribution is lost. If the bubbles are close enough, the distortion of the electric potential distribution caused by the presence of the bubbles impacts the distribution of the forces acting on the fluid particles, leading to the repulsion between the bubbles. This loss of symmetry is the cause of the modification of the bubble interactions in Fig. 6.18 to 6.21.

6.3 Bubble departure and rise

As detailed in Section 5.4, bubble motion and rise after detachment plays an important role in boiling heat transfer by enhancing liquid motion and convection. However, bubble rise is complex and bubble trajectory and velocity are not simple to predict. Bubble rise presents stochastic parameters due to the influence of:

- bubble exact shape at departure and during rise
- bubble shape oscillations due to previous coalescence events or interaction with other bubbles
- convective motion of the liquid around the bubble during its rise
- bubble exact volume at departure

The consequence of these unpredictable parameters is a large variation of the behaviour of bubbles during their rise.

In the presence of electric fields, bubble rise can be modified due to the changes, induced by EHD, of:

liquid motion: the convective motion of the liquid phase is strongly affected by the electrohydrodynamic effects (see Section 4.1.4).

bubble shape: the shape of the interface is strongly modified by EHD (see Section 6.1.4). The bubble tends to be elongated in the direction of the electric field. This is the case for the shape of the bubble at departure. This is probably also the case for the shape of the bubble during its rise.

bubble volume at departure: as detailed in Section 6.1.1, many variations are observed concerning the volume of the departing bubble at departure.

To the author's best knowledge, the impact of a homogeneous electric field on bubble rise, and particularly on the bubble maximum velocity, has not been investigated before the present study. The following results have been presented during the 7th International Conference on Boiling Heat Transfer [170], as well as in a publication in Experimental Thermal and Fluid Science [171].

As for bubble rise in the absence of electric field[17], it has been observed in the presence of EHD that the departing bubble accelerates vertically until reaching a maximum velocity. When this maximum velocity is reached, the bubble randomly changes its direction. The present investigation focuses on the maximum vertical velocity reached before the change of trajectory.

The grid mesh electrode was located at a distance of 1.42 mm above the heated surface in order to follow the trajectory of the bubbles over a distance of approximately 1.2 mm. Several independent bubble rises were recorded for electrode voltages of -30, -15, 0, 15 and 30 kV. For each voltage conditions, the data samples included images for 8 to 20 independent rises. The recorded images were post-processed in order to measure the maximum vertical velocity.

The measured maximum velocities were scattered around a mean value in each data sample. The scattering was due to the measurement uncertainty and to the stochastic features of the phenomenon itself. It was assumed that the measured values were following a normal distribution and that the mean value of each sample could be evaluated using a Student t-distribution. The mean values of maximal velocities and the 95 % confidence intervals associated are shown in Fig. 6.23.

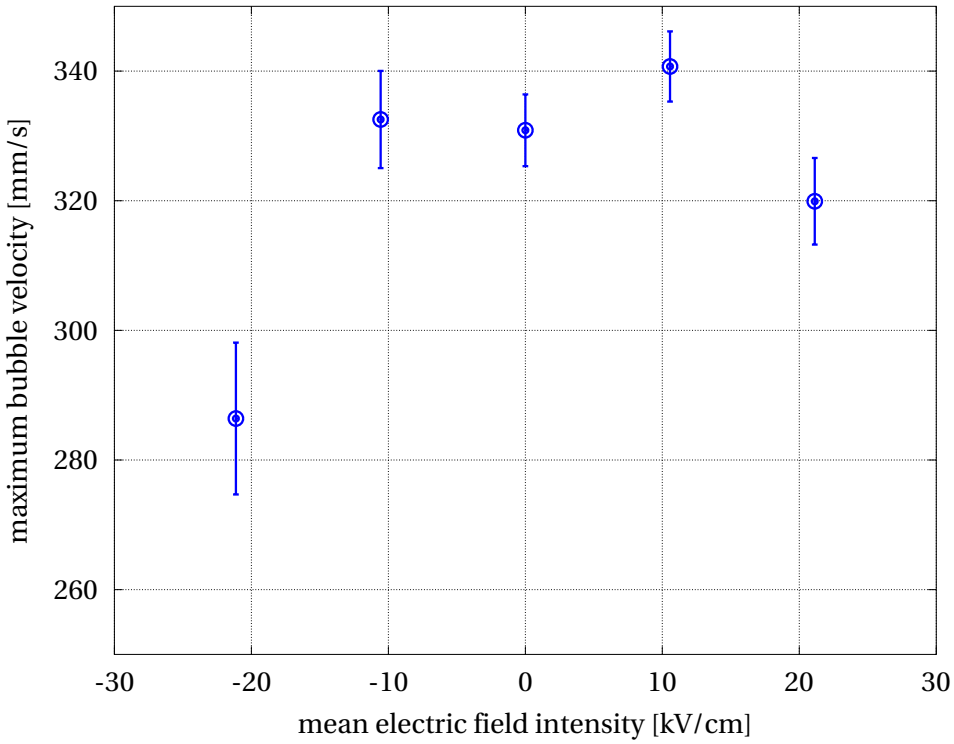

Figure 6.23: Maximum velocities of rising bubbles in the presence of electric fields. Mean values and 95 % confidence interval on the mean values of the data samples.

It is evident that the peak vertical velocity of the bubbles decreases with increasing electric field intensity and the effect is more prominent with negative polarity. The fact that the

[17] See Section 5.4 for a detailed analysis.

same general trend is observed for both polarities suggests that the dielectrophoretic component of the force might be responsible for this trend, since this force is independent of polarity. For the negative polarities, it seems that the dielectrophoretic force and the electrophoretic force tend to act together to cause the drop in the peak velocity to be more pronounced.

The present chapter presents original results concerning bubble dynamics during boiling in the presence of electric fields. As a continuation of chapter 5, the results are organized as a comparative study between bubble dynamics with and without EHD.

- *The repeatability of the bubble growth cycles has first been investigated, outlining more stochastic features and hence more scattering in the results in the presence of electric fields.*
- *No clear modification of the trend of the bubble frequency vs. the wall superheat was found. Similarly, no clear impact of electric field on the volume of departing bubbles was observed. It can thus be concluded that the electric forces acting on the bubble play a minor role in the bubble detachment.*
- *The bubble growth curve was found to be strongly modified by electrohydrodynamic effects. The convective motion of the liquid being enhanced by EHD, the thermal boundary layer thickness is modified, leading to changes in heat and mass transfer at the bubble interface.*
- *Bubbles were elongated in the direction of the electric field, in accordance with other studies on the subject. The relationship between the aspect ratio and the electric Weber number compared well with other experimental results.*
- *The coalescence phenomenon between bubbles growing side by side was investigated. It was noted that for high electric fields applied above the heated surface, the bubbles were repealing each other. Consequently, the bubbles were merging later or the coalescence was even suppressed. This electrohydrodynamic effect was explained as a loss of symmetry of the electric field intensity around the bubbles.*
- *The modification of bubble rise and particularly of the bubble maximum velocity was eventually investigated. It was found that for high electric fields, the maximum velocity was reduced. In the case of negative polarities of the upper electrode, the velocity reduction was more noticeable.*

Chapter 7

Conclusion

7.1 Synthesis

The complexity of boiling heat transfer and bubble dynamics has been explored in the present thesis. The up-to-date knowledge and hypotheses concerning several aspects of boiling have been compared to experimental measurements. The effects of electrohydrodynamics on heat transfer and on bubble dynamics were also investigated experimentally.

To achieve such objectives, an experimental facility has been designed and built along with experimental test samples allowing boiling on a single or on two neighbouring artificial nucleation sites. Boiling of *n*-pentane took place on a copper surface in a saturated bulk liquid at atmospheric pressure. In EHD experiments, an electric field was imposed between the boiling surface and a grid mesh electrode located above the heated surface. Several heat flux conditions were investigated, causing wall superheats ranging from about 1 to 10 K. Several electric field conditions were investigated up to a mean absolute electric field of about 40 $kV \cdot cm^{-1}$.

The heat flux transmitted to the liquid through the heated surface was measured, as well as the bulk and surface temperatures. The boiling events were recorded by a high-speed camera, and a specifically-developed image processing allowed the determination of instantaneous geometric parameters of the bubbles such as the volume, the height of the center of gravity, the angle of the interface to the horizontal plane and the curvature along the interface. Videos of convective motion of the fluid were also recorded at high frequency using a directional back-light.

The convective heat transfer was first studied. The convective structure was observed experimentally and simulated numerically with relatively good agreement. The existence of a central plume located above the center of the heated surface was highlighted, showing the natural flow of superheated liquid towards the nucleation site vicinity. Convective instabilities were observed experimentally and in the simulation, revealing periodic variations of the

thermal conditions above the nucleation site. The enhancement of convective heat transfer by means of electrohydrodynamics was quantified, and the modifications of the convective structures that cause such an enhancement were described experimentally and partially explained.

The bubble growth dynamics was analysed experimentally and empirical growth laws were compared to existing analytical models. Significant differences were highlighted which lead us to discuss the validity of the assumptions on which the common models are based. Bubble shape and oscillations were investigated, showing the interaction between successive bubbles from the same nucleation site. A extensive review of the forces acting on the bubble was proposed, and the full computation of the momentum balance during bubble growth was performed. The evolution of the curvature of the bubble along its interface and during its growth was measured. These measurements gave original indications for the mechanisms governing bubble detachment. The coalescence phenomenon between two bubbles growing side by side was investigated, and the propagation at high velocity of a wave front during the merging process was shown. Bubble rise trajectory and velocity was studied, and the maximum velocity reached was compared to existing models.

The bubble dynamics was also investigated in the presence of electric fields. The bubble growth curve was shown to be modified by electrohydrodynamic effects. On the contrary, no clear influence of the electric field was found concerning the bubble departing frequency and the volume at departure. The bubble elongation during the growth was quantified and compared to existing experimental data. The interactions between two bubbles growing side by side were also studied. At high electric field intensity, because of the non symmetric character of the electric field caused by the presence of the bubbles, the electric forces tend to make the bubbles repel each other, preventing them from merging. The bubble maximum rise velocity has eventually been investigated in the presence of electric fields of positive and negative polarities. Whatever the polarity, increasing the electric field intensity decreases the bubble maximum velocity. This is nevertheless more noticeable for negative polarities.

7.2 Perspectives

The boiling phenomenon being highly complex and a constant subject of research for over a century, the present study does not claim to resolve and explain all of the key issue encountered in its mechanical description and prediction. However, the author hopes that this work brings its own contribution to the global understanding of boiling. Some aspects of boiling were deeply studied, but other angles of inquiry were just introduced. Specific areas that should be given priority for future works in the continuity of this thesis are suggested below:

- After the investigation of the forces acting on a bubble in the absence of electric field, a similar study should be performed in the presence of electric fields. Multi-physics numerical simulations could be realised simultaneously in order to estimate to resultant of the electric forces acting on the interface. In such way, the computation of the

momentum balance during bubble growth could be performed and yield a fine description of the impact of the electric forces on bubble dynamics. Knowledge of the electric forces and of their influence on boiling provides a new tool to investigate boiling. By changing the relative influence of the different forces, the application of EHD on a boiling surface can be used to further understand boiling itself.

- This work has shown a decreasing vapour production rate during bubble growth. This trend differs from usual models of bubble growth and questions the validity of the assumptions these models rely on. Although explanations concerning the actual thermal field around the bubble have been introduced to account for this trend, an accurate numerical simulation of boiling in the conditions of these experiments could provide a better understanding of the thermal environment in which the bubble grows. However, such a simulation requires the development of a specialized code and arise issues such as the modelling of the nucleation process, of the triple line and of the interface. It is a multi-scale problem to properly simulate the triple line and the whole bubble. Furthermore, the thermal field, the velocity field and the phase change process are intimately coupled.

- Bubble nucleation remains a key problem for the prediction of boiling, but was not included in this study. The nucleation process strongly affects the stability of the nucleation site, as well as the waiting time between successive bubbles. Obtaining a stable nucleation site (i.e. a nucleation site in which bubbles nucleate at a reasonably constant frequency) was a challenge in the design and fabrication of the experimental test sample, and the waiting time influences the thermal field in which a new bubble nucleate and the interaction between successive bubbles. A better understanding of the nucleation process is required and necessitates specific studies on the subject as mid to long term perspectives.

  Different approaches have been attempted in past studies in an attempt to describe and predict nucleation. A purely theoretical description of the process is able to correctly predict homogeneous nucleation within a pure liquid, but already shows its limits when predicting nucleation on a plane surface. This approach is not suitable in the case of nucleating from a nucleation site like in the present experimental study as only very basic geometrical shapes can be taken into account. Another approach statistically predicts the size of the active nucleation sites depending on the wall superheat. This was attempted with varying success ([41], page 142), and coupled with a nucleation site size distribution, the active nucleation site density may be obtained. These can be used for the description and prediction of boiling on a natural surface, but it is not a suitable method for the case of a single nucleation site.

  Another approach and promising technique is the molecular dynamics numerical simulation of nucleation (e.g. [165]). Combined with boiling experiments on a perfectly controlled nucleation site, much information concerning the nucleation process and its prediction could be achieved. The main issue when using this approach would be to investigate the transition from the microscopic scale to the scale of a bubble.

List of references

[1] A.W. Adamson. *Physical chemistry of surfaces*. John Wiley and Sons, New-York, 1976. (Cited on page 8)

[2] A. Albadawi. Contribution to the simulation of isolated bubble dynamics under TransAT simulation code. Master's thesis, INSA Lyon, 2009. (Cited on page 47)

[3] P.H.G. Allen and P. Cooper. The potential of electrically enhanced evaporators. In *Third International Symposium on the Large Scale Application of Heat Pumps, Oxford, UK*, pages 221–229, 1987. (Cited on page 20)

[4] P.H.G. Allen and T.G. Karayiannis. Electrohydrodynamic enhancement of heat transfer and fluid flow. *Heat Recovery Systems and CHP*, 15:389–423, 1995. (Cited on pages 16 and 18)

[5] ANSYS©. FLUENT 6.3 user's guide. http://my.fit.edu/itresources/manuals/fluent6.3. (Cited on page 49)

[6] C.T. Avedisian. The homogeneous nucleation limits of liquids. *Journal of Physics and Chemical Reference Data*, 14(3):695–729, 1985. (Cited on page 11)

[7] N.M. Aybers and A Tapucu. Studies on the drag and shape of gas bubbles rising through a stagnant liquid. *Wärme- und Stoffübertragung*, 2:171–177, 1969. (Cited on page 141)

[8] S.G. Bankoff. Ebullition from solid surfaces in the absence of a pre-existing gaseous phase. *ASME Journal of Heat Transfer*, 79:735–740, 1957. (Cited on page 12)

[9] S.G. Bankoff. Entrapment of gas in the spreading of a liquid over a rough surface. *AIChE Journal*, 4(1):24–26, 1958. (Cited on page 13)

[10] S.G. Bankoff. The prediction of surface temperature at incipient boiling. *Chemical Engineering Progress Symposium Series*, 55(29):87, 1959. (Cited on page 13)

[11] S. Di Bari. *Bubble growth dynamics including gravitational and electric field effects*. PhD thesis, University of Dublin, Trinity College, 2010. (Cited on page 122)

[12] S. Di Bari and A.J. Robinson. Experimental study of bubble growth form a submerged orifice considering the dynamic pressure field. In *7th ECI International Conference on Boiling Heat Transfer, Florianopolis, Brazil*, 2009. (Cited on page 122)

[13] M. Barthès. *Ébullition sur site isolé : étude expérimentale de la dynamique de croissance d'une bulle et des transferts associés*. PhD thesis, Université de Provence, 2006. (Cited on page 42)

[14] M. Barthès, C. Reynard, R. Santini, and L. Tadrist. Non-condensable gas influence on the Marangoni convection during a single vapour bubble growth in a subcooled liquid. *Europhysics Letters*, 77:5, 2007. (Cited on page 104)

[15] H. Beer. Das dynamische Blasenwachstum beim Sieden Flüssigkeiten an Heizflächen. *Forschung im Ingenieurwesen*, 37:85–90, 1971. (Cited on pages 64, 77 and 78)

[16] L. Bernath. Theory of bubble formation in liquids. *Industrial and Engineering Chemistry*, 44(6):1310–1313, 1952. (Cited on page 11)

[17] R.A. Blachowicz, B.W. Brooks, and K.B. Tan. Boiling heat transfer in an electric field. *Chemical Engineering Science*, 35:761–762, 1980. (Cited on page 20)

[18] J. Bonjour, M. Clausse, and M. Lallemand. Experimental study of the coalescence phenomenon during nucleate pool boiling. *Experimental Thermal and Fluid Science*, 20:180–187, 2000. (Cited on pages 135 and 162)

[19] J.E. Bryan and J. Seyed-Yagoobi. Heat transport enhancement of monogroove heat pipe with electrohydrodynamic pumping. *Journal of Thermophysics and Heat Transfer*, 11(3):454–460, 1997. (Cited on page 17)

[20] D. Butrymovicz, M. Trela, and J. Karwacki. Enhancement of condensation heat transfer by means of EHD condense drainage. *International Journal of Thermal Sciences*, 41:646–657, 2002. (Cited on page 18)

[21] Y.A. Buyevich and B.W. Webbon. Dynamics of vapour bubbles in nucleate boiling. *International Journal of Heat and Mass Transfer*, 39(12):2409–2426, 1996. (Cited on pages 64, 73, 89, 99 and 105)

[22] Capillary action. Encyclopædia Britannica 11^{th} Edition, 1910-1911. (Cited on page 8)

[23] V.P. Carey. *Liquid-vapor phase-change phenomena*. Series in Chemical and Mechanical Engineering, 1992. (Cited on pages x, xi, 6, 43, 77, 96, 133, 139 and 162)

[24] A. Cattide, G.P. Celata, P. Di Marco, and W. Grassi. Experimental study on bubble detachment under variable heat load and the action of electric field. *Fluid Dynamics Research*, 40:485–496, 2008. (Cited on pages 17, 21, 64, 67, 148 and 152)

[25] G.P. Celata, M. Cumo, F. D'Annibale, P. Di Marco, A. Tomiyama, and C. Zovini. Effect of gas injection mode and purity of liquid on bubble rising in two-component systems. *Experimental Thermal and Fluid Science*, 31(1):37–53, 2006. (Cited on page 144)

[26] L.H. Chai, X.F. Peng, and D.J. Lee. Interfacial effects on nucleate boiling heat transfer of binary mixtures. *International Journal of Thermal Sciences*, 40(2):125–132, 2001. (Cited on page 102)

[27] J.S. Chang and A. Watson. Electromagnetic hydrodynamics. *IEEE Transactions on Dielectrics and Electrical Insulation*, 1(5):871–895, 1994. (Cited on page 17)

[28] S. Chatpun, M. Watanabe, and M. Shoji. Experimental study on characteristics of nucleate pool boiling by the effects of cavity arrangement. *Experimental Thermal and Fluid Science*, 29:33–40, 2004. (Cited on page 64)

[29] F. Chen, Y. Peng, Y.Z. Song, and M. Chen. EHD behavior of nitrogen bubbles in DC electric fields. *Experimental Thermal and Fluid Science*, 32:174–181, 2007. (Cited on pages xiii, 21, 36, 79, 147, 158, 160 and 161)

[30] W.C. Chen and J.F. Klausner. A simplified model for predicting vapor bubble growth rates in heterogeneous boiling. *ASME Journal of Heat Transfer*, 117:976–980, 1995. (Cited on pages 64 and 99)

[31] Y. Chen and M. Groll. Dynamics and shape of bubbles on heating surfaces: A simulation study. *International Journal of Heat and Mass Transfer*, 49:1115–1128, 2006. (Cited on pages 99, 101 and 102)

[32] Y. Chen, M. Groll, R. Mertz, and R. Kulenovic. Study of forces acting on a growing bubble from smooth and enhanced tubes. *International Journal of Heat and Technology*, 20:31–40, 2002. (Cited on page 102)

[33] Y. Chen, M. Groll, R. Mertz, and R. Kulenovic. Bubble dynamics of boiling of propane and iso-butane on smooth and enhanced tubes. *Experimental Thermal and Fluid Science*, 28(2-3):171–178, 2004. (Cited on pages 89 and 105)

[34] K. Cheung, M.M. Ohadi, S. Dessiatoun, and A. Singh. EHD-enhanced boiling coefficients and visualization of R-134a over enhanced tubes. *ASME Journal of Heat Transfer*, 119:332–338, 1997. (Cited on page 20)

[35] H.J. Cho, I.S. Kang, Y.C. Kweon, and M.H. Kim. Study of the behavior of a bubble attached to a wall in a uniform electric field. *International Journal of Multiphase Flow*, 22(5):909–922, 1996. (Cited on pages xiii, 21, 79, 160 and 161)

[36] D.M. Christopher, H. Wang, and X. Peng. Heat transfer enhancement due to Marangoni flow around moving bubbles during nucleate boiling. *Tsinghua Science & Technology*, 11(5):523–532, 2006. (Cited on page 104)

[37] S. Cioulachtjian, S. Siedel, S. Di Bari, A.J. Robinson, and J. Bonjour. Nucleate boiling on a wire coated with maghemite nanoparticles or with carbon nanotubes. In *8th ECI International Conference on Boiling and Condensation Heat Transfer, Lausanne, Switzerland*, 2012. (Cited on page 3)

[38] S. Cioulachtjian, S. Siedel, and J. Bonjour. Bubble growth, detachment and rise during boiling on artificial nucleation site. In *2nd Rhône-Alpes/Brazil Meeting on Micro and Nano-Technologies applied to Heat Transfer with Liquid-Vapour Phase Change, São Carlos, Brazil*, 2010. (Cited on pages 139 and 145)

[39] H.B. Clark, P.S. Strenge, and J.W. Westwater. Active sites for nucleate boiling. *Chemical Engineering Progress Symposium Series*, 55(29):103–110, 1958. (Cited on page 13)

[40] R. Cole. Boiling nucleation. *Advances in Heat Transfer*, 10:85–163, 1974. (Cited on pages 10 and 12)

[41] John G. Collier and John R. Thome. *Convective boiling and condensation*. Oxford Science Publication, 1994. (Cited on pages ix, 10, 11, 12, 13, 14 and 171)

[42] M.G. Cooper. The 'mirage' in boiling. *International Journal of Heat and Mass Transfer*, 26(7):1088–1090, 1983. (Cited on pages 64 and 110)

[43] M.G. Cooper and A.J.P. Lloyd. The microlayer in nucleate pool boiling. *International Journal of Heat and Mass Transfer*, 12:915–933, 1969. (Cited on pages 64 and 73)

[44] M.G. Cooper and J.M.D. Merry. A general expression for the rate of evaporation of a layer of liquid on a solid body. *International Journal of Heat and Mass Transfer*, 16:1811–1815, 1973. (Cited on page 73)

[45] M.G. Cooper and R.M. Vijuk. Bubble growth in nucleate pool boiling. In *4th International Heat and Mass Transfer Conference, Paris-Versailles, France*, volume 5, pages B1–B5, 1970. (Cited on page 73)

[46] P. Cooper. EHD enhancement of nucleate boiling. *ASME Journal of Heat Transfer*, 112:446–458, 1990. (Cited on page 20)

[47] J.S. Cotton, A.J. Robinson, M. Shoukri, and J.S. Chang. A two-phase flow pattern map for annular channels with and without a DC applied voltage and the application to electrohydrodynamic convective boiling analysis. *International Journal of Heat and Mass Transfer*, 48(25-26):5536–5579, 2005. (Cited on page 147)

[48] C. Damianidis, T.G. Karayiannis, R.K. Al-Dadah, R.W. James, M.W. Collins, and P.H.G. Allen. EHD boiling enhancement in shell-and-tube evaporators and its application in refrigeration. *ASHRAE Trans.*, 98:462–72, 1992. (Cited on page 20)

[49] M. Danti, P. Di Marco, W. Grassi, and G. Memoli. Effect of an external electric field on bubble dynamics: Preleminary study. In *XVIII Congresso Nationale UIT sulla Trasmissione del calor, Cernobbio, Italy*, pages 715–728, 2000. (Cited on page 147)

[50] P.-G. de Gennes, F. Brochard-Wyart, and D. Quéré. *Gouttes, bulles, perles et ondes*. Belin, 2002. (Cited on pages 8, 66, 96, 97, 102 and 135)

[51] F. Demiray and J. Kim. Heat transfer from a single nucleation site during saturated pool boiling of FC-72 using an array of 100 micron heaters. In *AIAA/ASME Thermophysics and Heat Transfer Conference, St. Louis, MO, USA.*, 2002. (Cited on page 64)

[52] P. Deng, Y.K Lee, and P. Cheng. An experimental study of heater size effect on micro bubble generation. *International Journal of Heat and Mass Transfer*, 49:33–40, 2006. (Cited on page 64)

[53] V.K. Dhir. Mechanistic prediction of nucleate boiling heat transfer – achievable or hopeless task ? *ASME Journal of Heat Transfer*, 128(1):1–12, 2006. (Cited on pages 2 and 64)

[54] W. Dong, R.Y. Li, H.L. Yu, and Y.Y. Yan. An investigation of behaviours of a single bubble in a uniform electric field. *Experimental Thermal and Fluid Science*, 30:579–586, 2006. (Cited on pages 36, 79 and 147)

[55] G. Duhar. *Croissance et détachement de bulles en paroi d'un écoulement cisaillé : étude expérimentale de l'injection et de l'ébullition nucléée*. PhD thesis, Institut National Polythechnique de Toulouse, 2003. (Cited on pages 89, 91, 105 and 197)

[56] G. Duhar and C. Colin. Bubble injection at the wall of a viscous shear flow. *Comptes Rendus Mécanique*, 331(1):91–98, 2003. (Cited on page 105)

[57] E. Durand. *Électrostatique*. Masson & Cie, 1966. (Cited on page 17)

[58] G.S. Dzakowic and W. Frost. Vapor bubble growth in saturated pool boiling by microlayer evaporation of liquid at the heated surface. In *4th International Heat and Mass Transfer Conference, Paris-Versailles, France*, volume 5, pages B1–B5, 1970. (Cited on page 73)

[59] W. Eames and H.M. Sabir. Potential benefits of electrohydrodynamic enhancement of two-phase heat transfer in the design of refrigeration systems. *Applied Thermal Engineering*, 17:79–92, 1997. (Cited on pages 16 and 20)

[60] K. Ellingsen and F. Risso. On the rise of an ellipsoidal bubble in water: oscillatory paths and liquid-induced velocity. *Journal of Fluid Mechanics*, 440:235–268, 2001. (Cited on page 141)

[61] T. Elperin and A. Fominykh. Heat and mass transfer during bubble growth in an alternating electric field. *International Communications in Heat and Mass Transfer*, 31(8):1047–1056, 2004. (Cited on page 147)

[62] N.J. Felici. La conduction électrique dans les liquides diélectriques. Phénomènes d'instabilités et de transport : mécanismes chimiques et hydrodynamiques. *Journal de Physique*, 37:C1–117, 1976. (Cited on page 18)

[63] Y. Feng and J. Seyed-Yagoobi. Linear instability analysis of a horizontal two-phase flow in the presence of electrohydrodynamic extraction force. *ASME Journal of Heat Transfer*, 124:102–110, 2002. (Cited on page 20)

[64] H.K. Forster and N. Zuber. Growth of a vapor bubble in a superheated liquid. *Journal of Applied Physics*, 25:474–478, 1954. (Cited on pages 64 and 73)

[65] Y. Fujita and Q. Bai. Critical heat flux of binary mixtures in pool boiling and its correlation in terms of Marangoni number. *International Journal of Refrigeration*, 20(8):616–622, 1997. (Cited on page 102)

[66] M.V. Fyodorov and V.V. Klimenko. Vapour bubble growth in boiling under quasi-stationary heat transfer conditions on a heating wall. *International Journal of Heat and Mass Transfer*, 32(2):227–242, 1989. (Cited on page 73)

[67] N. Ginet. *Analyse des mécanismes contrôlant la croissance et l'ascension d'une bulle isolée en ébullition nucléée*. PhD thesis, INSA de Lyon, 1999. (Cited on pages 89, 102 and 105)

[68] I. Golobic, J. Petkovsek, H. Gjerkes, and D.B.R. Kenning. Horizontal chain coalescence of bubbles in saturated pool boiling on a thin foil. *International Journal of Heat and Mass Transfer*, 54(25-26):5517–5526, 2011. (Cited on page 162)

[69] I. Golobic, J. Petkovsek, and D.B.R. Kenning. Bubble growth and horizontal coalescence in saturated pool boiling on a titanium foil, investigated by high-speed IR thermography. *International Journal of Heat and Mass Transfer*, In Press, doi:10.1016/j.ijheatmasstransfer.2011.08.021. (Cited on page 162)

[70] P. Griffith. Bubble growth rates in boiling. *ASME Journal of Heat Transfer*, 80:721–727, 1958. (Cited on page 73)

[71] Z. Guo and M.S. El-Genk. Liquid microlayer evaporation during nucleate boiling on the surface of a flat composite wall. *International Journal of Heat and Mass Transfer*, 37(11):1641–1655, 1994. (Cited on page 64)

[72] W.L. Haberman and R.K. Morton. An experimental investigation of the drag and shape of air bubbles rising in various liquids. Report 802 NS 715-102, Navy department, 1953. (Cited on page 139)

[73] C.Y. Han and P. Griffith. The mechanism of heat transfer in nucleate pool boiling - part 1: Bubble initiation, growth and departure. *International Journal of Heat and Mass Transfer*, 8:887–904, 1965. (Cited on pages 64 and 73)

[74] T.Z. Harmathy. Velocity of large drops and bubbles in media of infinite or restricted extent. *AIChE Journal*, 6(2):281–288, 1960. (Cited on page 139)

[75] J.F. Harper. Bubbles rising in line: why is the first approximation so bad? *Journal of Fluid Mechanics*, 351:289–300, 1997. (Cited on page 139)

[76] A.P Hatton and I.S. Hall. Photographic study of boiling on prepared surfaces. In *3rd International Heat Transfer Conference, Chicago*, pages 24–37, 1966. (Cited on pages 64 and 72)

[77] S. Hein, C. Ikier, H. Klein, and K. Wittmann. Bubble motion induced by Marangoni convection under the influence of gravity. *Chemical Engineering and Technology*, 21:41–44, 1998. (Cited on pages 103 and 104)

[78] C. Herman, E. Iacona, T. Acquaviva, B. Coho, N. Grant, H. Nahra, A. Taylor, E. Julian, D. Robinson, and D. Van Zandt. Enhancement of pool boiling heat transfer and control of bubble motion in microgravity using electric fields. Tech. note TM 2001-211317, NASA, 2001. (Cited on pages 17 and 147)

[79] C. Herman, E. Iacona, I.B. Földes, G. Suner, and C. Milburn. Experimental visualization of bubble formation from an orifice in microgravity in the presence of electric fields. *Experiments in Fluids*, 32:396–412, 2002. (Cited on pages 17 and 147)

[80] G. Hetsroni, A. Mosyak, E. Pogrebnyak, I. Sher, and Z. Segal. Bubble growth in saturated pool boiling in water and surfactant solution. *International Journal of Multiphase Flow*, 32(2):159–182, 2006. (Cited on page 102)

[81] H.C.J. Hœfsloot, L.P.B.M. Janssen, and H.W. Hoogstraten. Marangoni convection around a ventilated air bubble under microgravity conditions. *Chemical Engineering Science*, 49(1):29–39, 1994. (Cited on page 104)

[82] Y. Hristov, D. Zhao, D.B.R. Kenning, K. Sefiane, and T.G. Karayiannis. A study of nucleate boiling and critical heat flux with EHD enhancement. *Heat and Mass Transfer*, 45(7):999–1017, 2009. (Cited on page 147)

[83] Y.Y. Hsu. On the size range of active nucleation cavities on a heated surface. *ASME Journal of Heat Transfer*, 84:207–213, 1962. (Cited on page 13)

[84] H.Y. Hu, G.P. Peterson, X.F. Peng, and B.X. Wang. Interphase fluctuation propagation and superposition model for boiling nucleation. *International Journal of Heat and Mass Transfer*, 41:3483–3489, 1998. (Cited on page 10)

[85] C. Hutter, D.B.R. Kenning, K. Sefiane, T.G. Karayiannis, H. Lin, G. Cummins, and A.J. Walton. Experimental pool boiling investigations of FC-72 on silicon with artificial cavities and integrated temperature microsensors. *Experimental Thermal and Fluid Science*, 34(4):497–508, 2009. (Cited on pages 40 and 64)

[86] E. Iacona, C. Herman, S. Chang, and Z. Liu. Electric field effect on bubble detachment in reduced gravity environment. *Experimental Thermal and Fluid Science*, 31:121–126, 2006. (Cited on pages 79 and 147)

[87] M. Jenny, J. Dušek, and G. Bouchet. Instabilities and transition of a shpere falling or ascending freely in a newtonian fluid. *Journal of Fluid Mechanics*, 508:201–239, 2004. (Cited on page 141)

[88] S.G. Kandlikar and B.J Stumm. A control volume approach for instigating forces on a departing bubble under subcooled flow boiling. *ASME Journal of Heat Transfer*, 117:990–997, 1995. (Cited on pages 89 and 105)

[89] T.G. Karayiannis. EHD boiling heat transfer enhancement of R123 and R11 on a tube bundle. *Applied Thermal Engineering*, 18:809–817, 1998. (Cited on page 20)

[90] T.G. Karayiannis, M.W. Collins, and P.H.G. Allen. Electrohydrodynamic enhancement of nucleate boiling heat transfer in heat exchangers. *Chemical Engineering Communications*, 81:15–24, 1989. (Cited on page 20)

[91] R. Kempers, P. Kolodner, A. Lyons, and A.J. Robinson. A high-precision apparatus for the characterization of thermal interface materials. *Review of Scientific Instruments*, 80:095111, 2009. (Cited on page 34)

[92] E.G. Keshock and R. Siegel. Forces acting on bubbles in nucleate boiling under normal and reduced gravity conditions. Technical note TN D-2299, NASA, 1964. (Cited on page 139)

[93] J. Kim. Review of nucleate pool boiling heat transfer mechanisms. *International Journal of Multiphase Flow*, 35:1067–1076, 2009. (Cited on pages 2 and 40)

[94] J. Kim, J.F. Benton, and D. Wisniewski. Pool boiling heat transfer on small heaters: effect of gravity and subcooling. *International Journal of Heat and Mass Transfer*, 45:3919–3932, 2002. (Cited on page 64)

[95] J. Kim and M.H. Kim. On the departure behaviors of bubble at nucleate pool boiling. *International Journal of Multiphase Flow*, 32:1269–1286, 2006. (Cited on page 40)

[96] J.F. Klausner, R. Mei, D.M. Bernhard, and L.Z. Zeng. Vapor bubble departure in forced convection boiling. *International Journal of Heat and Mass Transfer*, 36(3):651–662, 1993. (Cited on pages 92 and 198)

[97] R.T. Knapp. Cavitation and nuclei. *ASME Journal of Heat Transfer*, 80:1321, 1958. (Cited on page 11)

[98] L.D. Koffman and M.S. Plesset. Experimental observations of the microlayer in vapor bubble growth on a heated solid. *ASME Journal of Heat Transfer*, 105:625–632, 1983. (Cited on page 64)

[99] R. Kurose, R. Misumi, and S. Komori. Drag and lift forces acting on a spherical bubble in a linear shear flow. *International Journal of Multiphase Flow*, 27(7):1247–1258, 2001. (Cited on page 105)

[100] Y.C. Kweon and M.H. Kim. Experimental study on nucleate boiling enhancement and bubble dynamic behavior in saturated pool boiling using a nonuniform dc electric field. *International Journal of Multiphase Flow*, 26:1351–1368, 2000. (Cited on page 147)

[101] Y.C. Kweon, M.H. Kim, H.J. Cho, and I.S. Kang. Study on the deformation and departure of a bubble attached to a wall in d.c./a.c. electric fields. *International Journal of Multiphase Flow*, 24(1):145–162, 1998. (Cited on page 79)

[102] L.D. Landau and E.M. Lifšitz. *Electrohydrodynamics of continuous media*. Pergamon, NY, 1986. (Cited on page 17)

[103] L.D. Landau and E.M. Lifšitz. *Physique théorique 8 – Electrohydrodynamique des milieux continus*. Librairie du Globe, 1986. (Cited on page 17)

[104] S. Laohalertdecha, P. Naphon, and S. Wongwises. A review of electrohydrodynamic enhancement of heat transfer. *Renewable and Sustainable Energy Reviews*, 11(5):858–876, 2007. (Cited on pages 3, 16, 18, 20 and 147)

[105] B.K. Larkin. Thermocapillary flow around hemispherical bubble. *AIChE Journal*, 16(1):101–107, 1970. (Cited on page 104)

[106] H.C. Lee, J. Kim, B.D. Oh, and M.H. Kim. Single bubble growth in saturated pool boiling of binary mixtures. *International Journal of Multiphase Flow*, 30:697–710, 2004. (Cited on pages 36 and 64)

[107] H.C. Lee, B.D. Oh, S.W. Bae, and M.H. Kim. Single bubble growth in saturated pool boiling on a constant wall temperature surface. *International Journal of Multiphase Flow*, 29:1857–1874, 2003. (Cited on page 64)

[108] H.C. Lee, B.D. Oh, S.W. Bae, M.H. Kim, J.Y. Lee, and I.S. Song. Partial nucleate boiling on the microscale heater maintaining constant wall temperature. *Journal of Nuclear Science and Technology*, 40(10):768–774, 2003. (Cited on page 64)

[109] H.S. Lee and H. Merte Jr. Hemispherical vapor bubble growth in microgravity : experiments and model. *International Journal of Heat and Mass Transfer*, 39(12):2449–2461, 1996. (Cited on pages 64 and 99)

[110] R.C. Lee and J.E. Nydhal. Numerical calculation of bubble growth in nucleate boiling from inception through departure. *ASME Journal of Heat Transfer*, 111:474–479, 1989. (Cited on page 99)

[111] D. Legendre, C. Colin, and T. Coquard. Lift, drag and added mass of a hemispherical bubble sliding and growing on a wall in a viscous linear shear flow. *Philosophy Transactions of the Royal Society*, 366:2233–2248, 2008. (Cited on pages 92 and 198)

[112] J.H. Lichtenbelt. Improvement of flight hardware and isothermal Marangoni convection under micro-gravity conditions. *Advances in Space Research*, 6(5):97–100, 1986. (Cited on page 104)

[113] J.-L. Liow. Quasi-equilibrium bubble formation during top-submerged gas injection. *Chemical Engineering Science*, 55:4515–4524, 2000. (Cited on page 99)

[114] Y. Liu, R. Li, F. Wand, and H. Yu. The effect of electrode polarity on EHD enhancement of boiling heat transfer in a vertical tube. *Experimental Thermal and Fluid Science*, 29:601–608, 2005. (Cited on page 21)

[115] Y. Liu, R. Li, F. Wang, and H. Yu. The effect of electrode polarity on EHD enhancement of boiling heat transfer in a vertical tube. *Experimental Thermal and Fluid Science*, 29:601–608, 2004. (Cited on page 20)

[116] Z. Liu, C. Herman, and J. Kim. Heat transfer and bubble detachment in subcooled pool boiling from a downward-facing microheater array in a nonuniform electric field. *Annals of the New York Academy of Sciences*, 1161:182–191, 2009. (Cited on page 147)

[117] Z. Liu, C. Herman, and D. Mewes. Visualization of bubble detachment and coalescence under the influence of a nonuniform electric field. *Experimental Thermal and Fluid Science*, 31:151–163, 2006. (Cited on pages 147 and 162)

[118] K. Lunde and R. Perkins. Observations on wakes behind spheroidal bubbles and particles. In *ASME Fluids Engineering Division Summer Meeting, Vancouver, Canada*, 1997. (Cited on page 141)

[119] J. Madadnia and H. Koosha. Electrohydrodynamic effects on characteristic of isolated bubbles in the nucleate pool boiling regime. *Experimental Thermal and Fluid Science*, 27:145–150, 2003. (Cited on page 147)

[120] J. Magnaudet and I. Eames. The motion of high-reynolds-number bubbles in inhomogeneous flows. *Annual Review of Fluid Mechanics*, 32:659–708, 2000. (Cited on page 141)

[121] J. Magnaudet, M. Rivero, and J. Fabre. Accelerated flows past a rigid sphere or a spherical bubble. i: steady straining flow. *Journal of Fluid Mechanics*, 284:97–135, 1995. (Cited on pages 91 and 197)

[122] M. Mann, K. Stephan, and P. Stephan. Influence of heat conduction in the wall on nucleate boiling heat transfer. *International Journal of Heat and Mass Transfer*, 43:2193–2203, 2000. (Cited on page 67)

[123] P. Di Marco, A. Faini, W. Grassi, and G. Memoli. Electric field effects on bubbles of nitrogen in FC-72 originating from a flat plate. In *3rd International Symposium on Two-Phase Modelling and Experimentation, Pisa, Italy*, 2004. (Cited on pages 17 and 147)

[124] P. Di Marco and W. Grassi. Effects of external electric field on pool boiling: Comparison of terrestrial and microgravity data in the ARIEL experiment. *Experimental Thermal and Fluid Science*, 35:780–787, 2011. (Cited on page 17)

[125] P. Di Marco, W. Grassi, S. Hosokawa, G. Memoli, T. Takamasa, and A. Tomiyama. Influence of electric field on single gas-bubble growth and detachment in microgravity. In *39th European Two-Phase Flow Group Meeting, Aveiro, Portugal*, pages H–5, 2001. (Cited on pages 17 and 147)

[126] P. Di Marco, W. Grassi, G. Memoli, T. Takamasa, A. Tomiyama, and S. Hosokawa. Influence of electric field on single gas-bubble growth and detachment in microgravity. *International Journal of Multiphase Flow*, 29:559–578, 2003. (Cited on pages 17 and 147)

[127] M. Markels and R.L. Durfee. The effect of applied voltage on boiling heat transfer. *AIChE Journal*, 10:106–110, 1964. (Cited on page 147)

[128] G. Marrucci, G. Apuzzo, and G.A. Astarita. Motion of liquid drops in non-Newtonian systems. *AIChE Journal*, 16(4):538–541, 1970. (Cited on page 143)

[129] R. Mei and J.F. Klausner. Shear lift force on spherical bubbles. *International Journal of Heat and Fluid Flow*, 15(1):62–65, 1994. (Cited on page 105)

[130] H.D. Mendelson. The prediction of bubble terminal velocities from wave theory. *AIChE Journal*, 13(2):250–253, 1967. (Cited on page 143)

[131] B.B. Mikic, W.M. Rohsenow, and P. Griffith. On bubble growth rates. *International Journal of Heat and Mass Transfer*, 13:657–666, 1970. (Cited on pages 64 and 73)

[132] S. Moghaddam and K. Kiger. Physical mechanisms of heat transfer during single bubble nucleate boiling of FC-72 under saturation conditions-1. Experimental investigation. *International Journal of Heat and Mass Transfer*, 52:1284–1294, 2009. (Cited on pages 40 and 64)

[133] A. Mukherjee and V.K. Dhir. Study of lateral merger of vapor bubbles during nucleate pool boiling. *ASME Journal of Heat Transfer*, 126:1023–1039, 2004. (Cited on page 137)

[134] A. Mukherjee and S.G. Kandlikar. Numerical study of single bubbles with dynamic contact angle during pool boiling. *International Journal of Heat and Mass Transfer*, 50:127–138, 2007. (Cited on page 67)

[135] Y. Nam, E. Aktinol, V.K. Dhir, and Y.S. Ju. Single bubble dynamics on a superhydrophilic surface with artificial nucleation sites. *International Journal of Heat and Mass Transfer*, 54:1572–1577, 2011. (Cited on page 68)

[136] D.A. Nelson and E.J. Shaughnessy. Electric field effects on natural convection in enclosures. *ASME Journal of Heat Transfer*, 108:749–754, 1986. (Cited on page 17)

[137] R.S. Neve and Y.Y. Yan. Enhancement of heat exchanger performance using combined electrohydrodynamic and passive methods. *International Journal of Heat and Fluid Flow*, 17:403–409, 1996. (Cited on page 20)

[138] S. Nukiyama. The maximum and minimum values of the heat transmitted from metal to boiling water under atmospheric pressure. *Japan Society of Mechanical Engineering*, 37:367–374, 1934. (Cited on pages 14 and 63)

[139] S. Nukiyama. The maximum and minimum values of the heat transmitted from metal to boiling water under atmospheric pressure. *International Journal of Heat and Mass Transfer*, 9:1419–1433, 1966. (Cited on page 63)

[140] J. Ogata and A. Yabe. Augmentation of boiling heat transfer by utilizing the EHD effect – EHD behaviour of boiling bubbles and heat transfer characteristics. *International Journal of Heat and Mass Transfer*, 36(3):783–791, 1993. (Cited on page 147)

[141] H.N. Oguz and A. Prosperetti. Dynamics of bubble growth and detachment from a needle. *Journal of Fluid Mechanics*, 257:111–114, 1993. (Cited on page 99)

[142] M.M. Ohadi, N. Sharaf, and D.A. Nelson. Electrohydrodynamic enhancement of heat transfer in a shell-and-tube heat exchanger. *Experimental Thermal and Fluid Science*, 4(1):19–39, 1991. (Cited on page 147)

[143] S.M. O'Shaughnessy and A.J. Robinson. Numerical investigation of bubble induced Marangoni convection: some aspects of bubble geometry. *Microgravity Science and Technology*, 20:319–325, 2008. (Cited on page 104)

[144] H.J. Van Ouwerkerk. The rapid growth of a vapour bubble at a liquid-solid interface. *International Journal of Heat and Mass Transfer*, 14:1415–1431, 1971. (Cited on page 64)

[145] I.M. Paderin, V.S. Uskov, and G.V. Ermakov. The kinetics of boiling of superheated liquid in the presence of porous and smooth surfaces. *High Temperature*, 32(6):806–809, 1994. (Cited on page 13)

[146] J. Pakleza, M.C. Duluc, and T. Kowalewski. Experimental investigation of vapor bubble growth. In *12th International Heat Transfer Conference, Grenoble, France*, pages 479–484, 2002. (Cited on page 64)

[147] W. Panofsky and M. Phillips. *Classical electricity and magnetism, second ed.* Addison-Wesley Publishing Co., Reading, Massachusetts, 1962. (Cited on page 17)

[148] P. Papon and J. Leblond. *Thermodynamique des matériaux*. Editions Hermann, Paris, 1990. (Cited on pages 8 and 9)

[149] C.C. Pascual, S.M. Jeter, and S.I. Abdel-Khalik. Visualization of boiling bubble dynamics using a flat uniformly heated transparent surface. *International Journal of Heat and Mass Transfer*, 45:691–696, 2002. (Cited on page 64)

[150] F.N. Peebles and H.J. Garber. Studies on the motion of gas bubbles in liquids. *Chemical Engineering Progress*, 49:88–97, 1953. (Cited on pages 139 and 143)

[151] Y. Peng, F. Chen, Y. Song, and M. Chen. Single bubble behavior in direct current electric field. *Chinese Journal of Chemical Engineering*, 16(2):178–193, 2008. (Cited on pages xiii, 21, 36, 79, 147, 158, 160 and 161)

[152] A.S. Perkins and J.W. Westwater. Measurements of bubbles formed in boiling methanol. *AIChE Journal*, 2(4):471–476, 1956. (Cited on page 64)

[153] S. Petrovic, A.J. Robinson, and R.L. Judd. Marangoni heat transfer in subcooled nucleate pool boiling. *International Journal of Heat and Mass Transfer*, 47:5115–5128, 2004. (Cited on pages 103 and 104)

[154] M.S. Plesset and S.A. Zwick. The growth of vapor bubbles in superheated liquids. *Journal of Applied Physics*, 25:493–500, 1954. (Cited on pages 64 and 73)

[155] W. Porteus and M. Blander. Limit of superheat and explosive boiling of light hydrocarbons, halocarbons, and hydrocarbon mixtures. *AIChE Journal*, 21:560–566, 1975. (Cited on page 11)

[156] A.K. Rajvanshi. Measurement of bubble frequency, vapour mass frequency and macrolayer thickness by probe method. In *1st International Conference on Two-Phase Flow Modelling and Experimentation, Rome, Italy*, 1995. (Cited on page 64)

[157] Lord Rayleigh. On the pressure developed in a liquid during the collapse of a spherical cavity. *Philosophical Magazine*, 34:94–98, 1917. (Cited on page 64)

[158] S.T. Revankar. Coalescence and breakup of fluid particles in multiphase flow. In *4th International Conference on Multiphase Flow, New Orleans, USA*, page 352, 2001. (Cited on page 137)

[159] C. Reynard, M. Barthès, R. Santini, and L. Tadrist. Experimental study of the onset of the 3D oscillatory thermocapillary convection around a single air or vapor bubble: influence on heat transfer. *Experimental Thermal and Fluid Science*, 29(7):783–793, 2005. (Cited on page 104)

[160] A.J. Robinson and R.L. Judd. The dynamic of spherical bubble growth. *International Journal of Heat and Mass Transfer*, 47(23):5101–5113, 2004. (Cited on pages 70 and 92)

[161] A.I. Rusanov and A.K. Shchekin. The condition of mechanical equilibrium for a non-spherical interface between phases with a non-diagonal stress tensor. *Colloids and Surfaces A: Physicochemical and Engineering Aspects*, 192:357–362, 2001. (Cited on page 96)

[162] H. Sakashita, H. Yasuda, and T. Kumada. Studies on pool boiling heat transfer (modification of correlation of macrolayer thickness and measurements of macrolayer thickness at low heat fluxes). *Heat Transfer - Japanese Research*, 25(8):522–536, 1996. (Cited on page 64)

[163] A. Sanna, T.G. Karayiannis, D.B.R. Kenning, C. Hutter, K. Sefiane, A.J. Walton, I. Golobič, E. Pavlovič, and R.A. Nelson. Steps towards the development of an experimentally verified simulation of pool boiling on a silicon wafer with artificial sites. *Applied Thermal Engineering*, 29:1327–1337, 2009. (Cited on page 64)

[164] L.E. Scriven. On the dynamics of phase growth. *Chemical Engineering Science*, 10(1):1–13, 1959. (Cited on page 73)

[165] M. Sekine, K. Yasuoka, T. Kinjo, and M. Matsumoto. Liquid-vapor nucleation of lennard-jones fluid by molecular dynamics method. *Fluid Dynamics Research*, 40(7-8):597–605, 2008. (Cited on page 171)

[166] M. Shoji and Y. Takagi. Bubbling features from a single artificial cavity. *International Journal of Heat and Mass Transfer*, 44:2763–2776, 2001. (Cited on page 64)

[167] S. Siedel, S. Cioulachtjian, S. Di Bari, A.J. Robinson, and J. Bonjour. Experimental investigation on the local curvature of bubble interface during boiling on a single nucleation site. In *8th ECI International Conference on Boiling and Condensation Heat Transfer, Lausanne, Switzerland*, 2012. (Cited on page 122)

[168] S. Siedel, S. Cioulachtjian, and J. Bonjour. Experimental analysis of bubble dynamics: Without and with the application of an electric field. In *46th European Two-Phase Flow Group Meeting, Pisa, Italy*, 2008. (Cited on pages 77 and 145)

[169] S. Siedel, S. Cioulachtjian, and J. Bonjour. Experimental analysis of bubble growth, departure and interactions during pool boiling on artificial nucleation sites. *Experimental Thermal and Fluid Science*, 32(8):1504–1511, 2008. (Cited on pages 36, 65, 79, 84, 136, 145 and 196)

[170] S. Siedel, S. Cioulachtjian, and J. Bonjour. Electric fields effect on the rise of single bubbles during boiling. In *7th ECI International Conference on Boiling Heat Transfer, Florianopolis, Brazil*, 2009. (Cited on pages 44, 139, 145 and 165)

[171] S. Siedel, S. Cioulachtjian, A.J. Robinson, and J. Bonjour. Electric field effects during nucleate boiling from an artificial nucleation site. *Experimental Thermal and Fluid Science*, 35(5):762–771, 2011. (Cited on pages 70, 145, 148 and 165)

[172] S. Siedel, S. Cioulachtjian, A.J. Robinson, and J. Bonjour. Experimental determination of the forces acting on a bubble during boiling on a single nucleation site. In *8th ECI International Conference on Boiling and Condensation Heat Transfer, Lausanne, Switzerland*, 2012. (Cited on page 88)

[173] H.C. Simpson and A.S. Walls. A study of nucleation phenomena in transient pool boiling. In *Symposium on Boiling Heat Transfer in Steam Generating Units and Heat Exchangers, Manchester, UK*, 1965. (Cited on page 11)

[174] P. Stephan and J. Hammer. A new model for nucleate boiling heat transfer. *Wärme- und Stoffübertragung*, 30:119–125, 1994. (Cited on page 40)

[175] S. Van Stralen. The growth rate of vapour bubbles in superheated pure liquids and binary mixtures - part 1. *International Journal of Heat and Mass Transfer*, 11:1467–1489, 1968. (Cited on page 64)

[176] S. Van Stralen and R. Cole. *Boiling phenomena*, volume 2. Hemisphere Publishing Corp., 1979. (Cited on pages 14, 64 and 77)

[177] J.A. Stratton. *Electromagnetic Theory*. McGraw-Hill, 1941. (Cited on page 18)

[178] B. Stutz, C.H. Silveira Morceli, M. de Fàtima da Silva, S. Cioulachtjian, and J. Bonjour. Influence of nanoparticle surface coating on pool boiling. *Experimental Thermal and Fluid Science*, 35(7):1239–1249, 2011. (Cited on page 67)

[179] B. Suman, S. De, and S. Das Gupta. Transient modeling of micro-grooved heat pipe. *International Journal of Heat and Mass Transfer*, 48(8):1633–1646, 2005. (Cited on page 98)

[180] C.L. Sun and Van P. Carey. Marangoni effects on the boiling of 2-propanol/water mixtures in confined space. *International Journal of Heat and Mass Transfer*, 47(25):5417–5426, 2004. (Cited on page 102)

[181] R.B.H. Tan and I.J. Harris. A model for non-spherical bubble growth at a single orifice. *Chemical Engineering Science*, 41(12):3175–3182, 1986. (Cited on page 99)

[182] G.I. Taylor. Studies in electrohydrodynamics: I. the circulation produced in a drop by an electric field. *Proceedings of the Royal Society of London*, A 291:159–166, 1966. (Cited on page 19)

[183] T.G. Theofanous and P.D. Patel. Universal relations for bubble growth. *International Journal of Heat and Mass Transfer*, 19:425–429, 1976. (Cited on page 73)

[184] A. Tomiyama, G.P. Celata, S. Hosokawa, and S. Yoshida. Terminal velocity of single bubbles in surface tension force dominant regime. *International Journal of Multiphase Flow*, 28:1497–1519, 2002. (Cited on pages 140, 143 and 144)

[185] A. Tomiyama, I. Kataoka, I. Zun, and T. Sakagushi. Drag coefficients of single bubbles under normal and micro gravity conditions. *JSMA International Journal - Serie B*, 41(2):472–479, 1998. (Cited on page 143)

[186] M. Treuner, V. Galindo, G. Gerbeth, D. Langbein, and H.J. Rath. Thermocapillary bubble migration at high Reynolds numbers under low gravity. *Journal of Colloid and Interface Science*, 179(1):114–127, 1996. (Cited on page 104)

[187] H. Tsai Jr. and L. Lin. Transient thermal bubble formation on polysilicon microresisters. *ASME Journal of Heat Transfer*, 124:375–382, 2002. (Cited on page 64)

[188] R.J. Turnbull. Effect of a non-uniform alternating electric field on the thermal boundary layer near a heated vertical plate. *Journal of Fluid Mechanics*, 49(4):693–703, 1971. (Cited on page 17)

[189] C.W.M. van der Geld. Prediction of dynamic contact angle histories of a bubble growing at a wall. *International Journal of Heat and Fluid Flow*, 25(1):74–80, 2004. (Cited on page 67)

[190] C.M. Voutsinos and R.L. Judd. Laser interferometric investigation of the microlayer evaporation phenomenon. *ASME Journal of Heat Transfer*, 97(1):88–92, 1975. (Cited on page 64)

[191] J.W. Westwater. Boiling of liquids. *Advances in Chemical Engineering*, 2, 1958. (Cited on page 11)

[192] A. Yabe. Augmentation of convective and boiling heat transfer by applying an electrohydrodynamical liquid jet. *International Journal of Heat and Mass Transfer*, 31(2):407–417, 1988. (Cited on page 17)

[193] Y.M. Yang and J.R. Maa. On the criteria of nucleate pool boiling enhancement by surfactant addition to water. *Chemical Engineering Research and Design*, 79(4):409–416, 2001. (Cited on page 102)

[194] Z. Yin, A. Prosperetti, and J. Kim. Bubble growth on an impulsively powered microheater. *International Journal of Heat and Mass Transfer*, 47:1053–1067, 2004. (Cited on page 64)

[195] Z. Yu, R.K. Al-Dadah, and R.H.S. Winterton. A theoretical investigation of electrohydrodynamically (EHD) enhanced condensation heat transfer. In Edizioni ETS, editor, *Two-Phase Flow Modelling and Experimentation, Pisa, Italy*, volume 1, pages 463–473, 1999. (Cited on pages 18 and 19)

[196] M.C. Zaghdoudi. *Amélioration des transferts de chaleur en ébullition sous l'action d'un champ électrique*. PhD thesis, INSA Lyon, 1996. (Cited on pages 17, 19 and 24)

[197] M.C. Zaghdoudi and M. Lallemand. Study of the behaviour of a bubble in an electric field: steady shape and local fluid motion. *International Journal of Thermal Sciences*, 39:39–52, 1999. (Cited on page 19)

[198] M.C. Zaghdoudi and M. Lallemand. An analysis of the steady shape of a bubble in an electric field. *International Journal Transport Phenomena*, 2:9–26, 2000. (Cited on pages 19 and 147)

[199] L.Z. Zeng, J.F. Klausner, and R. Mei. A unified model for the prediction of bubble detachment diameters in boiling systems. *International Journal of Heat and Mass Transfer*, 36:2261–2270, 1993. (Cited on pages 89 and 105)

[200] H.B. Zhang, Y.Y. Yan, and Y.Q. Zu. Numerical modelling of EHD effects on heat transfer and bubble shapes of nucleate boiling. *Applied Mathematical Modelling*, 34(3):626–638, 2010. (Cited on page 147)

[201] Y.Q. Zu and Y.Y. Yan. A numerical investigation of electrohydrodynamic (EHD) effects on bubble deformation under pseudo-nucleate boiling conditions. *International Journal of Heat and Fluid Flow*, 30:761–767, 2009. (Cited on pages xiii, 147, 163 and 164)

[202] N. Zuber. The dynamics of vapor bubbles in nonuniform temperature fields. *International Journal of Heat and Mass Transfer*, 2:83–98, 1961. (Cited on page 73)

[203] I. Zun and J. Groselj. The structure of bubble non-equilibrium movement in free-rise and agitated-rise conditions. *Nuclear Engineering and Design*, 163:99–115, 1996. (Cited on page 141)

Appendices

Appendix A

Nomenclature

Latin letters

A	Helmholtz free energy	J
c_p	specific heat capacity	$J{\cdot}kg^{-1}{\cdot}K^{-1}$
C	curvature	m^{-1}
D	bubble diameter	m
E	electric field intensity	$V{\cdot}m^{-1}$
$\mathscr{E}$	energy	J
f_d	bubble departure frequency	s^{-1}
f	body force	$N{\cdot}m^{-3}$
F	force	N
g	gravity acceleration	$\approx 9.8\,m{\cdot}s^{-2}$
h	heat transfer coefficient	$W{\cdot}m^{-2}$
h_{cg}	height of the center of gravity	m
h_{fg}	latent heat of vaporization	$J{\cdot}kg^{-1}$
h_z	height of the bubble	m
I_R	Robinson and Judd criterion	–
K	Added mass coefficient	–
L_c	capillary length	m
n	number of molecules	mol
N	number of elements per unit of volume	m^{-3}
P	pressure	Pa
q	heat flux	$W{\cdot}m^{-2}$
r	length in the radial direction	m
R	radius	m
R_a	arithmetic average of absolute values of height	m
S	surface	m^2
$\mathscr{S}$	entropy	$J{\cdot}kg^{-1}{\cdot}K^{-1}$
t	time	s
T	temperature	K

u	velocity	$m \cdot s^{-1}$
U	voltage	V
v	velocity	$m \cdot s^{-1}$
V	volume	m^3
W	work	J
x	length in the x-direction	m
y	length in the y-direction	m
z	length in the z-direction	m

Greek letters

α	angle	rad
α_i	thermal diffusivity of phase i	$m^2 \cdot s^{-1}$
β	thermal expansion coefficient	K^{-1}
ε	absolute electric permittivity	$F \cdot m^{-1}$
ε_r	relative electric permittivity	–
ε_{res}	residual error on the force balance	N
λ	thermal conductivity	$W \cdot m^{-1} \cdot K^{-1}$
λ_C	collision frequency	s^{-1}
μ	dynamic viscosity	$kg \cdot m^{-1} \cdot s^{-1}$
μ_c	chemical potential	$J \cdot mol^{-1}$
ρ	density	$kg \cdot m^{-3}$
ρ_e	free charges density	$C \cdot m^{-3}$
σ	surface tension	$N \cdot m^{-1}$
θ	contact angle	rad

Hebrew letter

$\aleph$	surface	m^2

Subscripts and superscripts

b	relative to the bubble
$base$	relative to the base of the bubble
$buoy$	buoyancy

cg	center of gravity
CL	contact line
Cu	copper
d	at detachment or departure
l	liquid phase
LI	liquid inertia
mom	momentum
nc	nucleation site
r	radial direction
sat	saturation
v	vapour phase
vf	viscous forces
vs	viscous stress
W	heated wall or surface
x	x-direction
y	y-direction
z	z-direction
σ	surface tension
$*$	dimensionless, or at equilibrium

Non dimensional numbers

A_s	Siedel aspect ratio parameter
Fr	Froude number
Gr	Grashof number
Ja	Jakob number
Ma	Marangoni number
Prd	Prandtl number
Ra	Rayleigh number
Re	Reynolds number
We	Weber number
We_e	Electric Weber number

Constants

k	Boltzmann constant	$\approx 1.380\,650\,3 \times 10^{-23}\,\mathrm{m^2{\cdot}kg{\cdot}s^{-2}}$
ε_0	electric permittivity of absolute vacuum	$\approx 8.85 \times 10^{-12}\,\mathrm{F{\cdot}m^{-1}}$

Appendix B

Measurement of the height of the center of gravity

For volume and center of gravity calculations, the bubble is divided into slices of 1 pixel height, as shown in Fig. B.1. Each slice is considered as a cylinder (thus axisymmetric), and the volume is the sum of each cylinder. Two methods were considered in order to compute the height of the center of gravity:

Method 1: The height of the center of gravity h_{cg} is obtained by dividing the sum of the volume each cylinder V_i weighted by its average height z_i by the total volume of the bubble V.

$$h_{cg} = \frac{\sum_i V_i z_i}{V} \tag{B.1}$$

Method 2: The height of the center of gravity h_{cg} is considered as the height at which half of the volume is below and half of the volume is above.

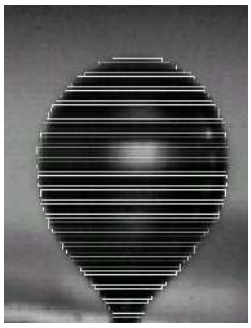

Figure B.1: Volume discretization of a bubble

The second method is inaccurate and represents rather a volume median height. It was used by Siedel *et al.* [169], and the present Appendix estimates the error that can be caused by the use of Method 2.

For a bubble growing at a superheat of 2.6 K, the evolution of the height of the center of gravity is shown in Fig. B.2 using both Method 1 and Method 2. It can been seen that Method 2 slightly overestimates h_{cg}. However, the trends and evolutions are similar, and the overestimation remains below 1 % in all cases.

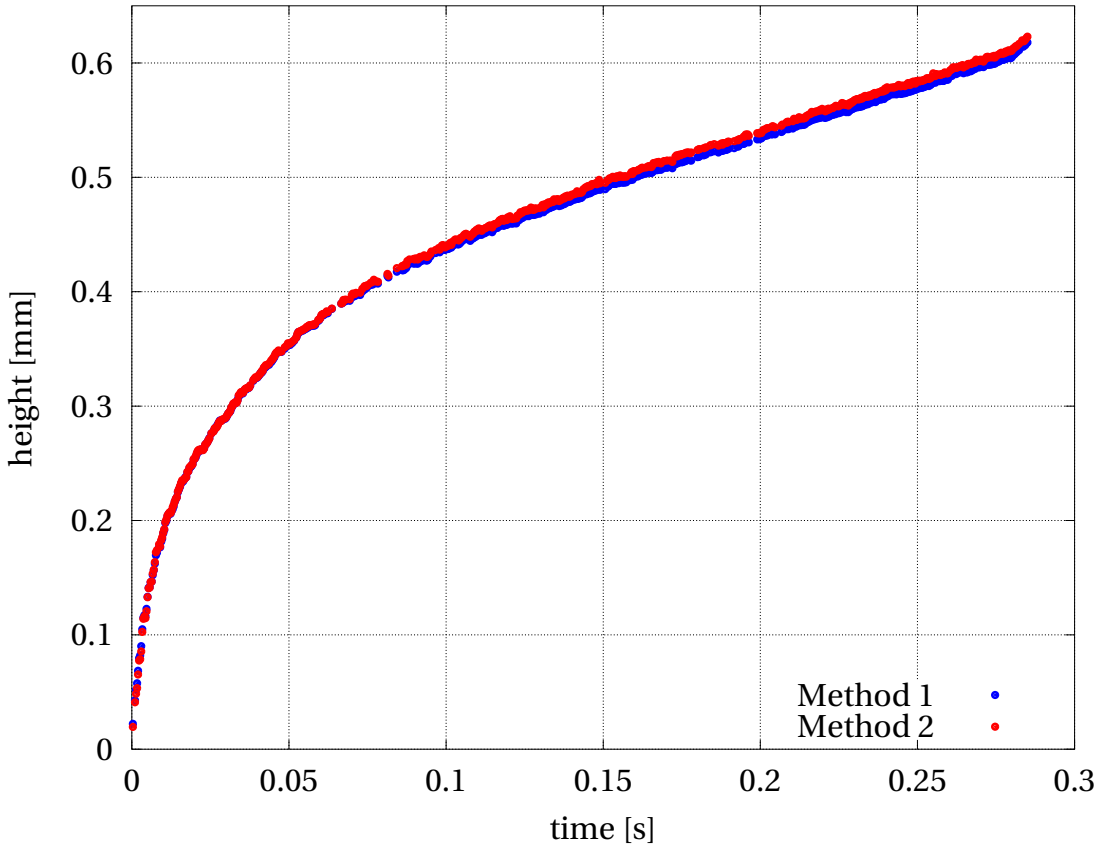

Figure B.2: Height of the center of gravity for a bubble at a wall superheat of 2.6 K.

Appendix C

Added mass coefficients

The expression considered for the liquid inertia and added mass force is equation 5.17:

$$\overrightarrow{F}_{LI} = K_1 \rho_l \frac{\mathrm{d}h_{cg}}{\mathrm{d}t} \frac{\mathrm{d}V}{\mathrm{d}t} \overrightarrow{k} + K_2 \rho_l V \frac{\mathrm{d}^2 h_{cg}}{\mathrm{d}t^2} \overrightarrow{k} \tag{C.1}$$

with K_1 and K_2 the added mass coefficients, ρ_l the liquid density, h_{cg} the height of the center of gravity and V the volume of the bubble.

Some values of the added mass coefficients K_1 and K_2 may be found for study cases with simplistic geometries. Two different study cases are considered here.

C.1 Spherical bubble growing in an infinite liquid at rest

The case of a spherical bubble growing in an infinite liquid at rest, in the absence of a wall was investigated by Magnaudet *et al.* [121] and cited by Duhar [55]. The expression of the liquid inertia and added mass force given is:

$$\overrightarrow{F}_{LI} = \frac{1}{2} \rho_l \frac{\mathrm{d}}{\mathrm{d}t} \left[V \overrightarrow{u_{cg}} \right] \tag{C.2}$$

with $\overrightarrow{u_{cg}}$ the velocity of the center of gravity of the bubble.

Equation C.2 can be developped into:

$$\overrightarrow{F}_{LI} = 0.5 \rho_l \frac{\mathrm{d}h_{cg}}{\mathrm{d}t} \frac{\mathrm{d}V}{\mathrm{d}t} \overrightarrow{k} + 0.5 \rho_l V \frac{\mathrm{d}^2 h_{cg}}{\mathrm{d}t^2} \overrightarrow{k} \tag{C.3}$$

the added mass coefficients being here $K_1 = 0.5$ and $K_2 = 0.5$.

C.2 Hemispherical bubble growing on a plane wall

The case of a hemispherical bubble growing on a wall was investigated by Klausner *et al.* [96] in a fluid at rest and by Legendre *et al.* [111] in a linear shear flow. In such a study case, the height of the center of gravity and the volume of the bubble can both be expressed as functions of the radius R of the hemisphere, and their time derivatives as functions of $\dot{R}$ and $\ddot{R}$:

$$h_{cg} = \frac{3}{8}R \tag{C.4}$$

$$\frac{\mathrm{d}h_{cg}}{\mathrm{d}t} = \frac{3}{8}\dot{R} \tag{C.5}$$

$$\frac{\mathrm{d}^2h_{cg}}{\mathrm{d}t^2} = \frac{3}{8}\ddot{R} \tag{C.6}$$

$$V = \frac{2}{3}\pi R^3 \tag{C.7}$$

$$V = \frac{6}{3}\pi R^2\dot{R} = \frac{3V}{R}\dot{R} \tag{C.8}$$

Equation C.1 can be reformulated into:

$$\overrightarrow{F}_{LI} = \rho_l V\left(K_1 \times \frac{9}{8R}\dot{R}^2 + K_2 \times \frac{3}{8}\ddot{R}\right)\overrightarrow{k} \tag{C.9}$$

The liquid inertia force expressed by Legendre *et al.* [111] consists of two terms: the first term depends on the velocity of the shear flow and is equal to zero if the liquid is at rest, and the second term is of the same form that Equation C.9 with $K_1 = 2$ and $K_2 = 4$.

Equation C.1 can also be reformulated into:

$$\overrightarrow{F}_{LI} = \rho_l\pi R^2\left(K_1 \times \frac{3}{4}\dot{R}^2 + K_2 \times \frac{1}{4}\ddot{R}R\right)\overrightarrow{k} \tag{C.10}$$

The liquid inertia force expressed by Klausner *et al.* [96] is of the same form than Equation C.10 with $K_1 = 2$ and $K_2 = 4$.

Appendix D

Interpolation of the angle α for the force computation

The angle α, defined in the liquid phase at the base of the bubble between the *liquid-vapour* interface and the horizontal plane is measured of the recorded images as described in Section 5.2.2.2.1. The experimental data points of α are shown in Fig. D.1.

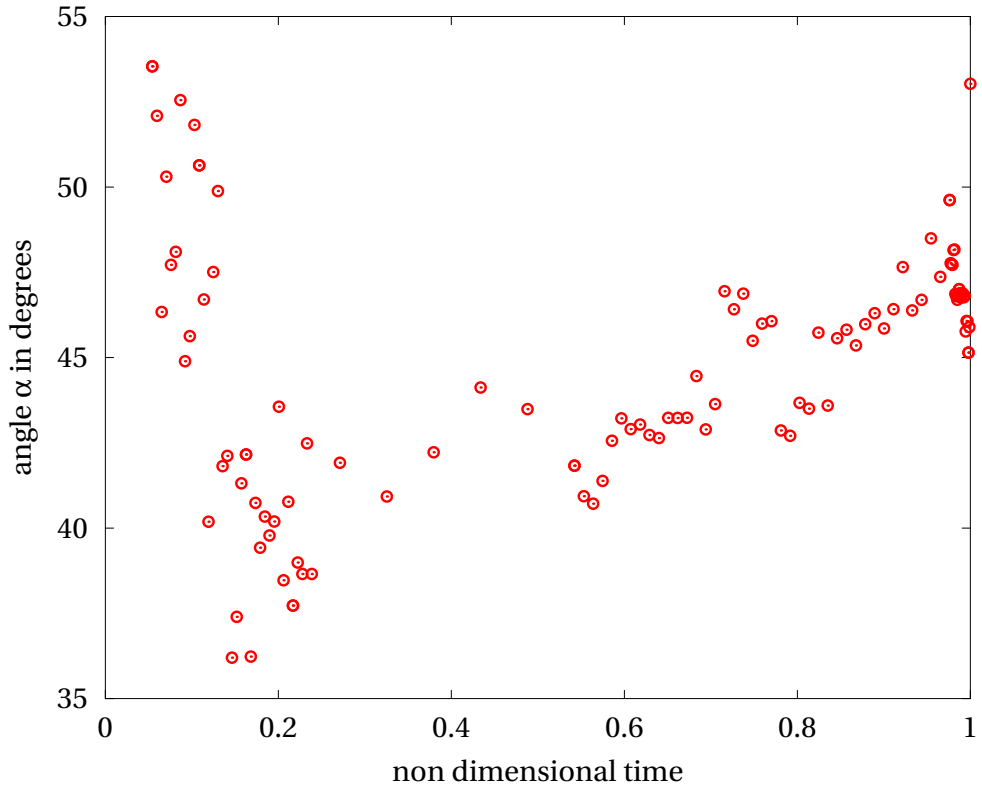

Figure D.1: Values of α measured on the images with a wall superheat of 2.1 K.

The uncertainty on the measurement of α is not possible to estimate except from the dis-

tribution of the data points, and no particular function is expected to describe the evolution of α during the bubble growth. The only hypothesis chosen is to consider a smooth time evolution of α.

It is however comfortable for the computation of the forces to fit the time evolution of α with a simple function. *A priori*, any function can be chosen. It is common to choose simple functions such as a straight line, a polynomial function, a power or an exponential function. A polynomial data fit is chosen due to its simplicity .

Figure D.2 shows the data fit of the time evolution of α with several polynomial functions of orders ranging from 3 to 9. The decrease of α for $t^* < 0.2$ is fairly represented by all functions. For $0.2 < t^* < 0.6$, the angle is underestimated by polynomials of order 3 and 4. The wavy shape of the polynomial function does not necessarily represents the real evolution of α, and the amplitude of the waves is high for the highest orders. It can thus be concluded that polynomial functions of order between 5 and 8 fairly represent the experimental data.

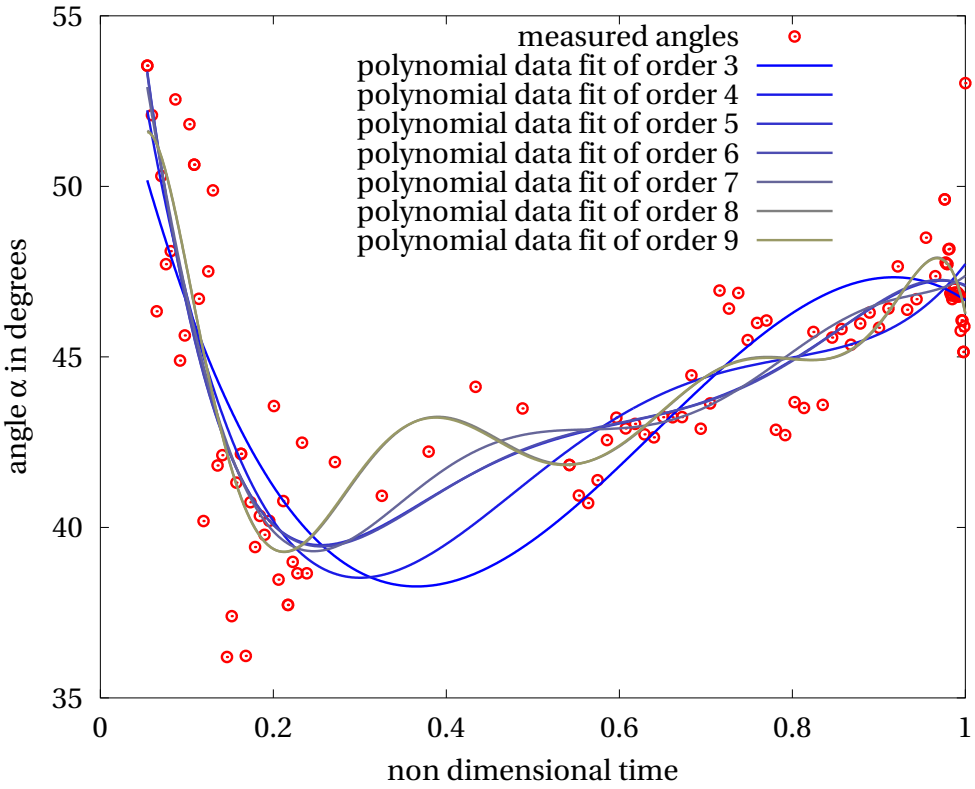

Figure D.2: Data fit of the time evolution of α with polynomial functions of several orders between 3 and 9.

The consequence of the order of the polynomial function chosen can be evaluated in Fig. D.3. Few differences can be observed between the curves. It can be concluded that any polynomial function of order ranging from 5 to 8 is suitable for the interpolation of α. It should also be noted that the wavy shape of the curve might be only due to the use of a polynomial function.

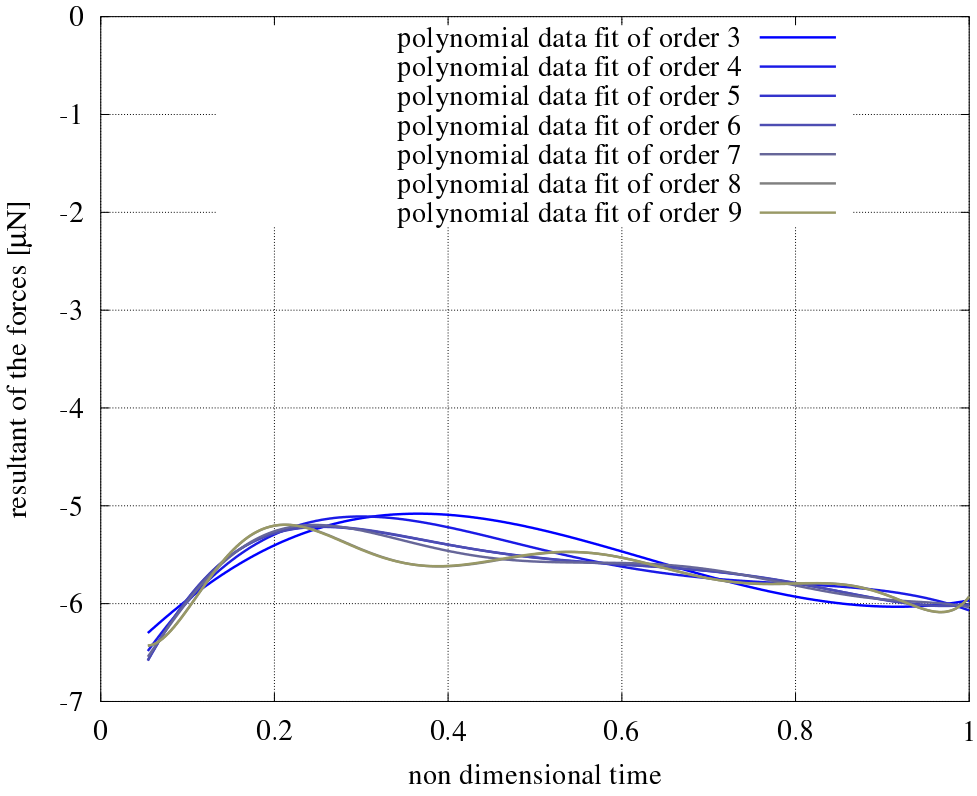

Figure D.3: Resultant of the adhesion forces using several polynomial data fit of α.

Appendix E

Derivation of the height of the center of gravity and of the volume of the bubble

The momentum variation of the bubble can be expressed as follows (see Section 5.2.1.1):

$$\vec{F}_{mom} = \rho_v \frac{\mathrm{d}h_{cg}}{\mathrm{d}t} \frac{\mathrm{d}V}{\mathrm{d}t} \vec{k} + \rho_v V \frac{\mathrm{d}^2 h_{cg}}{\mathrm{d}t^2} \vec{k} \tag{E.1}$$

with $\vec{k}$ the unit vertical vector in the upward direction and h_{cg} the height of the center of gravity.

Similarly, the resultant of the liquid inertia forces can be expressed as follows (see Section 5.2.1.2):

$$\vec{F}_{LI} = K_1 \rho_l \frac{\mathrm{d}h_{cg}}{\mathrm{d}t} \frac{\mathrm{d}V}{\mathrm{d}t} \vec{k} + K_2 \rho_l V \frac{\mathrm{d}^2 h_{cg}}{\mathrm{d}t^2} \vec{k} \tag{E.2}$$

with $0.5 < K_1 < 2$ and $0.5 < K_2 < 4$. For the present appendix, unity is arbitrary chosen for the values of both K_1 and K_2.

Apart from the thermodynamic properties of pentane, these equations include the volume of the bubble and its first time derivative, and the first and second time derivatives of the height of the center of gravity. Both the volume of the bubble and the height of its center of gravity are measured on the recorded images.

In order to obtain the time derivatives of the measured data, it is suggested to fit the data with a simple and derivable function. No particular function is expected to describe accurately these measures, so a polynomial function is chosen due to its simplicity. It should be noted that a relatively high uncertainty is expected for the first time derivative, and even more for the second time derivative of the measurements.

Figure E.1 shows the height of the center of gravity of a bubble at a wall superheat condition of 2.1 K. Several polynomial functions are used to fit the experimental data, with orders

ranging from 7 to 8. Although all curves capture the experimental data with an overall good agreement, two observations can be made:

- The fitting of the first instants are strongly related to the location of the time origin. Yet, this time origin is arbitrary chosen by visual observation of the recorded images.
- An acceleration of the bubble can be observed just before departure. Yet, only polynomial functions with odd orders can capture such an evolution. It is shown that only polynomial functions of order 7 and 9 correctly fit the data before departure.

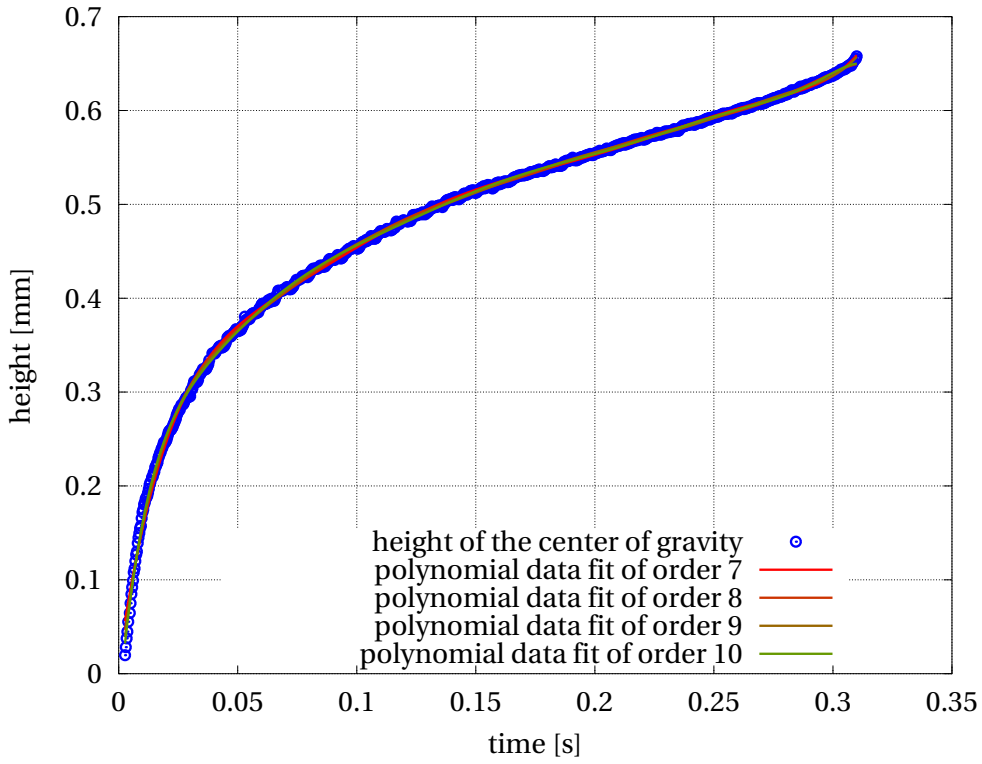

Figure E.1: Polynomial data fit of several orders of the time evolution of the height of the center of gravity of a bubble at a wall superheat of 2.1 K.

Figures E.2 and E.3 show the time evolution of the first and second derivatives of the polynomial functions defined in Fig. E.1. It is again observed that only polynomial functions of order 7 and 9 correctly capture the behaviour of the bubble before detachment. It can be concluded that only an odd order polynomial function can be used for the fitting of the height of the center of gravity.

Figure E.4 shows the time evolution of the volume of the bubble. The oscillations that can be observed come from the shape oscillations of the bubble (see Section 5.1.5) that impact the measurement of the bubble, but should not necessarily be interpreted as volume oscillations. The fitting function should thus smooth the oscillations.

The time evolution of the volume is fitted with several polynomial functions of order ranging from 5 to 8 (see Fig. E.4). No obvious differences can be observed visually from the different fitting functions.

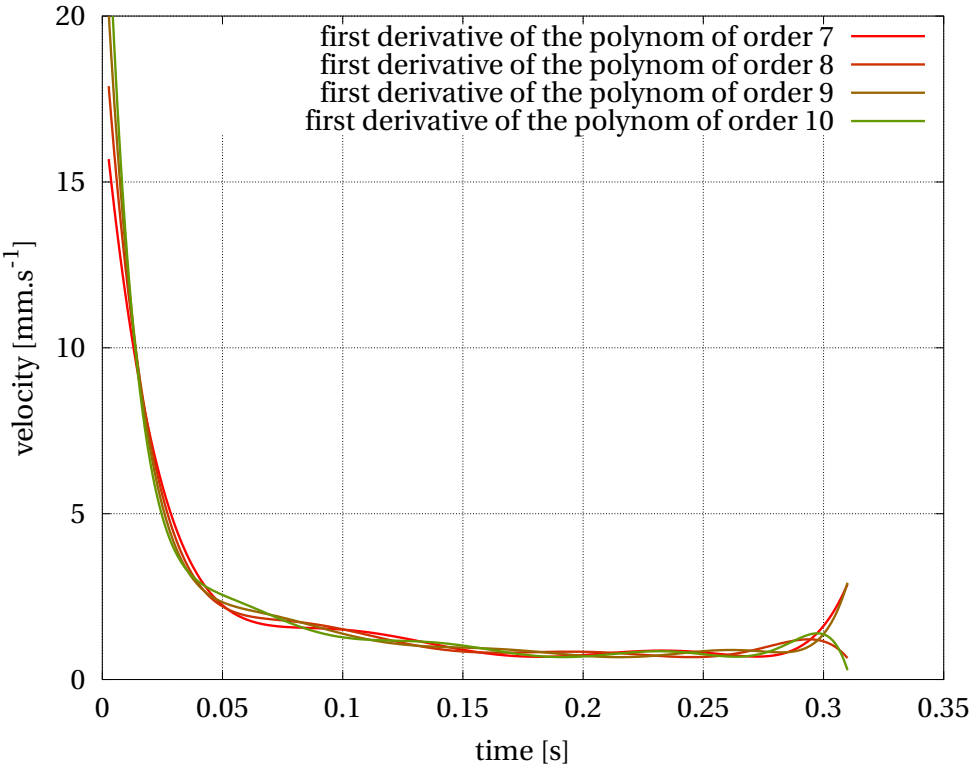

Figure E.2: Time first derivative of the previously defined polynomial functions.

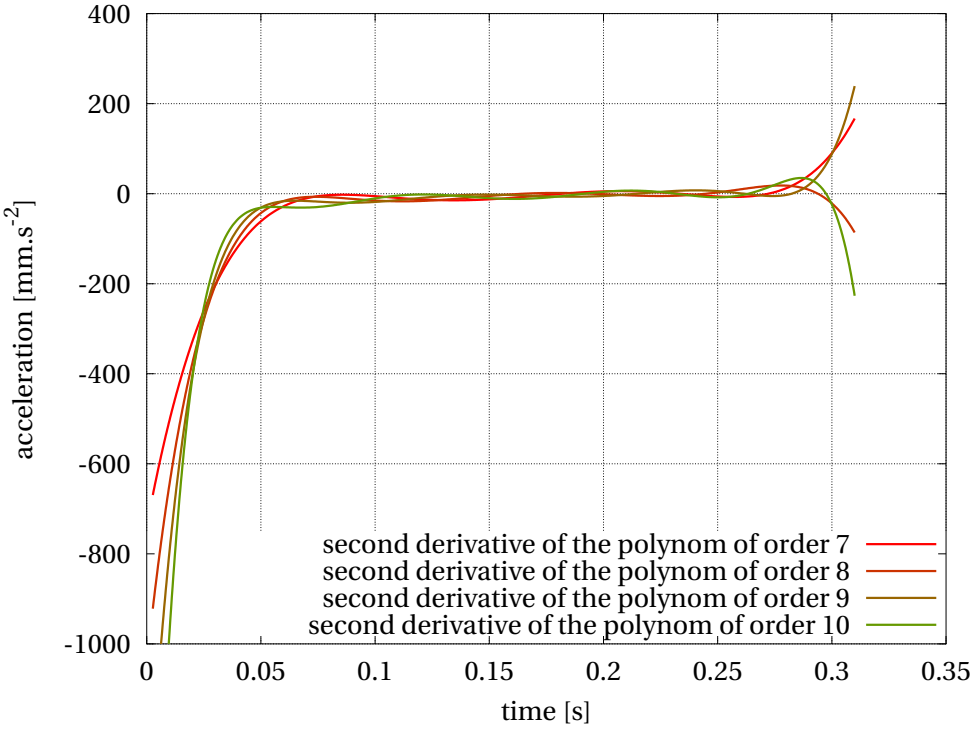

Figure E.3: Time second derivative of the previously defined polynomial functions.

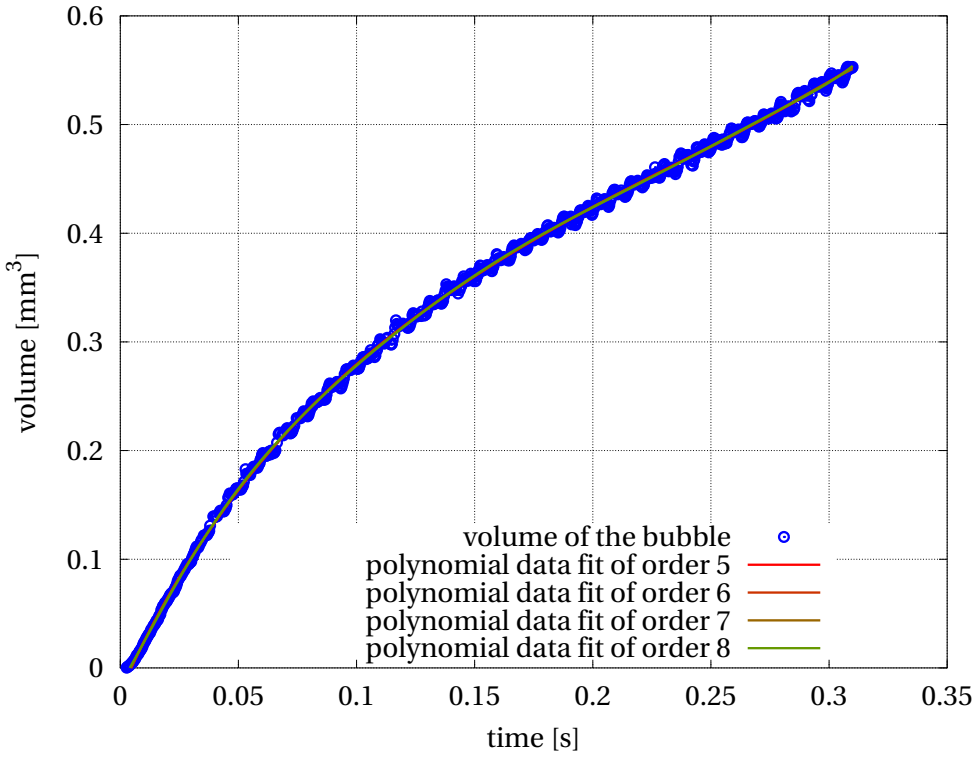

Figure E.4: Polynomial data fit of several orders of the time evolution of the volume of a bubble at a wall superheat of 2.1 K.

The derivative of the fitting functions are computed and plotted in Fig. E.5 in order to obtain the time derivative of the volume of the bubble. The evolutions observed are smooth for polynomial functions of 5^{th} and 6^{th} order, whereas waves appear for higher orders. These waves can not be explained by a physic mechanism and are probably due to mathematical artefacts. For a proper description, a polynomial function of 5^{th} order seems suitable.

The impact of the order of the polynomial function chosen on the momentum variation and on the resultant of the liquid inertia forces needs to be estimated. As both forces are proportional to each other, only the resultant of the liquid inertia forces will be investigated.

Following the previous remarks, two different cases will be considered:

Case A: A 7^{th} order polynomial function is used to fit the time evolution of the height of the center of gravity of the bubble, and a 5^{th} order polynomial function is used to fit the time evolution of its volume.

Case B: A 9^{th} order polynomial function is used to fit the time evolution of the height of the center of gravity of the bubble, and a 5^{th} order polynomial function is used to fit the time evolution of its volume.

Figure E.6 shows the time evolution of the resultant of the liquid inertia forces for cases A and B. As other forces are not estimated at the beginning of the bubble growth, the computation is performed only for $0.05 < t^* < 1$.

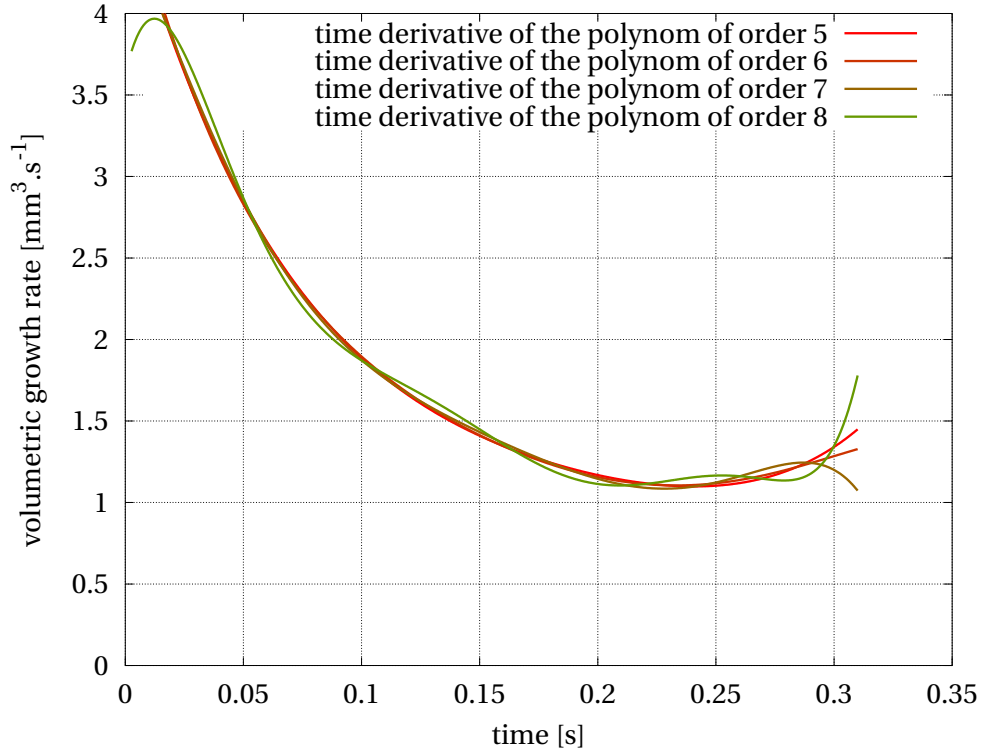

Figure E.5: Time first derivative of the previously defined polynomial functions.

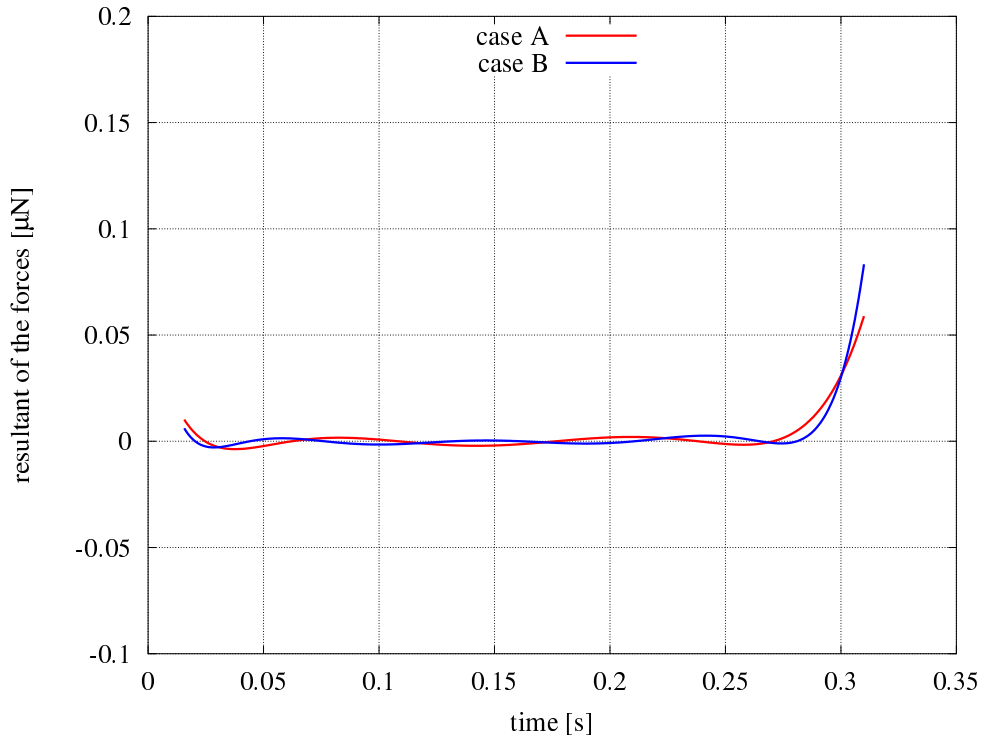

Figure E.6: Resultant of the liquid inertia forces for two different set of polynomial data fit for the volume and the center of gravity of the bubble.

It can be observed from Fig. E.6 that both cases show similar results. The same trends and order of magnitude are found.

Appendix F

Measurement and computation of the forces at a wall superheat of 4.7 K

The present appendix contains numerical data and plots for the computation of the force balance at a wall superheat of 4.7 K. Only raw figures are provided as the full development of the calculation is presented in Section 5.2.2.2 at a wall superheat of 2.1 K.

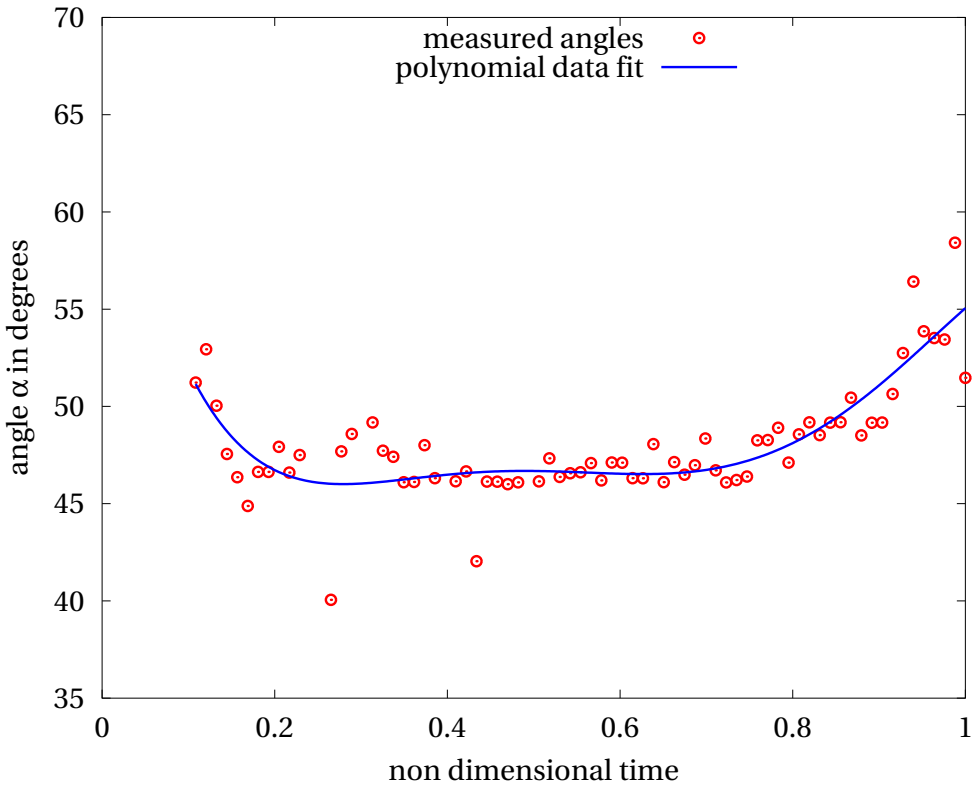

Figure F.1: Angle α during bubble growth at a wall superheat of 4.7 K.

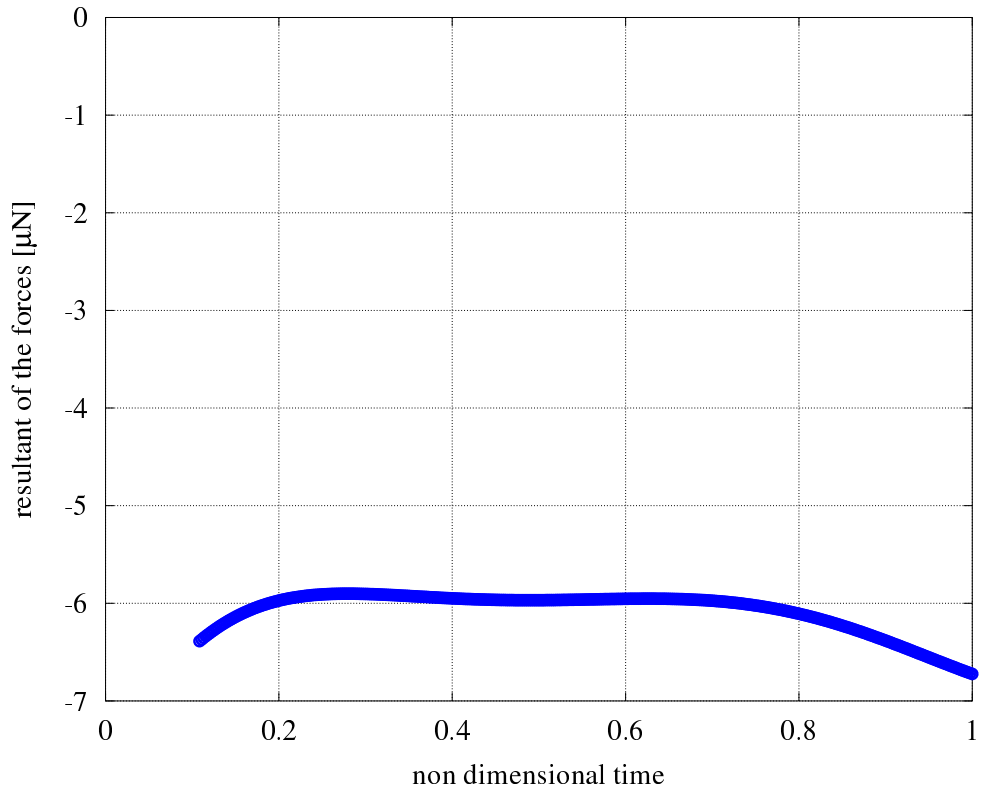

Figure F.2: Resultant of the adhesion forces acting on a bubble at a wall superheat of 4.7 K.

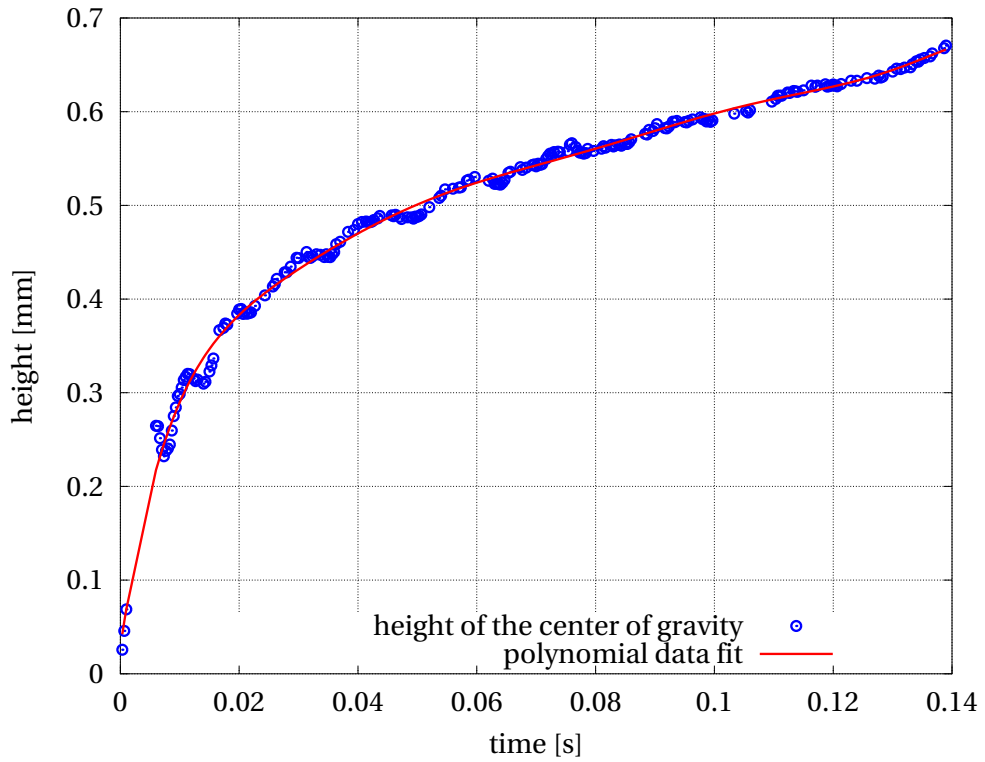

Figure F.3: Height of the center of gravity of a bubble at a wall superheat of 4.7 K.

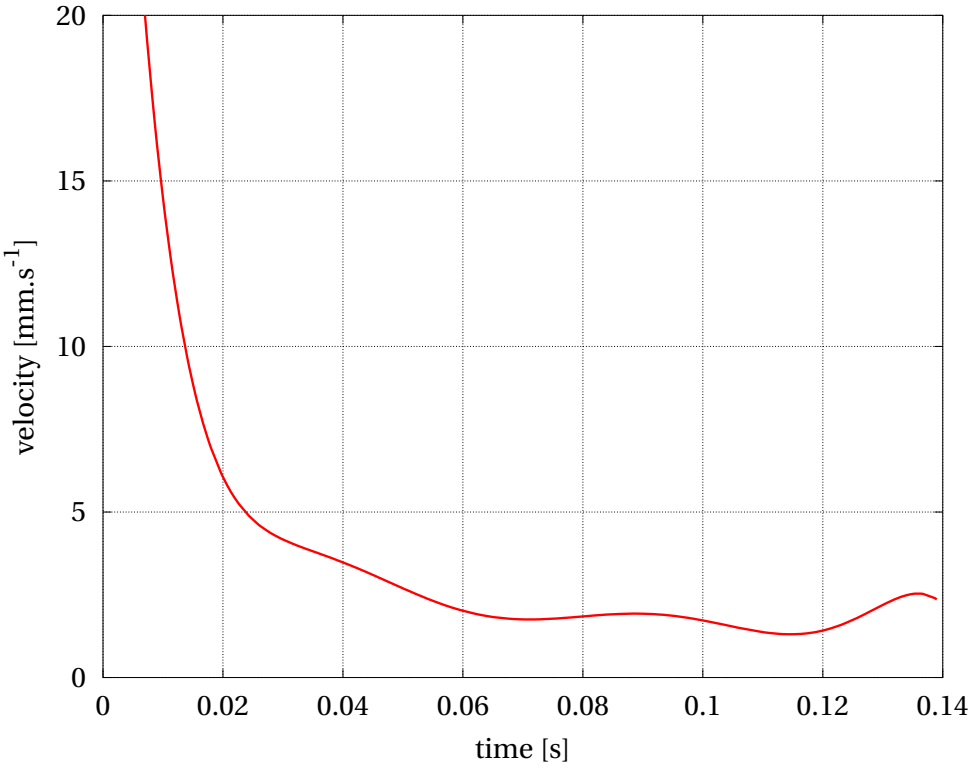

Figure F.4: Time first derivative of the height of the center of gravity of a bubble at a wall superheat of 4.7 K.

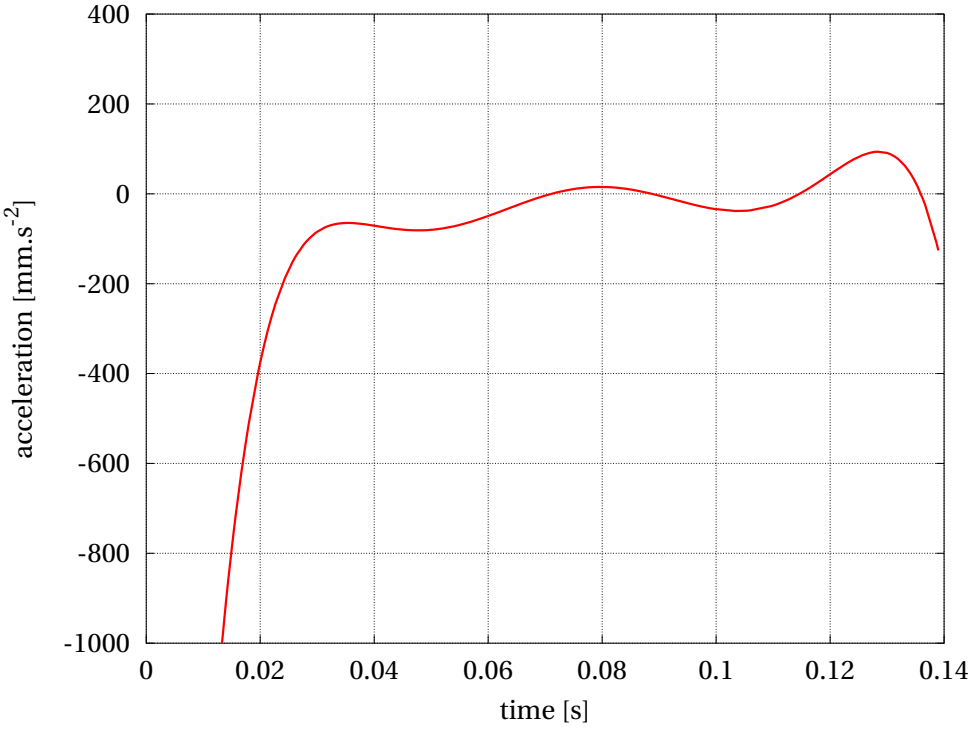

Figure F.5: Time second derivative of the height of the center of gravity of a bubble at a wall superheat of 4.7 K.

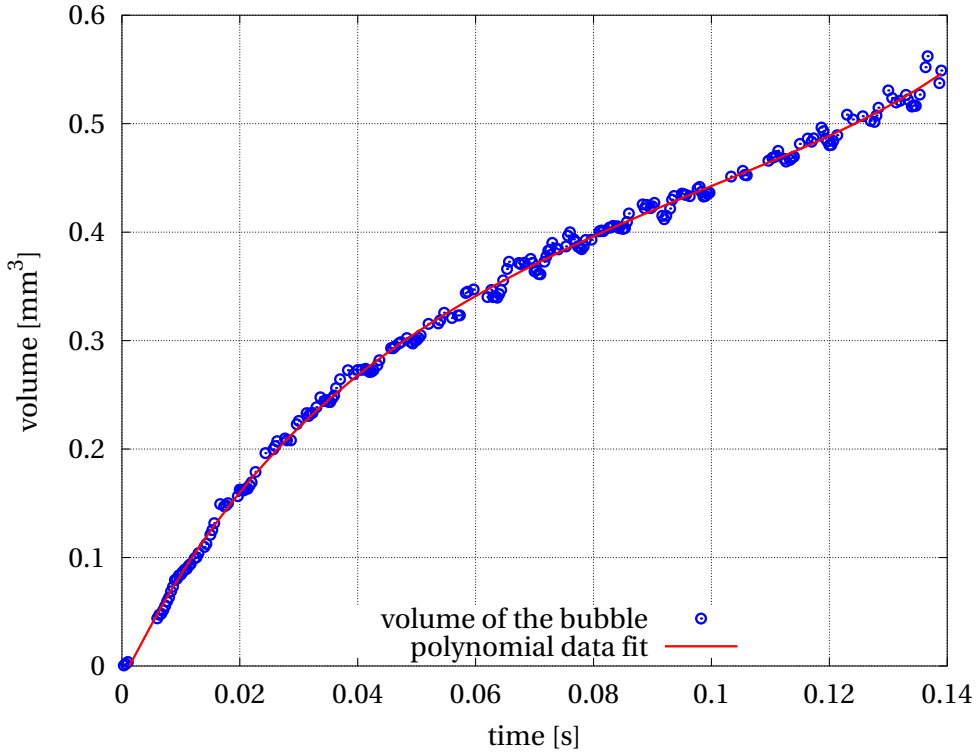

Figure F.6: Volume of a bubble at a wall superheat of 4.7 K.

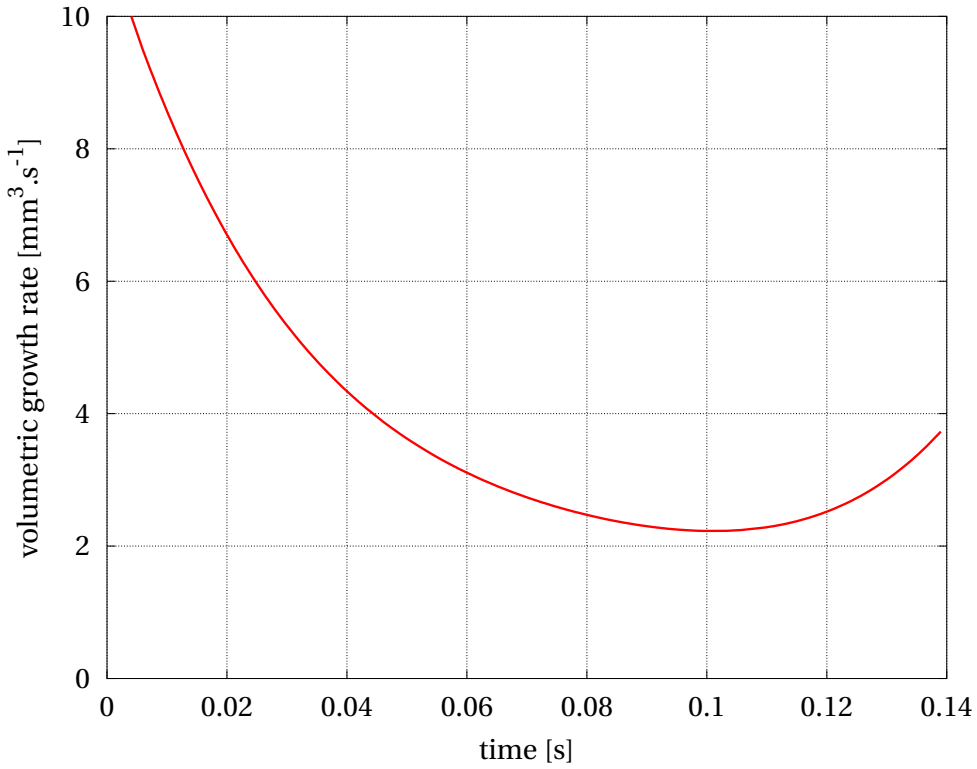

Figure F.7: Volumetric growth rate of a bubble at a wall superheat of 4.7 K.

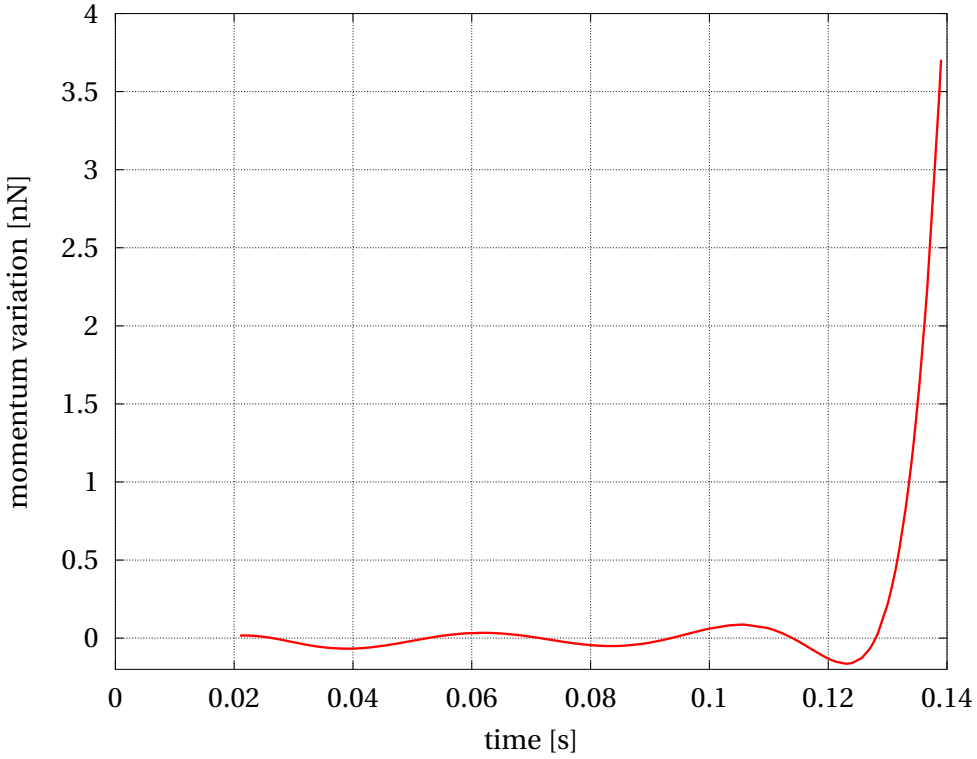

Figure F.8: Momentum variation of a growing bubble at a wall superheat of 4.7 K.

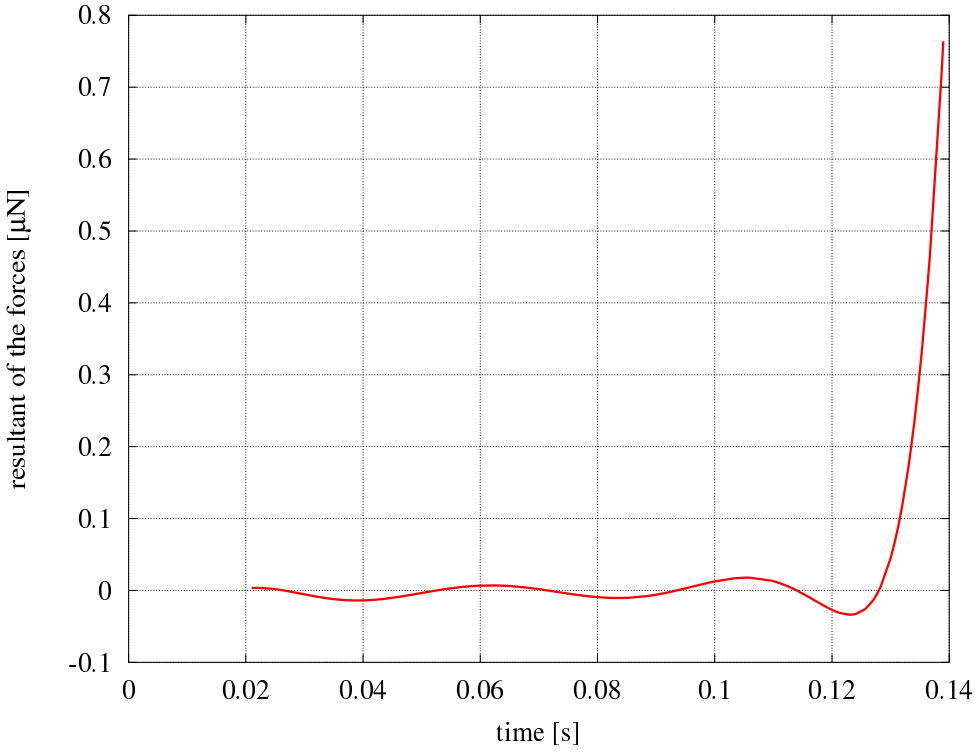

Figure F.9: Resultant of the liquid inertia forces acting on a growing bubble at a wall superheat of 4.7 K.

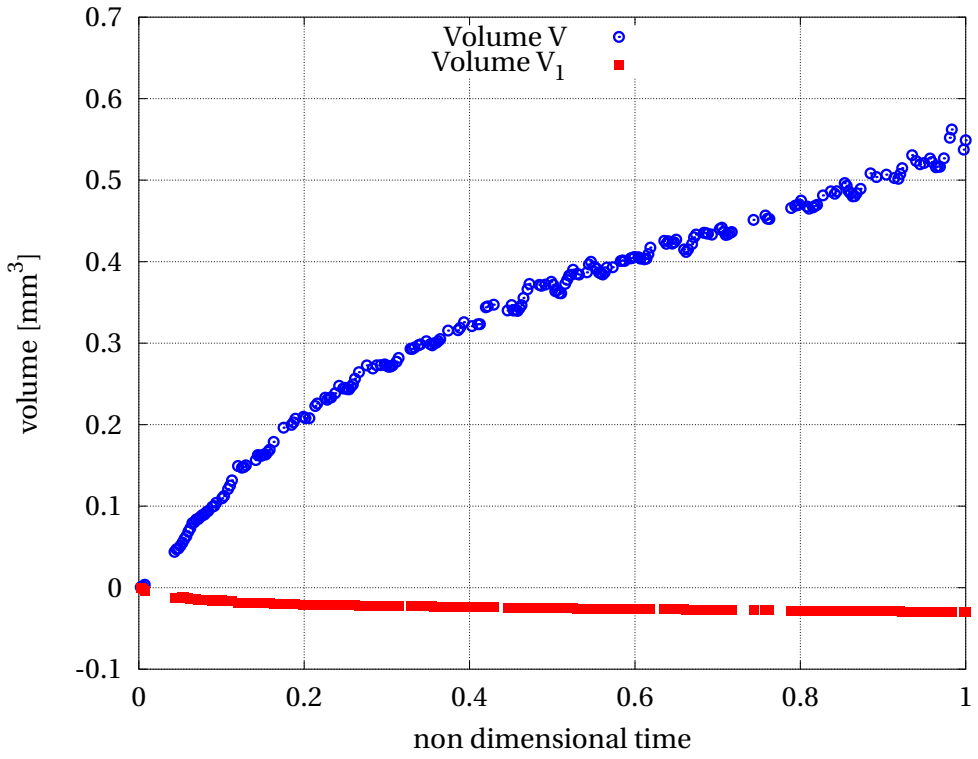

Figure F.10: Growth of the volume V and V_1 of a bubble at a wall superheat of 4.7 K.

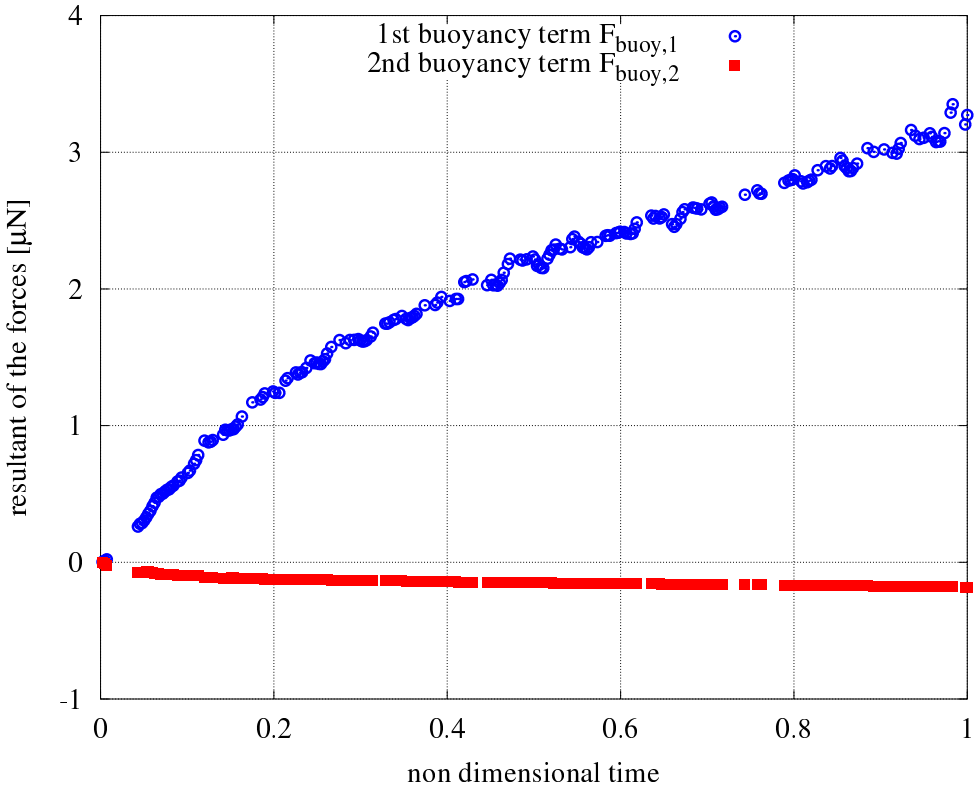

Figure F.11: Resultant of the first and second buoyancy terms acting on a bubble at a wall superheat of 4.7 K.

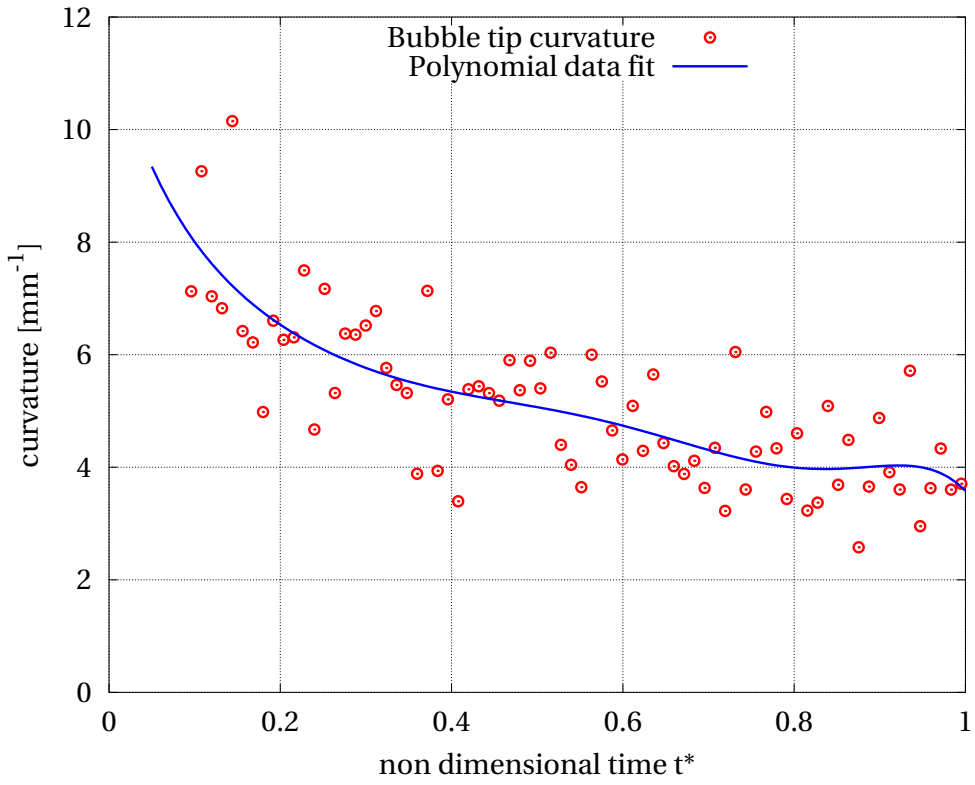

Figure F.12: Curvature at the apex of a bubble at a wall superheat of 4.7 K.

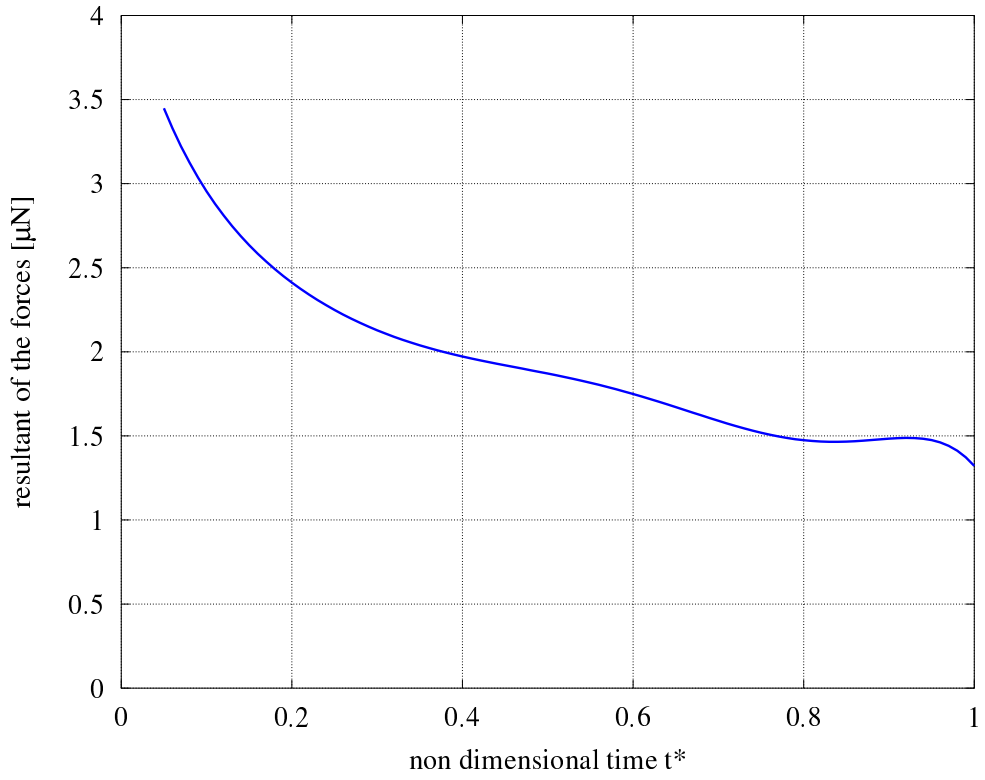

Figure F.13: Resultant of the third buoyancy term acting on a bubble at a wall superheat of 4.7 K.

Appendix G

Non dimensional bubble growth at various electrode voltage

This Appendix shows detailed non-dimensional bubble growth for various wall superheat conditions for an upper electrode voltage of 12 kV, 18 kV and 24 kV in respectively Fig. G.1, Fig. G.2 and Fig. G.3.

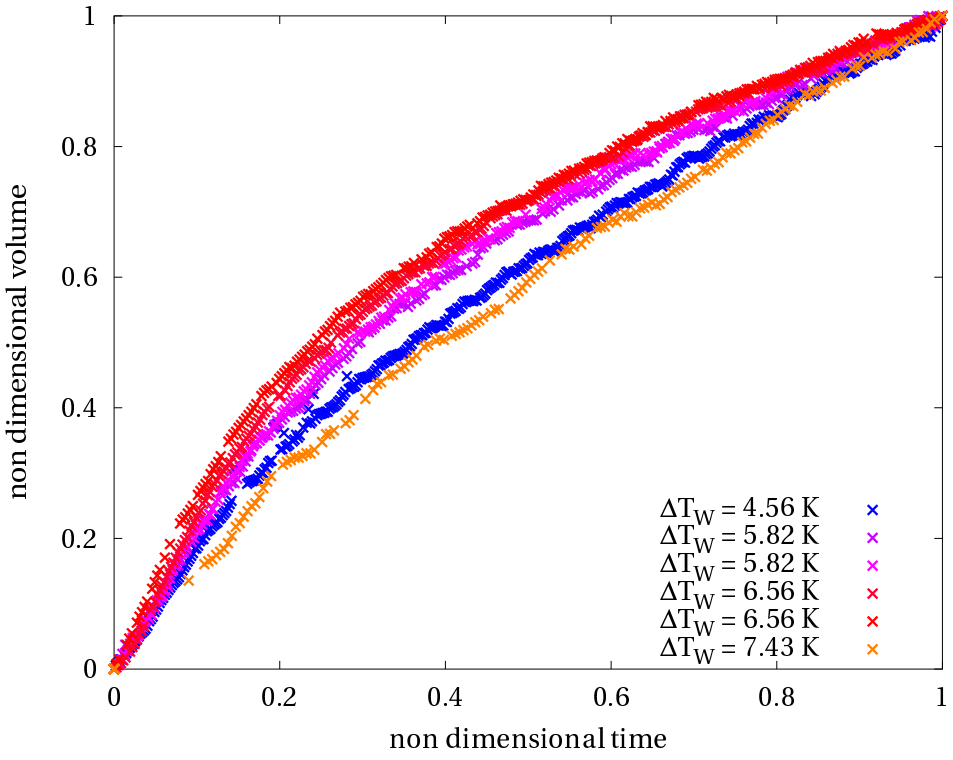

Figure G.1: Non dimensional bubble growth for different wall superheat conditions with an upper electrode voltage of 12 kV.

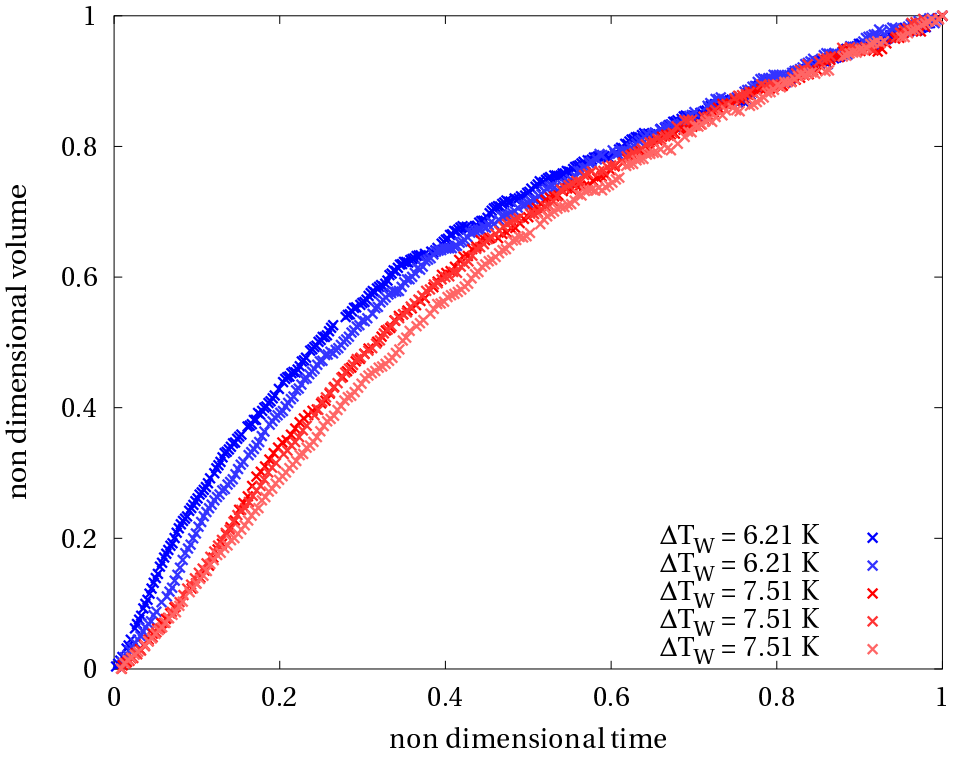

Figure G.2: Non dimensional bubble growth for different wall superheat conditions with an upper electrode voltage of 18 kV.

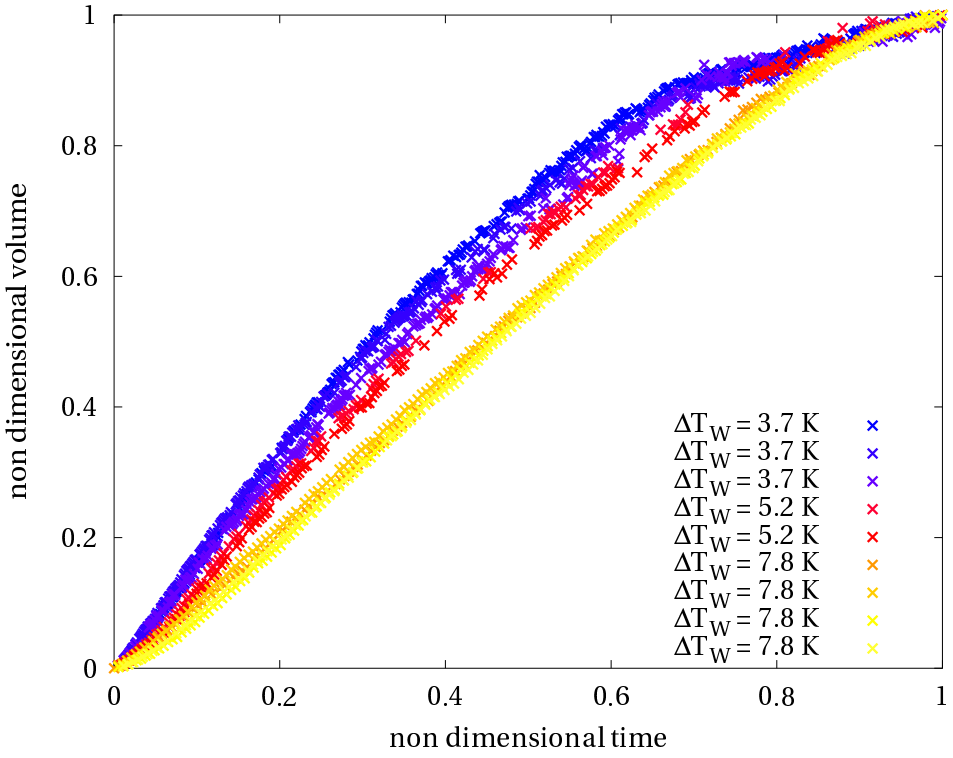

Figure G.3: Non dimensional bubble growth for different wall superheat conditions with an upper electrode voltage of 24 kV.

Appendix H

Aspect ratio at various electrode voltages

This Appendix shows height over width aspect ratios for various wall superheat conditions for an upper electrode voltage of 12 kV, 18 kV and 24 kV in respectively Fig. H.1, Fig. H.2 and Fig. H.3.

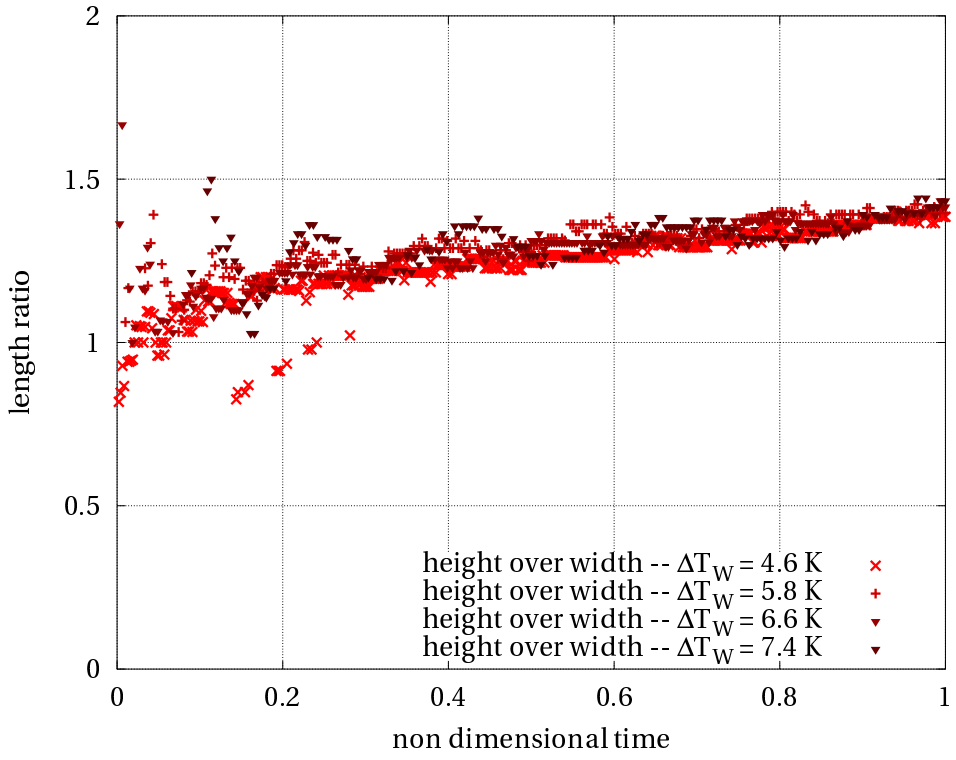

Figure H.1: Height over width aspect ratio for different wall superheat conditions with an upper electrode voltage of 12 kV.

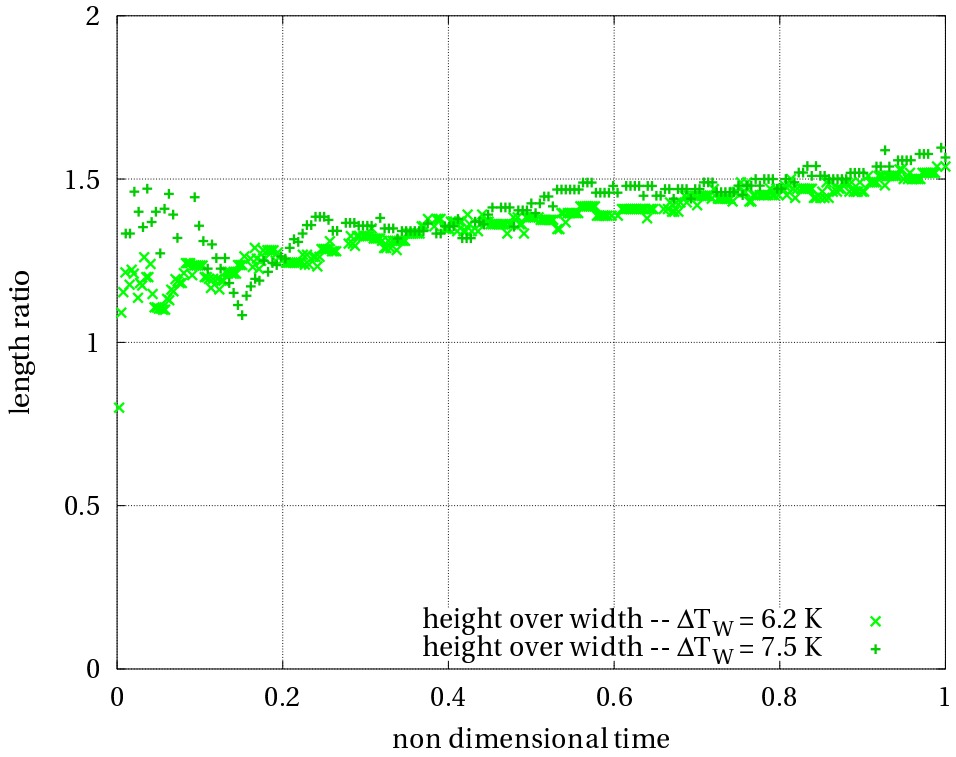

Figure H.2: Height over width aspect ratio for different wall superheat conditions with an upper electrode voltage of 18 kV.

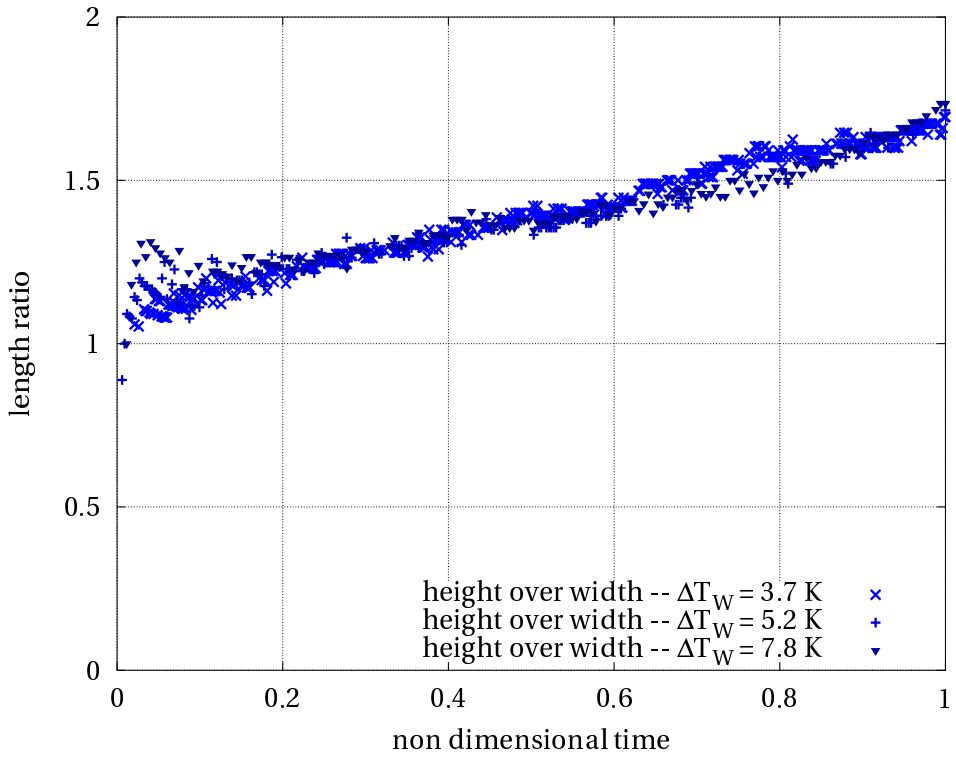

Figure H.3: Height over width aspect ratio for different wall superheat conditions with an upper electrode voltage of 24 kV.

Appendix I

List of Publications by the Author

Articles in peer-reviewed journals

- S. Siedel, S. Cioulachtjian, and J. Bonjour. Experimental analysis of bubble growth, departure and interactions during pool boiling on artificial nucleation sites. *Experimental Thermal and Fluid Science*, 32(8):1504-1511, 2008.
- S. Siedel, S. Cioulachtjian, A.J. Robinson, and J. Bonjour. Electric field effects during nucleate boiling from an artificial nucleation site. *Experimental Thermal and Fluid Science*, 35(5):762-771, 2011.

Communications in conferences or workshops

- S. Siedel, S. Cioulachtjian, S. Di Bari, A.J. Robinson and J. Bonjour. Experimental investigation on the local curvature of bubble interface during boiling on a single nucleation site. *8th ECI International Conference on Boiling and Condensation Heat Transfer*, Lausanne, Switzerland, 2012.
- S. Siedel, S. Cioulachtjian, A.J. Robinson and J. Bonjour. Experimental determination of the forces acting on a bubble during boiling on a single nucleation site. *8th ECI International Conference on Boiling and Condensation Heat Transfer*, Lausanne, Switzerland, 2012.
- S. Cioulachtjian, S. Siedel, S. Di Bari, A.J. Robinson and J. Bonjour. Nucleate boiling on a wire coated with maghemite nanoparticles or with carbon nanotubes. *8th ECI International Conference on Boiling and Condensation Heat Transfer*, Lausanne, Switzerland, 2012.
- S. Siedel, S. Cioulachtjian, and J. Bonjour. Electric fields effect on the rise of single bubbles during boiling. *7th ECI International Conference on Boiling Heat Transfer*, Florianópolis, Brazil, 2009.
- S. Siedel, S. Cioulachtjian, and J. Bonjour. Experimental analysis of bubble dynamics: Without and with the application of an electric field. *46th European Two-Phase Flow*

Group Meeting, Pisa, Italy, 2008.

- S. Cioulachtjian, S. Siedel, and J. Bonjour. Bubble growth, detachment and rise during boiling on artificial nucleation site. *2nd Rhône-Alpes/Brazil Meeting on Micro and Nano-Technologies applied to Heat Transfer with Liquid-Vapour Phase Change*, São Carlos, Brazil, 2010.